# The SCUBA-2 Instrument: An Application of Large-Format Superconducting Bolometer Arrays for Submillimetre Astronomy

Matthew Ian Hollister

Institute for Astronomy
School of Physics and Astronomy


University of Edinburgh
Doctor of Philosophy

2009

**Abstract**

This thesis concerns technical aspects related to the design and operation of the sub-millimetre common-user bolometer array 2 (SCUBA-2) instrument, a new wide-field camera for submillimetre astronomy currently undergoing commissioning on the James Clerk Maxwell Telescope on Mauna Kea, Hawaii. Offering unprecedented sensitivity and mapping capabilities, SCUBA-2 is expected to make a major impact in surveys of the sky at submillimetre wavelengths, a largely unexplored part of the electromagnetic spectrum, and provide better understanding of the formation and evolution of galaxies, stars and planets by providing large, unbiased samples of such objects.

SCUBA-2 uses large arrays of bolometers, with superconducting transition edge sensors (TESs) as the temperature-sensitive element. TES devices are a relatively new technology, utilising the sharp resistance change between the normal and superconducting states to make a sensitive thermistor. Kilopixel arrays of such devices are multiplexed using superconducting quantum interference devices (SQUIDs). This thesis derives the key detector performance parameters, and presents analysis of engineering data to confirm the detector performance on array scales.

A key issue for bolometric instruments for far infrared and submillimetre astronomy is the need to operate at extremely low temperatures in the sub-kelvin and millikelvin ranges to achieve the necessary detector sensitivity. This work describes the design, testing and performance of the liquid cryogen-free millikelvin cryostat, the first such instrument to be deployed for astronomy. Subsequent chapters detail the design and testing of a magnetic shielding scheme for the instrument, an important aspect of the operation of superconducting devices.

Based on experience with the construction and testing of this instrument, a number of potential improvements for future instruments are presented and discussed.

# Declaration

I declare that this thesis is not substantially the same as any that I have submitted for a degree or diploma or other qualification at any other University. I further state that no part of my thesis has already been or is being concurrently submitted for any such degree, diploma or other qualification.

This thesis is the outcome of my own work except where specifically indicated in the text.

Matthew Hollister

Edinburgh

16 January 2009

# Acknowledgements

So, we finally come to the end of a four year stretch, and now I must think back over the good and bad experiences of my time in Edinburgh and put some coherent thoughts on paper. I will no doubt miss a considerable number of people during this exercise, for which I can only apologise. In any case, here goes.

Firstly, I would like to extend my thanks to my supervisors. Wayne Holland, for giving me the opportunity to work on this project in the first place, for his subsequent support, and for generally being a good sport. Also, Peter Brand on the IfA side. Peter in particular deserves a mention for always being encouraging and enthusiastic, despite having little idea of what I was doing a lot of the time.

I would like to thank my examiners, Peter Ade and Ross McLure, for a thorough viva and useful feedback subsequently. My thanks also to Alan Heavens for surviving the experience.

A very large thank you is deserved to the members of the SCUBA-2 project, for accepting me into the team, freely exchanging knowledge and experience, and of course tolerating me appearing around office doors with "quick" questions. In no particular order: Helen, Jimmy, Mark, Mike, Brian, Dan, Stuart, all the Daves, Eli, Damian, Tom, George, Ian, other Brian, Lynn, Peter, Dennis, Gao, and Alasdair. A particular mention for Adam Woodcraft, from whom I have learnt a considerable amount over the years. Many of these people have become friends as well as colleagues, especially in the blitz spirit of the instrument commissioning. In that line, my thanks to everyone at the JAC in Hilo for making us feel welcome during our stay. A honourable mention must also go to Merle at the Hilo Hawaiian Hotel, for the ready supply of refreshment.

While I'm on the subject, I should probably thank the SCUBA-2 instrument for not being broken *all* the time. After so long with the thing, many late nights, early

mornings and weekends, I felt rather strange walking away for the last time and leaving it on the mountain. Still, I trust it is in good hands.

There are a large number of people at the IfA and the UK ATC with whom I have crossed paths over the years. The first mentions here definitely go to Tom and Jess. The quiz teams will always hold memories of good times, strong drink and dubious knowledge, so here's to Ross, Jo, Olivia, Martin, Michael, Kate, and all the others who have shown up over the years. All the other students at the IfA with whom I have shared the last few years, and of course those from the staff and postdocs. I won't list everyone, which is good since I never bothered to learn half the names. A few folk who do get a mention, however, for various reasons are Anita, Eric, Caz and Miller, Stuart, Mark and Gila, Jenny and Michael, Emma and Bruce, Rita and Simon, Michael D, Chris, Angela, Ben, Michele, Peder, Morag, Alina, Brian, Julia, Niall, Neil, Ed, Barney, Briggs, Campbell and Wing-Fai. It's certainly been ... interesting.

Finally, the biggest thanks goes to my family, without whom none of this would have been possible.

MH
Edinburgh
January 2009

# Table of Contents

# List of Tables

# List of Figures

# Chapter 1

# Introduction

Astronomy at submillimetre and near-millimetre wavelengths does not have a long heritage. It has been only in the last forty years that the importance of observation in this wavelength range (from 200 $\mu$m to 3 mm) has been fully recognised, with an associated increase in interest and effort on instrument development. However, development in instruments and technology for these wavelengths has been slow, primarily hampered by a number of factors, foremost of which being limited atmospheric transmission in the submillimetre, combined with low flux from the observed sources. From a technology standpoint, the limiting factors have been inherently challenging detector technologies, and a lack of telescopes with large collecting areas, good surface accuracy, and at good sites. Despite these problems, a number of pioneering measurements with crude instruments were made in the 1970s, such as solar [1] and planetary [2] maps, and millimetre photometry of extragalactic sources [3, 4].

In the submillimetre and millimetre wavelength range, the Earth's atmosphere is largely opaque, populated by absorption lines due to rotational transitions in molecules, predominately water and oxygen. Atmospheric transmission between 3 mm and 200 $\mu$m is limited to a series of windows of partial visibility between these absorption features, the transmission of the windows being dependant upon the water vapour content of the atmosphere. This is quantified by the precipitable water vapour (pwv) value (pwv

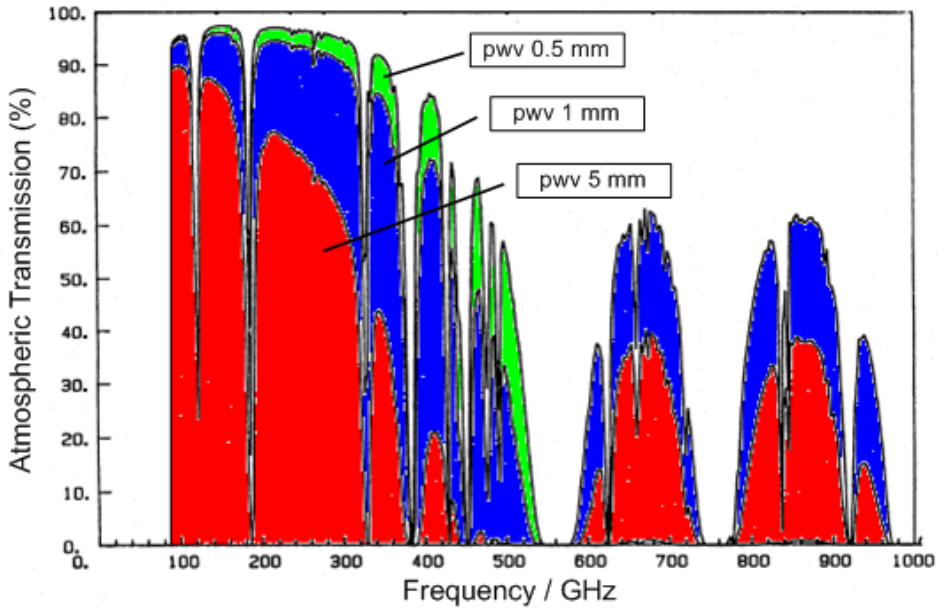


**Figure 1.1:** Atmospheric transmission for the summit of Mauna Kea at submillimetre wavelengths for three precipitable water vapour values. Measurements from the work described in Ref. [5], figure adapted from Ref. [6].

is defined as the total atmospheric water vapour in a vertical column of unit cross-sectional area between the Earth's surface and the "top" of the atmosphere, expressed as the depth of water vapour condensed into a container of the same unit cross section). Fig. 1.1 shows the atmospheric transmission for the summit of Mauna Kea, Hawaii, for a series of pwv values, illustrating the transmission dependency on the atmospheric water vapour. Typically, average pwv decreases with altitude, making high altitude "dry" sites the best choices for ground-based submillimetre observation. The population of spectral features in the wavelength range also results in atmospheric emission being the fundamental limiting factor for the sensitivity of ground-based observation.

The first dedicated submillimetre telescope, the 15 m James Clerk Maxwell, opened in 1987. Operated jointly by the UK, Canada and the Netherlands, the JCMT is located at 4000 m altitude near the summit of Mauna Kea. Prior to this, there were few suitable telescopes for observation in the submillimetre. A number of large radio dishes were operational, but despite the large collecting areas the surface accuracy of the reflectors were very poor for submillimetre observation, and the telescopes tended

to be sited at low altitudes with poor atmospheric transmission at shorter wavelengths. Conversely, although optical and infrared telescopes tend to be at higher altitude sites and have excellent surface accuracy for the submillimetre, the relatively small apertures and collecting areas are of limited use. Despite this, much of the pioneering work in the submillimetre was carried out using telescopes such as the UK Infrared Telescope (UKIRT) on Mauna Kea.

Technologically, development for submillimetre astronomy has always lagged behind that for optical, infrared and radio observation. Detection at the shorter wavelengths is possible with photoconductors, which have been the subject of considerable commercial and military development for numerous applications. Radio receivers too are constructed from commercially available components. Until very recently, there has been no application for submillimetre detector systems outside of the scientific community, so detectors are produced on small scales for individual instruments. Furthermore, incoherent detectors (discussed in §1.2) must be operated at extremely low temperatures ($<$1 K) to achieve the required sensitivity. Heterodyne detection systems in the submillimetre, as with radio frequencies, only require a more modest 4 K operational temperature, while for CCDs in optical astronomy operational temperatures of 100–200 K are sufficient. The operating temperatures of photoconductors are defined by the energy of the bandgap, in turn dictated by the wavelength of operation,[1] but can range from a few kelvin at 200 $\mu$m to 100 K at a few $\mu$m [7]. The use of sub-kelvin temperatures greatly complicates the design of submillimetre instruments, requiring multiple radiation shields and filters to reduce the optical loading on the detectors, which would otherwise cause excess heating.

Despite the difficulties associated with working at these wavelengths, pioneering work with basic photometers in the late 1970s and early 1980s began to show the scientific importance of submillimetre observation, as discussed in the next section.

[1]The longer the wavelength of the radiation to be detected by the photoconductor, the bandgap energy must be smaller to allow promotion of electrons into the conduction band by photon absorption. However, the operating temperature of a photoconductor with a smaller bandgap must also be lower to reduce the thermal promotion of electrons across the bandgap.

## 1.1 Science in the Submillimetre

A number of key discoveries have been made at submillimetre wavelengths concerning the origins of fundamental objects in astronomy - galaxies, stars and planets. In particular, submillimetre astronomy is most sensitive to cold gas and dust. For example, from the Wien displacement law

$$\lambda_{peak} T_{bb} \approx 2900\,[\mu\mathrm{mK}]\,, \tag{1.1}$$

where $\lambda_{peak}$ is the peak emission wavelength and $T_{bb}$ is the temperature of the blackbody, emission from a 10 K blackbody peaks at $\sim$290 $\mu$m. Continuum observation of dust is a better unbiased mass tracer in cold regions than emission from molecules such as CO. Fig. 1.2 shows a series of examples of maps at submillimetre wavelengths made with the submillimetre common-user submillimetre array (SCUBA) instrument on the JCMT, one of the first multipixel instruments to operate in the submillimetre. SCUBA is discussed in the §1.3, while the science examples in the figure are described in more detail below.

On galaxy scales, studies of molecular clouds in the Milky Way have revealed populations of protostars [8] and pre-stellar cores (objects in the process of accreting material to form stars) [9], allowing the early stages of star formation and evolution to be studied. Surveys of star formation in local galaxies, such as NGC891, have also been conducted [10]. A key advantage to such studies in the submillimetre is that at longer wavelengths, the continuum emission from nearly all objects is optically thin, allowing the core of such objects to observed. While at optical and infrared wavelengths, observations are made of stellar surfaces or light scattered from dusty discs, submillimetre observation is able to trace material collapsing onto the central object. Observations of the earliest stages of star formation are vital in order to understand the evolutionary process (or indeed, processes) that give rise to evolved stars, brown dwarfs and small, free-floating planetary mass objects.

A major discovery in the submillimetre was made from observations of young, main sequence stars that showed excess emission in the infrared in IRAS (the Infrared Astronomical Satellite) observations. Four objects ($\epsilon$-Eridani, $\tau$-Ceti, Vega and Fomalhaut) were found to include discs of cold dust around the host star. Perturbations in the discs

were found to be consistent with the presence of planetary mass objects orbiting within the dust [11].

Early measurements of the star formation rate as a function of redshift using optical and infrared observations appeared to indicate that the star formation rate peaked at a redshift of $\sim$1. However, with the discovery of a previously unknown population of high redshift, ultraluminous galaxies in maps such as the SCUBA image of the Hubble Deep Field (Fig. 1.2(b)), the peak of the star formation rate is moved to higher redshift, and crucial observational evidence is provided that, for at least some massive galaxies, the epoch of star formation occurred at higher redshifts than predicted by the standard models of hierarchical galaxy formation available at the time [15, 16].

On very large scales, the cosmic microwave background (CMB) spectrum, emanating from the epoch of recombination 300 000 years after the Big Bang, peaks at 1.1 mm (peak emission for a 2.7 K blackbody). Studies of the structure of the primordial universe are made in the submillimetre and near-millimetre wavebands (e.g. [17]). Of perhaps equal importance is the presence of a far-infrared/submillimetre cosmic background. Fig. 1.3 illustrates the radiation spectrum from the cosmic background between 1 cm and 0.1 $\mu$m. The dominant component is the microwave background from the primordial universe. The second largest component, at about 5.9% of the mean intensity of the microwave background, is the optical/infrared background originating from stars and galaxies in the evolved universe. The smallest component is the FIR/submillimetre background, the origin of which is known to be ultraluminous galaxies in the young universe ($z$>2) [13]. While microwave and optical backgrounds have been mapped in detail over the entire sky, only an area of around 1 square degree has been imaged in the submillimetre to any appreciable depth.

Submillimetre observation also contributes to many other areas of astronomy. Fundamentally, the ability of submillimetre astronomy to probe cold, dusty environments is of key importance to an understanding of evolutionary processes. However, as will be discussed in subsequent sections, technological limitations mean that there is still considerable territory to explore.

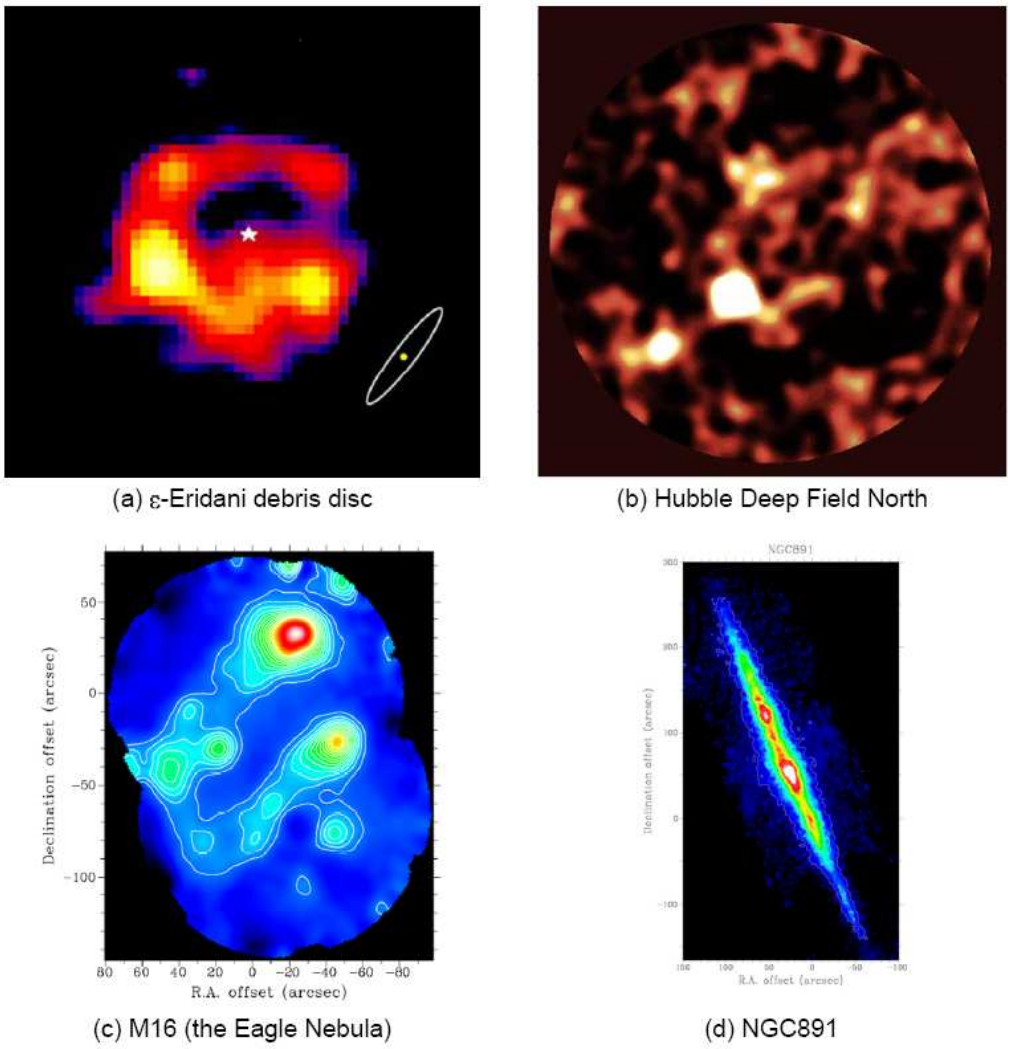


**Figure 1.2:** A selection of submillimetre observations made with the original submillimetre common-user bolometer array (SCUBA) camera on the JCMT. (a) debris disc around the main sequence star $\epsilon$-Eridani at 850 $\mu$m, showing the non-uniform features of the dust. The ellipse in the bottom right corner of the image shows the orbit of Pluto in our own solar system for scale [12]. (b) 850 $\mu$m image of the Hubble Deep Field North, showing 6 resolved sources that contribute to the submillimetre and FIR background [13]. (c) 450 $\mu$m image of M16, the Eagle Nebula, a star forming region in our own galaxy, illustrating the dust concentration near the ends of the "finger" structures, consistent with high rate star formation [14]. (d) 850 $\mu$m image of NGC891, a nearby edge-on spiral galaxy, showing the dust concentration in the galaxy centre and secondary peaks indicative of spiral arms or a ring structure [10].

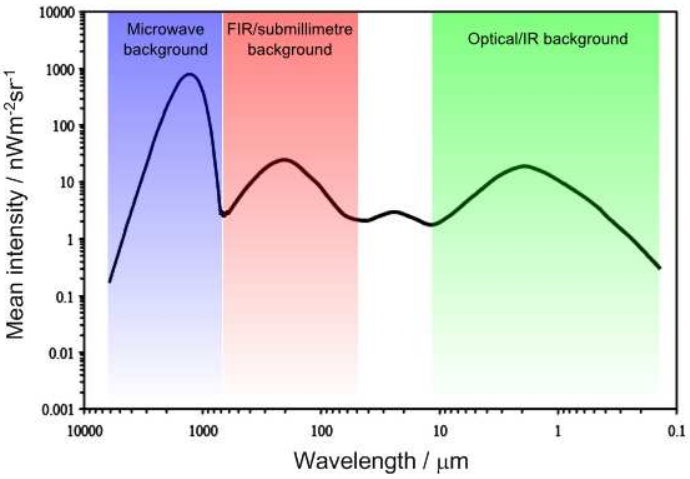


**Figure 1.3:** The spectrum of the cosmic background radiation from 0.1 $\mu$m to 1 cm. Adapted from Refs. [18, 19].

## 1.2 Detection of Submillimetre Radiation

As a consequence of lying between infrared and radio wavelengths, submillimetre detection has seen almost independent development of techniques from both disciplines. There are two detection schemes generally in use for this wavelength range, which will be discussed briefly.

Coherent (heterodyne) systems detect the intensity and phase of the incident radiation. Heterodyne systems are mostly used in the submillimetre for studies of discrete spectral lines (typically from rotational transitions of molecules such as $H_2O$ and CO). A heterodyne detection system is illustrated schematically in Fig. 1.4(a). A high frequency signal from an astronomical source (typically a few hundred GHz) is converted to a lower intermediate frequency (IF) signal by mixing a strong local oscillator frequency with the weaker science signal and taking the difference signal. The IF signal (typically 3–4 GHz) is then output to a spectrometer. A number of different devices may be used as mixers in the submillimetre spectral range, including SIS (superconductor-insulator-superconductor) tunnel junctions [20,21] and hot electron bolometers (HEBs) [22]. Note that for high frequency heterodyne detection there is no preamplifier in front of the mixer since above 40 GHz stable amplifiers are difficult to construct, and so the IF must be generated before amplification [23].

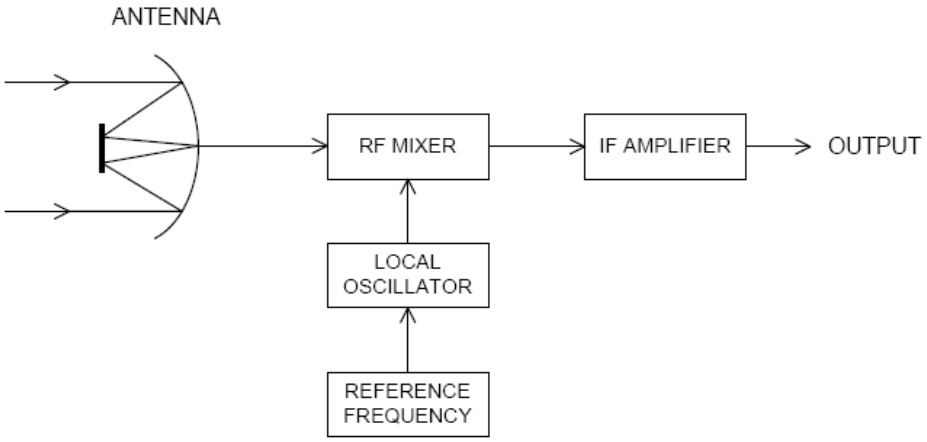


**Figure 1.4:** Block diagrams representing (a) coherent and (b) incoherent detection schemes for submillimetre radiation. In the coherent (or heterodyne) scheme, the science signal is mixed with a reference frequency injected by a local oscillator to an RF mixer. The difference (or intermediate) frequency (IF), which is considerably lower than the observing frequency, is then amplified. In the incoherent scheme, the signal from the antenna is detected directly by a bolometer (or other detector) and then amplified. Adapted from Refs. [24, 25].

Incoherent detection, generally using a bolometer as the detecting element, is used primarily for broadband photometry or low resolution spectrometry when combined with appropriate optics. The sensitivity of incoherent detection systems for continuum observation is considerably greater than coherent systems as a result of the large pre-detection bandwidth of bolometers (mixers are essentially monochromatic). The downside to the large pre-detection bandwidth of bolometers is that the observing band must be carefully defined through the use of cryogenic filters.[2] The principle of operation is discussed below. An incoherent detection scheme is illustrated in Fig. 1.4(b). The astronomical signal is detected directly by the bolometer, and the output of the detector is amplified. Since this thesis concerns incoherent detection systems, bolometric detectors will be described in more detail below and in §1.3.

### 1.2.1 Bolometric Detectors

Bolometers, also referred to as "microcalorimeters", are thermal detectors which measure the power of incident electromagnetic radiation using a temperature-sensitive thermistor. When cooled below 1 K, bolometers are the most sensitive broadband detectors for millimetre and submillimetre wavelengths [27, 28] (the limit for stressed photoconductors is around 200 $\mu$m, while above 3 mm heterodyne receivers become competitive). Although initial development occurred for use at far infrared to millimetre wavelengths, the versatility of the detectors has led to adoption in other areas of astronomy, such as for x-ray spectroscopy [29, 30] and particle detection for dark matter experiments [31].

The thermistor is strongly coupled to incident power by an absorber of heat capacity $C$, and is weakly coupled to a cold bath at temperature $T_0$ by a thermal link of conductance $G$. The absorbed power, $Q$, causes the temperature, $T$, of the absorber to rise. This is detected as a change in resistance, $R(T)$, of the thermistor element. A schematic of a bolometer is depicted in Fig. 1.5.

The theory and principles of operation of bolometric detectors have been described in detail elsewhere (for example, Refs. [26, 32]. The two major performance parameters

[2] Although the sensitivity of the system is essentially proportional to the square root of the pre-detection bandwidth, a narrow bandwidth is advantageous since the reduction in the thermal background on the detector offers a sensitivity increase by lowering photon noise [26]. The best sensitivity is achieved by balancing these effects.

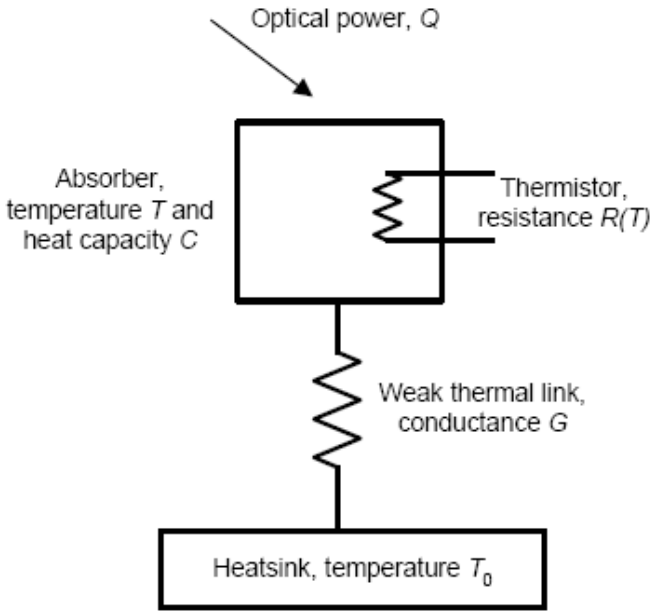


**Figure 1.5:** Schematic representation of a bolometer. The absorber, with heat capacity $C$ and at a temperature $T$ is coupled to the heat sink at temperature $T_0$ by a weak thermal link of conductance $G$. The incident optical power, $Q$, produces a temperature change in the absorber, which is measured as the change in resistance, $R(T)$, of a thermistor element.

for a bolometer are the time constant, $\tau$, and the noise equivalent power, NEP. The time constant is given by the ratio of the heat capacity of the bolometer, $C$, to the thermal conductance, $G$, of the link to the cold bath. The NEP of a detector is defined as the smallest amount of power a device can detect with a signal-to-noise of unity and a 1 Hz post-detection bandwidth.

Noise sources in the operation of bolometers will come from a combination of statistical fluctuations in the power falling on the absorber ("photon noise"), and the inherent noise of the detector itself. For an ideal bolometer, the detector noise contribution should arise from only two sources: Johnson noise and phonon noise. Johnson noise results from the random motion of electrons in the thermistor element. The contribution of Johnson noise to the overall NEP, $\mathrm{NEP_j}$, for a device resistance $R$ and at a temperature $T$, is given by [33]

$$\mathrm{NEP_j^2} = \frac{4kTR}{S^2}, \tag{1.2}$$

where $k$ is the Boltzmann constant and $S$ is the responsivity of the device (the output voltage per input power). The phonon noise contribution, due to the quantisation of the phonons transporting energy in the thermal link to the cold bath, $\mathrm{NEP_p}$, is given by

$$\mathrm{NEP_p^2} = 4\gamma k T^2 G, \tag{1.3}$$

where $G$ is the thermal conductance of the link to the cold bath and $\gamma$ is a factor, of order unity, that describes the temperature gradient along the link. Other sources of "electronic" noise, such as Johnson noise in the readout electronics, if designed with care, will contribute only a small noise level and therefore may be neglected.

The photon noise includes contributions from the sky, telescope and the instrument itself. For a radiation passband with a frequency interval $\Delta\nu$ about a central frequency $\nu_0$, assuming the Rayleigh-Jeans approximation is valid ($h\nu < kT$), then the NEP due to photon noise may be written as

$$\mathrm{NEP_{ph}^2} = 2Q(h\nu_0 - \eta\epsilon kT), \tag{1.4}$$

where $\eta$ is the transmission, $\epsilon$ the emissivity of the background, and $Q$ is the absorbed incident power, given by

$$Q = A\Omega B(\nu_0, T_b)\Delta\nu\eta\epsilon, \tag{1.5}$$

where $A\Omega$ is the telescope throughput, and $B(\nu_0, T_b)$ is the Planck function for a background temperature $T_b$.

The photon and the phonon noise are frequency-independent. However, the responsivity, $S$, varies with the signal frequency, and so the Johnson noise NEP as a function of frequency, $\omega$, becomes

$$\mathrm{NEP_j}(\omega) = \mathrm{NEP_j}(0)(1 + \omega^2\tau^2)^{\frac{1}{2}}, \tag{1.6}$$

where $\mathrm{NEP_j}(0)$ is the DC value of the Johnson noise NEP. This frequency dependance can have consequences if a modulated detection scheme is employed.

The NEP contributions are added in quadrature since the individual components are uncorrelated and the noise fluctuations are Gaussian [32]. The total system NEP is then given by

$$\mathrm{NEP}_{\mathrm{total}} = \sqrt{\mathrm{NEP}_{\mathrm{ph}}^2 + \mathrm{NEP}_{\mathrm{j}}^2 + \mathrm{NEP}_{\mathrm{p}}^2}. \tag{1.7}$$

Even for an idealised bolometer with no detector noise, the photon noise will still limit the total NEP of the detector, $\mathrm{NEP}_{\mathrm{det}}$, given by the quadrature sum of the Johnson and phonon noise NEPs. In an ideal device, $\mathrm{NEP}_{\mathrm{det}}$ will be sufficiently small that the photon noise will dominate. This is referred to as background limited performance.

It can be shown that the inherent $\mathrm{NEP}_{\mathrm{det}}$, , of a bolometer with no background optical loading and for a fixed time constant can be written as $\mathrm{NEP}_{\mathrm{det}} \propto T^x$, where $1.5 \leq x \leq 2.5$, as a consequence of the temperature dependance of the heat capacities of the materials composing the bolometer ($T$ for metals and $T^3$ for dielectrics) [33]. The ultimate sensitivity of the bolometer can therefore be improved by lowering the operating temperature of the device (at least, until the photon noise begins to dominate). Since early work on the noise performance and speed of response of cryogenic bolometers (for example, at helium temperatures [34]), continual performance improvements have been achieved by operation at low temperatures to the point where bolometers may be background limited at even the shortest submillimetre wavelengths.

The development and specific design of bolometric detectors are discussed in more detail in §1.3.

## 1.3 Technological Advances for Submillimetre Astronomy

As discussed previously, development of astronomy in the submillimetre has been driven by the availability of technologies for both detector and telescope construction. The difficulties associated with detection of submillimetre radiation led to development both of ground-based telescopes and experiments for balloon flights, and eventually space-based platforms such as the Submillimetre Wave Satellite (SWAS) [35] and the upcoming European Space Agency far-infrared mission, Herschel [36]. Observation from balloon platforms has greatly contributed to our understanding of the submillimetre universe, particularly in the field of the CMB, with observations from MSAM [37],

BOOMERanG [38] and BLAST [39] amongst numerous others, and has benefitted from the same instrument development as ground-based astronomy. This section aims to provide a brief overview of the development of instrument technologies for the millimetre and submillimetre wavebands, with particular emphasis on ground-based observation.

### 1.3.1 Early Instruments

The first instruments for observation in the submillimetre were single-pixel photometers, early examples of which being the Queen Mary College/University of Oregon No. 2 $^3$He System [40] and UKT14 [6]. Both instruments covered the submillimetre spectrum by using a series of selectable filters matched to the atmospheric windows between 300 $\mu$m and 2 mm, detecting radiation with a single composite bolometer [41] in a hemispherical integrating cavity. Operating from a $^3$He bath at 350 mK, the UKT14 bolometer achieved an NEP close to background limited performance at 1.1 mm. UKT14 was initially used on UKIRT, transferring to the JCMT when the new telescope came online.

### 1.3.2 Array Cameras

With the availability of the first dedicated telescopes for the submillimetre, and single bolometer photometers approaching fundamental performance limits, the next development step was a move towards multipixel array instruments in order to maximise the scientific output of the telescopes. The use of array cameras was particularly important for mapping of extended sources, since raster-scanning a single pixel across a source to produce maps is a time-consuming process. In the early 1990s, a small number of array cameras were planned or already in operation, such as the Firenze 9 Channel $^3$He Bolometer Array for the TIR balloon telescope [42]. Arguably the most important of these early array cameras, at least in terms of scientific impact, was the submillimetre common-user bolometer array (SCUBA) instrument for the JCMT [43]. SCUBA used two focal planes, with 91 pixels optimised for 450 $\mu$m observation (with filters for 450 and 350 $\mu$m), and 37 pixels optimised for 850 $\mu$m detection (850 and 750 $\mu$m filters), in addition to single pixels for photometry at 1.1, 1.3 and 2 mm. The two arrays of bolometers operated from a 100 mK bath provided by a dilution refrigerator. While

earlier instruments had essentially been limited by detector noise, SCUBA was designed to be background noise limited.

In parallel to the the success of SCUBA, a number of other bolometer array cameras using similar technology were constructed for various telescopes. An example of these "first generation" cameras was SHARC (submillimetre high-angular resolution camera), a 24 bolometer array for 350 and 450 $\mu$m observation on the Caltech Submillimetre Observatory [44]. Currently, the largest array camera in operation is SHARC II, with 384 silicon "pop-up" bolometers (see discussion below), also on CSO, and operating in the 350 and 450 $\mu$m windows [45].

The array cameras currently operating have reached background limited performance, and so the limiting factor for deep- and wide-field astronomy with the current generation of array cameras is the scalability of the detector technology. With the exception of the SHARC instruments, the early instrument examples use essentially the same technology as the original SCUBA detectors, with individually assembled bolometers building up an unfilled array. Using such architecture to construct larger arrays is unfeasible. The technology used for the SHARC and SHARC II detectors forms linear arrays of pixels than may be butted together to form small two-dimensional focal planes, but even this has limited potential for scaling. New technologies and bolometer designs, discussed in the next section, are now evolving that allow kilopixel arrays to be realised, leading to a new generation of sensitive, wide-field instruments. Observations with unprecedented angular resolution and sensitivity will be possible using interferometer arrays working in the submillimetre (SMA and ALMA), but as discussed in §1.1, the small area of sky surveyed in the submillimetre means that sensitive, wide-field cameras still have an important role to play, particularly for survey astronomy.

### 1.3.3 Bolometer designs

As discussed in §1.2, a bolometer is essentially an absorber with a temperature-sensitive element attached. The two components are not necessarily separate, as was the case for the earliest examples of this type of detector, although there are considerable advantages to separating the absorber and thermistor components.

The earliest work on bolometers used simple thermocouples at ambient temperature to detect incident radiation, but such devices rapidly reached a sensitivity limit imposed by Johnson noise in the circuits. However, cooling such devices, while lowering the detector noise, also reduced the device responsivity and resulted in a net decrease in sensitivity [46]. The first cryogenic bolometers used superconducting materials as the thermistor, an approach suggested some years earlier [47]. Strips of tantalum at 4 K or niobium nitride at 15 K were epoxied to copper heat sinks and proved practical for detection of shortwave infrared sources [46, 48]. The drawback of such devices was that the sensitivity was not high, and the thermistors displayed poorly understood $R(T)$ characteristics. Later work used carbon thermistors [49], and germanium [34], both of which showing better resistance-temperature characteristics.

**Semiconductor Composite Bolometers**

Separation of the absorber and thermistor elements allows the two components to be optimised separately, leading to the concept of a "composite" bolometer. A number of different designs have been used, but the general construction of the devices is a metal-coated dielectric absorber coupled to a temperature-sensitive semiconductor element such as germanium or silicon. Such devices are still the most common implementation of the bolometer design, although, as discussed below, a move towards superconducting thermistors is underway.

The detectors for the original SCUBA instrument [50] used chips of neutron transmutation doped (NTD) germanium [51] epoxied to the centre of hexagonal sapphire substrates. The substrates were coated with a bismuth film to provide an impedance match to incoming radiation. Each bolometer was hand assembled as a "plug in" package, incorporating an overmoded integrating cavity, as shown in Fig. 1.6.

NTD germanium thermistors are an excellent choice for bolometers, since the material displays a very well understood $R(T)$ characteristic that can be described by a simple model [52]. This understanding of the resistance characteristic is vital in order to predict the behaviour of the bolometer under different bias and background load conditions [26]. Semiconductor thermistors typically have impedances of a few M$\Omega$, making the devices well-matched for use with JFET amplifiers since the Johnson noise in the

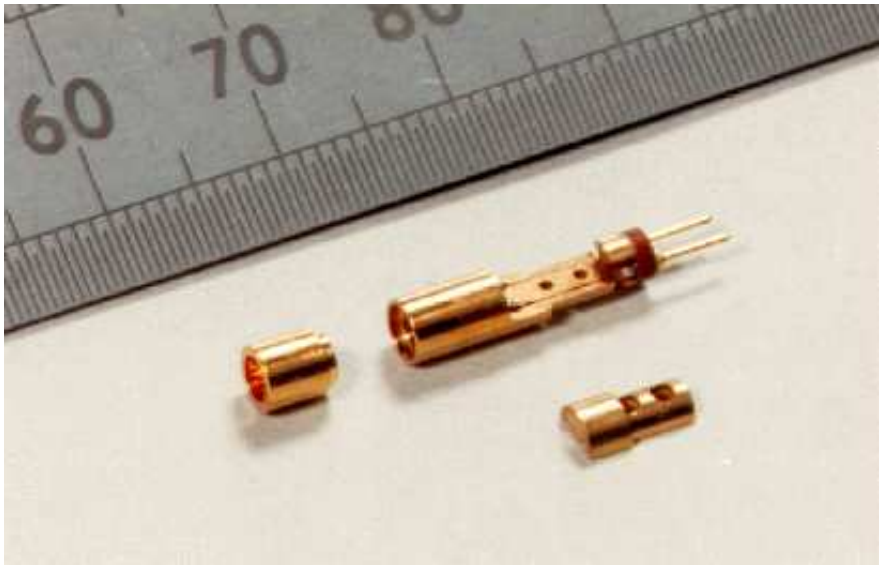


**Figure 1.6:** Germanium composite bolometer from the SCUBA instrument. Figure adapted from Ref. [33].

bolometer will dominate the amplifier noise. Limited multiplexing may be achieved with MOS devices.

At present, the best available semiconductor bolometer design is the so-called "spider web" layout, with a metallised silicon nitride web structure as the absorber, and an NTD germanium thermistor chip bump-bonded to the centre [53]. The spacings of the web are smaller than the wavelength of the incident radiation, and hence the structure acts as a plane surface, while the mesh layout has a very small cross section, reducing the heat capacity of the absorber and so decreasing the time constant for a given set of operating parameters. An example of a bolometer with a spider web absorber is shown in Fig. 1.7. The small cross section of the mesh structure has a further advantage in that the susceptibility to ionising radiation is reduced, which is particularly important for application in space. Bolometers of this type are in use for the Planck high frequency instrument (HFI) [54], and formed into arrays [55] for the SPIRE instrument of the Herschel FIR space observatory [56].

### Silicon Pop-Up Bolometers

In addition to the composite bolometers described above, another implementation that has found use in the SHARC and SHARC II instruments on the CSO and is intended for use in instruments for the SOFIA airborne observatory is the silicon "pop-up" bolometer [57]. These detectors use ion-implanted silicon thermistors, forming a linear array of pixels with the electrical and thermal connections behind the array. This allows lines of pixels to be butted together to form a close-packed two-dimensional structure in the instrument focal plane. The SHARC II focal plane, with 12 arrays of 32 pixels, is shown in Fig. 1.8.

### Transition Edge Sensors

More recently, practical temperature-sensitive devices based on superconducting materials have been realised. Known as transition-edge sensors (TESs), the devices are designed to exploit the large change in resistance in the transition between the superconducting and normal states of the material [59, 60]. Early devices, mostly developed for x-ray detection [61], used elemental superconductors, frequently titanium or tungsten since these have the lowest transition temperatures of the superconducting elements (400 mK and 120 mK, respectively[3]) [62]. However, the relatively high transition temperature of titanium limits the ultimate noise performance of such devices, while sensors fabricated with tungsten thin films were found to show large variations in $T_c$.

The transition temperature of the TES may be reduced (and tuned) by using the proximity effect, in which a bilayer or multilayer of superconducting and normal metal thin films will exist in a "mixed" state, rather than a pure superconducting state, with a lower transition temperature than the elemental superconductor alone (see Chapter 7 for additional discussion of the proximity effect). The suppression of $T_c$ may be controlled by varying the thickness of the layers. Tuning of $T_c$ in this way gives more accurate and consistent results than elemental thin films, and allows the use of a wider range of materials in the fabrication process. The first bilayer TESs were composed of iridium and gold, and showed excellent performance [63]. However, Ir/Au bilayers are difficult

[3]The transition temperature of thin superconducting films will often differ slight from the bulk material, and will show sensitivity to a variety of processing and deposition parameters.

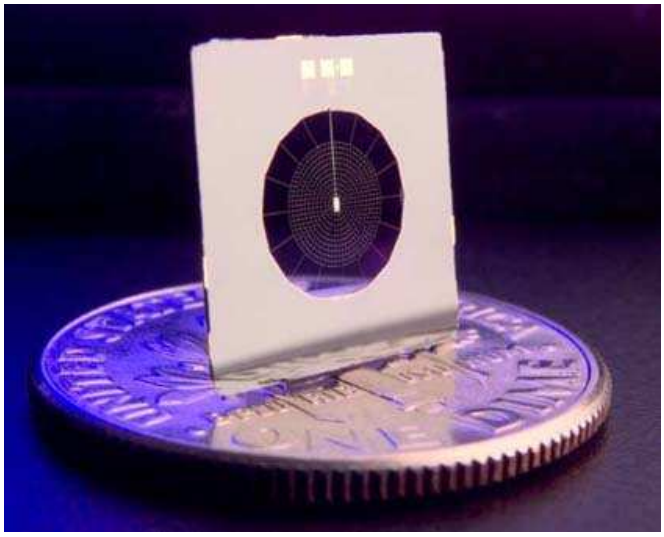

**Figure 1.7:** Spiderweb composite bolometer, with a US ten cents coin for scale. The metallised absorbing mesh may be seen, with the NTD germanium chip at the centre. Image taken from Ref. [58].

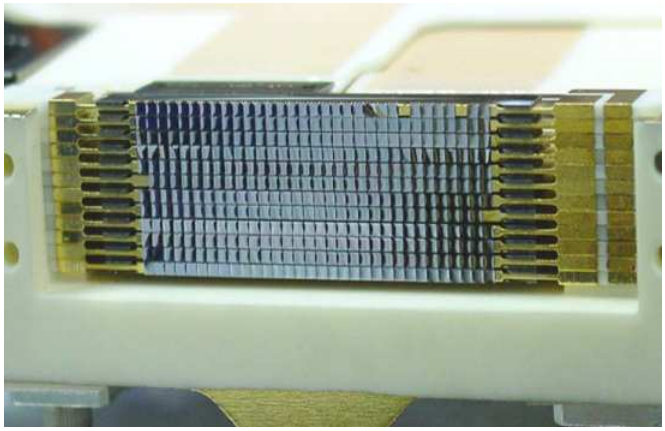

**Figure 1.8:** Silicon pop-up bolometers in the SHARC II focal plane. The focal plane is populated with 12 linear arrays of 32 pixels, for 384 pixels in total. Each pixel is 1 mm square. Figure taken from Ref. [45].

to fabricate, requiring deposition of iridium films onto high-temperature substrates. Later work showed that higher-$T_c$ superconductors, such as aluminium ($T_c$ = 1.1 K) and molybdenum ($T_c$ = 0.95 K) could be used in bilayer fabrication far more easily. Common bilayer combinations are titanium-copper [64] and molybdenum-copper [65].

The TES devices have a low normal state impedance (typically $\sim$1 $\Omega$ or less), making the detectors poorly matched to FET amplifiers. The low TES resistance greatly reduces the level of Johnson noise in the detector, so the noise of the FET would dominate the overall system noise. However, this issue has been eliminated by the use of superconducting quantum interference devices (SQUIDs), which are inherently low impedance and low noise devices. SQUID readouts have a further advantage in that they can be easily multiplexed, making large arrays of TESs at low temperature highly practical [66]. SQUIDs can also act as low-noise amplifiers. The SQUIDs have low power dissipation, making it possible to construct multiplexers and amplifiers at the same operational temperature as the detectors, decreasing noise in the readout electronics. As a result of the low impedance of the thermistor, TESs have a low susceptibility to microphonic pickup, which can be a serious issue for semiconductor bolometers.

One of the major advantage of TES devices over semiconductor bolometers are a higher sensitivity to temperature changes due to the steep $R(T)$ characteristic in the transition. The sensitivity of the devices is essentially given by the gradient of the $R(T)$ characteristic at the bias point, described by the temperature coefficient of resistance, $\alpha$, given by [33]

$$\alpha = \frac{T}{R}\frac{\mathrm{d}R}{\mathrm{d}T}. \tag{1.8}$$

For semiconductor bolometers, $\alpha$ will have values of 5–10, while for TES devices values of 50–2000 are easily achieved. The difference in the $R(T)$ characteristic for the two types of devices is illustrated schematically in Fig. 1.9.

However, there are problems associated with the TES devices in that the detector must be biased in the transition. This issue was a major impediment to the development of TESs as practical devices. When current biased, as is done with semiconductor thermistors, Joule heating in the TES can lead to thermal runaway, while small fluctuations in the bath temperature have a major effect on the device performance. Furthermore,

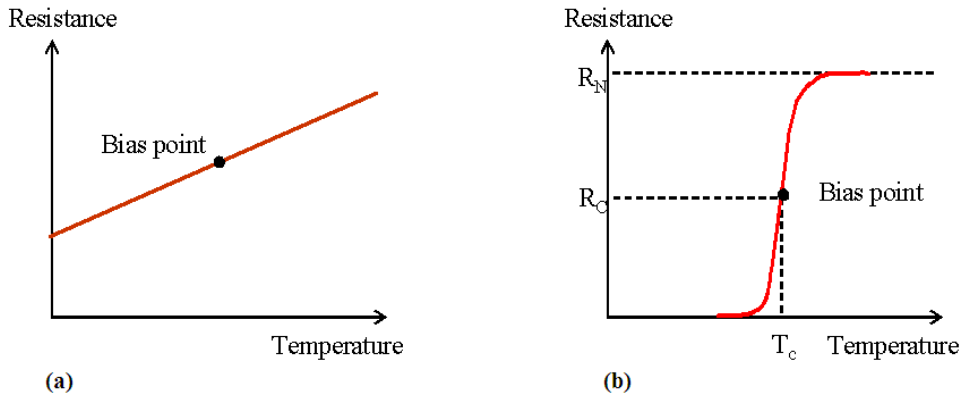


**Figure 1.9:** Schematic representation of the $R(T)$ characteristic for (a) a semiconductor thermistor and (b) a superconducting TES device. For the TES device, $R_N$ is the normal state resistance, while $R_c$ is the resistance at the critical temperature, $T_c$, of the transition.

small variations in $T_c$ between devices would make simultaneous biasing of a number of detectors in the transition for a given bath temperature virtually impossible. If the TES is instead voltage-biased and read out with a current amplifier, the devices can be stably biased and will self-regulate within the transition, with lower sensitivity to fluctuations in the bath temperature [59]. The electrothermal feedback (ETF) resulting from voltage-biasing also suppresses the Johnson noise contribution to the detector NEP by a factor of $\alpha^2$ [33, 67]. More discussion of noise in TES devices in included in Chapter 3. NEPs of $\sim 10^{-17}$ W/$\sqrt{\text{Hz}}$ and lower are easily achieved with TES devices, while semiconductor thermistors typically have NEPs of $\sim 10^{-16}$ W/$\sqrt{\text{Hz}}$. Bolometer NEPs may be reduced by changing physical parameters such as lowering the thermal conductance, $G$, but this is at the expense of degrading the time constant and making the detectors slower. Depending upon the application, it may be desirable to make the bolometers faster, or with lower noise, or a compromise between the two characteristics.

A further consequence of the narrow transition is that the TES can only handle a fixed power level before being driven into the normal state and becoming unresponsive. This is a particular problem for the use of TESs in submillimetre astronomy due to the variability in the background loading from the sky. This issue is partially overcome in the SCUBA-2 design by bringing the TES into the transition region with a combination of bias power and power supplied by individual pixel heaters. This approach is discussed

further in Chapter 3. A similar problem exists in the application of TESs for space-based observation, where the background loading environment is not well understood.

A key advantage of the TES is in fabrication. TES detectors may be produced with standard lithographic techniques, making the production of large arrays a practical proposition. Semiconductor bolometers are essentially individually assembled (or at best produced in small arrays), limiting pixel counts.[4] Initially, TES bolometers used a similar design approach to the composite semiconductor bolometers already described, in which the TES is coupled to an absorber element. Antenna-coupled TES bolometers have also been demonstrated. This scheme offers advantages in that the fabrication process is simplified, allowing better scalability to large arrays, and that the time constant of the detectors can be reduced since there is no absorber to contribute to the pixel heat capacity [68].

Kilopixel arrays of absorber-coupled TES detectors are utilised for the SCUBA-2 focal planes. A number of other instruments using TES bolometers are operational, generally with ∼100 pixels and operating at millimetre wavelengths. The first instrument to use TES devices in the submillimetre was the FIBRE spectrometer on the CSO, with a linear array of 8 pixels [69]. Recently commissioned instruments with multiplexed TES detectors are GISMO, with 128 pixels operating at 2 mm on the IRAM telescope [70], and the 64 pixel MUSTANG instrument for 3.3 mm observation on the 100 m Greenbank Telescope [71].

Current SQUID-based multiplexers operate as time-domain multiplexing (TDM) systems. The is considerable interest the development of frequency-domain multiplexing (FDM), since this could further reduce the necessary wire counts and offer much greater scalability of detector arrays. A limitation of current implementations is that the length of cable between the SQUIDs at the focal plane and the warm electronics is limited to a few hundred millimetres, making construction of instrument cryostats for such schemes difficult. This cable length limit is due to the propagation time of signals. In these designs, it is necessary to perform feedback operation on high frequency signals, so the propagation time of the signals along the cables to the focal plane must be short [72,73].

[4]Newer semiconductor bolometer designs, such as the spider web absorber, are produced by patterning the absorbers by lithography, but the thermistor element must be attached manually.

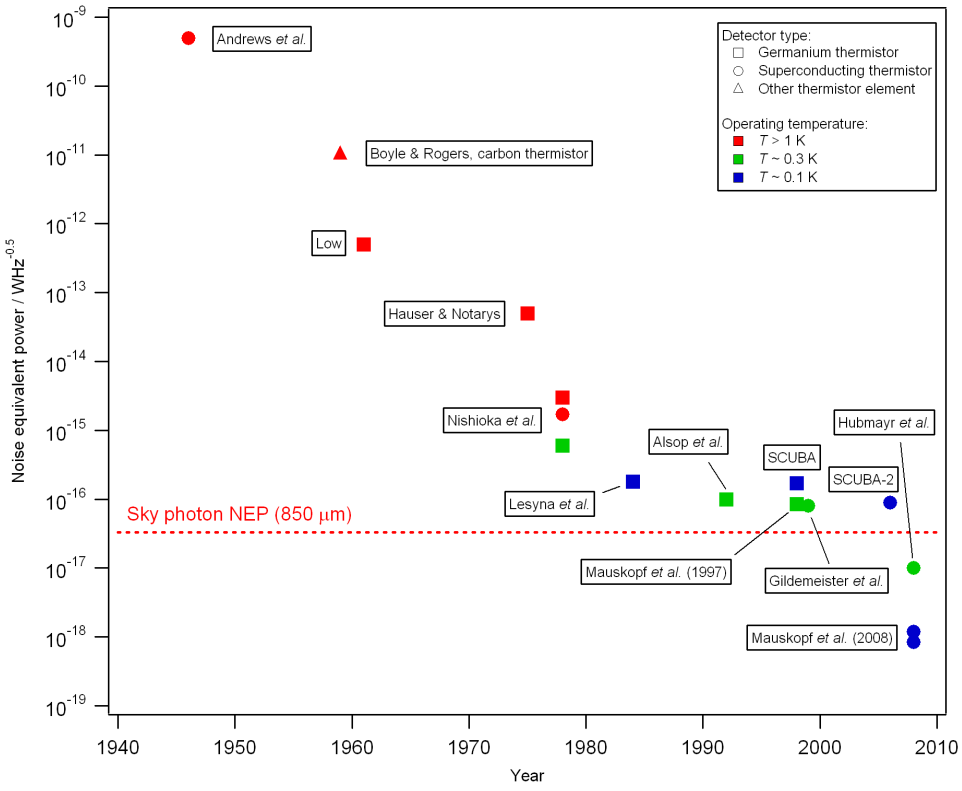


**Figure 1.10:** Graph illustrating the improvement in noise performance for a selection of detectors described in the literature since initial work by Andrews *et al.* [46] in 1946. Referenced work includes the 4 K carbon bolometer of Boyle & Rogers [49]; the work of Low with germanium composite bolometers at 2 K [34]; the InSb hot electron bolometer of Kinch & Rollins [74]; the 1.8 K Ge bolometer of Hauser & Notarys [75]; a series of measurements with Ge and superconducting Al thermistors at 1.2 and 0.3 K by Nishioka *et al.* [76]; measurements at 0.1 K with Ge bolometers by Lesyna *et al.* [77]; the bolometers of Alsop *et al.* [78] and Mauskopf *et al.* (1997) [53] at 0.3 K; the spiderweb TES bolometers described by Gildemeister *et al.* [79]; the TES detectors of Hubmayr *et al.* for balloon observations [80]; and the low-noise TES devices for the SAFARI instrument on the space telescope SPICA, reported by Mauskopf *et al.* (2008) [81]. Also included are NEP figures for SCUBA [11] and SCUBA-2 (at 450 $\mu$m) as representative examples of functional instruments rather than isolated detectors. The horizontal line is the sky photon NEP for 850 $\mu$m at 80% sky transmission, generated from the SCUBA-2 photon noise model (see Chapter 3). A number these measurements are seen to converge towards this limit, since they are intended to background limited operation from the ground. The examples of Hubmayr *et al.* and Mauskopf *et al.* (2008) are intended to work in lower background environments.

**Table 1.1:** Comparison of details of a selection of submillimetre and millimetre wave instruments, including operation wavelength; telescope and primary reflector diameter; period of operation; and number and type of detector.

| Instrument | Wavelength / $\mu$m | Telescope (Diameter) | Year of operation | Number of pixels | Detector type | Reference |
|---|---|---|---|---|---|---|
| UKT14 | 350–2000 | JCMT (15 m)[a] | 1988–1996 | 1 | Germanium | [6] |
| SCUBA | 350–850[b] | JCMT (15 m) | 1996–2006 | 128[c] | Germanium | [43] |
| SHARC | 350 and 450 | CSO (10 m) | 1996–2002 | 24 | Germanium | [44] |
| BoloCAM | 350 and 450 | CSO (10 m) | 1998– | 144 | Germanium[d] | [82] |
| MAMBO | 1200 | IRAM (30 m) | 1998– | 37 | Germanium | [83] |
| SHARC-II | 350 and 850 | CSO (10 m) | 2002– | 384 | Silicon pop-up | [45] |
| GISMO | 2000 | IRAM (30 m) | 2004– | 128 | TES | [70] |
| MUSTANG | 3300 | GBT (100 m) | 2006– | 64 | TES | [71] |
| LABOCA | 870 | APEX (12 m) | 2007– | 295 | Germanium[d] | [84] |
| SCUBA-2 | 450 and 850 | JCMT (15 m) | 2009 (expected) | 10240[e] | TES | [85] |

[a] Initially used on UKIRT (3.8 m).

[b] Also single photometry pixels at 1.1, 1.3 and 2.0 mm.

[c] 128 bolometers in two arrays. 37 bolometers in the longwave array, and 91 in the shortwave.

[d] Spider web absorber.

[e] Two focal planes of 5120 pixels once instrument upgrade is complete.

### Performance Improvements with Time

The improvement in bolometer noise performance during the sixty years of development is represented in Fig. 1.10, with noise equivalent power for a number of examples from the literature plotted against the year of publication. As discussed previously, much of the improvement in detector NEP is the result of the move towards lower operating temperatures. The photon NEP from the sky background at 850 $\mu$m is indicated as a representative target noise level. A number of the measurements close to this limit are representative of instrument systems, and are therefore designed to operate close to the background limit. Other examples represent low-NEP devices to use at lower backgrounds, either from better sites or in space.

Table 1.1 summarises and compares the specifications for selection of millimetre and submillimetre instruments, including wavelengths of operation, the diameter of the telescope on which the instrument has been used, the period of operation and the number of type of pixels. This list is not complete, but is intended to illustrate the development in the instrument field for this waveband over the last two decades. The examples listed are representative of common-user continuum instruments, and excludes spectroscopic or specialised instruments.

### Other Detector Technologies

The use of superconducting materials in the construction of detectors for submillimetre and x-ray wavelengths opens a number of other possibilities for the detection methods. These detectors are beyond the scope of the current discussion, but will be described briefly for completeness.

Superconducting tunnel junctions (STJs), also referred to as SIS (superconductor-insulator-superconductor) detectors, were first demonstrated as x-ray detectors [86], and later for submillimetre and terahertz photon detection [87]. Such detectors are composed of two pieces of superconductor seperated by an insulating junction. When a photon is incident on the superconductor, Cooper pairs are broken, forming a large number of excited electrons ("quasiparticles") that are able to tunnel through the insulating junction and be detected as a pulse of current.

A newer type of "pair-breaking" detector that is seeing considerable development interest is the kinetic inductance detector (KID) [88]. KIDs are designed to operate in an $LC$ resonance circuit. The absorption of a photon by the KID causes a similar quasiparticle production event as in the STJ described above, but in this case the quasiparticle density is detected as a change in the surface impedance of the KID, which changes the resonance of the $LC$ circuit. Such detectors have a considerable multiplexing advantage in that many detectors may be coupled to a single transmission line for implementation of FDM (at least within the limits discussed previously), rather than the complex SQUID-based multiplexer scheme used for the TES detectors described above.

## 1.4 The SCUBA-2 Project

The original proposal for SCUBA-2 was developed in 1999 following a design study for possible upgrade routes for the original SCUBA instrument. A number of upgrades had been implemented for SCUBA during that year, resulting in minor improvements in performance, but it was judged that further improvements would be impossible without considerable effort and cost. A call was issued for conceptual designs for an entirely new instrument to succeed SCUBA.

A key component of the new instrument was the selection of detector technology and array architecture. At that time, considerable development of close-packed arrays of TES devices with SQUID multiplexed readout for x-ray astronomy applications was underway in the United States. An instrument with a fully sampled focal plane was identified as being the best approach to ensure major breakthroughs in submillimetre astronomy, making multiplexed TES arrays the best choice for implementation [89]. Although SCUBA had offered observation in four wavebands between 350 and 850 $\mu$m, the majority of observations were made at 850 and 450 $\mu$m. The decision was made to design SCUBA-2 to work in these wavebands only.

The main science drivers for the new instrument built on the work already carried out with SCUBA, with particular emphasis on large scale surveys both for unbiased samples of objects for statistical studies, and to act as a pathfinder to complement future high-resolution observations using facilities such as ALMA. In addition to the

"all-sky" survey, a number of other key science programmes will be explored through a series legacy surveys, including a large, unbiased survey of stars for protoplanetary discs [90] and a survey of nearby star forming regions [91].

The SCUBA-2 project is an international collaboration involving groups from the JCMT partner countries and beyond. The UK Astronomy Technology Centre held responsibility as prime contractor for the project, overall management, and the verification, integration and test programme. The Astronomy Instrumentation Group at the Cardiff University was given responsibility for the design of the detector enclosure and focal plane structures; the design and manufacture of the system optical filters; and for testing the completed prototype and production detector arrays. The arrays themselves are produced by the Quantum Sensors Project group at the US National Institute of Standards and Technology (NIST) based in Boulder, Colorado, with some processing carried out in the UK by the Scottish Microelectronics Centre of Edinburgh University. Finally, a consortium of Canadian universities would be responsible for development of the warm readout electronics and data acquisition system, and the data reduction and pipeline processing software. Two auxiliary instruments would also be provided by the Canadian consortium: a polarimeter from the University of Montreal [92], and a Fourier transform spectrometer (FTS) from the University of Lethbridge [93].

## 1.5 Outline of the Thesis

This thesis deals with a number of technical aspects related to the SCUBA-2 instrument. The organisation of the chapters is detailed below.

Chapter 2 gives an overview of the design of the SCUBA-2 instrument. The main features of the instrument cryostat and optical design are described, as is the design of the detector arrays and cold electronics modules.

Chapter 3 discusses the detector performance requirements and derives the detector parameters necessary to meet those requirements. Representative test data is presented and discussed, and comparisons between the measured parameters and the derived requirements are made.

Chapters 4–6 concern the instrument cryogenic design and performance. As for the SCUBA instrument, SCUBA-2 operates from a 100 mK bath temperature provided

by a dilution refrigerator. Chapter 4 discusses the theory and operation of dilution refrigerators, and details the design of the refrigerator built for SCUBA-2. Chapter 5 the key performance parameters for the dilution refrigerator, and Chapter 6 describes the performance and testing of the full instrument cryogenics system.

Chapters 7 and 8 describe work carried on the development of a scheme to control magnetic fields at the detector, an important consideration for the operation of superconducting devices such as TESs and SQUIDs. Chapter 7 reviews methods of magnetic field control and discusses the properties of shielding materials. This chapter then describes a programme of finite-element modelling to develop a shielding strategy for the instrument. Chapter 8 goes on to describe the shielding manufacture and installation, and presents test data.

Finally, Chapter 9 summarises the work described in the preceding chapters, and reviews a number of issues associated with the instrument design, particularly in the context of future, similar instruments.

# Chapter 2

# The SCUBA-2 Instrument

As discussed in Chapter 1, instrumentation for submillimetre astronomy is a relatively difficult field technologically. Detectors for these wavelengths are designed and manufactured specifically for a particular instrument, while the need to operate at extremely low temperatures to meet sensitivity requirements leads to complex cryostat designs.

Developments in technology and increases in performance requirements for astronomical instruments has led to considerable increases in the size of instruments, in parallel with the increases in the size of the telescopes on which the instruments are used. Until recently, instruments for millimetre and submillimetre continuum observation were relatively small. SCUBA-2 is representative of a new generation of large, facility-class instruments operating at extremely low temperatures for long wavelength continuum observation. One of the key science drivers for the instrument, that SCUBA-2 be a wide-field camera, complicated the cryogenic design since large, cooled optical components and a fully-sampled focal plane matching the telescope field of view were required to meet this goal.

This chapter reviews the design of the SCUBA-2 instrument and detector arrays to provide a background for much of the work discussed in this thesis.

## 2.1 Instrument Design

SCUBA-2 uses a large cryostat, with approximate external dimensions of 2.4 by 2.0 by 1.8 metres, and weighing 3700 kg fully assembled. The size of the instrument is dictated by the arrangement of the cold optics. The cryostat is designed as a single vacuum space, with a volume of 6.6 $m^3$ and no inner vacuum can. A cross-section of the cryostat is shown in Fig. 2.1, with the major structural features indicated. The major details of the cryostat design are summarised here. More detailed descriptions are available elsewhere [94, 95].

The cryostat is split into four temperature stages. Within the outer vacuum vessel, the first stage is an aluminium radiation shield at a nominal temperature of 60 K (the "60-K shield"). The first stage shield is supported by G10 composite supports from the vacuum vessel. The radiation load from 300 K is reduced by multilayer insulation (MLI) blankets, consisting of aluminised Mylar sheets spaced with polyester netting. The second stage is a further shield at a nominal temperature of 4 K (the "4-K box"), containing three cold mirrors. The 4-K box is also mounted on G10 supports from the first stage shield. The first two stages are cooled by a pair of two-stage pulse tube coolers (Cryomech[1] PT410). To aid the precool of the instrument, liquid nitrogen tanks are attached to the 60-K and 4-K shields. During the initial cooldown of the cryostat, liquid nitrogen is run into the tanks on the 4-K shield, cooling the structure as the liquid evaporates. The cold gas is then used to cool the 60-K shield.

The third stage is at a nominal temperature of 1 K, with a further radiation shield (the "1-K box"), cooled by the still of a liquid cryogen-free dilution refrigerator. The 1-K box is supported by a system of carbon fibre trusses to the 4-K shield. Carbon fibre has a low thermal conductivity, but a high strength. The trusses are designed to give maximum rigidity while minimising the conduction load to the third stage. Finally, the fourth stage (at millikelvin temperatures), comprising the detector arrays and focal planes, is cooled by the mixing chamber of the dilution refrigerator. The layout of the third and fourth stage structures is shown in Fig. 2.2. More details of the dilution refrigerator are given in Chapter 4.

[1] Cryomech, Inc., http://www.cryomech.com.

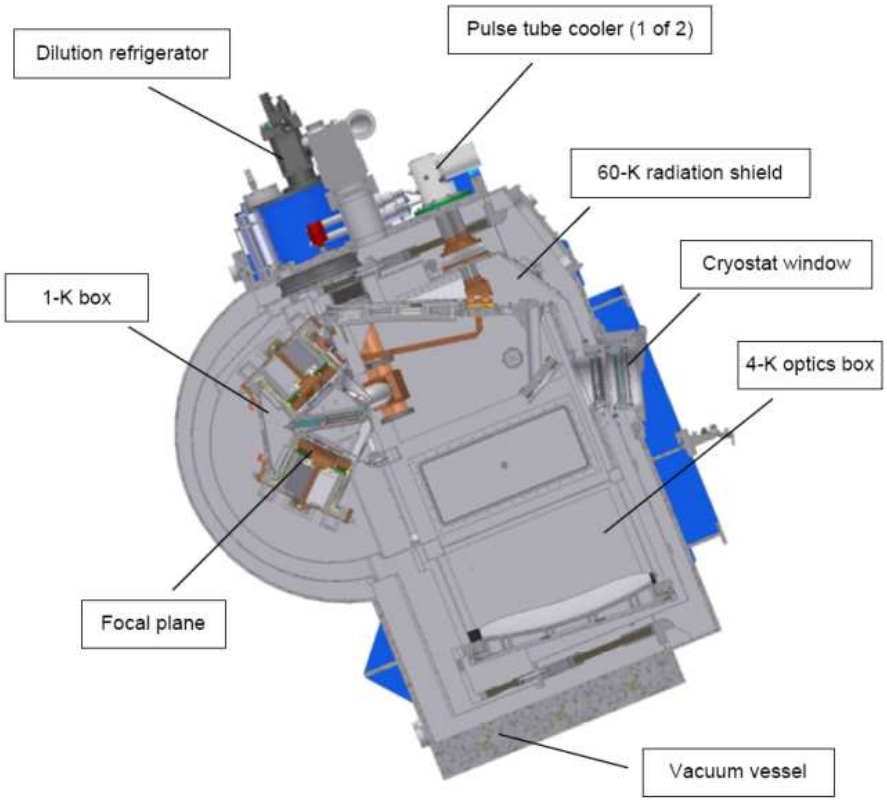


**Figure 2.1:** Cross-section model of the SCUBA-2 cryostat.

The 1-K box is shown in Fig. 2.3. A shutter mechanism is mounted on the 1-K box to allow the detectors to be blanked off from the telescope beam to allow calibration images and "dark" measurements of the detector arrays. The shutter is wicked to the box and so has a nominal temperature of <1.5 K, while the motor is isolated using carbon fibre trusses. The shutter motor is wicked to the 4-K structure.

The detector subarrays are contained within separate focal plane units (FPUs), as shown in Fig. 2.4. The main structure and the outer cover of the FPU are at 1 K, while the millikelvin link to the dilution refrigerator passes through the centre of the structure to the back of the detectors. Connections from the room temperature electronics to the cold electronics modules are made by harnesses of woven niobium titanium ribbon cables. The cables are continuous, with heat sinks at the 60-K, 4-K and 1-K stages. Further details of the design of the 1-K and mK systems are described in Chapter 6.

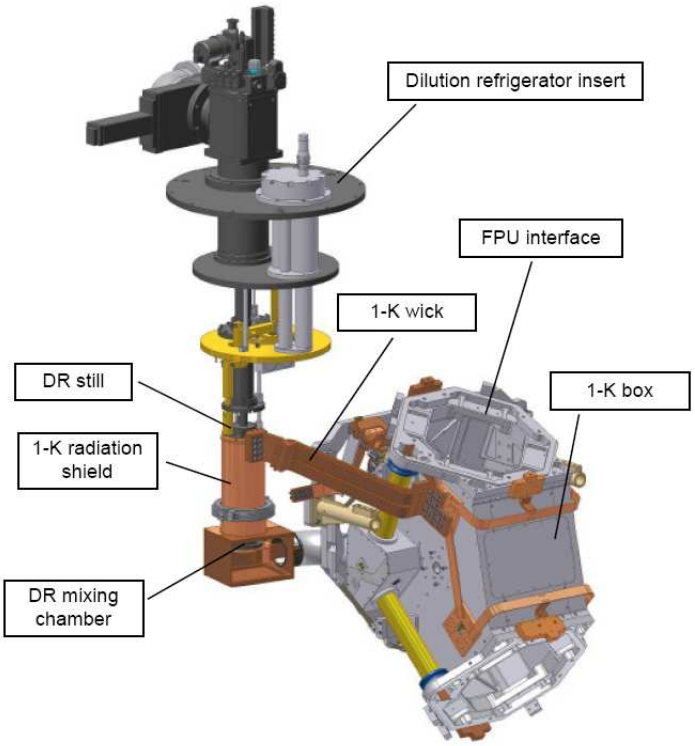


**Figure 2.2:** Layout of the third (1 K) and fourth (millikelvin) instrument stages showing the 1-K box detector enclosure and the dilution refrigerator.

As discussed in Chapter 1, bolometric detectors require careful filtering both to define the observation band, and to reduce the background thermal loading on the focal plane. This is achieved through stacks of filters at the apertures of the various temperature stages of the cryostat. The cryostat window is composed of 8 mm polyethylene, with a clear aperture of 180 mm. Anti-reflection layers are attached to the front and back surfaces of the window. Immediately behind the window is a high frequency thermal blocking filter that cuts out the majority of radiation at $\lambda$ <25 $\mu$m. A stack of three filters at the 60-K shield and two each at the 4-K and 1-K shields block radiation at $\lambda \lesssim$330 $\mu$m. Within the 1-K box, a dichroic splits the beam into the two channels (769–1000 $\mu$m in transmission and 400–526 $\mu$m in reflection). Finally, the observing bands are defined by a blocking and bandpass filter at each focal plane unit. All of the filters and the dichroic are metal mesh filters [96], produced by the Astronomy Instrumentation Group at Cardiff University. A schematic of the filter arrangement is shown

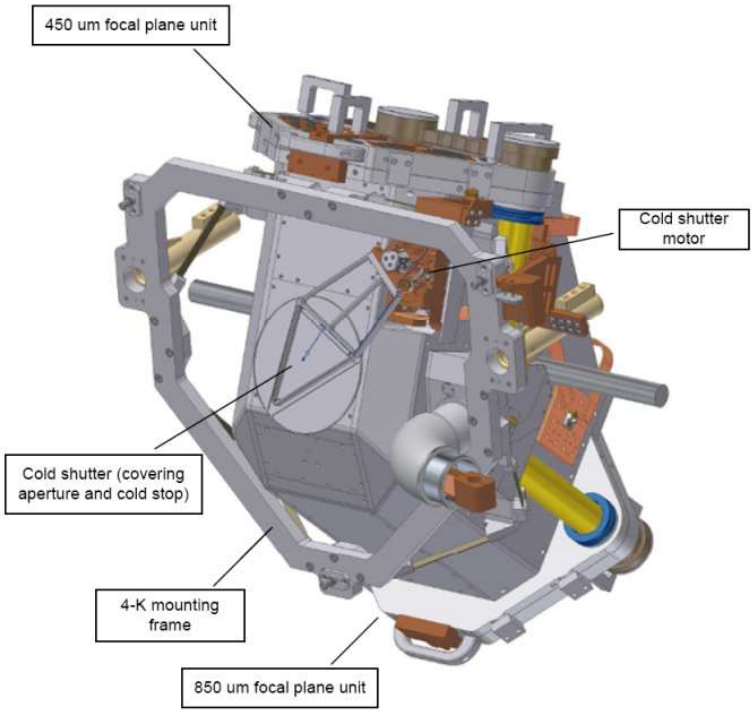


**Figure 2.3:** CAD model of the 1-K box, with the major components indicated.

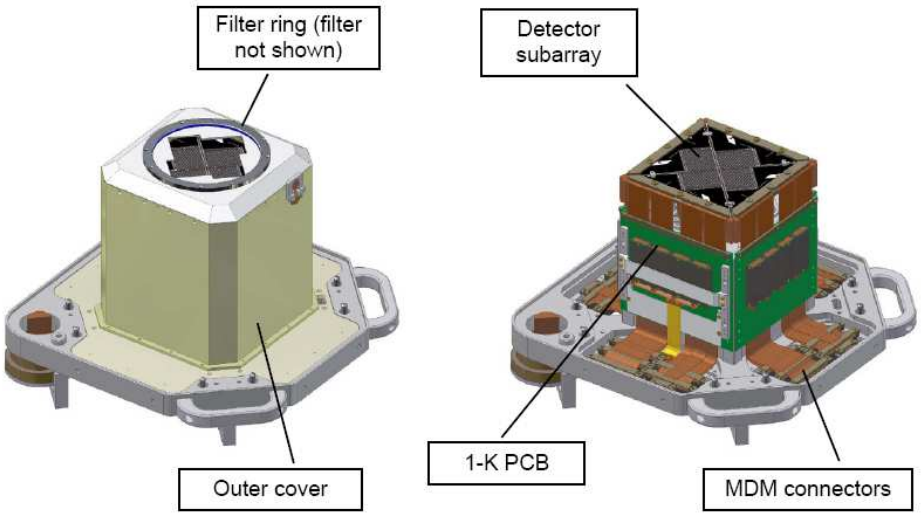


**Figure 2.4:** CAD model of the focal plane unit. Left: the outer cover in place over the detector modules. Right: outer cover removed.

in Fig. 2.5, along with the layout of the SCUBA-2 optics from the telescope tertiary mirror to the focal plane.

SCUBA-2 is the largest instrument ever designed for submillimetre wavelengths. Submillimetre telescopes such as the JCMT were not designed to accommodate instruments of this size, and therefore considerable infrastructure work was required to allow sufficient clearance to mount SCUBA-2 at the telescope [97]. The original SCUBA cryostat was positioned at one Nasmyth focus of the telescope, but this location was unsuitable for SCUBA-2. The mounting position for the cryostat is below the original Nasmyth platform, with a complex optical chain to reimage the telescope beam at the new focal plane position. The optical chain is fully reflective, with three mirrors in the telescope receiver cabin (C1–C3 in Fig. 2.5) after the telescope tertiary mirror, and two more on the Nasmyth frame around the cryostat (N1 and N2). A further three mirrors (N3–N5) are inside the cryostat, cooled to $\sim$4 K to reduce the background loading on the focal planes. The mirrors are all freeform aluminium structures, produced by TNO in the Netherlands [98, 99].

## 2.2 Pixel and Array Architecture

This section aims to summarise the physical design and the operation of the SCUBA-2 detector arrays.

### 2.2.1 Pixel Design

The pixel design for SCUBA-2 was based on a Salisbury screen arrangement to maximise the efficiency of the absorber. A cross-section of the absorber is shown in Fig. 2.6, consisting of a resistive layer and a metal backshort, separated by a silicon brick.

At the interface between free space (refractive index, $n = 1$) and the absorber, the coefficient of reflection, $R$, is given by

$$R = \left(\frac{1-n}{1+n}\right)^2, \tag{2.1}$$

where $n$ is the refractive index of the absorber brick. Assuming $n = 3.388$ for cold silicon, this gives $R = 30\%$. By spacing the reflecting backshort at an integer multiple of $\lambda/4n$, where $\lambda$ is the wavelength of the incident radiation, the waves emerging after

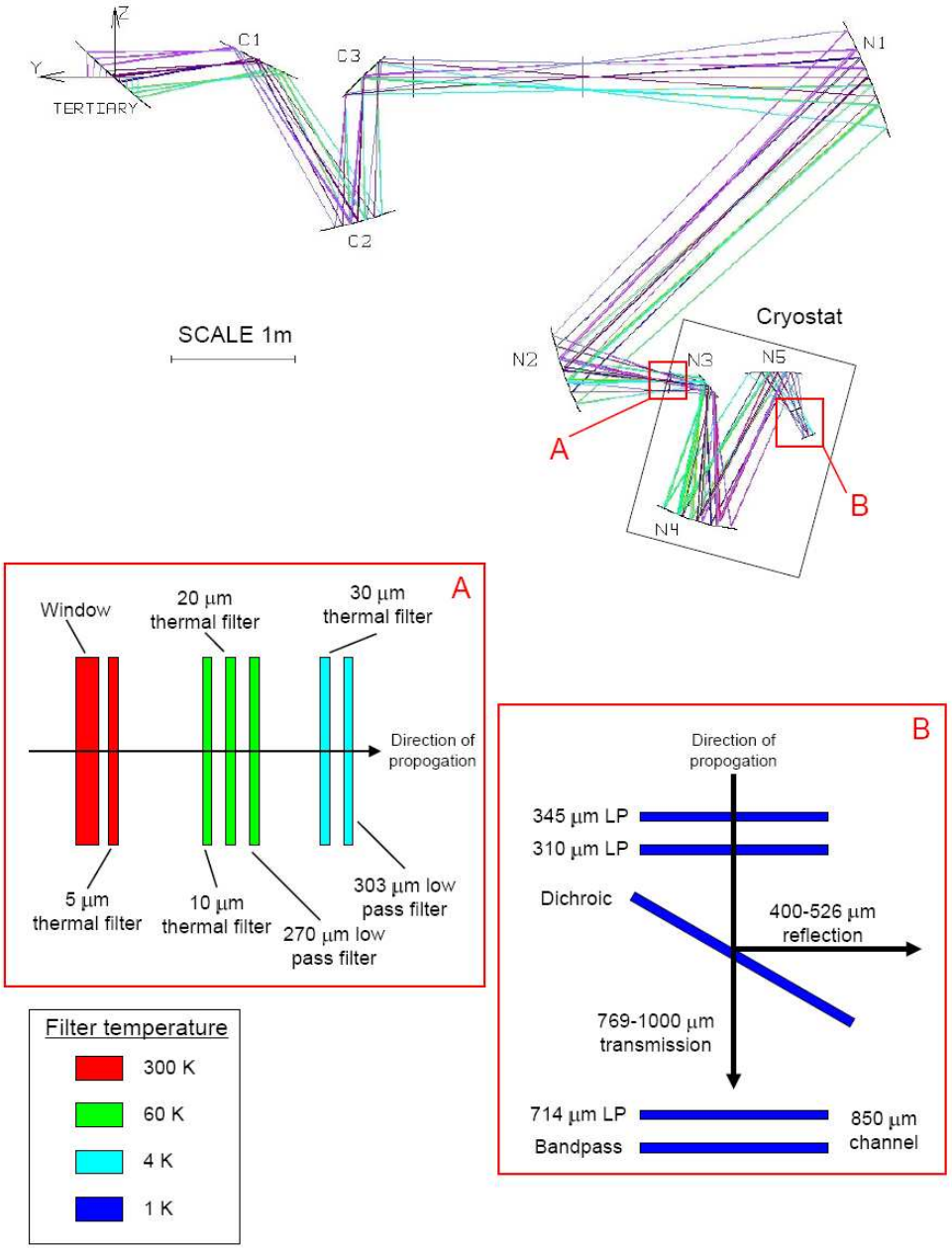


**Figure 2.5:** Schematic of the SCUBA-2 optical layout from the tertiary mirror to the focal plane. Two callouts show the arrangement of filters in the cryostat. In callout B, the 850 $\mu$m channel only is shown for clarity. The 450 $\mu$m filters have a low pass at 385 $\mu$m rather than 714 $\mu$m as in the long wave channel. The temperature of the filters is indicated by the colour coding.

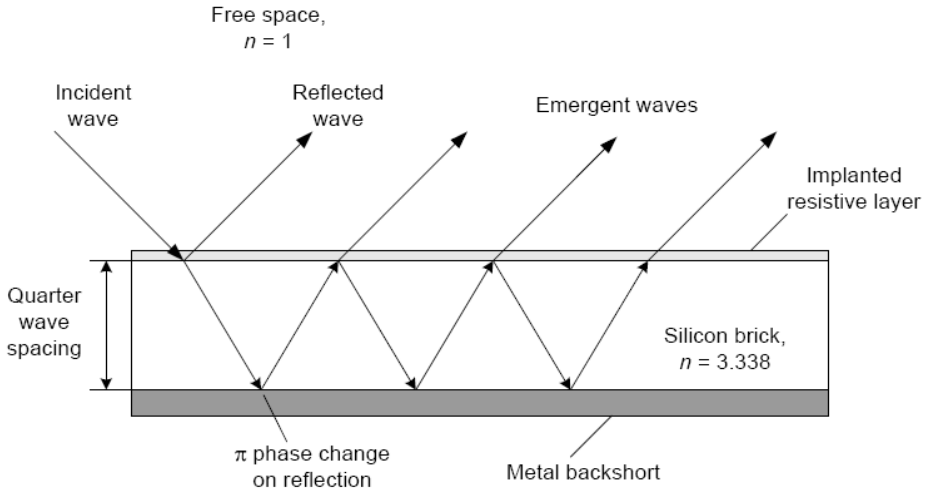


**Figure 2.6:** Cross-section of the Salisbury screen absorber. The pixel consists of a metal backshort (the TES device) and a resistive layer separated by a silicon brick. The emergent waves (after reflection from the backshort) interfere destructively with the wave reflected from the front face of the brick, dissipating the energy of the wave in the resistive layer and heating up the pixel. Adapted from Ref. [101].

being reflected by the backshort will interfere destructively with the waves reflected from the front surface of the silicon brick. This reduces the reflectivity, and maximises the absorption efficiency. Since cold silicon has minimal dissipation at submillimetre wavelengths, the resistive layer is used to dissipate the energy of the radiation and heat up the pixel. The resistive layer is formed by degeneratively doping the front face of the block to $\sim$400 $\Omega/\mathrm{m}^2$ (impedance-matched to free space to maximise the absorber efficiency). The TES, a molybdenum-copper bilayer [100], forms the backshort.

A quarter wave spacing at 850 $\mu$m gives a the silicon bricks 70 $\mu$m thick. At 450 $\mu$m, a quarter wave block would be too thin to fabricate successfully, so a three-quarter wave block was adopted, giving a thickness of 100 $\mu$m. Electromagnetic modelling of the pixels predicted absorption efficiencies in excess of 80% at both wavelengths [101].

A cross-section of a pixel is shown in Fig. 2.7, with the main features indicated. The size of the pixel at 850 $\mu$m is 1.13 mm for Nyquist-sampled images (see discussion in Chapter 3). The same pixel size is used at 450 $\mu$m (even though this undersamples the image) due to size restrictions on the multiplexer cells, described below. In order to

maintain the rigidity of the silicon structure, a 50 $\mu$m wall surrounds each pixel, with a 10 $\mu$m trench thermally isolating the absorber from the heat sink. The absorber is supported by a 0.5 $\mu$m silicon nitride membrane. It is conduction through the membrane at the base of the isolating trench that forms the weak thermal link to the cold bath (the width of the trench controlling the thermal conductance, $G$). The active area of the pixel is therefore slightly larger than 1 mm square. This is large enough to avoid diffraction effects since the pixel size is $>\lambda$ at both wavelengths. Thermal and electrical connections are made to an in-focal plane multiplexer via indium bump bonds. An electron microscope image of a section of the SCUBA-2 detector array is shown in Fig. 2.8.

### 2.2.2 Multiplexer Scheme

To realise kilopixel arrays operating at millikelvin temperatures, it is necessary to reduce the wire count going to the focal plane. No practical multiplexing scheme was available for earlier generations of submillimetre instruments. Although semiconductor bolometers only require two wires per pixel, connections for $\sim$10 000 pixels would be an unsustainable wire count. The development of TES readouts based on superconducting interference devices (SQUIDs) as sensitive ammeters to measure the current change in the voltage biased TES from the change of $R(T)$ was advantageous, since schemes to multiplex arrays of SQUIDs may be easily realised. A single SQUID is instrumented using six wires to ambient temperature (two bias, two output and two feedback[2] connections). This number may be reduced by connecting the outputs of a number of SQUIDs in series, and turning on one SQUID at a time to multiplex in the time domain. In this way, a single column of SQUIDs may use common output and feedback connections, while $N$ SQUIDs will require $N + 1$ bias lines (in this case, also referred to as address lines) to allow each SQUID to be turned on in sequence. A SQUID in the "off" state is fully superconducting and therefore dissipates no power, which is a major advantage for cryogenic circuits. Using this method, $M$ columns of $N$ SQUIDs may form a two-dimensional array. In such a scheme, each column requires two output, two feedback,

[2]Operating in a "flux locked" mode with a feedback coil linearises the response of the SQUID (see Appendix B for further discussion).

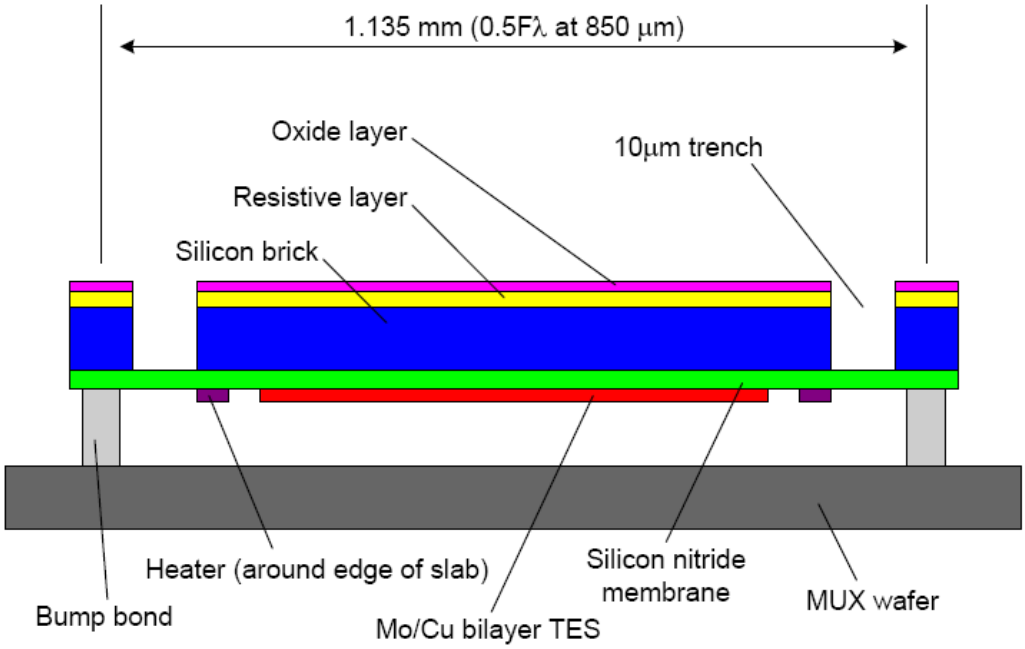


**Figure 2.7:** Schematic cross-section of a pixel.

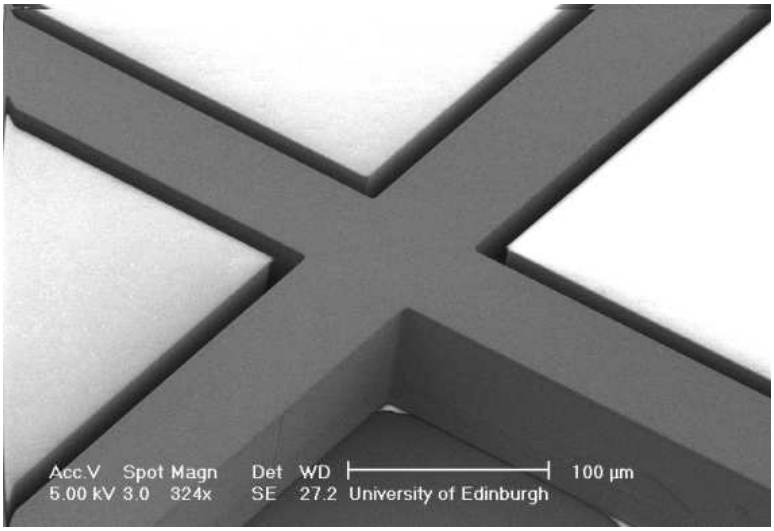


**Figure 2.8:** Electron microscope image of a section of detector array. The walls (dark grey) and isolation trenches around the pixel absorbers (light grey) are visible. The pixel in the foreground has been removed.

and $N+1$ bias lines, for a total of $M(N+5)$ connections [102]. Early multiplexers, such as the 1×8 arrays described in Ref. [102], connected the multiplexer SQUID outputs directly to the SQUID series array (SSA) amplifiers at a higher temperature.[3] Later, larger MUX arrays (such as the 1×32 arrays described in Ref. [103]) coupled the output of the multiplexer SQUIDs (or "first stage" SQUIDs, SQ1s) through a second stage SQUID (SQ2) operating at the MUX temperature. Coupling through the SQ2 reduces sensitivity to noise pickup by providing an additional amplification stage, and allows for better impedance matching between the SQ1s and SSAs [104].

To achieve in-focal plane multiplexing as required for a two-dimensional detector array, the SQ1 unit cells are designed to match the area of the bolometers on the detector array. The first and second stage SQUIDs form a 32 column array,[4] as shown in Fig. 2.9, at the same operating temperature as the detector array. An image of a MUX unit cell is shown in Fig. 2.10, with the key features indicated. As with the pixels, the cell is 1.135 mm on a side. Each cell is connected to the detector pixel by indium bump bonds, with the first stage SQUID inductively coupled to the pixel through an input transformer. A column of 41 SQUIDs (40 SQ1s plus one "dark" SQUID, described below) are coupled into a second stage SQUID on the multiplexer chip, which in turn connects to a SSA amplifier [105] at 1 K.

A concern for SQUID multiplexing schemes is crosstalk between pixels due to coupling between the common feedback signal for the column and the SQ1 input coils. When a feedback current is applied to the 'on' SQUID, currents are induced in the input coils of the other SQUIDs in that column. This coupling may be nulled by connecting the TES to the input coils of two SQUIDs with oppositely wound feedback coils. The "dummy" SQUID is never turned on, but forms a balanced pair such that the signal induced due to crosstalk in the two SQUIDs cancels [103].

Excess low-frequency noise in the MUX arrays [103] typically does not result from the SQUIDs themselves, but rather is caused primarily by system aspects such as current source instabilities or electromagnetic interference. A significant part of the low-

[3]The SSAs generally dissipate too much power to be sunk on the focal plane, so will be operated at the next temperature stage (either 1 K or 4 K, dependant on the thermal layout of the system).

[4]Although the original intention was to fabricate 40 column arrays, issues with the fabrication of devices near the edges of array wafers forced a reduction in size to 41 by 32.

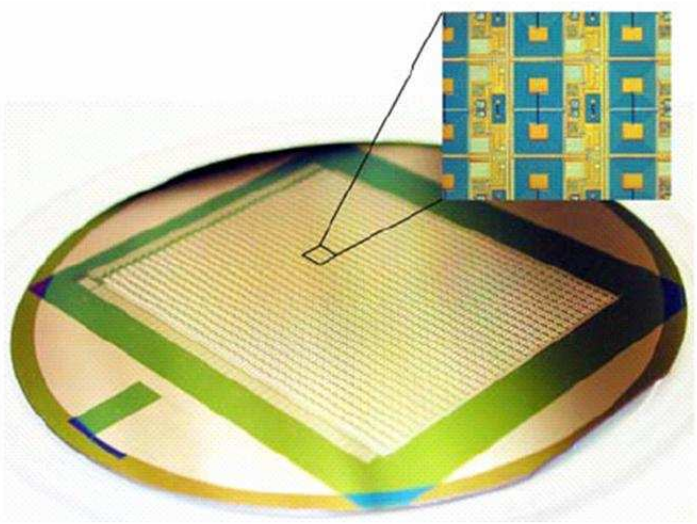

**Figure 2.9:** Image of a multiplexer array, with the inset showing the detail of cell layout on the wafer.

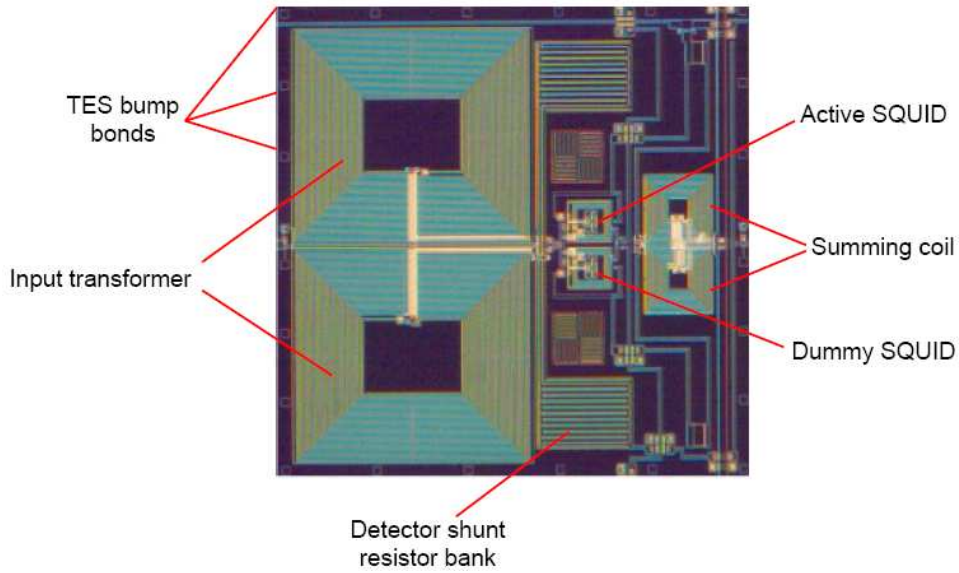


**Figure 2.10:** Image of a multiplexer unit cell.

frequency noise may be removed by chopping between the first stage SQUIDs and a "dark" SQUID. The dark SQUIDs, 1 per column, are identical to the other 40 SQ1s, but are not connected to a pixel. The dark SQUID is addressed once per multiplex cycle of 40 SQ1s, with the low-pass filtered signal from the dark SQUID subtracted from the other SQ1 outputs to remove low-frequency common mode noise, including noise added due to the signal multiplexing.

The basic outline of the operation of the readout chain is as follows. The absorption of a photon at a pixel is detected as a change in the current flowing through the TES device. The TES is biased with a constant voltage, so as the resistance changes due to the change in temperature of the absorber, the current will decrease. The TES is connected to an inductor, which in turn is flux coupled to a first stage SQUID on the multiplexer array. The change in current in the circuit causes the magnetic flux threading the SQUID to change. The operation of SQUIDs is discussed in more detail in Appendix B, but essentially the device behaves as a highly sensitive flux meter. The change in flux threading the SQUID is detected as a change in current flowing the device. The current change is read by the second stage SQUID, the voltage change in that device is then amplified by the SQUID series array at 1 K before being carried out of the cryostat by the array cabling to the room temperature electronics. To increase the dynamic range of the SQUIDs, the devices are typically operated as nulling detectors. The room temperature electronics applies a feedback signal such that the changes in the flux threading the SQUIDs are cancelled out.

### 2.2.3 Array and Electronics Packaging

The hybridised detector and multiplexer subarrays are packaged into a cold electronics module, shown in Fig. 2.11. The subarray is attached to a heat sink using epoxy. The heat sink, also known as a "hairbrush", is a beryllium-copper block spark eroded to produce a grid of individual tines, each of which is bonded to the back of a MUX unit cell. The hairbrush arrangement, shown in Fig. 2.12, allows a high conductivity cooling path while allowing for differential contractions effects that would otherwise stress the subarray wafers during cooling. The array is connected to a ceramic printed circuit board (PCB) via aluminium wirebonds. The ceramic PCB is connected to a PCB at

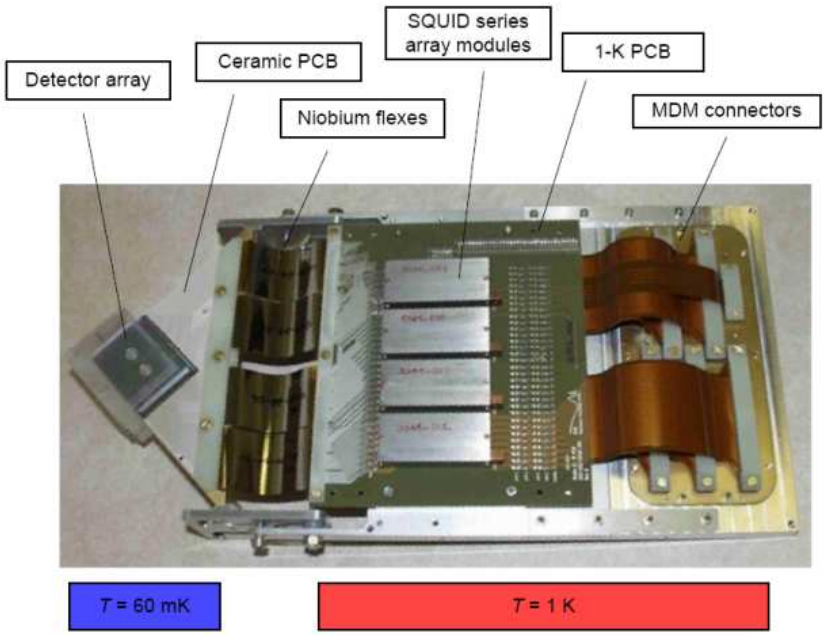


**Figure 2.11:** SCUBA-2 subarray cold electronics module, shown in the "flat" transport and storage configuration prior to integration. When integrated in the instrument, the subarray and circuit board on the cold side of the thermal break are folded at right angles to the 1 K circuit board. The approximate temperature of the two sections of the module is indicated, with the niobium flexes providing the thermal break.

**Figure 2.12:** Detector array heat sink for SCUBA-2, known as the "hairbrush". The heat sink is beryllium-copper, spark eroded to produce a grid of tines that are individually epoxied to the MUX unit cells. The tines give a good thermal path, while maintaining flexibility to compensate for differential contraction effects during cooling.

a temperature of 1 K by superconducting niobium flexes, providing a thermal break between the millikelvin and 1 K sections of module. The SQUID series array amplifiers are packaged in four magnetically-shield modules on the 1-K PCB. Connections to the cold electronics module are made via six MDM connectors on the array base plate. Further description of the subarray module design may be found elsewhere [100, 106].

Electrical connections are made from the MUX array to a ceramic circuit board by aluminium wire bonding. The detector and MUX array, hairbrush and ceramic circuit board operate at approximately the detector bath temperature. Niobium flex cabling allows electrical connection to a second circuit board operating at a temperature of ∼1 K, while providing a thermal break between the two temperature stages. The SSA amplifier modules are connected on the higher temperature circuit board.

## 2.3 Summary

This chapter has presented an overview of the design of the SCUBA-2 instrument to provide a background to the work discussed in this thesis. The main features of the cryostat were described, followed by discussion of the design of the SCUBA-2 detector arrays and cold electronics. In the next chapter, the key design parameters for the SCUBA-2 bolometers are derived, and compared to measured performance data.

# Chapter 3

# Detector Requirements and Performance

In Chapter 1, the principle of operation of bolometric detectors was discussed. The performance of such detectors is controlled by a number of physical parameters, such as the operating temperature, thermal conductance to the cold bath and pixel heat capacity. These parameters must be defined based on the desired operating characteristics of the bolometers. The physical layout and construction of the SCUBA-2 detector arrays was presented in the previous chapter, while this chapter concerns the design of the SCUBA-2 bolometers. The required detector parameters are derived based on the operational goals of SCUBA-2, and representative test data for pixels at each wavelength are presented and discussed.

The derivation of the bolometer parameters presented here was originally carried out during the early design stages of the SCUBA-2 project, but is repeated here by this author using updated inputs. The test data presented in §3.2 was collected during testing of the instrument prior to delivery and at the JCMT, primarily by D. Bintley. The data presented here has been analysed by the author. The discussion of the data and the performance comparisons made in this chapter are also the work of this author.

## 3.1 SCUBA-2 Detector Requirements

SCUBA-2 was designed to be a sensitive, wide-field camera, capable of mapping and point source imaging many times faster than SCUBA. To this end, a number of key design requirements were identified in order to achieve the science goals of the project:

1. The largest (undistorted) field of view allowed by the telescope.
2. The focal planes should be fully sampled to maximise the imaging speed and improve image fidelity.
3. Per-pixel sensitivity should be limited by photon noise.

These requirements, and the design steps to satisfy them, are discussed in detail below.

### 3.1.1 Field of view and Pixel Count

The field of view of the JCMT is a circle 13' in diameter, reducing to 11' at the Nasmyth platform (defined by the elevation bearing). With a square focal plane (as dictated by the array manufacturing process), a field of 8 by 8 arcminutes may be reimaged.

To fully sample the focal plane (i.e., to produce Nyquist-sampled images), the pixel spacing must by equal to $0.5F\lambda$, where $F$ is the focal ratio of the optics and $\lambda$ the observing wavelength. The $F$-number for the SCUBA-2 optics was set at 2.67 to keep the system compact. Hence, the pixel spacing for Nyquist-sampled images is 1.13 mm at 850 $\mu$m and 0.6 mm at 450 $\mu$m. From the plate scale at the focal plane (5 arcseconds/mm), this would require approximately 6400 pixels (80 by 80 in a square geometry) at 850 $\mu$m and 25600 (160 by 160) pixels at 450 $\mu$m.

Early work on the multiplexer design showed that there were size constraints on the circuit. Unit cells could not be made smaller than 1.1 mm, making implementation of a fully-sampled 450 $\mu$m focal plane extremely difficult. To overcome this, the pixel spacing on the 450 $\mu$m was increased to $F\lambda$, producing an array undersampled by a factor of 4. This also simplified the fabrication process, since the arrays are essentially identical at the two wavelengths. The maximum size of an individual detector or MUX array is 50 mm square, hence the focal planes would be populated with four seperate

quadrants, or subarrays. The architecture of the array was described in more detail in Chapter 2.

### 3.1.2 Detector Noise and Power Handling

Some of the key pixel design parameters are the maximum detector noise and the pixel power handling, both of which are dependant on the background photon noise. It was required that the SCUBA-2 detectors be limited by the background photon noise due to the sky and telescope, rather than intrinsic detector noise. To determine the required detector NEP, it was necessary to predict the background photon power on the detectors. The photon noise feeds into the power handling requirement for the pixels, since the detectors must work in both the best and the worst sky conditions. The power handling then determines the operating temperature of the pixels and the required value of the thermal conductance to the cold bath, $G$.

#### Photon Noise

The background power on the detectors was predicted by modelling the contribution from each optical element visible to the pixels. Each component of the optical system, such as the filters and mirrors, was treated as a black or grey body with known temperature, emissivity and transmission, and the power falling within the solid angle viewed by the pixel calculated. The photon power from each component is calculated using Eq. (3.5). For these calculations, the mesaured filter bandwidths, $\Delta\nu$, at 850 $\mu$m (352 GHz) is 40 GHz, and 70 GHz at 450 $\mu$m (666 GHz).

The contribution to the photon power from the telescope and instrument is constant, and ideally should be small compared to the contribution from the sky. The sky contribution is a function of the sky transmission, so the calculation was made for both good and bad sky conditions. The measured transmissions as a function of pwv comes from the data of the University of Lethbridge group (e.g. Ref. [107]). At 850 $\mu$m, a good sky was assumed to have a transmission of 80%, while a bad sky was taken as a transmission of 10%. At 450 $\mu$m, these values are reduced to 40% and 3%, respectively. These sky conditions bracket close to the best and the worst conditions under which the instrument may be used. These transmission values may be converted to precipitable

water vapour (pwv) values, as discussed in Chapter 1, by first calculating the extinction correction, $\tau$, and comparing this to pwv measurements made using the Tau monitor based at the Caltech Submillimetre Observatory on Mauna Kea, a radiometer measuring the sky opacity at the zenith at a frequency of 225 GHz (1.3 mm wavelength). The sky transmission at zenith (an airmass of 1) is equal to $e^{-\tau}$, while the extinction corrections[1] at 850 and 450 $\mu$m are related to $\tau$ at 1.3 mm by [108]

$$\tau_{850} = 4.02\,(\tau_{1.3mm} - 0.001)\,, \tag{3.1}$$

$$\tau_{450} = 26.2\,(\tau_{1.3mm} - 0.014)\,. \tag{3.2}$$

The pwv value, in millimetres, is then $\sim 20\tau_{1.3mm}$. Once the background power has been calculated, the photon NEP may be calculated using Eq. (1.4).

Tables 3.1 and 3.2 summarise the contribution of the sky, telescope and instrument to the background power and the photon NEP squared at 850 and 450 $\mu$m, respectively. Values are listed for good and poor sky conditions at each wavelength, including the transmission and equivalent pwv value for each condition. Note that these tables list $\mathrm{NEP}^2_{\mathrm{ph}}$, since NEPs are added in quadrature. A final summary of the maximum and minimum background power and photon NEP is included in Table 3.3.

### Detector NEP

A limit on the detector[2] NEP of half the photon NEP was adopted to minimise the reduction of the maximum imaging speed. A further 50% engineering tolerance was added as a goal to allow for variation in the performance of the pixels. The 850 $\mu$m photon noise imposes the more stringent limit, requiring a $\mathrm{NEP}_{\mathrm{det}}$ of $2.8 \times 10^{-17}$ W/$\sqrt{\mathrm{Hz}}$ with a goal of $1.9 \times 10^{-17}$ W/$\sqrt{\mathrm{Hz}}$. The higher $\mathrm{NEP}_{\mathrm{ph}}$ at 450 $\mu$m relaxes these requirements to $1.4 \times 10^{-16}$ W/$\sqrt{\mathrm{Hz}}$ and $0.9 \times 10^{-16}$ W/$\sqrt{\mathrm{Hz}}$.

The total NEP will also inevitably contain some contribution other than the background and detector noise, specifically from the readout electronics. In order that the

[1]The corrections were empirically derived for SCUBA. Discussion of these relationships is available at http://docs.jach.hawaii.edu/JCMT/SCD/SN/002.2/.

[2]Measured in the dark, with no photon noise.

**Table 3.1:** Predicted background power and photon NEP from the sky, telescope and instrument at 850 $\mu$m. Good sky conditions are taken to be 80% transmission, which is approximately 1 mm pwv, while bad sky conditions are assumed to be 10% transmission, or 11 mm pwv. The telescope and optics contribution includes the telescope membrane and all warm mirrors from the telescope primary to the instrument cryostat.

| Parameter | Background power / pW | | $NEP^2_{ph}$ / $W^2$/Hz | |
|---|---|---|---|---|
| | Good sky (80% trans, 1 mm pwv) | Poor sky (10% trans, 11 mm pwv) | Good sky (80% trans, 1 mm pwv) | Poor sky (10% trans, 11 mm pwv) |
| Sky | 2.7 | 12.0 | $1.3 \times 10^{-33}$ | $5.6 \times 10^{-33}$ |
| Telescope and optics | 2.2 | 2.2 | $1.1 \times 10^{-33}$ | $1.1 \times 10^{-33}$ |
| Instrument | 1.5 | 1.5 | $7.2 \times 10^{-34}$ | $7.2 \times 10^{-34}$ |
| Total | 6.4 | 15.7 | $3.1 \times 10^{-33}$ | $7.4 \times 10^{-33}$ |

**Table 3.2:** Predicted background power and photon NEP from the sky, telescope and instrument at 450 $\mu$m. Good sky conditions are taken to be 40% transmission, which is approximately 1 mm pwv, while bad sky conditions are assumed to be 3% transmission, or 3 mm pwv. The telescope and optics contribution includes the telescope membrane and all warm mirrors from the telescope primary to the instrument cryostat.

| Parameter | Background power / pW | | $NEP^2_{ph}$ / $W^2$/Hz | |
|---|---|---|---|---|
| | Good sky (40% trans, 1 mm pwv) | Poor sky (3% trans, 3 mm pwv) | Good sky (40% trans, 1 mm pwv) | Poor sky (3% trans, 3 mm pwv) |
| Sky | 50.1 | 88.9 | $4.8 \times 10^{-32}$ | $7.8 \times 10^{-32}$ |
| Telescope and optics | 15.7 | 15.7 | $1.4 \times 10^{-32}$ | $1.4 \times 10^{-32}$ |
| Instrument | 10.1 | 10.1 | $9.1 \times 10^{-33}$ | $9.1 \times 10^{-33}$ |
| Total | 76 | 115 | $7.2 \times 10^{-32}$ | $1.0 \times 10^{-31}$ |

**Table 3.3:** Summary of total background power and photon NEP at 450 and 850 $\mu$m from the detailed model breakdowns in Tables 3.1 and 3.2.

| Parameter | 450 $\mu$m | 850 $\mu$m |
|---|---|---|
| Minimum background power / pW | 76 | 6.4 |
| Maximum background power / pW | 115 | 15.8 |
| Minimum background power / W/$\sqrt{\text{Hz}}$ | $2.7 \times 10^{-16}$ | $5.6 \times 10^{-17}$ |
| Maximum background power / W/$\sqrt{\text{Hz}}$ | $3.2 \times 10^{-16}$ | $8.6 \times 10^{-17}$ |

**Table 3.4:** Summary of the NEP requirements for the 450 $\mu$m and 850 $\mu$m pixels.

| Parameter | Relative value | 450 $\mu$m | 850 $\mu$m |
|---|---|---|---|
| Background photon NEP ($\text{NEP}_{\text{ph}}$) / W/$\sqrt{\text{Hz}}$ | $\text{NEP}_{\text{ph}}$ | $2.7 \times 10^{-16}$ | $5.6 \times 10^{-17}$ |
| Required per-pixel NEP ($\text{NEP}_{\text{pixel}}$) / W/$\sqrt{\text{Hz}}$ | $0.7\text{NEP}_{\text{ph}}$ | $1.9 \times 10^{-16}$ | $3.9 \times 10^{-17}$ |
| Required detector NEP ($\text{NEP}_{\text{det}}$) / W/$\sqrt{\text{Hz}}$ | $0.5\text{NEP}_{\text{ph}}$ | $1.4 \times 10^{-16}$ | $2.8 \times 10^{-17}$ |
| Goal detector NEP / W/$\sqrt{\text{Hz}}$ | $0.33\text{NEP}_{\text{ph}}$ | $0.9 \times 10^{-16}$ | $1.9 \times 10^{-17}$ |

detector noise dominate the per-pixel NEP, $\text{NEP}_{\text{pixel}}$, the readout electronics and feedback circuit should increase the NEP by a factor of no more than $\sqrt{2}$. Therefore, the value of $\text{NEP}_{\text{pixel}}$ should be no more than $0.7\text{NEP}_{\text{ph}}$. The noise limits for the two wavelengths are summarised in Table 3.4.

### Pixel Power Handling

TES devices are brought into the superconducting transition by applying power via a heating element, at which point bias power may be applied to set the operating point of the device. Power from a heater must be used since a bias alone would dissipate no power in the superconducting state. However, in a variable background such as that

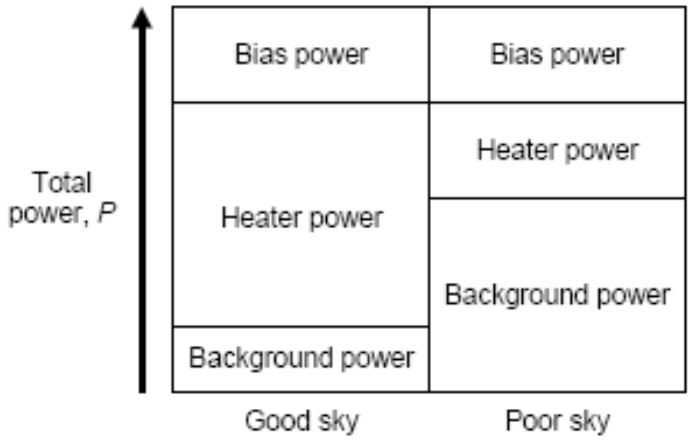


**Figure 3.1:** Schematic of the SCUBA-2 TES device power handling in good and poor sky conditions, showing the relative contributions of the different power sources.

which the SCUBA-2 detectors will operate, changes in background power will change the total power dissipated in the pixels and change the operating point. This would necessitate changes in the bias power to maintain a constant bias point in the transition. Changes in bias power in this way would cause changes in the pixel responsivity, making images impossible to calibrate.

The solution in SCUBA-2 was to add a heater to each pixel, and heat the pixels into the transition with a combination of heater and bias power. In this way, changes in sky background power (and variation in pixel properties) may be handled by changes to the heater power, maintaining a constant bias power across the array. The relative contributions from the different power sources is illustrated schematically in Fig. 3.1. The pixel heaters are wired in series, with a single software servo compensating for changes in the sky background.

A known issue with the operation of TESs is the effect of noise due to high currents flowing through the device [109]. High current will flow in the TES when the device is biased near the bottom region of the transition, close to the superconducting state, where there is very low resistance. To avoid high currents in the device, the TESs are operated with the pixel heater providing much of the power to heat the devices into the transition, with a bias power limit of 20 pW at 850 $\mu$m and 50 pW at 450 $\mu$m.

**Table 3.5:** Summary of the SCUBA-2 pixel power handling.

| Parameter | 450 $\mu$m | 850 $\mu$m |
|---|---|---|
| Maximum background power / pW | 115 | 16 |
| Heater power / pW | 60 | 10 |
| Bias power / pW | 10 | 10 |
| Total power (with 20% margin) / pW | 220 | 45 |

The power handling requirement for the detectors at the two wavelengths may be estimated by summing the contributions from the maximum sky power, the bias power and heater power. The maximum sky background was previously obtained from the photon noise model, as summarised in Table 3.3. The heater power is set at 50% of the maximum background power in order to maintain the detector dynamic range, while the bias power is set at 10pW at both wavelengths (within the maximum limit for the low current regime discussed above by a factor of at least 2). The total power handling figure includes a margin of ∼20% to allow for variation in the parameters. The total power handling requirements are summarised in Table 3.5.

### 3.1.3 Noise in TES Devices

Noise mechanisms in bolometers were discussed in general terms in Chapter 1, but that discussion will be extended with particular reference to TES detectors. The detector NEP, $\mathrm{NEP}_{\mathrm{det}}$, is composed of contributions from two sources, Johnson noise and phonon noise. In TES devices, there are additional mechanisms that may be significant, including current noise and Johnson noise in the normal-metal heater. However, many of these mechanisms will have small contributions to the overall noise and may be neglected in a simplified treatment of the TES.

Firstly, as described above, current noise is only significant at high bias power, which will not generally be encountered in the operation of the SCUBA-2 detectors. Johnson noise, which can be a significant contributor to the overall noise in high-impedance semiconductor bolometers, is less significant in TES detectors since the resistances in question are considerably smaller. Device resistances are of the order of tens of m$\Omega$,

rather than MΩ for semiconductor devices. Similarly for the pixel heaters, which have resistances of $\sim 3\Omega$. Assuming a TES and a semiconductor device of nominally the same responsivity and with the same operating temperature, then from Eq. (1.2), $\mathrm{NEP}_{\mathrm{j}}^2 \propto R$. For an operating temperature of 0.1 K, the Johnson noise in a 10 MΩ bolometer will be a factor $10^3$ higher than in a TES with a 3Ω pixel heater and a 25 mΩ device resistance. Furthermore, as discussed in Chapter 1, Johnson noise is effectively suppressed in TES devices since the signal and phonon noise are boosted due to electrothermal feedback (ETF). While the frequency dependance of the Johnson noise may make the contribution larger at higher frequencies, this will generally be outside the frequency range of interest. It is therefore reasonable, for the scope of this discussion, to make the assumption that the detector noise is dominated by the phonon component, given by Eq. (3.3)

$$\mathrm{NEP}_{\mathrm{det}}{}^2 = 4\gamma k T^2 G, \tag{3.3}$$

where $k$ is the Boltzmann constant, $T$ the detector temperature and $G$ the thermal conductance of the thermal link to the cold bath. Some work has used $\gamma = 1$ [110], while measurements of $\gamma$ for TES devices in the C$_l$OVER CMB experiment have indicated a value of 0.65 [111]. This discussion will use $\gamma = 0.5$ for simplicity.

It should be noted that TES devices are known to exhibit excess low frequency noise, generally referred to as "$1/f$" noise due to the form of the frequency dependance. The origin of this noise is not well understood, but is the subject of considerable study. Further discussion of this, and more detailed treatments of TES noise mechanisms, may be found in the literature (e.g. Ref. [109]).

### 3.1.4 Detector Operating Temperature and Thermal Conductance

The detector operating temperature is determined by the requirements on the detector NEP derived previously, and summarised in Table 3.4. The required operating temperatures and thermal conductances, $G$, to achieve these NEPs will now be derived.

The thermal conductance of the weak thermal link between the absorber and the cold bath, $G$, is a function of temperature. It may be assumed that $G(T)$ is described by a power law, given by Eg. (3.4), with $G_0$ being the value of $G$ when $T = T_0$, the bath temperature.

$$G(T) = G_0 T^{\beta}. \tag{3.4}$$

The power, $P$, flowing between the TES and the cold bath along the thermal link is described by

$$P = \int_{T_0}^{T} G(T)\mathrm{d}T, \tag{3.5}$$

where $T$ is the pixel temperature. Solving this integral gives

$$P = K(T^n - T_0^n), \tag{3.6}$$

where $n = \beta + 1$ and $K = G_0/n$. Hence, the thermal conductance may be described by

$$G(T) = nKT^{n-1}. \tag{3.7}$$

Making the assumption that[3] $T \gg T_0$, $P \sim KT^n$ from Eq. (3.6). Therefore, $G(T)$ may be written as

$$G(T) \sim \frac{nP}{T}. \tag{3.8}$$

From the requirement that the detector contribution to the total NEP be one third of the photon noise, we can substitute $0.11\mathrm{NEP}_{\mathrm{ph}}^2$ for $\mathrm{NEP}_{\mathrm{det}}^2$. Using this substitution and Eq. (3.8) in Eq. (3.3), with $\gamma = 0.5$, and rearranging gives

$$T \sim \frac{0.11\mathrm{NEP}_{\mathrm{ph}}^2}{2knP}. \tag{3.9}$$

Substituting the values of $\mathrm{NEP}_{\mathrm{ph}}$ from Table 3.3, the total power handling from Table 3.5, and using $n = 3.5$, operating temperatures of ∼377 mK and ∼79 mK for 450 and 850 $\mu$m. The value of $n$ is based on measurements of the conductance of silicon nitride membranes for test pixels.

The required operational temperature of the 850 $\mu$m pixels dictated the use of a dilution refrigerator to cool the focal planes. Early thermal models of the millikelvin system indicated a likely bath temperature of 60 mK. Since the pixel temperature should

[3]Practically, $T$ should be at least $2T_0$.

be $\geq 2T_0$, a practical $T_c$ for the 850 $\mu$m pixels is 120 mK with an associated increase in $\mathrm{NEP_{det}}$. Further, since both focal planes needed to operate from the same cooling source, a $T_c$ of 380 mK for the 450 $\mu$m pixels would not be feasible. Assuming that the basic geometry of the two pixel types is identical (the $K$ and $n$ parameters in Eq. (3.6) therefore being identical), a practical transition temperature may be derived from the relationship

$$\frac{P_{450}}{P_{850}} = \frac{T_{450}^n - T_0^n}{T_{850}^n - T_0^n}, \tag{3.10}$$

where $P_{450}$ and $P_{850}$ are the total power handling for the 450 and 850 $\mu$m pixels, and $T_{450}$ and $T_{850}$ are the transition temperatures of the two pixels. It is also assumed that the bath temperature for both focal planes is the same, although this is not unreasonable. Rearranging and substituting values gives a $T_{450}$ of 185 mK.

The required dynamic thermal conductance of the pixels may be estimated from Eq. (3.8). Again, using $n = 3.5$, the power handling estimates in Table 3.5, and the operating temperatures derived above, $G_0$ values of 4.2 and 1.3 nW/K are obtained for 450 and 850 $\mu$m, respectively.

We can produce a simple model of the transition region by assuming an $R(T)$ characteristic as shown in Fig. 3.2. The TES resistance is assumed to be zero at $T < T_L$ and $R_N$ for $T > T_U$. The transition width, $\Delta T$ is $T_U - T_L$, with a linear variation in resistance between $R_N$ and zero. The resistance at some general temperature $T$ in the transition, $R(T)$, is described by

$$R(T) = \frac{R_N}{\Delta T}(T - T_L) \tag{3.11}$$

and

$$\frac{\mathrm{d}R}{\mathrm{d}T} = \frac{R_N}{\Delta T}. \tag{3.12}$$

The temperature coefficient of resistance, $\alpha$, from Eq. (1.8) is then given by

$$\alpha = \frac{T}{R}\frac{\mathrm{d}R}{\mathrm{d}T} = \frac{T}{T - T_L}. \tag{3.13}$$

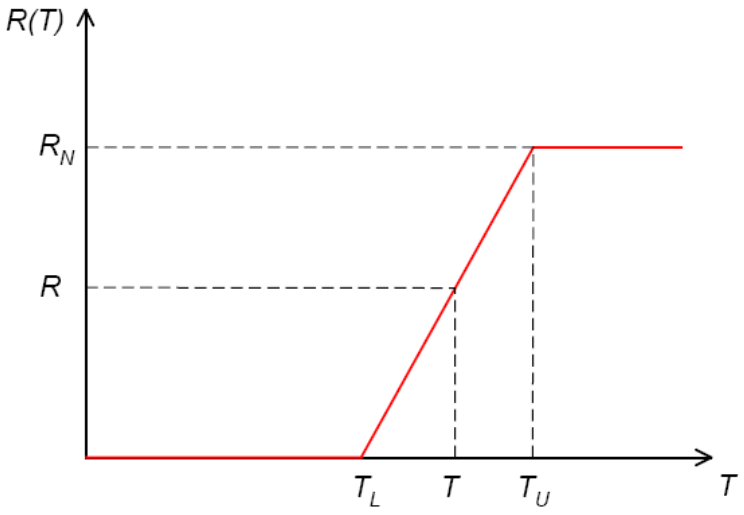


**Figure 3.2:** Simple representation of the TES transition between the normal and superconducting states. The device is assumed to have resistance $R_N$ above temperature $T_U$, and zero resistance below temperature $T_L$. The resistance at a general temperature in the transition, $T$, is $R$. The transition is taken to be linear, with width $\Delta T = T_U - T_L$.

If the TES is biased in the middle of the transition, which would generally be the goal since the midpoint would be expected to have the steepest gradient in a non-linear transition, then

$$T = \frac{T_U + T_L}{2} \tag{3.14}$$

and

$$\alpha = \frac{2T_c}{\Delta T}. \tag{3.15}$$

Note that in Eq. (3.15), the transition temperature $T_c$ has been substituted for the general temperature $T$ at the midpoint of the transition, since this is the definition of the transition temperature.

Taking the width of the TES transition to be ∼1.5 mK, which is consistent with measurements of test pixels in the early stages of the project, and taking the transition temperature of the 450 and 850 $\mu$m pixels to be 185 mK and 120 mK, $\alpha$ values of ∼250 and ∼160 are estimated.

### 3.1.5 Detector Response Time

Further to the detector NEP requirement, there is also a requirement on the detector time constant. One of the baseline observing strategies for SCUBA-2 was to conduct large-area surveys by scanning the telescope in a rapid, overlapping raster pattern across sources. The fastest speed at which astrometric information may be maintained in the detector output, determined by the detector response speed, will determine the maximum scanning speed. If the detector response is too slow, some of the higher spatial frequencies in the science signal will be attenuated.

The telescope acts as a spatial filter, since the measured system is the convolution of the response of the astronomical signal and the telescope beam [112]. The maximum frequency present in the system response is given by Eq. (3.16), where $p$ is the telescope plate-scale (arcseconds/mm), $F$ is the focal ratio, and $v_{telescope}$ the telescope scanning speed (arcseconds/s) [113].

$$\frac{1}{pF\lambda}(\text{arcsec}^{-1}) = \frac{v_{telescope}}{pF\lambda}(\text{Hz}). \tag{3.16}$$

In order to maintain a reasonable degree of astrometric accuracy, the maximum practical scanning speed for the JCMT would be approximately 600 arcseconds/s. With a plate scale of 5 arcseconds/mm at the SCUBA-2 focal plane and a focal ratio of 2.67, the maximum frequencies present in images at 850 and 450 $\mu$m are 50 and 100 Hz respectively. This is equivalent to detector time constants of 2.8 and 1.5 ms.

The thermal (or physical) time constant, $\tau_0$, is given by

$$\tau_0 = \frac{C}{G}, \tag{3.17}$$

where $C$ is the heat capacity of the absorber and $G$ the thermal conductivity of the link to the cold bath.

#### Pixel Heat Capacity

The heat capacity of the pixels may be calculated from literature values of the specific heats of the materials in the TES and absorber. At low temperatures, the heat capacity of the metals (the TES bilayer and the pixel heater) will dominate.

A convenient form for the heat capacity is

$$C(T) = \frac{\rho}{A}\gamma V T^x, \tag{3.18}$$

where $T$ is the sample temperature, $V$ is the sample volume, $\gamma$ the molar specific heat, $\rho$ the mass density, and $A$ the atomic weight (the product $\frac{\rho}{A}\gamma$ being the volumetric specific heat). The exponent $x$ defines the strength of the temperature dependance of $C$. For metals at low temperature, the heat capacity of normal metals is almost entirely due to the electron heat capacity, giving a linear temperature dependance ($x = 1$). In semiconductors, the phonon heat capacity dominates, giving a stronger dependance ($x = 3$ for silicon) [114].

According to the Bardeen, Cooper and Schrieffer (BCS) theory of superconductors, the heat capacity of a superconductor at $T_c$ is 2.43 times the value in the normal state. For a TES operating the transition, the heat capacity will vary between 1 and 2.43 times the normal state value as the resistance changes.[4] Table 3.6 lists the volumetric heat capacities for the main components of the SCUBA-2 pixels. The normal and superconducting state heat capacities, assuming the 2.43 increase in the superconducting state, are listed for molybdenum.

The calculation of the heat capacity of the pixels is summarised in Table 3.7. The major components of the pixel included are the molybdenum and copper in the TES bilayer, covering the approximate area of the absorber and with thicknesses of 40 and 70 nm, respectively. The pixel also includes a 250 nm thick copper bank as the heater element. The silicon brick absorber also contributes. Other pixel components, such as oxide layers and the silicon nitride membrane, are neglected since the contribution from these sources to the overall heat capacity will be small. The calculation assumes that $C$ for the molybdenum layer is the value in the superconducting state, and that $T$ is the transition temperature of the TESs for the two wavelengths. The calculated values of $C$ are 3.83 pJ/K at 110 mK for the 850 $\mu$m pixels, and 5.79 pJ/K at 160 mK for the 450 $\mu$m pixels.

[4]The actual value of $C$ within the transition may be determined through complex impedance measurements [115].

**Table 3.6:** Volumetric heat capacities of elements in the SCUBA-2 pixels.

| Element | Volumetric heat capacity / J/(K$^2$ cm$^3$) |
|---|---|
| Molybdenum (normal state) | $2.14 \times 10^{-4}$ |
| Molybdenum (superconducting state) | $5.20 \times 10^{-4}$ |
| Copper | $9.80 \times 10^{-5}$ |
| Silicon | $6.40 \times 10^{-7}$ |

**Table 3.7:** Summary of pixel heat capacity calculation. The calculated heat capacity of the molybdenum TES layer uses the volumetric heat capacity value for the superconducting state.

| Component | Volume / cm$^3$ | Heat capacity / pJ/K |
|---|---|---|
| *850 $\mu$m pixel, T = 120 mK* | | |
| TES molybdenum | $4.0 \times 10^{-8}$ | 2.50 |
| TES copper | $6.1 \times 10^{-8}$ | 0.72 |
| Heater bank (copper) | $7.4 \times 10^{-8}$ | 0.87 |
| Silicon brick | $9.0 \times 10^{-5}$ | 0.10 |
| 850 $\mu$m pixel | — | 4.19 |
| *450 $\mu$m pixel, T = 185 mK* | | |
| TES molybdenum | $4.0 \times 10^{-8}$ | 3.85 |
| TES copper | $6.1 \times 10^{-8}$ | 1.11 |
| Heater bank (copper) | $7.4 \times 10^{-8}$ | 1.34 |
| Silicon brick | $1.3 \times 10^{-4}$ | 0.53 |
| 450 $\mu$m pixel | — | 6.83 |

### Physical and Effective Time Constants

The physical time constants, $\tau_0$, as defined by Eq. (3.17) are found to be 1.6 ms for 450 $\mu$m and 3.2 ms at 850 $\mu$m, just outside the specification for the two wavelengths. However, the effect of electrothermal feedback acts to shorten the physical time constant, since the temperature of the TES is effectively constant, making the deviations from the equilibrium temperature small. We can define an effective time constant, $\tau_e$, that depends on the ETF loop gain, $\mathscr{L}_0$. The loop gain in turn depends on the coefficient of resistance, $\alpha$, and ratio of bias power, $P_{bias}$, to the total power, $P$. The effective time constant is given by

$$\tau_e = \frac{\tau_0}{1 + \mathscr{L}_0}, \tag{3.19}$$

where

$$\mathscr{L}_0 = \frac{G_{eff}}{G}. \tag{3.20}$$

The effective thermal conductance, $G_{eff}$, is defined as

$$G_{eff} = \frac{\alpha P_{bias}}{T}. \tag{3.21}$$

Using the values of $\alpha$ estimated previously, and assuming 10 pW of bias power at both wavelengths, the loop gains at 450 and 850 $\mu$m respectively are 3.2 and 10.2. The effective time constants for the pixels are 0.38 ms at 450 $\mu$m and 0.29 ms at 850 $\mu$m, both values well within the requirements described previously. The details of the physical and effective time constants are summarised in Table 3.8.

The derived time constants for the detectors has an implication for the design of the readout electronics, since the achievable frame rate must be sufficiently high that information in the detector response is not lost. Taking $\tau_e$ for the 850 $\mu$m devices, 0.29 ms, as the fastest time constant, the minimum frame rate is $\sim$ 3.5 kHz. Note that for each frame of data, all 41 lines of the multiplexer must be read out. Therefore, the minimum *line* rate of the readout must be 41 times the frame rate, $\sim$ 0.15 MHz. The multiplexer and readout electronics have been designed to give frame rates of up to 20 kHz. In practice, frame rates of at least 10 kHz have been adopted to minimise aliased noise [85].

**Table 3.8:** Summary of the expected SCUBA-2 detector physical and effective time constants.

| Parameter | 450 $\mu$m | 850 $\mu$m |
|---|---|---|
| Required time constant / ms | <1.5 | <2.8 |
| Pixel heat capacity, $C$ / pJ/K | 6.83 | 4.19 |
| Thermal conductance, $G$ / pW/K | 4200 | 1300 |
| Physical time constant, $\tau_0$ / ms | 1.6 | 3.2 |
| Effective thermal conductance, $G_{eff}$ / nW/K | 13.5 | 13.3 |
| Loop gain, $\mathscr{L}_0$ | 3.2 | 10.2 |
| Effective time constant, $\tau_e$ / ms | 0.38 | 0.29 |
| Minimum readout frame rate / kHz | 2.6 | 3.5 |

**Table 3.9:** Summary of the parameter requirements for the SCUBA-2 detectors

| Parameter | 450 $\mu$m | 850 $\mu$m |
|---|---|---|
| Total power handling / pW | 220 | 45 |
| Transition temperature / mK | 185 | 120 |
| Thermal conductance / nW/K | 4.2 | 1.3 |
| Time constant / ms | <1.5 | <2.8 |
| Per-pixel NEP / $10^{-17}$ W/$\sqrt{\text{Hz}}$ | 19 | 3.9 |

### 3.1.6 Summary of Detector Requirements

The requirements for the key detector parameters at 450 and 850 $\mu$m derived in this section are summarised in Table 3.9.

## 3.2 Sample Array Data

To date, six SCUBA-2 arrays have been produced and tested (three for each wavelength), variously in a test bed cryostat and in the main instrument. A considerable quantity of data has been collected during this testing. This section will present a series of measurements made with the most recent pair of arrays in the instrument

cryostat, with the aim of extracting the parameters derived in §3.1. The majority of these measurements were made prior to delivery of the instrument to the JCMT, with the exception of the data used for the noise measurements described in §3.2.4.

### 3.2.1 TES Voltage-Current Characteristics

A common method for the characterisation of detectors is to measure the device current as a function of voltage, referred to as a $V$-$I$ or "load" curve. Such measurements may be made by applying sufficient TES bias and heater current to drive the detectors into the normal state, and then stepping the bias current down and allowing the TES to pass through the transition and into the superconducting state. The load curves are useful since they allow selection of optimal bias conditions for the TES devices based on characteristics such as detector responsivity. As discussed in §3.2.3, load curves measured at a series of bath temperatures may be used to determine values of the thermal conductance, $G$, and the TES transition temperature.

Since the TES current is measured indirectly via the SQUIDs, which will display arbitrary DC offsets, it is necessary to calibrate the measured load curves. This is achieved by a linear fit to the raw load curve (a measurement of feedback current as a function of bias current) in the region where the TES is in the normal state. The feedback current gives a direct measure of the current flowing in the TES via an empirically determined calibration factor. When the TES is normal, the majority of the bias current flows through the shunt resistor connected in parallel with the TES (as shown in Fig. 3.3), since the 5 m$\Omega$ shunt resistance is much smaller than the normal state resistance of the TES. The current in the shunt is calculated by subtracting the TES current (with the SQUID offset removed) from the bias current. The voltage across the TES is obtained from the shunt current and the known value of the shunt resistance.

Typical characteristics for a TES on the 850 $\mu$m array are illustrated in Fig. 3.4. The calibrated load curve is displayed in Fig. 3.4(a), showing the expected shape of the response. At higher detector voltages (equivalent to higher bias currents) the TES is normal, and displays a constant $R$, the normal state resistance $R_N$. Once the bias current is stepped low enough that the detector power is less than the saturation power, there is a turnover and the gradient of the load curve becomes negative. This is a result

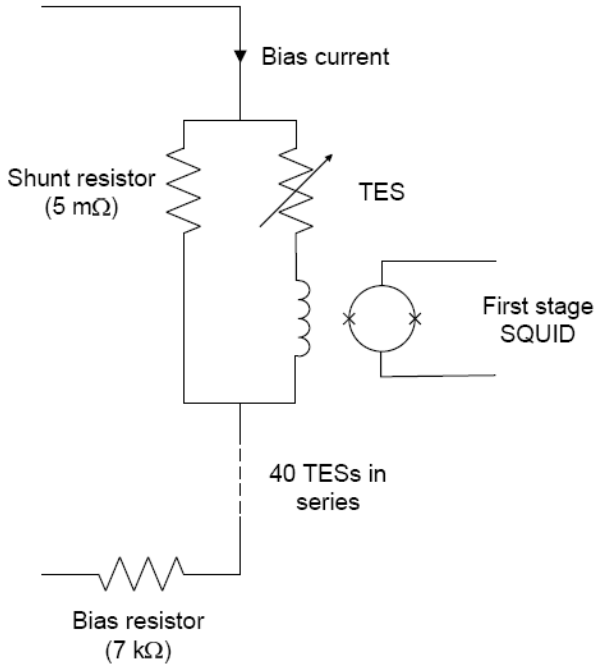


**Figure 3.3:** TES bias circuit.

of the falling TES resistance in the transition region. At lower bias currents, when the TES is fully superconducting, there is a second turnover. The load curve again displays a constant resistance, but on this branch all of the current flows through the superconducting TES.

Similarly, Fig. 3.4(b) shows the detector bias power as a function of detector voltage. A feature of the strong electrothermal feedback in the TES transition is that any change in the detector voltage also changes the TES resistance. The transition region is very narrow, so in the transition the detector power is approximately constant and $I \propto V^{-1}$. Above the transition, the TES acts as an ohmic resistor, the bias power will be proportional to $V^2$. Both characteristics may be seen here.

Fig. 3.4(c) depicts the TES resistance, with a normal state value in reasonable agreement with the expected value of 75 mΩ, and displaying the decreasing resistance in the transition region. Finally, Fig. 3.4(d) shows the theoretical responsivity of the TES, given by $V^{-1}$ [33]. The responsivities derived in this way are found to be in reasonable agreement to those determined from other methods.

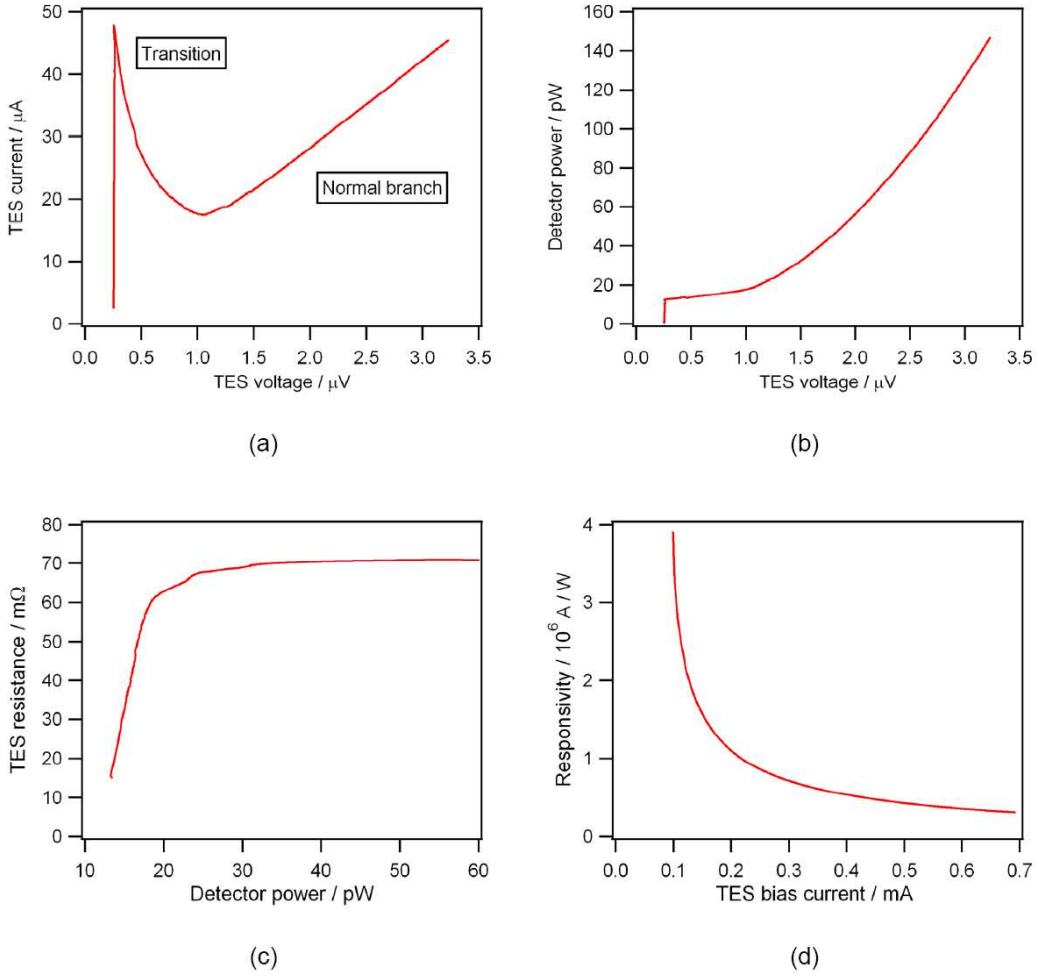


**Figure 3.4:** Typical TES characteristics obtained from load curve measurements. (a) Detector current response as a function of detector voltage. (b) Detector bias power as a function of detector voltage. (c) TES resistance as a function of detector power. (d) TES responsivity as a function of bias current.

Typically, a series of load curves are measured at different pixel heater powers. Since the TES is heated into the transition by a combination of bias and heater power, it would be expected that as the pixel heater power is increased, less bias power would be required to drive the pixel normal. An example of such a series for a pixel on the 850 $\mu$m array is depicted in Fig. 3.5, showing the expected trend with increasing heater power. The same load curves are shown in power-voltage space in Fig. 3.6, displaying approximately constant power in the transition region, and good agreement between the curves on the normal branch. Fig. 3.7 shows load curves for several pixels on a single row of the 850 $\mu$m array, demonstrating that multiple pixels show similar characteristics, and may potentially be biased in the transition simultaneously.

### 3.2.2 Power Handling

Measurements of the saturation power of pixels at each wavelength indicated average power handling of (100±20) pW at 850 $\mu$m, and (230±50) pW at 450 $\mu$m [116]. The estimated errors are based on the measured variation of the $T_c$ and $G$ parameters. The 450 $\mu$m value compares well to the requirement of 220 pW, but the 850 $\mu$m value is a factor 2 higher than the required 45 pW. The explanation for the elevated power handling, as discussed further below, is elevated G and $T_c$ values for the array used for this measurement.

### 3.2.3 Thermal Conductance and Transition Temperature

Measurements of the thermal conductance and transition temperature of pixels across the arrays may be obtained by measuring the pixel heater power required to drive the TES into the normal state as a function of bath temperature. This measurement may be made using TES load curves measured at a series of bath temperatures. Such a set of curves for an 850 $\mu$m pixel is depicted in Fig. 3.8. The bath temperature was varied by applying heat to the mixing chamber of the dilution refrigerator. For these measurements, the bath temperature is taken to be the temperature of the multiplexer wafer, as measured by a Lake Shore RX-102-BR ruthenium oxide temperature sensor on the wafer. The measurements were made at a constant pixel heater power (∼65 pW), and the load curve was obtained by stepping the TES bias.

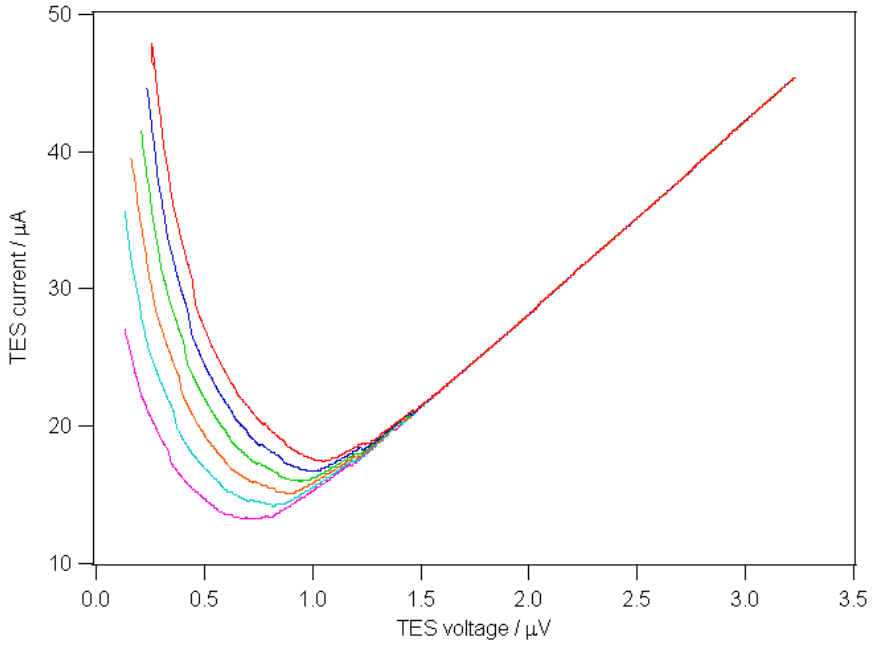


**Figure 3.5:** A series of load curves for one pixel on the 850 $\mu$m array measured at different pixel heater powers. As would be expected, for higher heater powers less bias power is required to drive the pixels into the normal state.

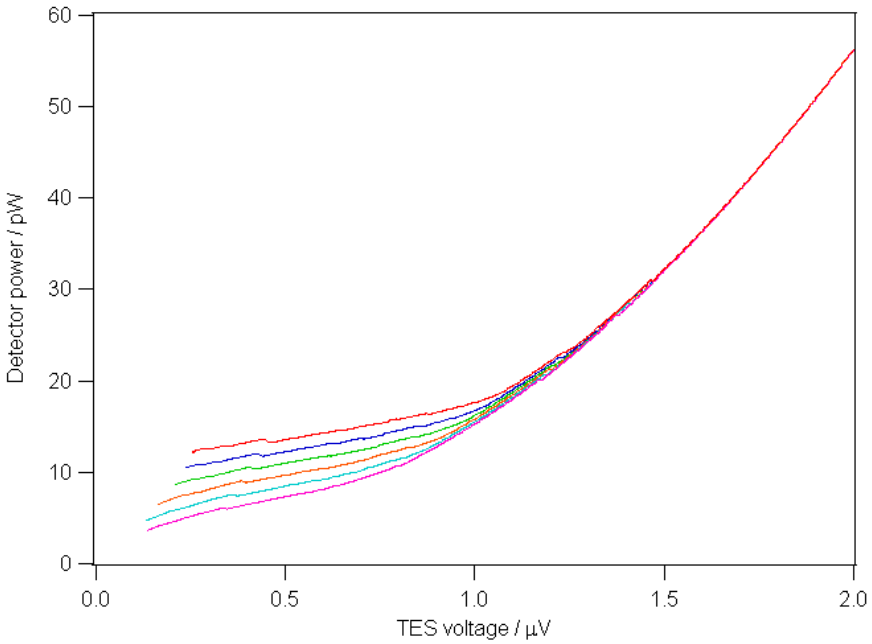


**Figure 3.6:** Detector power as a function of TES voltage for the load curves shown in Fig. 3.5. As expected for a TES, the power in the transition is approximately constant.

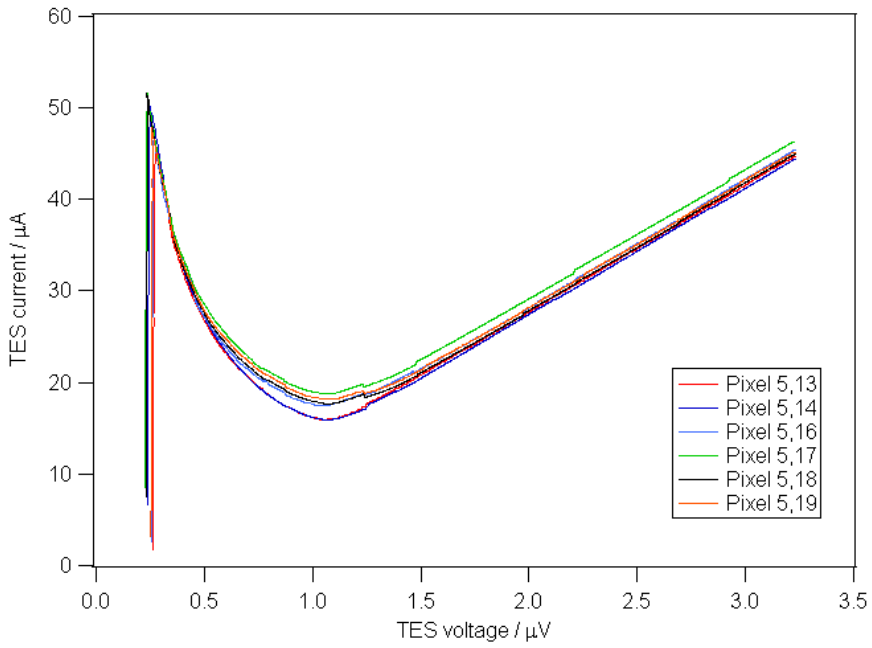


**Figure 3.7:** Example load curves measured simultaneously for a several pixels on a single row of the 850 $\mu$m array.

The bias power required to drive the TES normal at the constant heater power is determined by locating the turnover of each load curve, where the sign of the gradient changes as the TES enters the superconducting transition. Taking the resistance of the TES at the top of the transition to be the normal state resistance, the power dissipated in the TES by the bias current may be calculated. The total power to drive the TES into the transition is the sum of the bias power and the applied heater power.

For this series of load curves, the total power (bias power plus the heater power) to drive the TES normal is plotted as a function of the bath temperature in Fig. 3.9. This data is fitted to the form of Eq. (3.6), with $K$, $T_c$ and $n$ as free parameters. The thermal conductance, $G$, is then obtained by substitution of the recovered values into Eq. (3.7). The fitted curve is depicted in Fig. 3.9. For this data, the recovered transition temperature is $(141.5 \pm 0.3)$ mK, while the $K$ and $n$ parameters are $(55400 \pm 500)$ W/K and $(3.06 \pm 0.01)$, respectively. The quoted uncertainties are $\pm 1$ standard deviation. Using Eq. (3.7), $G$ is found to be $(3.03 \pm 0.03)$ nW/K.

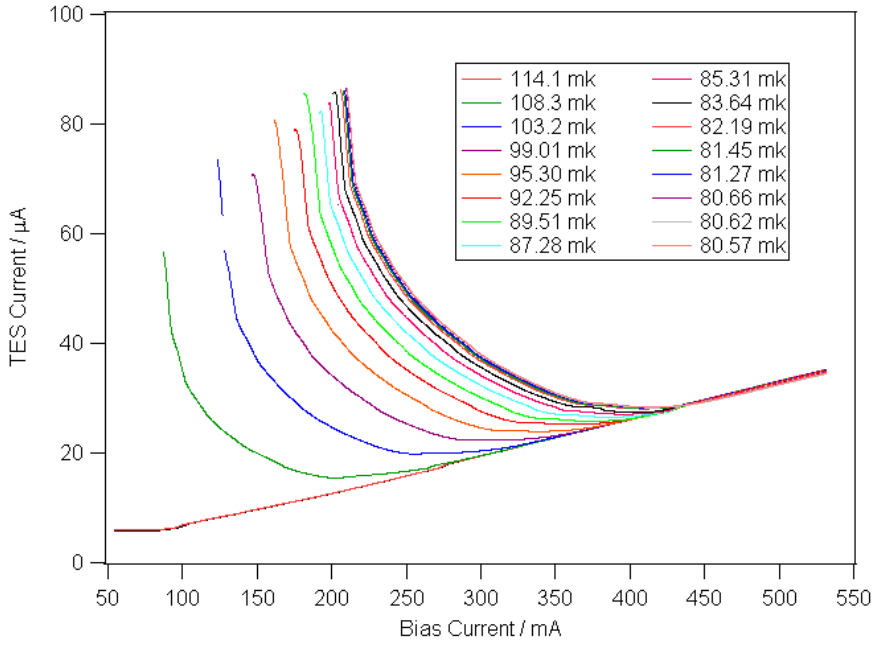


**Figure 3.8:** A series of load curves for one pixel on the 850 $\mu$m array measured at a series of bath temperatures between 80 and 115 mK. The bath temperature is taken to be the temperature of the MUX wafer.

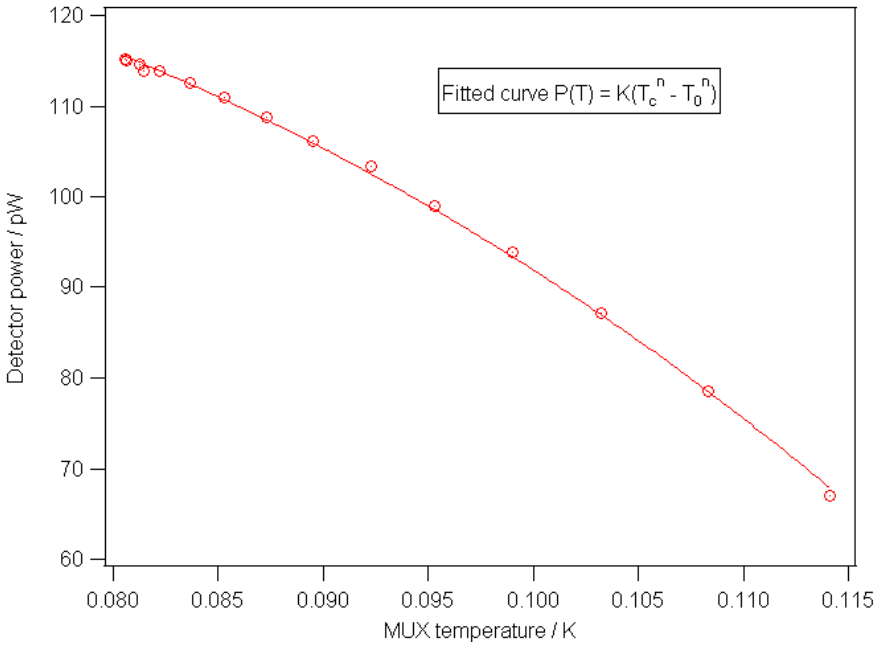


**Figure 3.9:** Pixel power required to drive the TES into the normal state as a function of bath temperature, as determined from the turnover of the load curves in Fig. 3.8.

For array scale measurements, a computationally faster (although less accurate) method may be employed. The bath temperature was again varied by applying heat to the dilution refrigerator mixing chamber. For a fixed bath temperature, the pixel heater was stepped down while applying a small modulated signal to the TES bias. A distinct feature is observed in the detector output as the TES passes through the transition due to the high responsivity of the TES in the transition region compared to the normal or superconducting states. The heater power, $P$, at the position of the feature was taken to be the heater power required to drive the pixel normal. $G$ and $T_c$ are then determined in the same way as described above.

Fig. 3.10 depicts the $G$ spatial distribution for the 850 $\mu$m array. For the 548 working pixels in this measurement, the mean thermal conductance was found to be 3.04 nW/K, with a standard deviation of 0.22 nW/K. Considering the spatial distribution of $G$, there is a slight linear gradient observed towards the lower end of the array. The origin of this effect is not clear, but may be associated with a procedural error in the hybridisation process in which a missed cleaning step resulted in additional indium oxide layers in the bump bonds between the detector and multiplexer wafers.

The $G$ distribution for the 450 $\mu$m array is shown in Fig. 3.11. For 710 working pixels, the mean $G$ was found to be 4.95 nW/K with a standard deviation of 0.36 nW/K. On the 450 $\mu$m array, a central feature of high thermal conductance is observed. Examination of the detector arrays indicated that the cause of the increased $G$ was poor control of the deep etch process used to isolate the pixel absorbers. As discussed previously, $G$ is controlled by the width of the isolating trench around each absorber. For these arrays, it was found that the trench widths were 2–3 times greater than the target values [117].

The required $G$ values for the two arrays derived previously were 1.3 and 4.2 nW/K for the 850 and 450 $\mu$m pixels, respectively. The measured values for these arrays are higher than the derived values, particularly for the 850 $\mu$m array. The consequence of the higher $G$ values will primarily be increased detector NEPs.

The distribution of transition temperature for the 850 $\mu$m array is shown in Fig. 3.12. As for the $G$ distribution on the 850 $\mu$m array, the transition temperature shows a similar linear trend towards elevated $T_c$ on the lower side of the array. The origin of this trend is believed to be the same for both parameters. For the 546 working pixels in this map,

the average $T_c$ is found to be 138 mK. The $T_c$ distribution for the 450 $\mu$m array is shown in Fig. 3.13. As would be expected, the $T_c$ distribution does not show the radial dependance seen in the $G$ measurements (the transition temperature is independent of the deep-etch process). The average $T_c$ for the 710 pixels in this map is 174 mK. The target values for the transition temperatures were 120 mK for the 850 $\mu$m array and 185 mK for the 450 $\mu$m array. The values determined from the parameter measurements compare reasonable well to the required values, and to measurements made on test pixels and previous arrays.

It should be noted that the measurement of the bath temperature for the determination of $G$ and $T_c$ may be flawed in that the thermometer is mounted at one edge of the MUX wafer. It may be the case that there is a temperature gradient across the wafer which will introduce a linear variation in the extracted parameters. Investigation of the behaviour of this thermometer suggests that if such a gradient exists, the effect is smaller than the intrinsic noise of the measurement.

### 3.2.4 Noise Equivalent Power

Per pixel NEP measurements are made by determining the responsivity, $S$, of a pixel and the average noise level. Responsivity is measured by applying a modulation to the pixel heater and measuring the feedback current. Fig. 3.14 shows two pixels (column 22, row 36 and column 2, row 24) responding to a heater modulation of $\sim$0.6 pW. The majority of working pixels on the 850 $\mu$m array were found to have responsivity values ranging from $\sim 10^5$ to $\sim 10^6$ A/W. The pixels plotted in Fig. 3.14 have responsivity values of 2.67 and 1.50 MA/W, respectively.

Pixel noise is measured from the Fourier transform of a timestream, such as that shown in Fig. 3.15. The average noise level is calculated in a frequency window between 2 and 10 Hz. These limits cover the range of the majority of the scan frequencies for the instrument, while being away from low frequency noise features and the $1/f$ contribution to the power spectrum. The majority of the pixels on the 850 $\mu$m array were found to have noise levels $<$300 pA/Hz$^{0.5}$.

The per pixel NEP is determined by dividing the average noise by the responsivity. A plot of the spatial distribution of NEP values for the 850 $\mu$m array is shown in

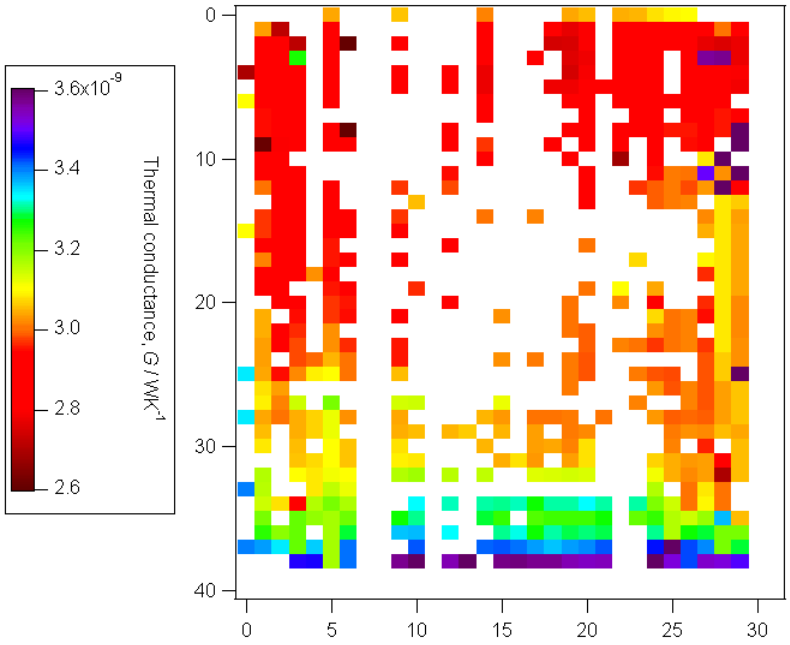


**Figure 3.10:** 850 $\mu$m array pixel thermal conductance distribution.

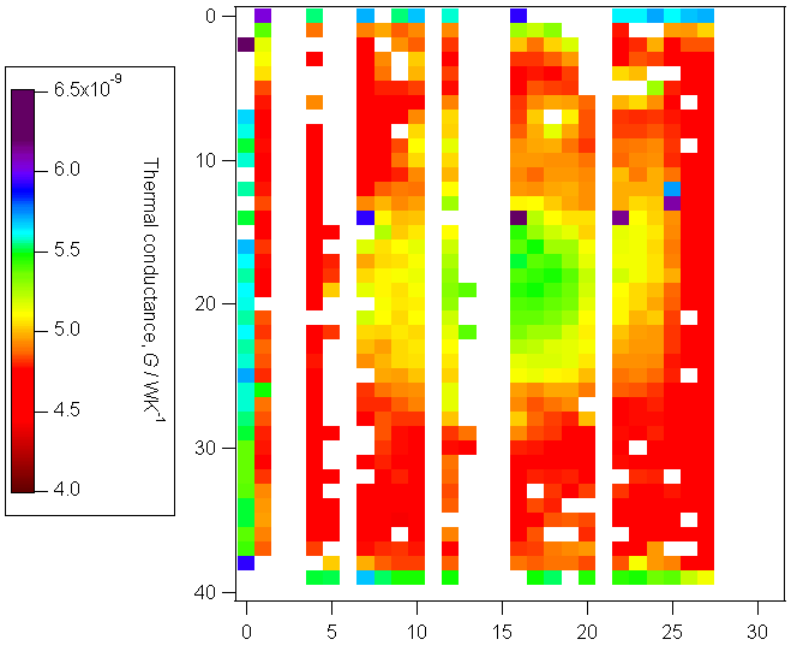


**Figure 3.11:** 450 $\mu$m array pixel thermal conductance distribution.

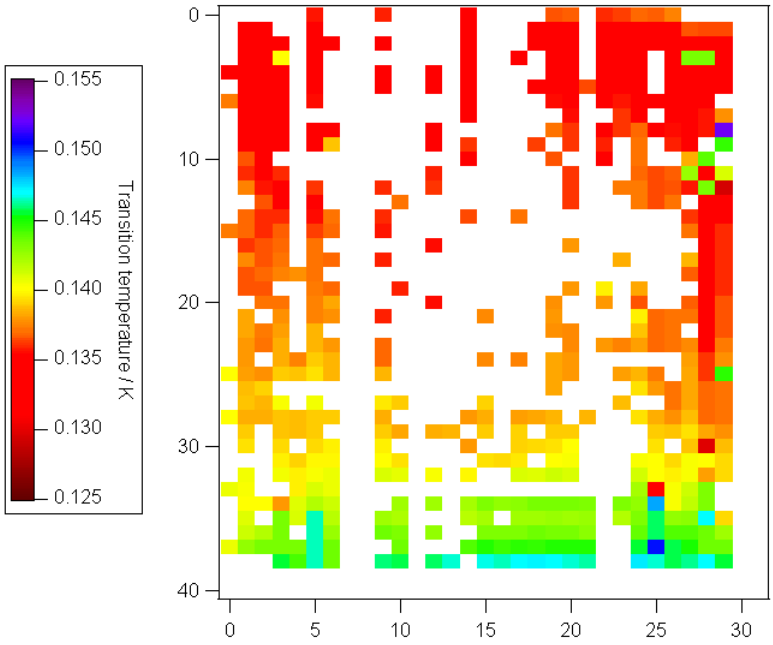


**Figure 3.12:** 850 $\mu$m array pixel transition temperature distribution.

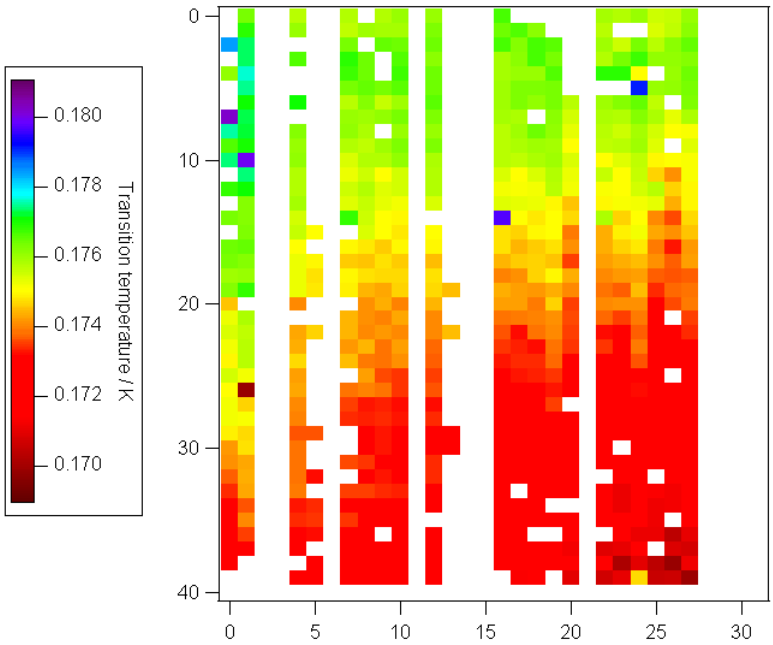


**Figure 3.13:** 450 $\mu$m array pixel transition temperature distribution.

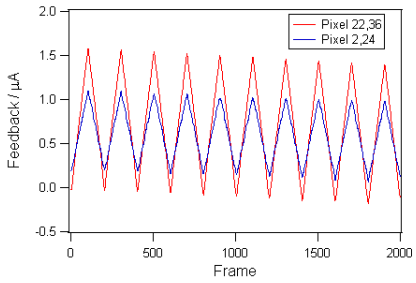


**Figure 3.14:** Two pixels on the 850 $\mu$m array responding to a heater modulation.

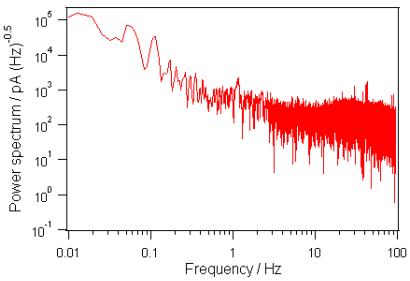


**Figure 3.15:** Typical noise spectrum for an 850 $\mu$m pixel.

Fig. 3.16, with a histrogram of the data depicted in Fig. 3.17. Due to the presence of a number of high NEP pixels in this data, values higher than $10^{-15}$ W/$\sqrt{\text{Hz}}$ have been excluded from the plots. The effect of applying masks at different NEP levels is discussed in more detail below. The majority of the pixels in these plots have NEP values in the $10^{-16}$ W/$\sqrt{\text{Hz}}$ range, although this is still an order of magnitude higher than the required value of $3.9\times10^{-17}$ W/$\sqrt{\text{Hz}}$. Taking account of all 514 working pixels in this data set, the average NEP is found to be $9.6\times10^{-15}$ W/$\sqrt{\text{Hz}}$, with a standard deviation of $6.1\times10^{-15}$ W/$\sqrt{\text{Hz}}$. It should be noted that the array setup for these data was made to maximise the number of working pixels at the expense of a degraded NEP performance, and hence does not represent the best possible pixel performance.

The high NEP values seen in this data appear to be the result of both elevated noise levels and low responsivity. The working pixels show responsivity values in the range 0.1–$\sim$1 MA/W (the average responsivity is $\sim$ 0.6 MA/W). However, at the typical detector voltages in the transition the of $\sim$ 1 $\mu$V, the expected responsivity would be greater that 1 MA/W. However, in ETF operation the responsivity, $S = V^{-1}$. The detector voltage [109], $V = (PR)^{-0.5}$, where $P$ is the power flowing to the heat sink and $R$ is the device resistance, and from Eq. (3.6) $P \propto G$. Therefore, the responsivity goes as $G^{-0.5}$, so the previous measurements of $G$ for this array would imply that the responsivity of these devices would be suppressed by factors of $\sim$ 1.5.

Even accounting for the measured values of $G$ and $T_c$ for this array being different from the design values, the measured NEPs are still higher than the theoretical values. The implication of this is that there is a high white noise level in the pixel readout. While the origin of this excess noise component is still under investigation, but two

possibilities immediately present themselves. Firstly, due to the fabrication errors for these arrays (particularly the 850 $\mu$m array), there is a possibility that normal-metal junctions have been introduced during the bump bonding process since a cleaning step to remove oxidised material from the bond pads was missed prior to hybridisation. The contaminating material will no go superconducting, leading to the possibility of additional Johnson noise components in the detector output.

A further possibility, and perhaps one which is a dominant effect, is the effect of magnetic flux noise. The measurements described here were made with the instrument installed at the JCMT, and it has been found that the pixels were considerably noisier in the telescope environment that in laboratory testing prior to delivery. This would imply that much of the excess noise is not inherent to the arrays themselves. Recent evidence suggests that the enhanced noise originates from magnetic flux at the focal planes. This is discussed in more detail in Chapter 9.

The NEP distribution for the 450 $\mu$m array is shown in Figs. 3.18 and 3.19, again with values greater than $10^{-15}$ W/$\sqrt{\text{Hz}}$ excluded. The distribution for the 450 $\mu$m array is highly skewed, with the vast majority of the NEP values below $4\times10^{-16}$ W/$\sqrt{\text{Hz}}$. This is to be expected, since the $G$ values on this array are closer to the derived target values. Average value for the full data set of 783 pixels is $2.1\times10^{-13}$ W/$\sqrt{\text{Hz}}$, with a standard deviation of $2.2\times10^{-12}$ W/$\sqrt{\text{Hz}}$. The high average is the result of a number of outlying pixels with NEPs of $10^{-12}$ and $10^{-11}$ W/$\sqrt{\text{Hz}}$. As with the 850 $\mu$m array, the origin of the elevated NEP values is likely the excess noise components in the detector output at the telescope. The effect of reduced responsivity is not as great on the 450 $\mu$m array as for the 850 $\mu$m, since the $G$ values determined for the 450 $\mu$m array are closer to the design values.

### The Effect of NEP, Noise and Responsivity Masks

To deal with noisy pixels on the arrays, it will be necessary to mask the arrays in some way to remove pixels showing poor performance. A crude way of achieving this would be reject pixels with NEPs above a certain threshold, effectively as in the plots displayed in Figs. 3.16–3.19. However, a limitation of this approach is that pixels with anomalous responsivity and/or noise levels, but with reasonable NEP values, could still

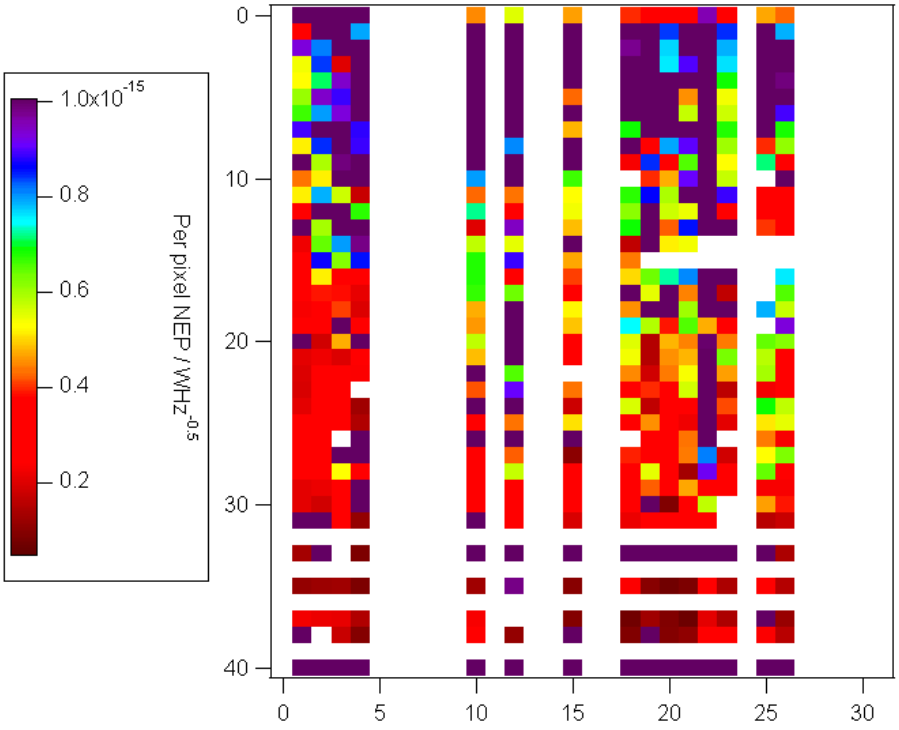


**Figure 3.16:** 850 $\mu$m array pixel noise equivalent power distribution. A cut has been applied at $10^{-15}$ W/$\sqrt{\text{Hz}}$ to remove a number of outlying values. See text for discussion.

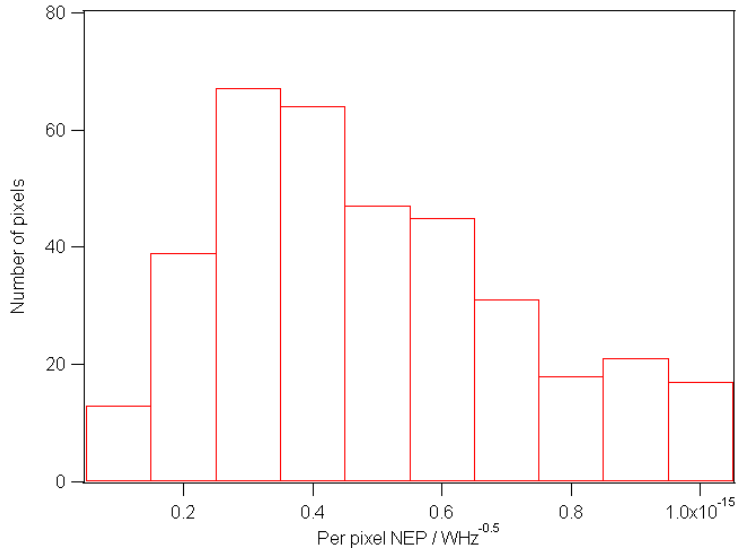


**Figure 3.17:** 850 $\mu$m array pixel noise equivalent power distribution histogram up to $10^{-15}$ W/$\sqrt{\text{Hz}}$.

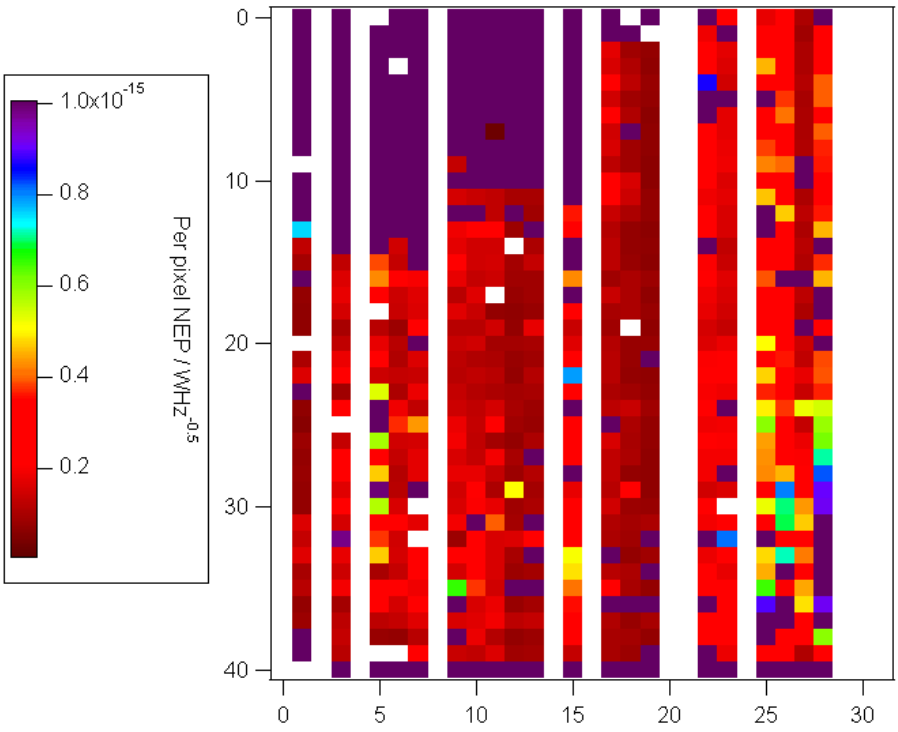


**Figure 3.18:** 450 $\mu$m array pixel noise equivalent power distribution. A cut has been applied at $10^{-15}$ W/$\sqrt{\text{Hz}}$ to remove a number of outlying values. See text for discussion.

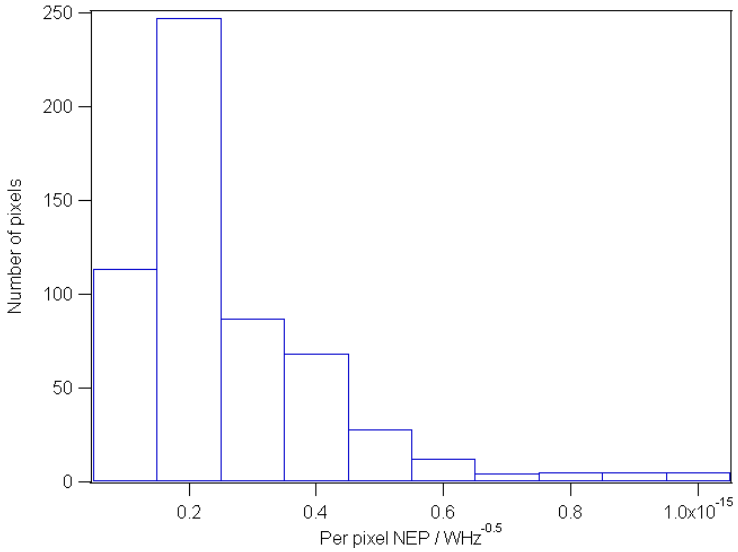


**Figure 3.19:** 450 $\mu$m array pixel noise equivalent power distribution histogram up to $10^{-15}$ W/$\sqrt{\text{Hz}}$.

**Table 3.10:** The effect of applying masks to array data based on noise equivalent power levels. The number of unmasked pixels in the sample, the average NEP and the standard deviation of the NEP are listed for the 850 and 450 $\mu$m arrays.

| | 450 $\mu$m array | | | 850 $\mu$m array | | |
|---|---|---|---|---|---|---|
| Mask | Number of pixels | Av. NEP / W/$\sqrt{\text{Hz}}$ | $\sigma$ / W/$\sqrt{\text{Hz}}$ | Number of pixels | Av. NEP / W/$\sqrt{\text{Hz}}$ | $\sigma$ / W/$\sqrt{\text{Hz}}$ |
| None | 783 | $2.1\times10^{-13}$ | $2.2\times10^{-12}$ | 514 | $9.6\times10^{-15}$ | $6.1\times10^{-14}$ |
| $10^{-12}$ | 770 | $2.4\times10^{-14}$ | $9.7\times10^{-14}$ | 513 | $7.5\times10^{-15}$ | $4.0\times10^{-14}$ |
| $10^{-13}$ | 725 | $5.8\times10^{-15}$ | $1.6\times10^{-14}$ | 506 | $3.6\times10^{-15}$ | $1.2\times10^{-14}$ |
| $10^{-14}$ | 625 | $5.4\times10^{-16}$ | $1.3\times10^{-15}$ | 466 | $9.2\times10^{-16}$ | $1.3\times10^{-15}$ |
| $10^{-15}$ | 574 | $2.2\times10^{-16}$ | $1.6\times10^{-16}$ | 362 | $4.4\times10^{-16}$ | $2.4\times10^{-16}$ |

be included. A more rigorous approach would therefore be to apply separate masks to the responsivity and noise measurements before the NEP values are calculated. The effect of using the two methods to apply masks to the array measurements described previously was briefly explored, and is discussed below.

The effect of applying masks based on NEP values to the two arrays is summarised in Table 3.10. As would be expected, as the level of the NEP mask is reduced, more pixels are removed from the set, and correspondingly the average NEP and the spread of the values decreases as outliers with high NEP values are excluding. For the $10^{-15}$ W/$\sqrt{\text{Hz}}$ mask applied to the data in Figs. 3.16–3.19, the average NEP for the 450 $\mu$m array is $2.2\times10^{-16}$, compared to a requirement of $1.9\times10^{-16}$, and for the 850 $\mu$m array the average value is $4.4\times10^{-16}$ against a requirement of $3.9\times10^{-17}$. For both arrays, less that 30% of the working pixels are masked at this level.

Application of NEP masks alone in order to remove bad pixels may not be the best solution, however. Firstly, as was found with these array maps, it is possible for a pixel to have a reasonable NEP, but display abnormal noise and responsivity performance, either with very high noise and responsivity, or very low noise but also low responsivity. Furthermore, measurements on these detector arrays have indicated that pixels that show a high responsivity can also be highly unstable, making the bolometers difficult to

**Table 3.11:** The effect of applying masks to array data based on responsivity and noise level. The number of unmasked pixels in the sample, the average NEP and the standard deviation of the NEP are listed for the 850 $\mu$m array only.

| Responsivity mask / A/W | Noise mask / pA/Hz$^{0.5}$ | Number of pixels | % pixels masked | Av. NEP / W/$\sqrt{\text{Hz}}$ | $\sigma$ / W/$\sqrt{\text{Hz}}$ |
|---|---|---|---|---|---|
| None | None | 514 | 0 | $9.6\times10^{-15}$ | $6.1\times10^{-14}$ |
| None | 500 | 445 | 13 | $7.7\times10^{-15}$ | $4.1\times10^{-14}$ |
| None | 300 | 305 | 41 | $1.0\times10^{-14}$ | $4.9\times10^{-14}$ |
| 100 000 | None | 454 | 12 | $1.8\times10^{-16}$ | $5.6\times10^{-17}$ |
| 100 000 | 500 | 387 | 25 | $1.9\times10^{-16}$ | $6.0\times10^{-17}$ |
| 100 000 | 300 | 256 | 50 | $2.4\times10^{-16}$ | $9.9\times10^{-17}$ |
| 500 000 | None | 246 | 52 | $1.8\times10^{-16}$ | $5.6\times10^{-17}$ |
| 500 000 | 500 | 194 | 62 | $1.9\times10^{-16}$ | $6.1\times10^{-17}$ |
| 500 000 | 300 | 94 | 82 | $2.6\times10^{-16}$ | $1.2\times10^{-17}$ |

calibrate and use [118]. The use of masks for the responsivity and noise independently offers greater flexibility in operation of the instrument, and is also a useful diagnostic tool for looking at these aspects of the array performance.

The effect of the application of such masks were explored using the data set for the 850 $\mu$m array. Based on maps of the responsivity and noise level from this data set, masks levels of 300 and 500 pA/Hz$^{0.5}$ were selected for the noise level, and masks at 100 000 and 500 000 A/W for the responsivity were selected. The distribution of NEP values obtained is summarised in Table 3.11. These tests appear to indicate that masking of the responsivity and noise level separately is generally more effective than a crude NEP mask. Similar or better average NEP values are obtained for similar numbers of unmasked pixels when separate masks are applied. These tests are extremely limited, however, in that only one data set has been explored with empirically-selected mask levels. Further work will be needed in this area before any firm conclusions may be drawn.

#### Dark SQUIDs and TES Noise Features

At present, the array data reduction process does not utilise the output of the dark SQUID for noise cancellation. Chopping between the first stage SQUIDs and the dark SQUID in each column was intended to suppress excess low-frequency noise in the MUX.

The output of a single pixel on the 850 $\mu$m array (column 22, row 36) while operational at the telescope is shown in Fig. 3.20, with the output from the dark SQUID in that column for comparison. It is apparent from this plot, representative of the overall array, that considerable instability is presented in the output of the first stage SQUIDs. The same pixel outputs are shown in Fourier space in Fig. 3.20, from which it may be seen that above 1 Hz the power spectrum of the pixel and dark SQUID are comparable, while at lower frequencies the pixel shows enhanced $1/f$ noise. Removal of the dark SQUID signal therefore has little effect on the noise performance of the pixels.

The origin of this instability is not clear. It was initially believed to result from bath temperature fluctuations, to which the TESs are sensitive. The SQUIDs are insensitive to such fluctuations, and so this signal does not appear in the dark SQUID output. A possible solution to such instability would be the application of a "dark bolometer", a TES blanked off from incoming radiation that could be used to remove noise features the other detectors, in the same way as the dark SQUID is used to remove noise in the multiplexer devices. While introduction of such devices was discussed, it would not be straightforward to fabricate such a device for the SCUBA-2 arrays without considerable modification of the array design. This work was subsequently abandoned, since later comparison of the observed TES instability with direct measurements of the temperature instabilities suggested that the effect of the temperature fluctuations is actually small compared to the observed instabilities. The implication of this is that the origin of the low frequency noise is actually inherent to the TES devices themselves (the excess $1/f$ noise discussed previously). A dark bolometer would not allow removal of such noise components, since the noise in different devices would not necessarily be correlated.

### 3.2.5 Detector Speed of Response

The detector response speed was measured by applying a square wave signal to the pixels heaters and recording the detector output at the frame rate of the electronics

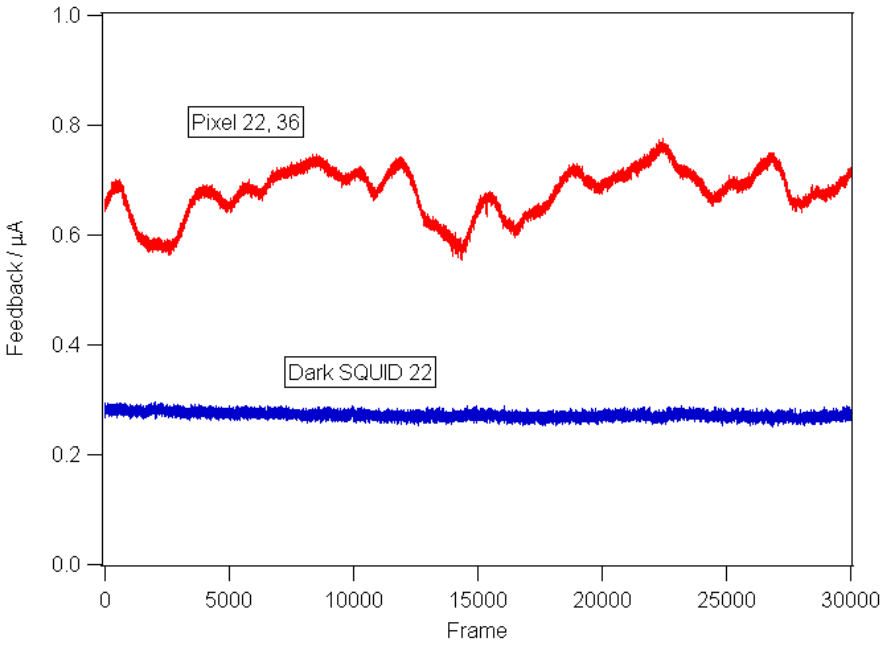


**Figure 3.20:** Time series output for pixel 22,36 on the 850 $\mu$m array, and the column 22 dark SQUID output.

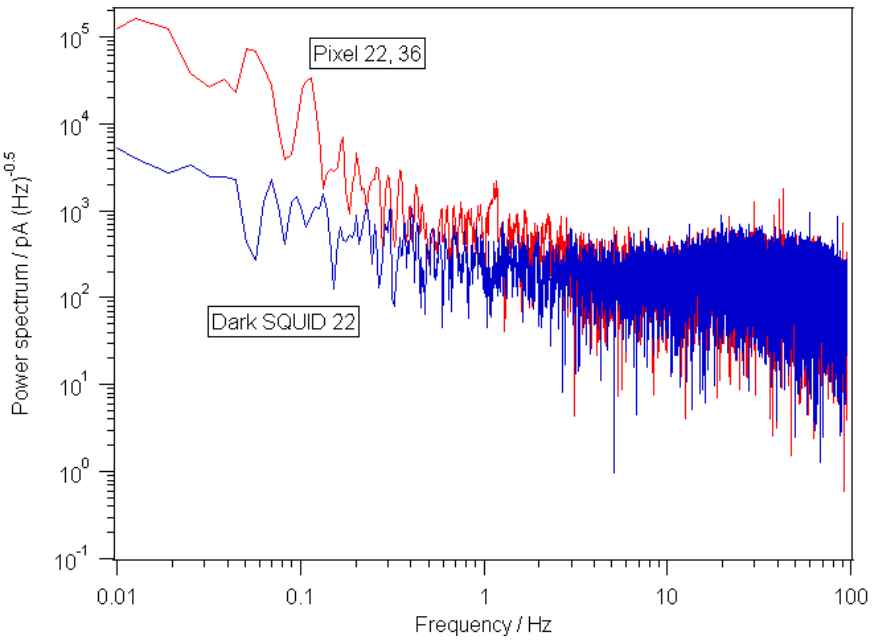


**Figure 3.21:** Output of 850 $\mu$m array pixel 22,36 and the column 22 dark SQUID in Fourier space.

(10 kHz). The pixel time constant was taken to be the time required for the pixel output to reach 66% of the amplitude of the heater signal. It is also assumed that the time constant of the heater is much shorter than the TES, which is not unreasonable due to the difference in the heat capacities (from Table 3.7, the heat capacity of the TES bilayer is ∼30 times that of the heater bank).

The response of a typical pixel on the 850 $\mu$m array to a square wave signal on the heater is shown in Fig. 3.22. Both the response of the pixel in closed loop operation, with feedback applied to the first stage SQUID, and open loop operation is shown. Operation of the detectors in the closed loop mode is typical in normal operation, with a feedback signal being applied to the first stage SQUIDs in real time in order to null the flux changes due to changes in the current in the TES. The open loop mode applies a constant level of feedback to the SQUIDs with no real time correction.

The average closed loop time constant was found to be 1 ms, while the open loop time constant was found to be 0.3 ms. The closed loop measurement easily meets the required time constant of 2.8 ms for the 850 $\mu$m detectors. However, the implication of this measurement is that the response of the detectors is actually being limited by the speed of the multiplexer electronics. This is not an issue in terms of operation of the devices, since the time constant in the normal operating mode still meets the time constant requirement. This measurement also demonstrates that the achievable frame rate from the readout electronics, in this case 10 kHz (1 sample every 0.1 ms), is sufficiently fast that information in the detector response is not being lost.

Although this measurement is for the 850 $\mu$m array, an estimate may be derived for the 450 $\mu$m detectors. From the estimated pixel heat capacities (see Table 3.7), $C$ for the 450 $\mu$m pixel is approximately 1.5 times that for the 850 $\mu$m pixels. Furthermore, measurements of the average thermal conductance for these arrays indicates that $G$ for the 450 $\mu$m pixels is ∼1.5 times that for the 850 $\mu$m (note that for these arrays, the 850 $\mu$m $G$ is a factor 2 higher that the specification). From this, it is estimated that the 450 $\mu$m detector time constant will also be ∼1 ms for the closed loop mode. This is within the specification of 1.5 ms for the 450 $\mu$m array.

As a consequence of the elevated $G$ for this 850 $\mu$m array, it should be expected that the detector speed of response is suppressed by a factor of ∼2 compared to the

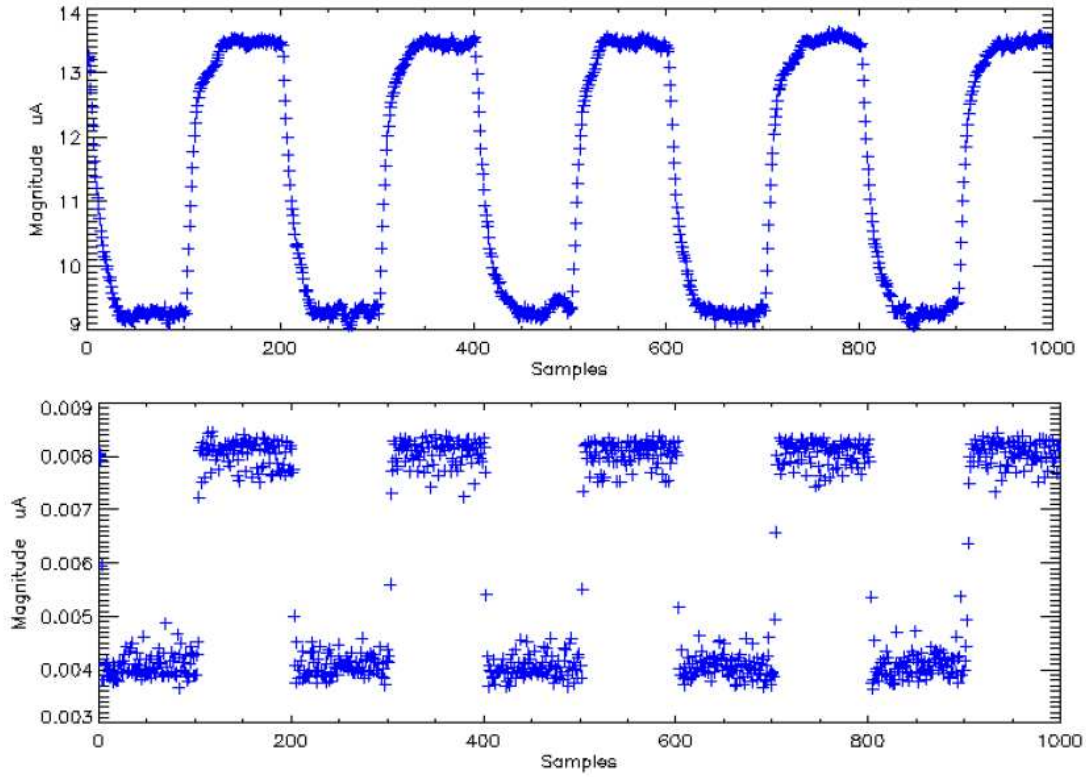


**Figure 3.22:** Response of a pixel to a square wave signal on the pixel heater for a speed of response measurement. The upper plot shows the pixel operating with a closed flux-locked loop (with a feedback signal applied to the first stage SQUIDs), while the lower plot shows the pixel response while running open loop. In both cases, the markers are at time intervals of 0.1 ms (10 kHz frame rate). Figure adapted from Ref. [119].

value for the correct $G$ specification. However, this is still within the requirement for the 850 $\mu$m detectors.

It is interesting to note that the open loop measurements, which should give a measure of the *effective* detector time constant, gives a value that is close to the $\tau_e$ values determined previously.

### 3.2.6 Comparison of Measured Parameters to Requirements

A summary of the comparison between the measured parameters for the two arrays discussed so far, and the requirements derived in §3.1 is displayed in Table 3.12. The key issues to note in this comparison, for the 850 $\mu$m array in particular, is the elevated

**Table 3.12:** Comparison of derived and measured parameters for the 450 and 850 $\mu$m detectors. The measurements of the transition temperature, thermal conductance and per-pixel NEP are quoted with $1\sigma$ errors.

| Parameter | 450 $\mu$m | | 850 $\mu$m | |
|---|---|---|---|---|
| | Requirement | Measured | Requirement | Measured |
| Total power handling / pW | 220 | (230±50) | 45 | (100±20)[a] |
| Transition temperature / mK | 185 | (174±2) | 120 | (138±4) |
| Thermal conductance / nW/K | 4.2 | (5.0±0.4) | 1.3 | (3.0±0.2)[b] |
| Time constant / ms | <1.5 | 1[c] | <2.8 | 1[d] |
| Per-pixel NEP / $10^{-17}$ W/$\sqrt{\text{Hz}}$ | 19 | (23±21)[e] | 3.9 | (19±6)[e] |

[a] Elevated power handling on the 850 $\mu$m array is a consequence of the high $G$ values.

[b] Elevated $G$ values primarily the result of poor control of the deep etch process used to isolate the pixel absorbers producing wider trenches than specified.

[c] Estimated from 850 $\mu$m array measurement and differences in heat capacity and thermal conductance for the two pixel types.

[d] Suppressed by a factor of $\sim$2 due to the elevated $G$ values for this array.

[e] Average per-pixel NEP from a data set masked to remove pixels with responsivity less than 100 000 A/W and average noise greater than 500 pA/Hz$^{0.5}$. Approximately 25% of the pixels from each array are removed from the data set using these masks.

values of the pixel thermal conductance and effects associated with the high $G$ values. As discussed previously, the origin of the enhanced $G$ values is a combination of variation in the width of the deep-etched isolated trenches around the pixel absorbers, and, for the 850 $\mu$m array, the effect of a missed cleaning step in the hybridisation process introducing indium oxide junctions into the bump bonds between the detector and MUX wafers. As a consequence of the high thermal conductance for the 850 $\mu$m pixels, the total power handling on this array is higher by a factor $\sim$2 than the specification, in addition to some enhancement of the detector NEP. The measured time constant for the 850 $\mu$m pixels will also be reduced, although the specified time constant for the 850 $\mu$m detectors will be met even if this suppression of $\tau$ is taken into account. The major issues with these array measurements are the high per-pixel NEPs. The elevated noise on the 850 $\mu$m array may again be partly explained by the elevated thermal conductance values reducing the pixel responsivity, combined with excess white noise levels measured in operation at the telescope. The elevation of the 450 $\mu$m NEPs is probably due to excess white noise rather than reduced responsivity, since the measured values of $G$ for the 450 $\mu$m array are closer to the design values.

## 3.3 Summary

This chapter has discussed the basic requirements of the SCUBA-2 detectors. Using calculated sky background powers at the observing wavelengths, the required detector NEPs were derived. Following from this, the required operating temperatures and link thermal conductances were obtained. Furthermore, the required detector time constants were derived based on the anticipated frequency content of the science signal. The physical time constants were calculated from the derived thermal conductance values and the estimated pixel heat capacities. The effective time constants due to operation with electrothermal feedback were then considered.

Data from a series of measurements with the most recent detector arrays at 850 and 450 $\mu$m were presented to allow the extraction of the parameters derived in the first part of the chapter. The pixels on the 850 $\mu$m array were found to have a high thermal conductance, both as a result of poor control of the deep etch process used to isolate the pixel absorbers, and possibly a processing error during the hybridisation. As a

consequence of the elevated $G$ values, the power handling on the 850 $\mu$m pixels was found to be much higher than the specified value. The extracted parameters for the 450 $\mu$m array were found to be closer to the specified requirements. The speed of response for the two arrays was found to be within specification. Noise measurements made on the arrays at the JCMT indicated that the per-pixel NEPs at both wavelengths exceeded the requirements, particularly for the 850 $\mu$m array where the measured average NEP was a factor of 5 higher than the specification, although as discussed previously the array setup for these measurements was designed to maximise the number of working pixels, rather than achieving the best NEP. While some contribution may be explained by the elevated $G$ values for that array, there is still considerable excess noise in the system at the telescope. A likely contributor to the noise levels is believed to be magnetic interference, although work is still ongoing in this area.

The quality of the arrays has improved with each generation of production. Despite a number of problems with this latest generation, the issues are sufficiently well understood that they can be corrected in the next production batch.

# Chapter 4

# Cryogenics I: The SCUBA-2 Dilution Refrigerator

As discussed in the previous chapter, bolometric detectors are cooled to below 1 K to achieve the necessary sensitivity for observations. Cooling to sub-kelvin temperatures using $^3$He cryostats is a common technique in low-temperature physics, and has been utilised for a number of submillimetre and millimetre instruments. However, the operating temperature required to achieve the sensitivity needed for the SCUBA-2 pixels demanded a bath temperature of less than 100 mK. Of the two refrigeration methods capable of reaching such temperatures, dilution refrigeration and adiabatic demagnetisation of a paramagnetic salt, only dilution refrigeration is able to provide millikelvin temperatures continuously. A dilution refrigerator (DR) was used in the original SCUBA instrument with some success, providing a heritage for the use of a DR in SCUBA-2.

This chapter provides a background to the technique of dilution refrigeration, outlining the theory behind the cooling mechanism and the design of practical refrigerators. Following on from this, the dilution refrigerator for SCUBA-2 is described, including details of the design and operation of the system. This discussion will then lead in to the commissioning and characterisation of the DR described in Chapter 5.

## 4.1 Dilution Refrigerator Design and Operation

This section aims to give an overview of the physical principles behind the operation of the dilution refrigerator, and an outline of the general design features of such refrigerators. More detailed discussions of the theory behind the dilution process and reviews of refrigerator design may be found in Refs. [120, 121] and references therein. An earlier account may be found in Ref. [122], although not all of the details are relevant to modern DR design.

### 4.1.1 Properties of $^3$He and $^4$He Mixtures

To understand the dilution process, it is necessary to consider some of the properties of liquid mixtures of $^3$He and $^4$He. The phase diagram of a $^3$He/$^4$He mixture at saturated vapour pressure is shown in Fig. 4.1, plotted as temperature as a function of the $^3$He concentration of the mixture, $x$, where $x = n_3/(n_3 + n_4)$ and $n_3$ and $n_4$ are the molar quantities of $^3$He and $^4$He, respectively. Above the curve of coexistence, the mixture will exist either as a $^3$He Fermi liquid in a superfluid $^4$He 'background' to the left of the $\lambda$-curve, or as a mixture of two normal fluids to the right of the curve, respectively. On the coexistence curve the mixture will spontaneously separate into two components, with one phase being rich in $^3$He and the other rich in $^4$He. The phases are represented by the right-hand and left-hand branches of the coexistence curve, respectively. Note that the $^3$He-rich phase (also known as the concentrated phase) will float on top of the $^4$He-rich (or dilute) phase due to the lower density of the lighter isotope.

The important consequence of the phase diagram is that as $T \to 0$, the $^3$He concentration in the concentrated phase, $x_C$ tends to 1, while $x_D$, the $^3$He concentration in the dilute phase, tends[1] to 0.064. Although the concept for a refrigerator based on the dilution process had been described sometime earlier [124], little development of the idea occurred until this property of "finite solubility" of $^3$He in $^4$He was discovered [125], since for a practical cooling process, it is necessary that the equilibrium concentration of $^3$He in the dilute phase at low temperature is finite, and it had been erroneously believed that the limit of $x_D(T)$ as $T \to 0$ was zero.

[1] Values for $x_D(0)$ determined by experiment range from 0.064 to 0.068, for this discussion numerical values are taken from Ref. [123].

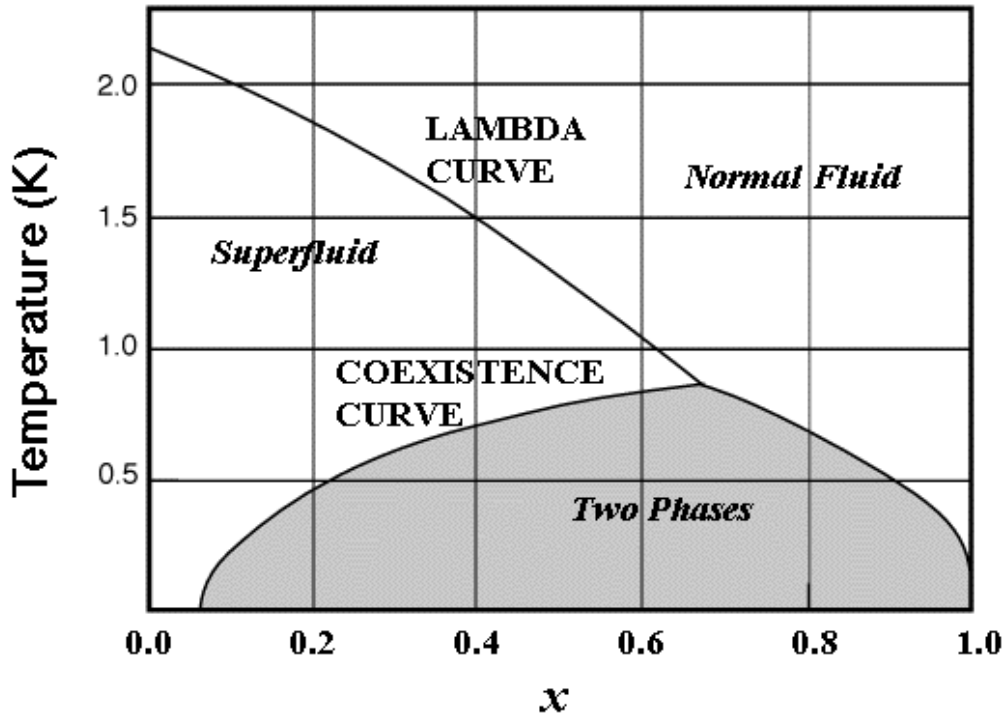


**Figure 4.1:** Phase diagram of $^3$He/$^4$He mixtures at low temperature, as a function of the $^3$He concentration of the mixture, $x$, where $x = n_3/(n_3+n_4)$ and $n_3$ and $n_4$ are the molar quantities of $^3$He and $^4$He, respectively. Adapted from Ref. [121].

The origin of the finite solubility is the different behaviour of the two helium isotopes at low temperature. Below 0.6K, liquid $^4$He is effectively in its quantum mechanical ground state, as described by Bose-Einstein statistics, and therefore is thermally and hydrodynamically inert. $^3$He is described by Fermi-Dirac statistics. The heat capacity and entropy of liquid $^3$He are approximately linear functions of temperature near 0 K, and are high over the range of temperatures relevant to the dilution process. To a reasonable approximation, liquid $^3$He can be treated as a Fermi liquid. Since the concentrated phase is effectively pure $^3$He, the phase may be treated with the same approximation. From thermodynamic arguments, it may be shown [122] that the binding energy of a single $^3$He atom at $T = 0$ is stronger to $^4$He atoms in liquid $^4$He at $x_D = 0$ than to other $^3$He atoms in liquid $^3$He. Dissolution of $^3$He across the phase boundary into superfluid $^4$He is therefore energetically favourable. However, as more $^3$He atoms

dissolve in the superfluid, the relative binding energy decreases as a consequence of the Pauli principle. The equilibrium condition is found to be at $x_D = 0.064$, when the chemical potential of the pure $^3$He phase and the mixture phase are equal. Conversely, a single $^4$He atom at $T = 0$ is more strongly bound to liquid $^4$He than to $^3$He. Therefore, as $T \to 0$, the concentration of $^4$He in the concentrated phase rapidly approaches zero. The binding energies are temperature dependant, and so $x_C$ and $x_D$ are both functions of temperature. However, in practice this dependance may be ignored in the temperature range of interest. Dilution refrigerators generally operate at <0.1 K, at which temperature $x_C = 0.99997$ and $x_D = 0.070$.

### 4.1.2 Cooling Using the Dilution Process

A simple representation of a system using the dilution process for cooling as the schematic in Fig. 4.2. In this arrangement, the boundary separating the two phases is contained by the mixing chamber. Cooling occurs as $^3$He atoms move across the phase boundary from the concentrated phase at the top of the chamber to dissolve in the dilute phase beneath. This process happens at a temperature $T_{mc}$, absorbing heat $\dot{Q}$ from the surroundings. In order to make the process continuous, $^3$He is returned to the concentrated phase at a temperature of $T_n$ from a system of heat exchangers. For the current discussion, it is assumed that $T_{mc} = T_n$.

As a consequence of the different behaviour of the concentrated and dilute phases, the specific heat, and therefore the enthalpy, of $^3$He in the dilute phase is larger than in the concentrated phase. The cooling effect occurs according to the enthalpy difference of the two phases. This "heat of mixing" is described by

$$\dot{Q} = \dot{n}_3 \left[ H_d(T) - H_c(T) \right], \tag{4.1}$$

where $\dot{Q}$ is the cooling power, $\dot{n}_3$ is the molar flow rate of $^3$He across the phase boundary, and $H_d(T)$ and $H_c(T)$ are respectively the enthalpy of the dilute and concentrated phases at temperature $T$. The enthalpy at a temperature $T$, $H(T)$, is given by

$$H(T) - H(0) = \int_0^T C(T) \mathrm{d}T, \tag{4.2}$$

where $H(0)$ is the enthalpy at absolute zero and $C(T)$ is the heat capacity.

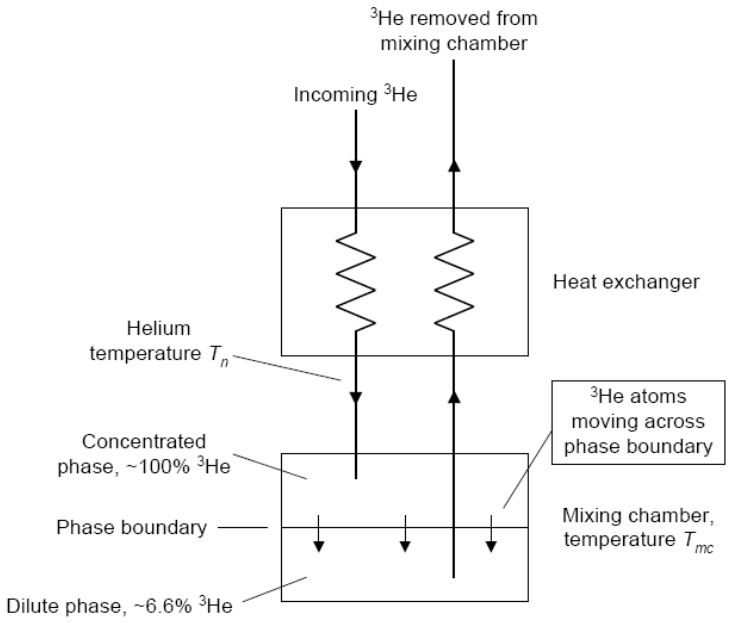


**Figure 4.2:** Schematic representation of a simple cooling apparatus using the dilution of $^3$He into a $^3$He-$^4$He mixture. The concentrated and dilute phases and the separating phase boundary are present in the "mixing chamber", with the less dense concentrated phase floating on the dilute mixture phase. Cooling occurs as $^3$He atoms move across the phase boundary from the concentrated to the dilute phase at a temperature $T_{mc}$, absorbing a heat $\dot{Q}$. $^3$He is cycled around a circuit, not shown in this schematic, to make the process continuous, with the $^3$He entering the concentrated phase at a temperature $T_n$. Adapted from Ref. [121].

The specific heat of both phases would be expected to vary linearly with temperature, since both are Fermi liquids. However, the concentrated phase is classified as a strongly interacting Fermi liquid and at present theoretical descriptions to not allow accurate calculation of specific heat [121]. Accurate measurements of the specific heat of liquid $^3$He are available in the temperature range of interest [126, 127]. At $T \simeq 60$ mK, the specific heat of pure $^3$He is $C_3(T) \cong 24T$ J/(mol K). The enthalpy of liquid $^3$He, and therefore the concentrated phase, $H_c(T)$, is

$$H_c(T) = H_c(0) + 12T^2. \tag{4.3}$$

Note that while here the notation $H_c(T)$ is used for the enthalpy of the concentrated phase, the enthalpy of pure $^3$He, $H_3(T)$, could be used interchangeably.

Measurements of the enthalpy of the dilute phase are not so readily available, but the enthalpy of $^3$He diluted in $^4$He may be calculated since the phase behaves as a weakly interacting Fermi liquid, for which it is a reasonable approximation to use the equations for a Fermi gas with the $^3$He mass, $m_3$, replaced by an effective mass, $m^*$, to account for the influence of neighbouring $^3$He and $^4$He atoms with which the $^3$He interacts [121]. By analogy to conduction electrons, the specific heat of the dilute phase per mole of $^3$He in the mixture, $C_{3,d}$, is

$$C_{3,d} = N_0 k \frac{\pi^2 T}{2T_F}, \tag{4.4}$$

where $N_0$ is the Avogadro number, $k$ is the Boltzmann constant, and $T_F$ the Fermi temperature, given by

$$T_F = \frac{\hbar^2}{2m^* k}\left(\frac{3\pi^2 N_0 x}{V_m}\right)^{\frac{2}{3}} = 55.2\frac{m_3}{m^*}\left(\frac{x}{V_m}\right)^{\frac{2}{3}}, \tag{4.5}$$

where $V_m$ is the molar volume of the mixture. For a mixture concentration $x$, $V_m$ is given by

$$V_m = V_{m,4}(1 + 0.284x), \tag{4.6}$$

where $V_{m,4} = 27.589$ cm$^3$mol$^{-1}$, the molar volume of pure $^4$He [128]. Note that Eq. (4.4) is only true for $T < 0.1T_F$. On substituting Eq. (4.5), Eq. (4.4) reduces to

$$C_{3,d} = 0.745\frac{m^*}{m_3}\left(\frac{V_m}{x}\right)^{\frac{2}{3}} T. \tag{4.7}$$

The effective mass is weakly dependant on the $^3$He concentration. For $x \simeq 0.066$, as would be expected under typical conditions for the dilution process, $m^* \simeq 2.5m_3$. This then gives a Fermi temperature of 0.38 K, and a specific heat at $T \simeq 50$ mK of

$$C_{3,d} = 106T. \tag{4.8}$$

When the two phases are in thermodynamic equilibrium, the chemical potentials of the $^3$He in the two phases, $\mu_{3,c}(x_c, T)$ and $\mu_{3,d}(x_d, T)$ for the dilute and concentrated phases, respectively, must be equal. Since

$$\mu = H - TS, \tag{4.9}$$

where $S$ is the entropy of the system, it follows that

$$H_d = H_c - TS_{3,c} + TS_{3,d}. \tag{4.10}$$

Using Eqs. (4.3) and (4.8),

$$H_d(T) = H_c(0) + 12T^2 + T\int_0^T \left(\frac{C_{3,d}}{T'} - \frac{C_{3,c}}{T'}\right) \mathrm{d}T' = H_c(0) + 96T^2. \tag{4.11}$$

Substituting Eqs. (4.3) and (4.11) into Eq. (4.1) gives the cooling power of the dilution process, $\dot{Q}$, for a $^3$He circulation rate of $\dot{n}_3$ as

$$\dot{Q} = \dot{n}_3 \left[H_d(T) - H_c(T)\right] = 84\dot{n}_3 T^2. \tag{4.12}$$

Eq. (4.12) may be used to estimate the cooling power of the dilution process for a given $^3$He flow rate and temperature, or to establish a minimum temperature for a given heat input. For example, if a $^3$He circulation rate, $\dot{n}_3$, of 100 $\mu$mol/s (a fairly small dilution refrigerator) is considered, the cooling power is 3.4 $\mu$W at $T_{mc} = 20$ mK. The cooling power rises to 21 $\mu$W at $T_{mc} = 50$ mK.

The dilution process is analogous to an evaporative or expansion process, in which the liquid $^3$He passes across the phase boundary into the "vapour" of $^3$He supported by the inert superfluid $^4$He. In this picture, the $^4$He behaves as a "mechanical vacuum". Removal of $^3$He from the dilute phase by pumping encourages the movement of atoms across the phase boundary to maintain the equilibrium concentration, producing a continuous cooling process. In contrast to evaporative refrigerators, in which the rapid fall of vapour pressure with temperature limits the cooling effect due to the reduction of atoms moving into the vapour, the finite solubility effect allows the rate of flow of $^3$He to be kept high, even at the lowest temperatures. The fundamental limit for dilution occurs when $^3$He becomes superfluid near 1 mK, at which point the approximation to a Fermi gas for the dilute phase is no longer valid.

### 4.1.3 Details of Dilution Refrigerator Operation

A schematic of a continuously operating DR is shown in Fig. 4.3, with the principal features indicated. The phase separation and the dilution process already discussed occurs in the mixing chamber, which is also the coldest point in the refrigerator. The concentrated phase lies in the upper section of the mixing chamber, on top of the dilute phase. Dissolution of $^3$He across the phase boundary is achieved by removing $^3$He atoms from the dilute phase. This pumping occurs higher up the system in the still, which is positioned at the top of a pipe feeding into the dilute phase in the mixing chamber. This pipe passes up through the heat exchangers between the still and mixing chamber, forming an unbroken column of the dilute phase.

The vapour pressure in the still is reduced by pumps at room temperature, encouraging evaporation of $^3$He from the free liquid surface in the same way as a pumped cryostat. In order to maintain sufficient flow of $^3$He, the still is electrically heated to approximately 0.7 K. The vapour pressure of $^3$He at 700 mK is $\sim$1 mbar, approximately an order of magnitude higher than the vapour pressure of $^4$He. This difference in vapour pressure causes $^3$He to be pumped preferentially, although a suitable scheme to suppress film creep of the superfluid $^4$He will generally be used. Efforts are made to minimise the pumping of $^4$He since any of the heavier isotope returning to the concentrated phase will have a detrimental effect on the performance of the fridge.

Without the application of additional heat, the still would cool to 0.3 K as for a pumped $^3$He cryostat, but giving a low flow rate due to the rapid fall off of the vapour pressure. Removal of $^3$He atoms from the still encourages $^3$He atoms to move into the vapour phase, causing a drop in the $^3$He concentration in the liquid in the still to around 1% [121]. This results in a flow of $^3$He atoms up the superfluid column due to the concentration gradient, reducing the overall concentration of $^3$He in the dilute phase and encouraging $^3$He atoms to cross the phase boundary from the concentrated phase.

To produce a continuous cooling process, $^3$He must be returned to the concentrated phase. If this is not done, then the cooling will last only as long as there is $^3$He available. Some DRs are designed to run in this way. Operation of a continuous DR without returning $^3$He is referred to as "single shotting", and can be a useful diagnostic technique.

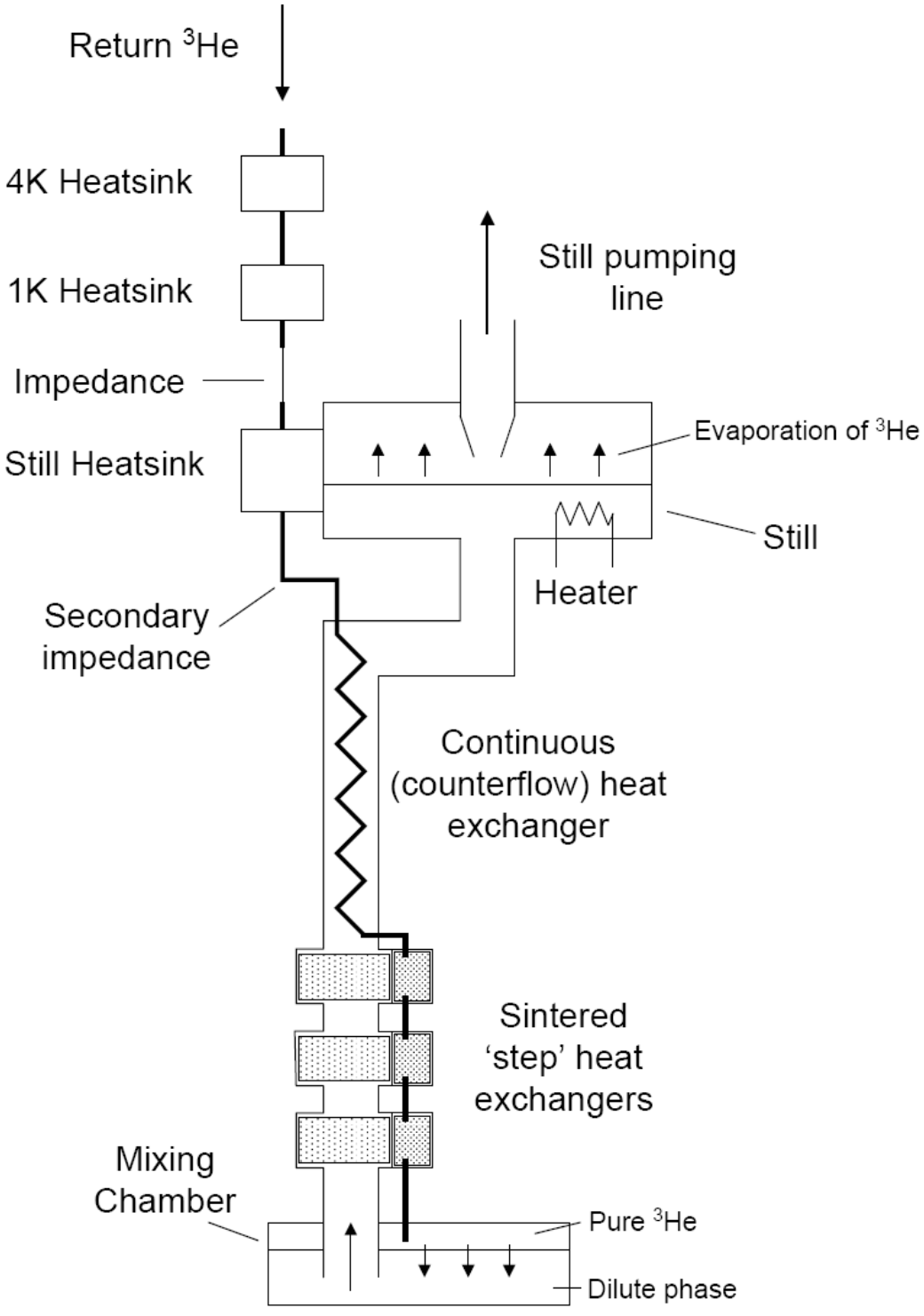


**Figure 4.3:** Schematic of a dilution refrigerator, adapted from Ref. [120]. See text for details.

Circulated $^3$He is precooled to 4 K by a liquid $^4$He bath, often in combination with counterflow exchange with the $^3$He removed from the still. Some cryostats will also use a liquid nitrogen bath in addition to the helium bath. The $^3$He is condensed by heat exchange with a 1-K pot, cooled to between 1 and 2 K by pumping of $^4$He admitted from the main helium reservoir. A flow impedance keeps the pressure of the returning $^3$He in the 0.1–1 bar range to ensure condensation. The condensed $^3$He is further cooled by heat exchange with the still, before passing into a combination of counterflow and 'step' heat exchangers. Finally, the $^3$He enters the concentrated phase in the mixing chamber.

**Heat Exchangers**

The heat exchangers are the most important component of a dilution refrigerator. Heat exchanger designs are broadly defined as either continuous or step exchangers, the two designs fulfilling slightly different roles in the overall system.

Continuous (counterflow) heat exchangers consist of two concentric capillaries, the inner capillary carrying the concentrated phase and the outer the dilute phase. The inner capillary will typically have a diameter of order 1 mm, with wall thicknesses around 20% of the diameter [121], and will be coiled to minimise the space envelope. The outer capillary will have a diameter of a few millimetres, with a wall thickness around 0.5 mm. The capillaries are composed of materials with a low thermal conductivity (copper-nickel, stainless steel or brass). In such a heat exchanger, the temperature of the flow changes as a continuous function along the length of the tube, with heat being transferred between the two flows perpendicular to the capillary wall, while the conduction along the length of the capillary is minimal. The inner capillary may be spiralled within the outer capillary to increase the surface area. A simple dilution refrigerator may be constructed using a single counterflow heat exchanger of the type described between the still and the mixing chamber, with a capillary length of a few metres, and would be capable of achieving a minimum temperature of about 40 mK [129].

For a dilution refrigerator with a lower minimum temperature and greater cooling capacity, it is necessary to use multiple heat exchangers. A continuous heat exchanger as described above would be used immediately below the still, flowed by a number

of step heat exchangers in series. Continuous heat exchangers cannot be used at low temperatures since they do not provide sufficient surface area to overcome the increasing boundary resistance between the helium streams and the heat exchanger materials. A simple form for a step exchanger is a copper block with two drilled channels filled with sintered metal powder (typically copper or silver), with channels drilled through the sinter for the helium flow. One sinter channel will carry the concentrated flow, while the other (with a larger diameter) carried the dilute flow. The sintered powder provides a large enough surface area to overcome the boundary resistance.

More details on the design of heat exchangers may be found in reviews by Frossati [129], Pobell [121] and Betts [130], and reference therein.

### Theoretical Performance

The cooling power of the dilution process derived in Eq. (4.12) is effectively the maximum theoretical performance. However, it a real system, the temperature of the $^3$He entering the concentrated phase at the top of the mixing chamber will not be at the mixing chamber temperature, $T_{mc}$, but at some higher temperature, $T_n$. If the enthalpy balance of the system, shown schematically in Fig. 4.2, is considered, then $T_n$ is the exit temperature of the last heat exchanger before the concentrated phase in the mixing chamber. Some of the cooling power of the dilution process will be used to complete the precool of the instreaming $^3$He from the higher temperature $T_n$ to $T_{mc}$. The enthalpy balance equation for the dilution process, Eq. (4.1), should, for a real system, be written

$$\dot{n}_3 \left[H_d(T_{mc}) - H_c(T_{mc})\right] = \dot{n}_3 \left[H_c(T_n) - H_c(T_{mc})\right] + \dot{Q}. \tag{4.13}$$

The first term is the cooling power provided by the dilution process at temperature $T_{mc}$ for a $^3$He flow rate of $\dot{n}_3$, the second term the cooling of the incoming $^3$He in the concentrated phase from temperature $T_n$ at the outlet of the last heat exchanger to temperature $T_{mc}$ in the mixing chamber, and the third term, $\dot{Q}$, the heat uptake from the environment. Substituting Eqs. (4.3) and (4.11) for $H_c(T)$ and $H_d(T)$ gives

$$\dot{Q}_{mc} = \dot{n_3}(96T_{mc}^2 - 12T_n^2), \tag{4.14}$$

where the general notation $\dot{Q}$ has been replaced by $\dot{Q}_{mc}$, the available cooling power of

the mixing chamber. The design goal of a dilution refrigerator should be to minimise the temperature difference $T_n - T_{mc}$ by extremely efficient heat exchange. For a DR with perfect precooling of the instreaming $^3$He, or a system running as in the "single shot" mode, discussed previously, with no incoming helium, $T_n = T_{mc}$. In this case, the cooling power reduces to Eq. (4.12), as would be expected. If the heat exchangers are not well designed, the instreaming $^3$He can put a large load on the mixing chamber. From Eq. (4.14), the limiting case is $Q = 0$ (no cooling available on the mixing chamber after balancing the heat leak). From this, the constraint on $T_n$ is that

$$T_n \leq \sqrt{8}\, T_{mc}. \tag{4.15}$$

This illustrates the importance of careful heat exchange design.

In practice, even with no load from circulating $^3$He, there will still be some background loading on the mixing chamber from conduction of heat down support structures, and due to radiation from higher-temperature stages of the cryostat. Conduction loads are minimised through careful choice of materials, while radiation shields sunk to intermediate temperature stages (such as at 4 K, ∼1 K attached to the condenser, or at 0.7 K sunk to the still) are used to reduce the radiative load.

### 4.1.4 Development of "Dry" Dilution Refrigerators

A feature of refrigerators operating in the sub-kelvin regime is the need to use liquid $^4$He baths as precooling stages, and in many cases pumped $^4$He 1-K pot condensers. Some work was conducted to simplify the operation of DRs and increase their reliability by removing the 1-K pot from the standard design. The pumped $^4$He stage is prone to blockages, interrupting the operation of the refrigerator, and also increases the frequency of liquid helium transfers since the pumped stage is fed from the main liquid $^4$He bath. The solution was to use a Joule-Thomson (JT) expansion stage to liquify the circulating $^3$He, as described in Refs. [131,132]. The stage, also referred to as a "JT heat exchanger", consists of a counterflow heat exchanger within the still pumping line, in which the incoming $^3$He is cooled by the outflowing gas from the still, followed by an isenthalpic expansion from a flow impedance and further cooling in the still heat exchanger to fully liquify the $^3$He. The JT heat exchangers used in Refs. [131, 132] are shown in Fig. 4.4.


**Figure 4.4:** Two designs of Joule-Thomson heat exchanger. The upper design is of the type developed by Uhlig [132], and the lower design is similar to that of Kraus [131]. Figure from Ref. [132].

With the continued development of efficient mechanical coolers capable of reaching temperatures approaching 4 K, it was a logical step to match the technology to lower-temperature coolers to produce "dry" systems that no longer required the difficultly and expense associated with liquid helium cryostats. The development and principles of mechanical coolers are discussed as part of the review of cryogenic techniques in Appendix A. Early pioneering work using Gifford-McMahon (GM) coolers was carried out by a number of groups, including Uhlig at the Walther-Meissner Institute for Low Temperature Research, Garching. The first reported DR from this work [133] reached a base temperature of 42 mK on the mixing chamber, using a Leybold GM refrigerator providing 5 W at 20 K and reaching a minimum temperature of 8.5 K. A JT stage was used to cool the helium to <3 K before liquefaction in the still.

This DR suffered from vibrational problems from the moving displacer on the second stage of the GM cold head. The system was later modified to use a smaller GM cooler, with reduced vibration, but with only 40% of the cooling power on the second stage. This system achieved a temperature of 35 mK [134]. A later design returned to a 5 W cold head, but incorporated improved vibration isolation in the form of braided copper straps to decouple the cold head from the precooling stages. In this configuration,

the DR reached 15 mK [135]. Later experiments to measure the vibrational heat leak on the mixing chamber from this configuration determined a value of 0.14 $\mu$W, easily containable by the cooling capacity of even small DRs [136].

An alternative example of a dry DR utilised a hybrid cryocooler to precool the circulating helium. The cooler consisted of a Gifford-McMahon stage, reaching a minimum temperature of 25 K, coupled to a pulse tube stage reaching a final temperature of 3.8 K unloaded [137]. The DR continued to use a JT stage to ensure condensation of the returning helium. The final temperature of this refrigerator was only 41 mK, although this was limited by the heat exchange between the still and mixing chamber, which did not include any step exchangers.

Later work by Uhlig used a pulse tube cooler in place of the Gifford-McMahon refrigerator for precooling. With essentially a direct substitution of a pulse tube cooler with 0.5 W cooling power at 4 K on the second stage into the existing GM-cooled DR, a temperature of 15 mK unloaded was achieved, with 41 $\mu$W of cooling power at 100 mK [138]. It was reported that the reduced level of vibration from the PTC compared to the GM coolers simplified the construction of the cryostat, although flexible links were still used between the cold head and cold plates. A later version of the PTC cooled DR reached a base temperature of 4.3 mK, although this example used a double mixing chamber arrangement[2] and considerable external vibration isolation for the cryostat [139]. Recently, other researchers have been able to achieve temperatures in the region of 10mK and below with a single mixing chamber (e.g. Ref. [140]).

The DR for SCUBA-2 was designed and built by Leiden Cryogenics.[3] This DR is described in detail in the next section. At the time, dry dilution refrigerators were not available commercially. Currently, a number of companies offer cryogen-free DRs, predominantly pulse tube based.

---

[2]The double mixing chamber is a little-used design in which only part of the concentrated phase is diluted in the first mixing chamber before flowing into the second for the remaining dilution process. This has the effect of removing the cooling load on the mixing chamber from the output of the final heat exchanger. The temperature of the first mixing chamber will always be higher than a single mixing chamber in an equivalent dilution refrigerator due to the incomplete dilution, but the temperature of the second chamber will always be lower than a single mixing chamber as a consequence of the reduced heat leak. For a more complete description, see Ref. [136].

[3]Leiden Cryogenics BV, http://www.leidencryogenics.com.

### 4.1.5 Condensation Pumped Dilution Refrigerators

In passing a different branch of dilution refrigerator development that has seen renewed work is described. The dilution refrigerators discussed so far require considerable apparatus at room temperature to condense the helium mixture and circulate $^3$He around the dilution circuit. This is not always an attractive proposition for some applications, such as those in astronomical instrumentation, that require relatively low cooling power at high (∼50 mK) temperature. In these applications, reliability and simplicity of operation may be preferable to high cooling power.

An alternative approach to a system with room temperature pumps was first demonstrated in the early 1970s, with helium being removed from the dilute phase in the still using a sorption pump [141]. The idea has recently been developed for use in the C$_l$OVER CMB polarisation instrument [142]. The dilution refrigerator uses a condenser coupled to a pair of He-7 sorption coolers[4] via heat switches, with the sorption coolers operating from a 4 K base plate. The condenser at ∼400 mK reduces the vapour pressure in the still, promoting migration of $^3$He across the phase boundary in the mixing chamber, as in a conventional DR. The liquid $^3$He in the condenser then passes back into the concentrated phase. Use of the two sorp coolers allows recycling of one cooler while the other maintains the condenser temperature. In this way, the dilution process is continuous. Although the DR is reliable due to the absence of fine capillary tubing required for normal condenser designs, the cooling power is severely limited due to the low flow rate of $^3$He (this DR provides only a few $\mu$W of cooling power at 100 mK).

## 4.2 Description of the SCUBA-2 Dilution Refrigerator

Details of the design of the SCUBA-2 dilution refrigerator will be discussed in this section. A number of modifications were made to the DR system post-delivery, and these changes will also be described. A brief overview of the system and performance requirements is included, followed by more detailed description of the major system elements. Many of the specific details of the DR design are not included due to the information being proprietary to Leiden Cryogenics.

[4] He-7 refers to a system with a $^4$He stage combined with a $^3$He stage. Also available are so-called He-10 coolers with a twin $^3$He stage for additional buffering of heat loads.

The specified performance for the SCUBA-2 DR required an unloaded mixing chamber base temperature of less than 10 mK, and a cooling power of 500 $\mu$W at 120 mK and 30 $\mu$W at 65 mK (with a goal of 30 $\mu$W at 35 mK). These figures are taken from the stated performance characteristics of the conventional Leiden Cryogenics dilution refrigerator upon which the DR was to be based. The still was to run at a temperature of $<$900 mK, with a goal of $<$700 mK, while providing at least 5 mW of capacity to cool the 1-K box.

The dilution refrigerator was designed as a self-contained insert for the instrument cryostat, allowing the DR to be tested independently. The "insert" refers to the full refrigerator, including the pulse tube cooler and precooling stages of the DR, as well as the dilution stage (still and mixing chamber). A schematic of the insert is shown in Fig. 4.5, with the major features indicated. The DR insert connects to a self-contained gas handling system containing a valve manifold and all the pumps for the refrigerator, as well as gas storage volumes. The handling system is described in detail below. A block diagram of the overall system is shown in Fig. 4.6.

The data presented in this chapter are from tests carried out with the DR insert in a test cryostat. The description of the refrigerator in this section applies to both the instrument and the test cryostat, with the exception of the arrangement and interfacing of radiation shields and wicking for cooling the instrument structures. The design details of the instrument configuration will be discussed in Chapter 6.

### 4.2.1 Pulse tube cooler

The PTC used for the SCUBA-2 DR is a Cryomech PT410, a two-stage refrigerator with a nominal cooling capacity of 1.0 W at a temperature of 4.2 K on the second stage and an unloaded base temperature of approximately 2.5 K. The first stage of the cooler will provide 40 W at 45 K. This is the same PTC system used for the main instrument radiation shields. A cold head of this type is shown in Fig. 4.7. The pulse tube is driven by a CP980 compressor package with an input power of 8 kW. The cooling power of the pulse tube was not measured independently, although test data supplied by Cryomech indicated nominal performance. Typical performance figures published by Cryomech [143] are plotted in Fig. 4.8 for a series of first stage power loads.

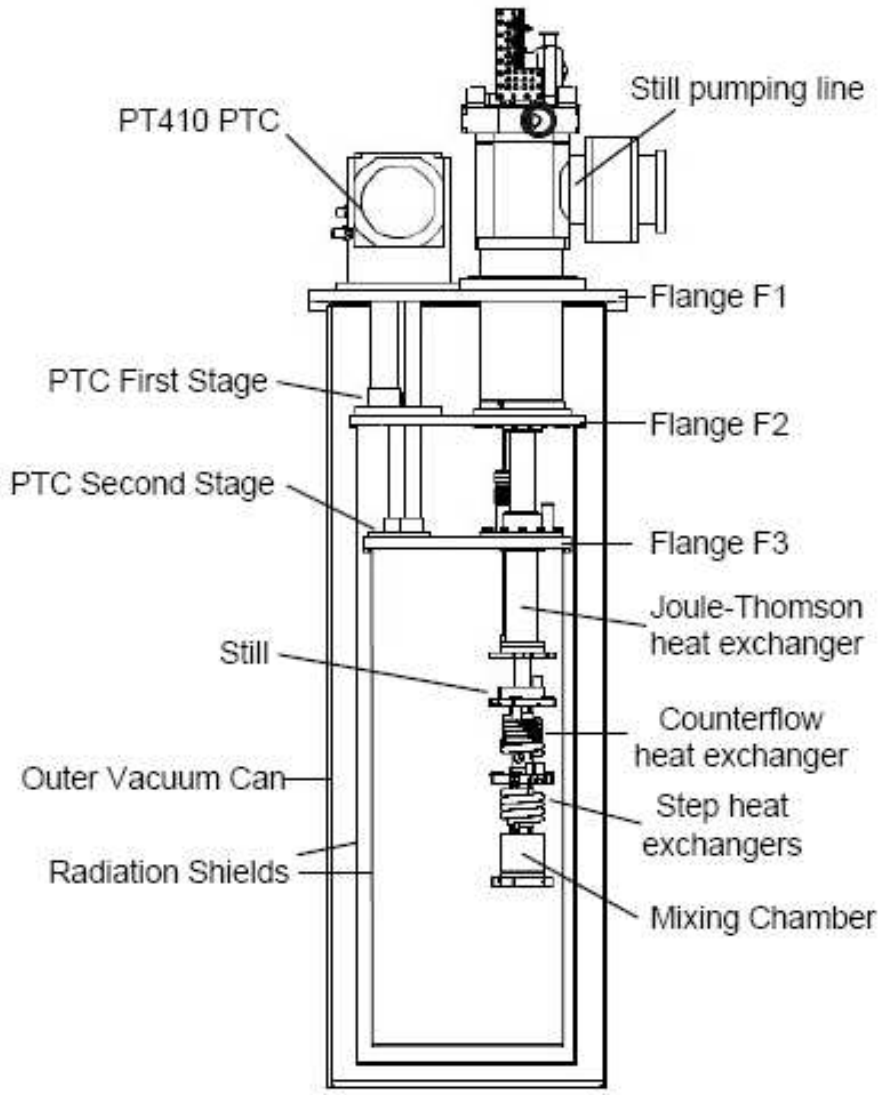


**Figure 4.5:** The SCUBA-2 dilution refrigerator insert in the test cryostat (shown in cross-section), with key features indicated. See text for details.

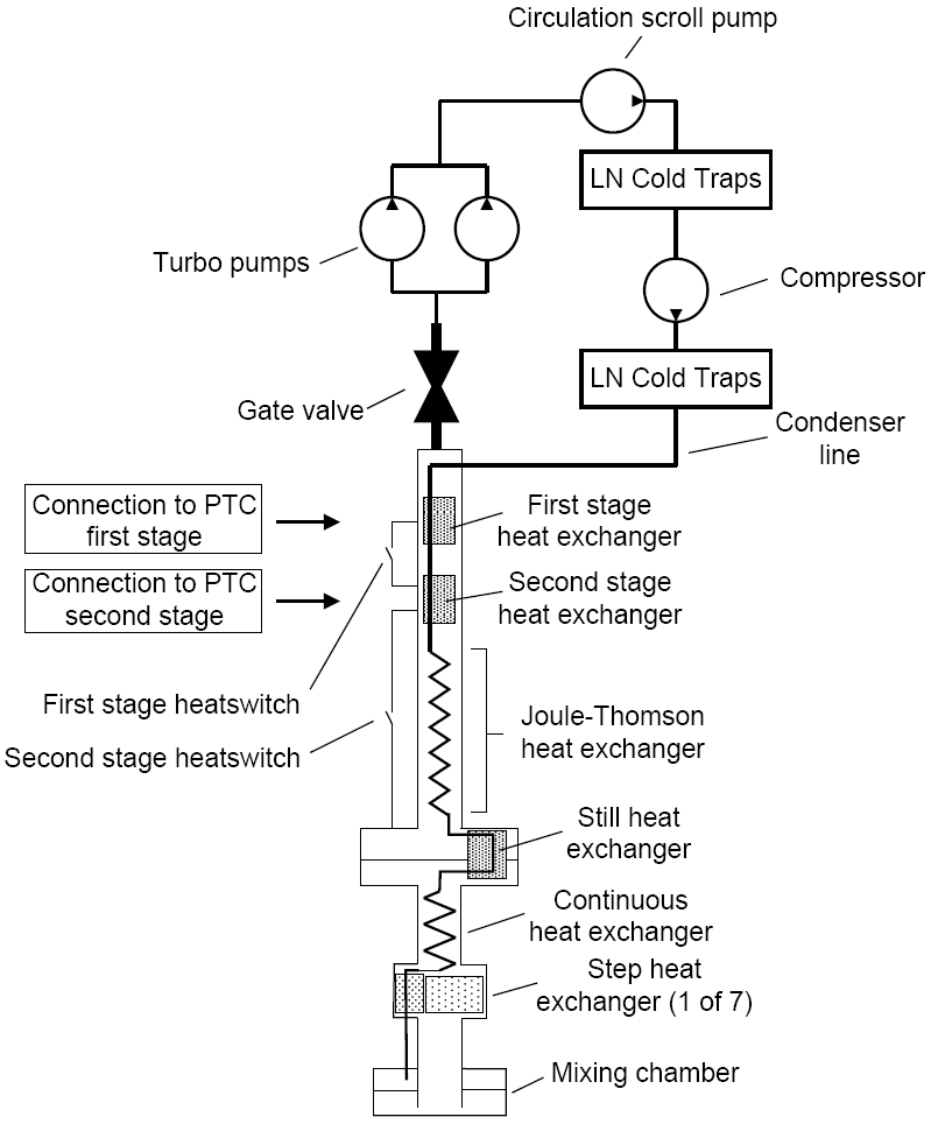


**Figure 4.6:** Block diagram of the dilution refrigerator system, including the room temperature pumping system. See text for full details.

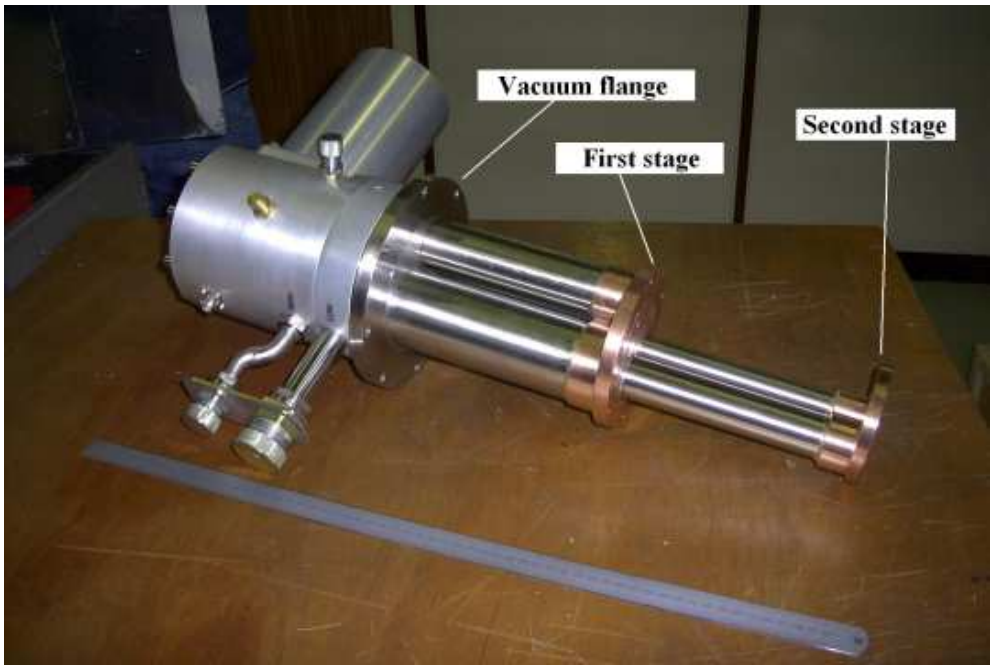


**Figure 4.7:** Cryomech PT410 pulse tube cold head, with the main structural features indicated.

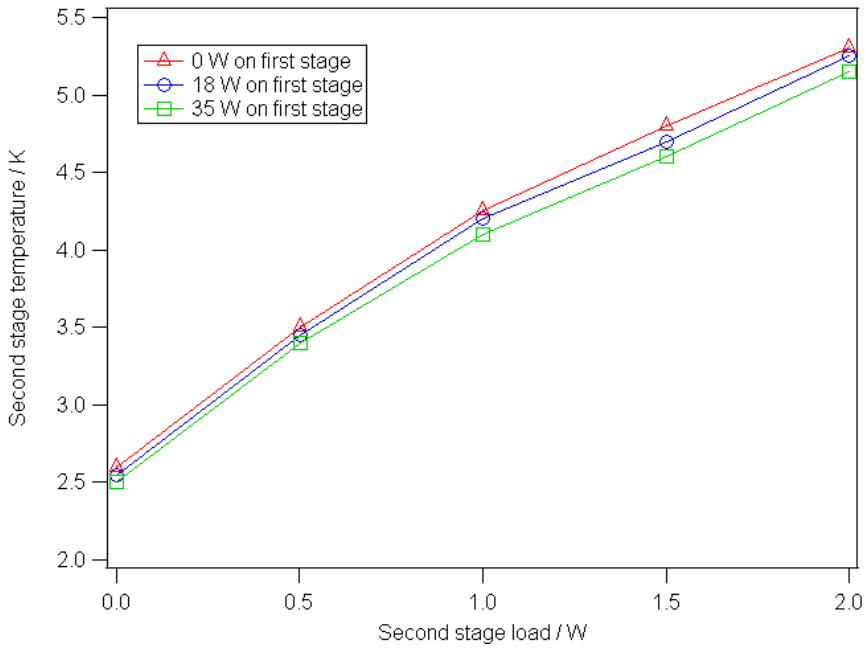


**Figure 4.8:** Published typical second stage cooling capacity figures for the Cryomech PT410 pulse tube cooler. The second stage capacity is plotted for three different first stage loads. Data from Ref. [143].

Discussion of the operating mechanisms associated with pulse tube and other cooler technologies are included in Appendix A. It should be noted that the nominal performance for the PTC depicted in Fig. 4.8 show that the available cooling power on the second stage increases slightly as the first stage load (and temperature) increases, at least over the range of parameter space included here. Such behaviour has been noted in other work with pulse tube systems [144, 145]. Two stage systems would be expected to have some interdependency of behaviour of the two stages. Changes in performance of the second stage as a result of changes on the first stage can be attributed to two mechanisms. The first is that as the temperature of the first stage decreases, there is a decrease in the average pressure, the pressure variation and the mass flow in the second stage, reducing the cooling power. Secondly, a lower first stage temperature will result in the working fluid in the second stage being at a lower temperature, increasing the efficiency of the cycle in the second stage and increasing the net cooling power available. These two competing effects can cause an increase in second stage cooling power as the first stage load and temperature increases, depending on the specific design of the system.

### 4.2.2 Insert construction

The dilution refrigerator insert is photographed in Fig. 4.9. The top of the insert (flange F1 in Fig. 4.5) is a stainless steel plate, supporting the top of the still pumping line and the room temperature vacuum flange of the pulse tube cooler. The top of the DR pumping line consists of a steel box supporting the output flange of the still pumping line (CF100 flange connected to a pneumatic gate valve with a CF100-ISO100 adaptor), the top of the helium input line (NW16 flange) and solenoid valve assemblies, two NW16 auxiliary ports with solenoid valves feeding into the vacuum can, and four clear shot ports. The clear shot tubes and the auxiliary ports come out in the vacuum can below the first stage plate. The clear shot tubes carry the DR wiring, and allow the drive mechanisms for mechanical heat switches and the impedance bypass valve (see below) to enter the vacuum can. The helium input port splits into two input lines with independent solenoid valves. A Pirani pressure gauge (Pfeiffer TPR 280) opens into the pumping line to monitor the pressure.

**Figure 4.9:** The SCUBA-2 dilution refrigerator insert, photographed during assembly.

The first stage plate (flange F2) is a copper plate that interfaces to the DR pumping line and is cooled by the first stage of the pulse tube cooler. The plate is bolted directly to the first stage heat exchanger flange of the PTC, with the second stage of the coldfinger passing through the first stage plate. The still pumping line is a solid stainless steel pipe, with the input capillaries running inside the pumping line. The capillaries exchange heat with a copper flange that is interfaced to the first stage plate, precooling the incoming helium.

The second stage plate (flange F3) is also of copper. The second stage of the PTC is bolted directly to this plate, although a construction error requires a 1 mm copper spacer between the plate and the PTC interface. The DR pumping line between the first and second stage plates is again stainless steel. The two helium input lines pass through 13 mm diameter cold trap volumes of copper and stainless steel shavings to clean the mixture. Heat exchange at the second stage is achieved with a sintered powder block heat exchanger bolted to the underside of the copper plate. The twin input capillaries (Cu-Ni, 1.4 mm outside diameter, 1.2 mm internal diameter) exit the still pumping line, pass through the sintered block, and reenter the stainless steel pumping line immediately below the F3 flange. The holes in the pumping line are plugged with solder.

To aid the precool of the dilution refrigerator, a heat switch is mounted on both the first and second stage plates. The heat switches are mechanical, driven manually by drive shafts from the top of the insert. The first stage switch is mounted on the underside of the first stage plate, closing on a gold plated copper bar bolted to the second stage plate. The second stage switch is mounted on the top side of the second stage plate, closing on a segmented bar feeding through the second stage plate and terminating at the still. The cold bar is isolated from the second stage plate by a support of Kevlar thread under tension. The primary purpose of the links is to aid the precool of the 1-K structures in the instrument by providing a thermal path to the DR pulse tube cooler. The layout of the switches and thermal links is shown in Fig. 4.10. The performance of the precool links is discussed in Chapter 5.

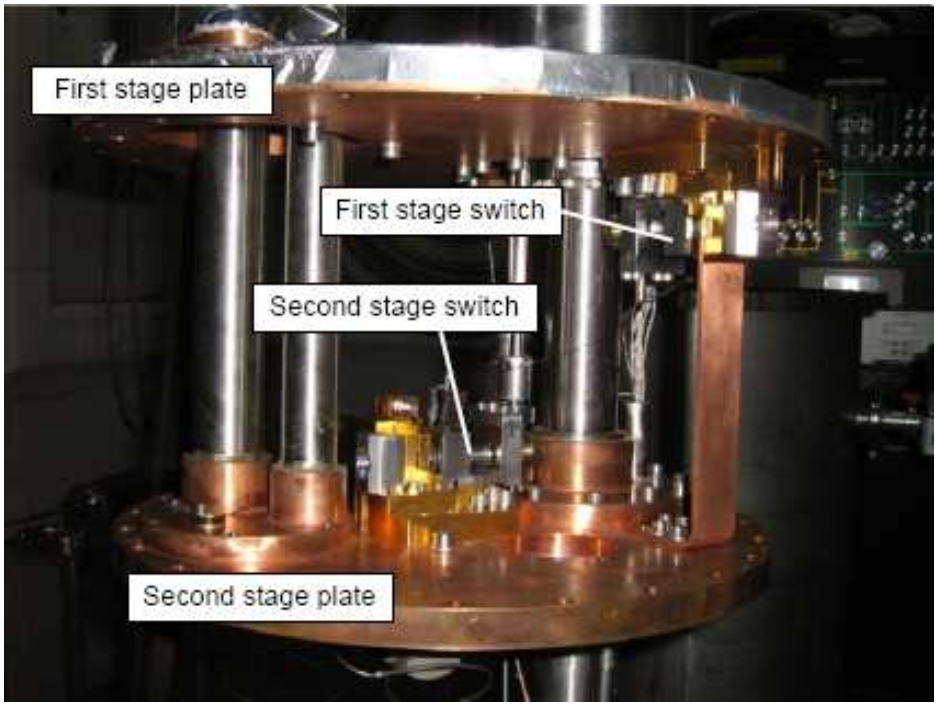


**Figure 4.10:** Photograph showing the arrangement of the dilution refrigerator insert precool heat switches.

### 4.2.3 Dilution unit

The dilution unit, shown in Fig. 4.11, is based on a Leiden Cryogenics MNK-126-500 DR, with a Joule-Thomson heat exchanger replacing the 1-K pot. The JT stage is similar to the Kraus design shown in Fig. 4.4, although since this DR has two independent inputs, the stage is essentially two JTs in parallel. The input lines pass independently through flow impedances at the end of the counterflow exchanger. One impedance line is fitted with a needle valve bypass to allow a high flow rate during initial helium condensation. The needle valve is manually driven by a micrometer mechanism on the top of the insert. A flange of gold-plated aluminium is sunk at the bottom of the JT stage.

The input capillaries join into a single line below the JT, and then enter the still. On leaving the still, the helium passes through a counterflow heat exchanger. The inner tube of the exchanger is a Cu-Ni capillary, and the outer tube is aluminium (1 metre in length). Below the counterflow exchanger, the liquid passes through a single sintered silver step exchanger [129]. A gold-plated aluminium intermediate plate is attached

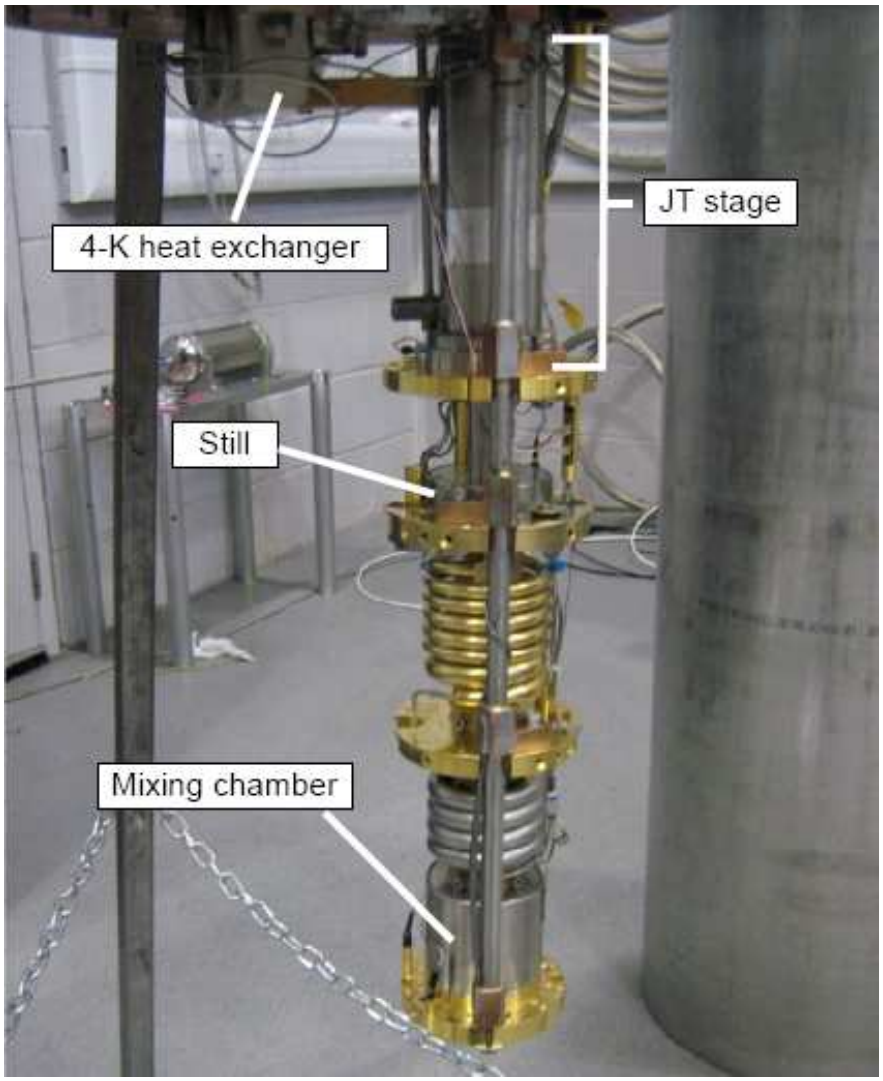


**Figure 4.11:** The dilution unit of the SCUBA-2 DR insert, with the major components indicated. See text for details.

below the step heat exchanger to provide heat sinking. The helium capillary passes through a further six step exchangers, before entering the mixing chamber. The mixing chamber is of aluminium, with a gold-plated aluminium plate welded to the bottom of the mixing chamber for sample mounting. The intermediate plate and the mixing chamber are supported by a G10 composite tube.

To aid the precool of the dilution unit, a neon heat pipe is fitted between the mixing chamber plate and the second stage plate. The heat pipe consists of a stainless steel tube with copper fittings soldered in the positions of each stage down the unit. The copper fittings bolt directly to the plates at each stage.

### 4.2.4 Test cryostat

The dilution refrigerator test cryostat consists of a stainless steel vacuum can. The top plate of the DR bolts directly to the flange of the vacuum can. The can is evacuated through an NW50 port. A copper can mounts to the first stage plate as a radiation shield. A similar can is bolted to the second stage plate. Both the radiation shield cans are covered with multilayer insulation.

### 4.2.5 Thermometry and services

The dilution refrigerator was delivered with a set of six Leiden Cryogenics thermometers on the various stages of the insert. 1 kΩ platinum RTDs (resistive temperature devices) are attached to the first stage plate and to the precool link between the first and second stages. 10 kΩ ruthenium oxide RTDs are attached to the second stage plate, the output flange of the JT heat exchanger, and in the bottom of the still (immersed in the dilute phase). The mixing chamber thermometer is a 360 Ω Speer carbon RTD. These thermometers were supplied with generic calibration curves. The mixing chamber thermometer was subsequently calibrated against a Lake Shore ruthenium oxide sensor. Checks of the calibration of the Leiden ruthenium oxide RTDs against calibrated Lake Shore ruthenium oxide RTDs indicated that the generic calibration was reasonable above 2 K. The sensors are read out using a Lake Shore 370 AC resistance bridge.[5].

[5]Lake Shore Cryotronics, Inc., http://www.lakeshore.com.

The thermometry was later supplemented with a number of Lake Shore RX-102 ruthenium oxide RTDs at the input and output of the JT heat exchanger, and on the still cold plate. These sensors were calibrated between 0.5 and 4 K against a Lake Shore germanium RTD by Cardiff University. An uncalibrated RX-102 was fitted to the second stage of the PTC as an additional diagnostic.

A cartridge heater of 100 Ω nominal resistance is attached to the mixing chamber plate. to allow control of the mixing chamber temperature. A similar heater is attached to the still plate, with a second heater (also nominally 100 Ω) composed of a wire coil is immersed in the liquid inside the still volume. A heater element of 470 Ω nominal resistance is attached to the second stage plate.

### 4.2.6 Gas handling system

The gas handling system (GHS) is a self-contained cabinet constructed from hollow square-section stainless steel tubing, welded to produce two leak-tight reservoirs for storage of the helium mixture. The upper tank, volume 36 litres, is used for the $^3$He-rich mixture, while the remaining volume (146 litres) holds the $^4$He-rich mixture. A photograph of the GHS cabinet is shown in Fig. 4.12.

Helium is circulated around the dilution circuit by twin turbo pumps (Varian Navigator 551) in parallel, backed by a sealed scroll pump (BOC Edwards XDS35i). A small diaphragm compressor (KNF Neuberger N143AN.12E) is in series after the scroll pump to increase the rate at which helium is condensed into the DR, and to reduce the output pressure of the scroll pump at high circulation rates. The DR is pumped through a 100 mm internal diameter pumping line, 2 m in length, connected to the gate valve on the insert. The instrument interface to the telescope required a large separation between the cryostat and GHS, so this pumping line was later replaced with a 10 m line.

A rotary vane pump (Pfeiffer Duo10), normally used to pump the 1-K pot in a conventional Leiden DR, was used as a roughing pump. This pump was later replaced with a small scroll pump (BOC Edwards XDS10) to remove the risk of oil back-streaming into the dilution circuit.

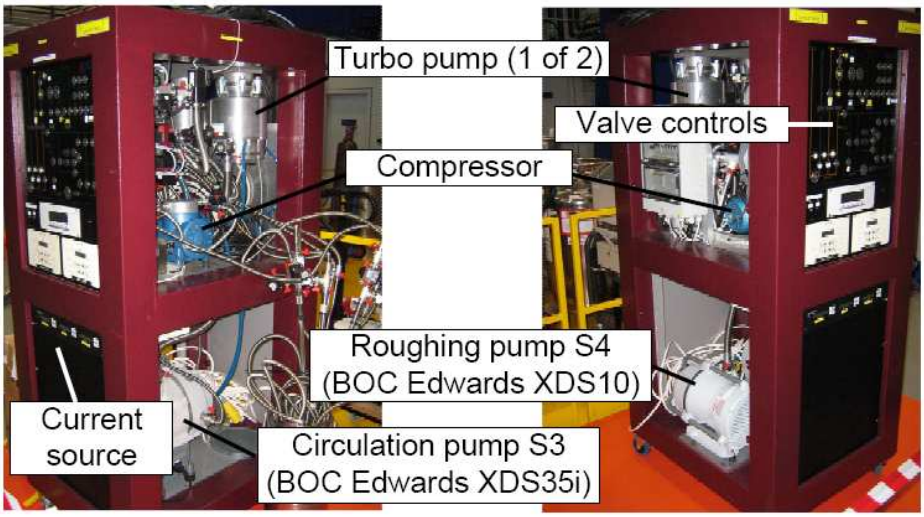


**Figure 4.12:** The gas handling system of the SCUBA-2 dilution refrigerator. The labels indicate the pumps and other major features in the system, see text for details.

Liquid nitrogen cold traps are used to clean the returning mixture, with two traps in parallel after the scroll pump and initially a single trap after the compressor. Helium is returned to the input side of the dilution circuit via a 4 m long NW10 flexible line. As with the still pumping line, the input line was also subsequently replaced by a 10 m line. A second trap was added in parallel after the compressor to allow purging of the traps during long-duration cooldowns without interrupting circulation. The cold traps were modified after delivery by fitting additional valves to isolate and pump out individual traps.

The GHS includes a manifold system of solenoid valves to direct the flow of gas as appropriate during operation. The valves are operated via piezoelectric switches on a manifold board on the front panel of the GHS cabinet. The system can also be operated using microprocessor automation or via a serial interface with a LabVIEW software application. Neither option is used for operation of the SCUBA-2 DR since the firmware and software have not been modified from that used for a standard wet refrigerator and are therefore not suitable for the system. The GHS also includes a triple current source for driving the heaters on the still and mixing chamber of the insert. Each current source is capable of supplying 100 mA (1 W of power with a 100 Ω heater).

A block diagram of the delivered handling system is shown in Fig. 4.13, including the location of pumps and pressure gauges. The GHS uses a series of ceramic cell pressure transmitters (Labom CB3010) with a useful operating range of 0–1.6 bar, although the gauges were found to be unreliable below ∼100 mbar. These gauges appear as P3 through P7 in Fig. 4.13. A high pressure gauge (Fischer ME6110) was fitted at the output of the compressor.

A series of modifications to the GHS system were initiated by the author following delivery as operational experience with the DR was gained. A block diagram of the final handling system is shown in Fig. 4.14. In addition to the changes to the nitrogen cold traps and the pump replacement described above, an additional manual valve (M7) was added to the pumping side of the circuit to regulate the flow of gas during initial circulation. During early cooldowns, it was found that the condensing pressure when first circulating gas could spike as high as 10 bar, greatly increasing the risks of leaks to atmosphere from the return side of the circuit. The use of this manual valve allows the flow of the helium mash to be regulated, keeping the condensing pressure within safer limits. This process is described in Sect. 4.3. The P4 gauge on the backing line of the turbo pumps was replaced with a piezoresistive gauge (Pfeiffer APR260, 0.1–1100 mbar range) and the P1 gauge on the compressor output with a similar gauge (Pfeiffer APR252, 1–10 bar range), both connected to the pressure controller (Pfeiffer MaxiGauge) already used for the still pressure gauge on the DR insert.

## 4.3 Operation of the Dilution Refrigerator

Once the cryostat is closed, the vacuum can is evacuated using an external pumping station. Due to the insert design of the DR, it is necessary to backfill the GHS and break the connecting lines to remove the insert from the cryostat, and so the handling system and NW10 helium input line are also pumped down using the auxiliary pump (S4), while the 100 mm DR pumping line and the insert are pumped out using the turbo pumps (S1 and S2). At this stage the charcoal cold traps are warm, and are pumped at the same time as the rest of the system, again using S4. Once the system is evacuated (typically 12 hours pumping time), the insert is isolated and the cold traps heated for 10 to 15 minutes while pumping to clean any residual gas from the charcoal. After

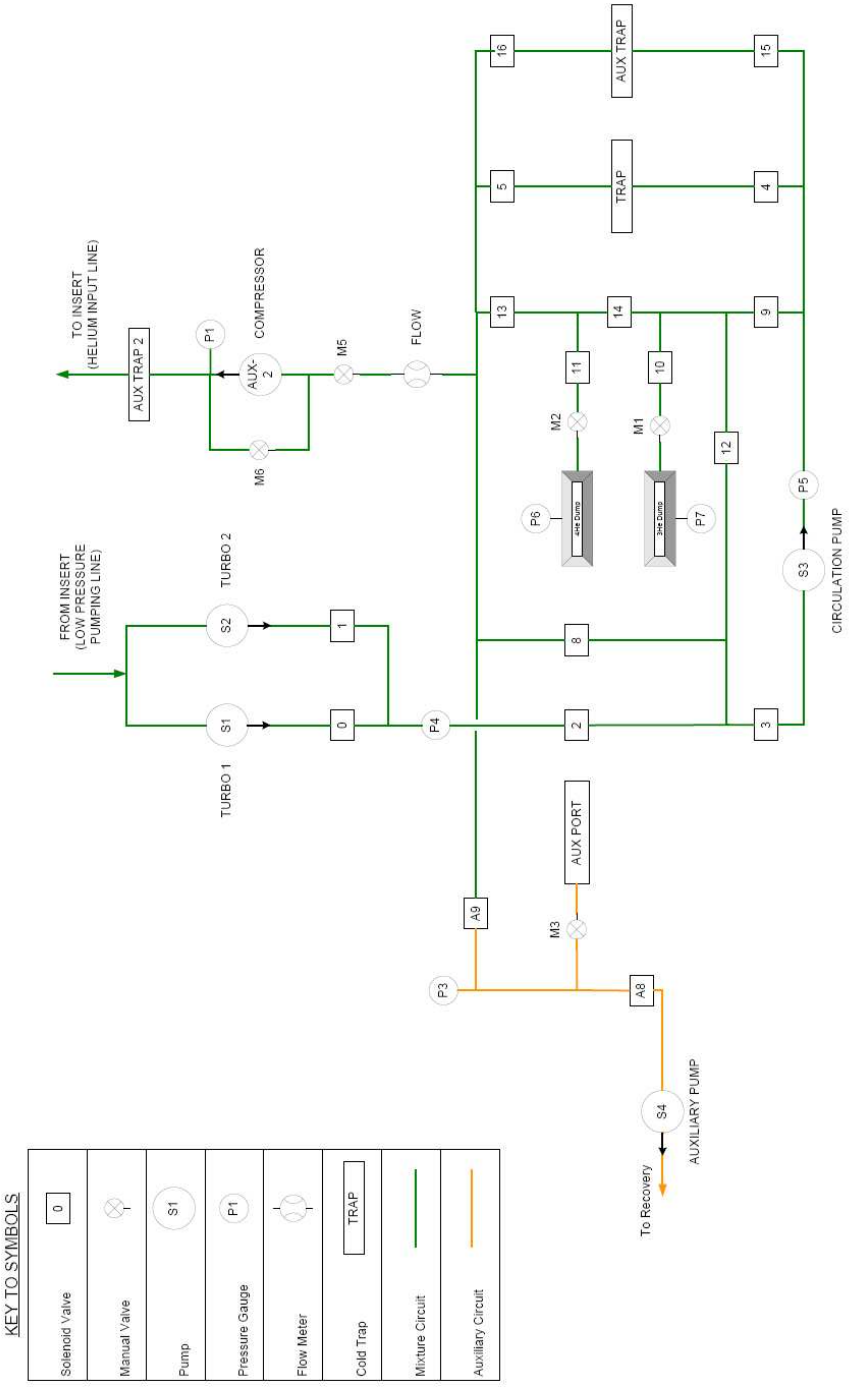


**Figure 4.13:** Block diagram for the dilution refrigerator gas handling system as delivered. The system is based on a standard Leiden Cryogenics GHS-2T-1T-700 handling system. See text for details.

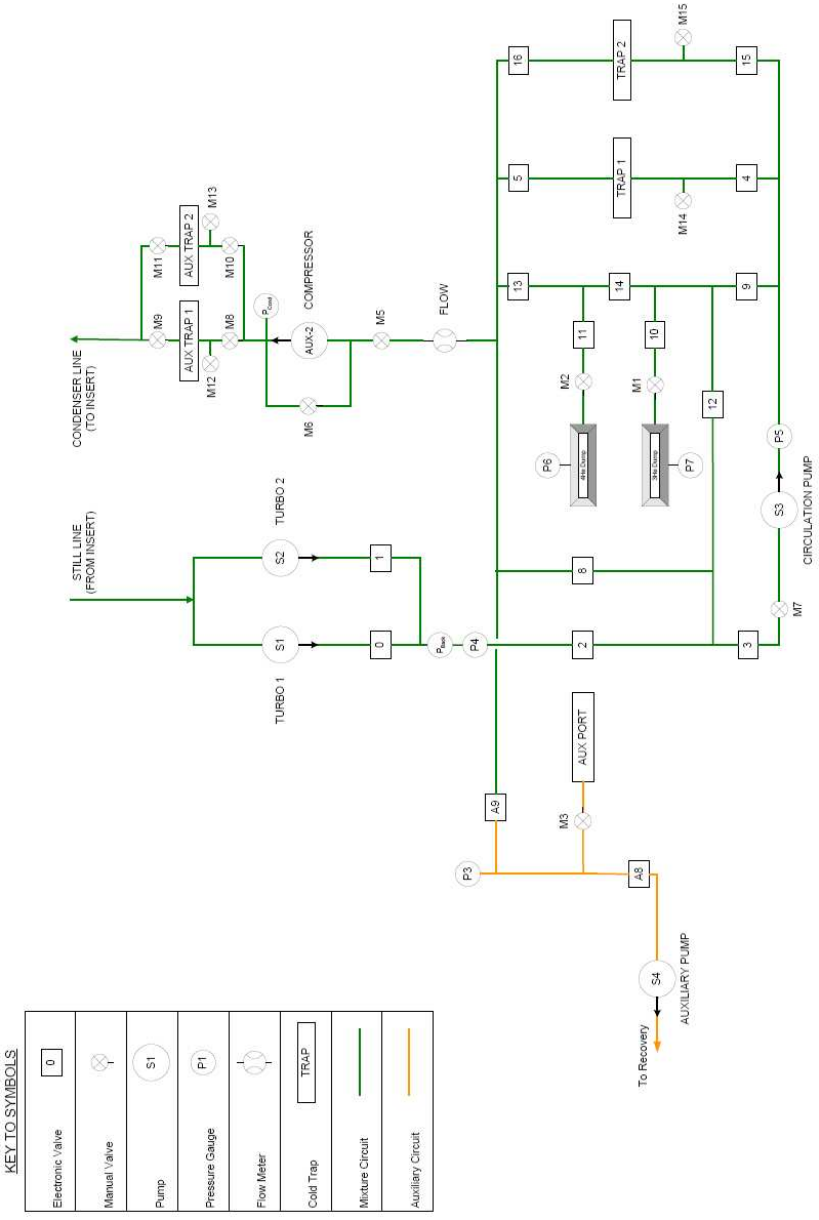


**Figure 4.14:** Block diagram for the dilution refrigerator gas handling system following modification to meet the requirements of operating the dry dilution refrigerator. Major changes included: Additional manual valve on the dilute side of the circuit (M7) to regulate flow; additional cold trap after the compressor (Aux Trap 2); additional pumping ports on the cold traps (M12–M15) to allow for independent cleaning of the traps; and an additional pressure gauge ($P_{back}$) on the still pumping line. See text for additional details.

heating, the circulation side of the gas handling circuit is isolated from the auxiliary circuit (closing valve A9) and the traps cooled in a liquid nitrogen dewar. Any residual air or water vapour in the handling system will then be adsorbed into the charcoal traps, leaving the circuit clean.

To aid the precool of the insert, the $^4$He-dump is opened to the input side of the dilution refrigerator through the cold traps. The PTC is then started. As the insert cools, the $^4$He will condense into the dilution unit. Although this process does not reduce the precool time in the test cryostat, it does reduce the time to condense the helium mash into the DR after precool since most of the $^4$He is already liquified, which lowers the temperature of the still and the JT heat exchanger (in previous cooldowns, the temperature of the still and JT remained at 10–15 K until $^4$He was added from the dumps, even with the precool link between the still and the second stage plate). The two mechanical heat switches are closed during the initial phase of the cooldown. No exchange gas is used during the precool phase, since this would not be possible in the main instrument cryostat.

A cooldown curve for the precool of the insert is shown in Fig. 4.15. The first and second stage plates, the still and JT all cool below 100 K in less than 10 hours, with the mixing chamber lagging due to the poor thermal path to the bottom of the insert. The first stage heat switch is opened after 8 hours once the second stage plate reaches the temperature of the first stage (approximately 50 K). Beyond this point, the short between the two stages offers no benefit. The second stage switch remains closed for the full period of the precool and condensing phases. The first stage plate cools to a temperature of 37 K, while the second stage plate cools below 3 K with no helium load. Due to the lag in the mixing chamber temperature, the full precool process (dilution unit temperatures below 4 K) takes 23 hours to complete.

Once the precool is complete, the majority of the $^4$He charge has been liquified in the dilution unit. The remaining charge is transfered to the insert using the circulation scroll pump (S3) and the compressor. The $^3$He charge is then added to the insert in the same way. The helium charge for the DR is composed of 140 standard litres of $^4$He and 32 standard litres of $^3$He. The transfer of gas to the insert causes the second stage and JT temperatures to rise to approximately 5 K, with smaller rises on the still and mixing

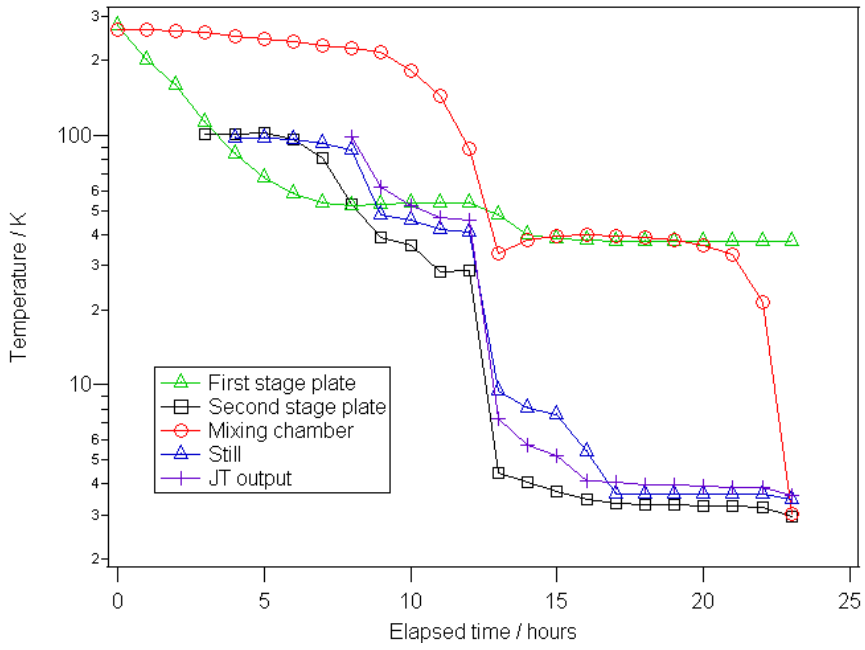


**Figure 4.15:** Cooldown curve for the precool of the dilution refrigerator insert in the test cryostat. The temperature of the first and second stage plates, mixing chamber still and Joule-Thomson stage are shown as a function of time.

chamber. This temperature spike lasts approximately 20 minutes before the stages cool and the gas liquifies. The second stage heat switch is closed during the gas transfers to reduce the temperature spike on the still associated with the warm gas flow. Without the short to the second stage plate, it was found that the still could rise to 10 K or more as gas was added from the dumps, increasing the input pressure and prolonging the process of condensing the gas mixture.

The condensing process and cooldown to final base temperature is shown in Fig. 4.16. Once the full charge is condensed in the insert, the second stage heat switch is opened and the mash is circulated using S3 and the compressor. The flow is regulated using the valve on the turbo pump backing line (M7), keeping the input pressure below 4 bar. Without regulation, the input pressure can spike to 10–15 bar, greatly increasing the risk of mixture loss from room temperature O-rings.

Once M7 is fully open and the mash flowing freely, the turbo pumps (S1 and S2) are started, spinning up to full speed over ∼20 minutes, reducing the still pressure and cooling the dilution unit. The temperature of the JT stage remains at approximately 3 K

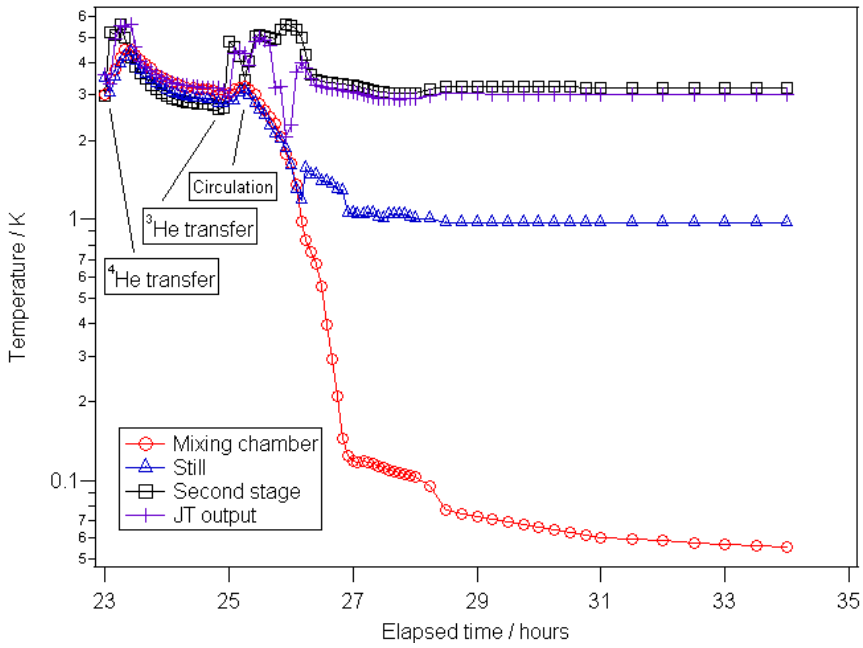


**Figure 4.16:** Cooldown curve transfer of helium to the insert, circulation and final cooldown to base temperature. The temperature of the second stage plate, Joule-Thomson stage, still and mixing chamber are shown as a function of time from the start of the precool phase. Key features of the process (transfer of $^4$He, transfer of $^3$He and the start of mash circulation) are indicated.

during the process, although at high input pressures (2–4 bar) early in the condensing process, the JT output temperature can reach 2 K.

When the mixing chamber cools below 1 K, the bypass valve on the primary input line is closed. This increases the flow impedance, and increases the cooling effect. The second input line (valve 7) is closed once the mixing chamber has cooled below 800 mK. The temperature falls rapidly to ∼100 mK, after which the cooling rate flattens out towards the final base temperature of ∼45 mK with 14 mW of heat applied to the still. The total cooldown time from room temperature to base temperature is 34 hours.

With the still heater on, the still temperature is ∼970 mK, at a pressure of $\sim 1.6 \times 10^{-1}$ mbar. With no power to the still heater, the still temperature falls to ∼850 mK. The typical condensing pressure during normal circulation is 0.9 bar.

## 4.4 Summary

This chapter has outlined the theory of operation of the dilution refrigerator, including discussion of the practical design of DRs. The development of "dry" dilution refrigerators, using mechanical coolers in place of liquid cryogen baths, and fast becoming a standard implementation of the technique, has also been described. The design and operation of the SCUBA-2 dry DR was discussed. The information contained in this chapter provides background material for the testing and characterisation of the DR discussed in the next chapter, and the testing of the full instrument cryostat described in Chapter 6.

# Chapter 5

# Cryogenics II: Performance of the SCUBA-2 Dilution Refrigerator

This chapter describes the commissioning and characterisation of the SCUBA-2 dilution refrigerator as a stand alone system, providing baseline data for comparison to the DR performance in the instrument cryostat.

The initial testing of DR following delivery is summarised, including discussion of the goals of the test programme. This work was carried out prior to the first run of the DR in the main instrument. Part of this programme included testing of the precool switch system for the instrument cryostat, and this evaluation is presented separately.

Subsequent work was conducted in order to fully characterise the system behaviour in order to evaluate the performance of the DR and the behaviour of the thermal stages in the main cryostat. This data is presented and discussed in this chapter.

The involvement of this author with work on the dilution refrigerator commenced at the time of acceptance and delivery of the system. The work to initially commission the DR was carried out in a joint effort with D. Gostick (SCUBA-2 cryo-mechanical engineer), with responsibility and leadership of the work package subsequently transferring to the author due to project staffing changes. The performance characterisation and analysis presented in §5.3–5.5 is the work of this author.

The characterisation data of the DR, including a summary of the testing in the instrument cryostat, has previously appeared in the *Proceedings of the SPIE* as "Performance of the SCUBA-2 Dilution Refrigerator" [146].

## 5.1 Summary and Goals of DR Cooldowns

The goal of initial work with the dilution refrigerator in the test cryostat was to confirm performance of the system following delivery, but prior to the first cooldown in the main instrument cryostat. Work was also carried out at this time to fit the hardware for the mechanical precool switches that would be used in the instrument for precooling the 1-K system. However, a series of problems with the DR during this period required more extensive work that originally planned. At the time of the first instrument cooldown, although the DR was nominally functional and the precool switches fitted and tested, the performance of the system was not fully characterised. A summary of this work and the testing of the precool switches is described below in §5.2 and §5.3.

A series of later cooldowns aimed to provide a full baseline for the DR performance. The results and analysis of this testing are described in §5.4 and §5.5. At this time, the system was tested with the long pumping lines required for operation at the telescope.

A final series of cooldowns explored solutions to some problems observed during testing in the instrument cryostat, such as suspected vibration from the DR pulse tube.

Tables 5.1–5.4 summarise the details of the dilution refrigerator cooldowns in the test cryostat. The start and end dates and the base temperature are listed, along with comments on the key features and outcomes of the cooldown. At least one cooldown in the instrument cryostat occurred between each of the four sets of DR runs. Cooldowns of the DR in the test cryostat are identified with a DRF prefix, while cooldowns in the instrument cryostat use a prefix of INS.

**Table 5.1:** Summary of dilution refrigerator cooldowns prior to the first cooldown in the instrument cryostat.

| Cooldown | Start date | End date | Base temperature | Comments |
|---|---|---|---|---|
| 1 | 19-08-2005 | 26-08-2005 | 36 mK | First cooldown. |
| 2 | 29-08-2005 | 02-09-2005 | 4 K | Aborted after precool due to helium leak into vacuum can. |
| 3 | 07-09-2005 | 08-09-2005 | 40 K | Aborted during precool. |
| 3a | 09-09-2005 | 12-09-2005 | 4 K | Blockage on transfer of helium mixture to insert. |
| 4 | 20-09-2005 | 28-09-2005 | 56 mK | High condensing pressure and low flow rate. Problem traced to build up of air in cold traps due to leak from atmosphere. |
| 5 | 18-10-2005 | 26-10-2005 | 4 K | High second stage temperature, unable to condense mash. |
| 6 | 29-10-2005 | 31-10-2005 | 40 K | Test of PTC. Cooler apparently functioning correctly. |
| 7 | 02-11-2005 | 07-11-2005 | 4 K | High second stage temperature, unable to condense mash. |
| 8 | 09-11-2005 | 14-11-2005 | 4 K | Improved second stage temperature after tightening interface screws. Cooldown aborted due to detection of helium leak into vacuum can. |
| 9 | 17-11-2005 | 23-11-2005 | 80 mK | High base temperature due to incorrect mixture ratio. |
| 10 | 24-11-2005 | 30-11-2005 | 4 K | Test of precool system. |

**Table 5.2:** Summary of dilution refrigerator cooldowns between INS_CD4 and INS_CD5.

| Cooldown | Start date | End date | Base temperature | Comments |
|---|---|---|---|---|
| 11 | 13-01-2006 | 20-01-2006 | 55 mK | Test run with additional thermometry. Problem with heater on still caused reduced flow rate and elevated base temperature. |
| 12 | 24-01-2006 | 06-02-2006 | 45 mK | Run to characterise DR performance after repair of heater on previous cooldown. |

**Table 5.3:** Summary of dilution refrigerator cooldowns between INS_CD6 and INS_CD7.

| Cooldown | Start date | End date | Base temperature | Comments |
|---|---|---|---|---|
| 13 | 30-08-2006 | 06-09-2006 | 43 mK | Characterisation of DR performance. |
| 14 | 08-09-2006 | 18-09-2006 | 46 mK | Characterisation of DR performance. |
| 15 | 20-09-2006 | 29-09-2006 | 41 mK | Characterisation of DR performance. Some temperature sensors repositioned. |
| 16 | 06-10-2006 | 18-10-2006 | 45 mK | Cooldown with 10 m pumping lines and GHS at 110 V/60 Hz. |

**Table 5.4:** Summary of dilution refrigerator cooldowns prior to INS_CD8.

| Cooldown | Start date | End date | Base temperature | Comments |
|---|---|---|---|---|
| 17 | 28-03-2007 | 16-04-2007 | 80 mK | First cooldown with remote motor PTC and reconfigured still pumping arrangement. Testing mostly concentrated on PTC. |
| 18 | 23-04-2007 | 30-04-2007 | 830 mK | Unable to dilute mixture. Helium recovery indicated loss of mixture. |
| 19 | 08-05-2007 | 17-05-2007 | 52 mK | Testing of alternative still pumping arrangement with old PTC. Partial warmup at end of run to change vacuum lines. |
| 19a | 18-05-2007 | 31-05-2007 | 54 mK | Testing of alternative still pumping arrangement with old PTC. Cooldown included controlled tilting of the test cryostat. |
| 20 | 05-06-2007 | 14-05-2007 | 50 mK | Experiments with closed-loop temperature control on mixing chamber. |
| 21 | 15-06-2007 | 22-06-2007 | 45 mK | Experiments with adjusting the PTC gas pressure to improve base temperatures. |
| 22 | 25-06-2007 | 28-06-2007 | 117 mK | Remote motor PTC refitted. Experiments with PTC gas pressure. PTC overpressured, forcing partial warmup to reduce helium pressure. |
| 22a | 29-06-2007 | 03-07-2007 | 128 mK | PTC performance improved with optimised gas pressure, but large $\Delta T$ across second stage wicks causing poor performance. |
| 23 | 04-07-2007 | 07-07-2007 | 43 mK | Wicks removed. Interface between second stage plate and PTC cleaned to minimise $\Delta T$ across joint. |

## 5.2 Commissioning and Early Performance Evaluation

The dilution refrigerator was delivered in August 2005 following acceptance testing at Leiden Cryogenics. This section describes the work carried out in a series of test cooldowns to commission the DR prior to integration in the main cryostat for the first full test of the instrument.

During development, the lowest mixing chamber temperature achieved was 28 mK, although during the acceptance test the mixing chamber base temperature was 30 mK. The first DR cooldown, DRF_CD1, achieved a minimum base temperature of 36 mK. Cooling power measurements during this run gave 46mK with a 30 $\mu$W load, and 60 mK with a 100 $\mu$W load.

Following the first cooldown, the DR insert was partially disassembled for modifications to the second stage plate ready for the precool links. Removal of this plate required that the input side of the dilution circuit be broken to remove the 4-K heat exchanger. After reassembly, a large leak into the vacuum can was found at the completion of the precool for DRF_CD2. The problem was identified by visual inspection following warm up to be a hole in the solder plug at the point where one of the input capillaries entered the still pumping line at the top of the JT heat exchanger. Two subsequent cooldowns were aborted, DRF_CD3 due to a thermometry wiring problem, and DRF_CD3a after a blockage as $^4$He was transferred to the insert following the precool.

The helium mash was condensed successfully on DRF_CD4, achieving a base temperature of 56 mK, although with a high condensing pressure ($\sim$2 bar during normal operation). Following warm up, a considerable quantity of gas was pumped out of the cold traps, implying the presence of an air leak in the gas handling system. Investigation of the GHS revealed a number of bad vacuum seals due to damaged O-rings.

Leak checks of the insert showed the presence of a further leak in the dilution circuit, which was localised to the input side of the insert. Further checks showed that one of the sections of external capillary at the 4-K heat exchanger was cracked and leaking helium to the vacuum space. An attempted repair fractured the capillary completely. The capillary was removed and a larger bore section (1.6 mm i.d. and 2 mm o.d.) spliced into the circuit. Room temperature tests showed the repair to be leak tight.

A series of cooldowns followed in which large temperature spikes (up to 15 K) were observed on the second stage plate when helium was run into the insert. The problem was eventually traced to poor joints between the PTC stages and the copper plates resulting from loose screws and poor surface quality at the contact. The surfaces were cleaned, and Belleville springs and washer stacks were added to the bolted interfaces to take up slack from differential contraction. Measurements of the joint conductance during DRF_CD8 showed that the interface was greatly improved in comparison to earlier measurements. It was not possible to condense the helium at this stage due to a further leak into the vacuum space from the dilute side of the circuit. The source of this leak was again traced to the poor solder joint in the pumping line at the top of the JT (the original repair after DRF_CD2 having been only partially successful). The mixture was successfully condensed during the next cooldown, although a base temperature of only 90 mK was reached as a result of low $^3$He content in the mash from the earlier leaks. Due to time constraints on the start of the first full instrument cooldown, further helium was not added to the system at this stage.

The precool switches were fitted to the system, and tested during DRF_CD10. The results of this test are discussed in the next section. A further attempt to condense the helium mash during this cooldown failed due to a faulty valve on the top of the insert that shorted the concentrated and dilute sides of the circuit. At this stage, further commissioning work on the DR was abandoned, and the insert transferred to the instrument cryostat in preparation for INS_CD4, the first full cooldown of the instrument.

## 5.3 Evaluation of the Precool Switches

The DR insert precool links were fitted between DRF_CD9 and CD10. The precool curves for these runs are shown in Fig. 5.1 for comparison. The precool procedure used on DRF_CD10 was to keep the first stage switch closed to short the first and second stage of the pulse tube cooler together to take advantage of the high cooling power on the first stage, until the temperature of the two stages were approximately equal. The first stage heat switch was then opened, and the lower temperature stages allowed to cool to 4 K. The second stage heat switch, shorting the second stage to the still,

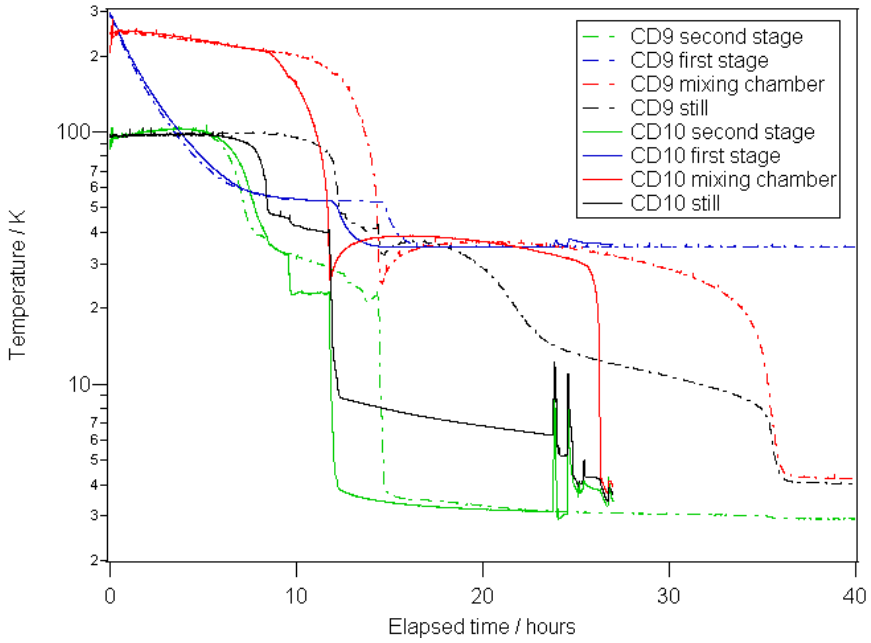


**Figure 5.1:** Comparison of cooldown curves for the precool of the dilution refrigerator insert in the test cryostat. The temperature of the first and second stage plates, mixing chamber and still are shown as a function of time for a cooldown without the mechanical precool heat switches fitted (DRF_CD9, indicated by the broken lines on the graph) and a precool after the switches were fitted (DRF_CD10, solid lines).

remained closed. The time from the start of the cooldown to the first stage switch being opened was approximately 6 hours. Comparison of the first and second stage temperatures between the two cooldowns in Fig. 5.1 shows that the stages cool more slowly in CD10 (solid lines) than CD9 (broken lines) without the precool links, implying a greater load on the PTC during the early stages of the precool.

The precool link to the still has a marked effect on the cooldown curve at this stage, with the still temperature falling below 10K approximately 20 hours sooner than before the link was fitted. Without the precool link, the cooling path for the dilution unit is via the stainless steel structure, which at low temperature is a poor thermal conductor, and by gas conduction in the heat pipe and the helium charge in the insert. Even with the precool links, removal of heat from the mixing chamber is still via these mechanisms, maintaining a considerable lag between the mixing chamber temperature and the higher stages.

The considerable drop in the mixing chamber temperature after ∼25 hours on CD10 is due to the helium mash being condensed into the insert. Without the precool link to the still, the cooldown of the dilution unit is such that helium will not condense in the dilution unit until later in the precool process. As the helium charge condenses into the dilution unit, the remaining heat is removed quickly due to conduction through the liquid. The precool link to the still was kept closed during the transfer of the mash to minimise heating on the still due to the addition of warm gas.

The addition of the heat switches to the insert reduced the precool time (time to 4 K) by approximately 10 hours to ∼27 hours. Arguably, the time reduction was greater than this (∼13 hours), since the addition of helium mash to the system was possible sooner than on early cooldowns.

## 5.4 Full Performance Evaluation

In the following section, characterisation data of the dilution refrigerator are presented. The majority of these measurements were carried out during two cooldowns of the DR (DRF_CD14 and DRF_CD15) between 8-09-2006 and 29-09-2006. At this point, the DR had been successfully run in the instrument cryostat for more than 3000 hours during 3 cooldowns. Some variation in performance of a dilution refrigerator between cooldowns is to be expected due to small variations in helium content and isotope ratio in the mash, and external influences such as heat leaks from wiring. Furthermore, the problems experienced during the commissioning of the DR and the time pressure for the first cooldown of the insert in the instrument cryostat had not allowed sufficient opportunity to make all of the measurements necessary to characterise the system performance. These measurements were intended to give as complete a set of consistent characterisation data as possible.

The performance of the DR pulse tube cooler was measured in order to estimate the heat loading on the second stage of the DR insert, both due to the static load of the structure and from the circulating helium. The measurements were made after a precool of several days, without any helium mash in the circuit, to allow the stage temperatures to settle at static values without the additional loading from the condensation of the mixture. The cooling power of the PTC was measured by applying up to

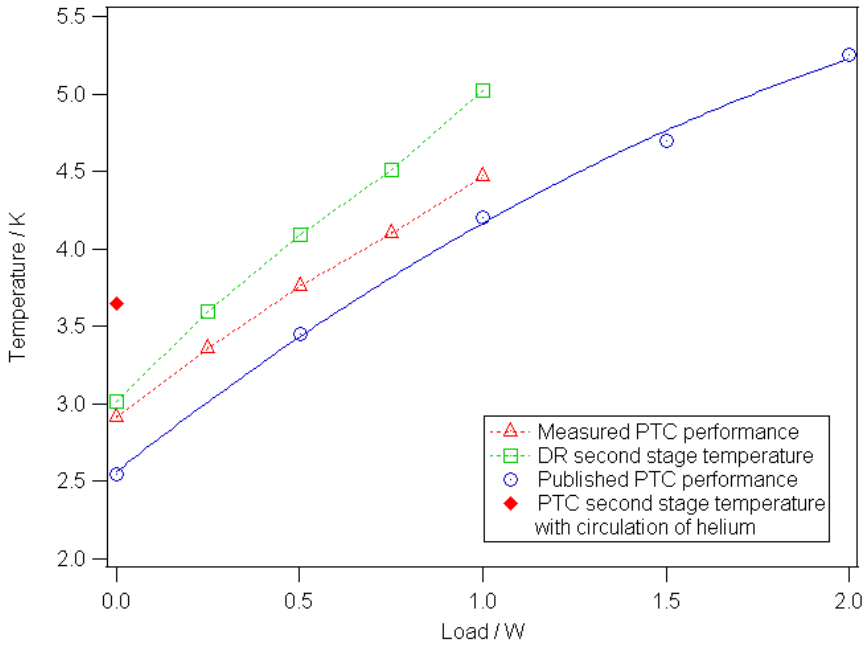


**Figure 5.2:** Measured pulse tube cooler performance in the dilution refrigerator insert and a curve from the published PT410 results with a representative first stage load of 18W.

1 W of additional electrical power to the second stage plate heater and recording the temperature of the pulse tube cold finger. The measured data is shown in Fig. 5.2. The ruthenium oxide thermometer on the pulse tube second stage was not calibrated; the temperature conversion used the standard curve published by Lake Shore for that type of device. However, comparisons between the standard curve and thermometers that were independently calibrated showed good agreement above 2 K.

An estimate of the background load on the pulse tube may be extracted from these measurements by comparing the measured values to measurements of the cooling power with the pulse tube in isolation. The PTC performance was not checked independently during this project. However, comparison to the typical data published by Cryomech is reasonable. Cryomech data for the PT410 second stage cooling power is shown in Fig. 5.2 for a first stage load of 18 W (giving a temperature of 36 K, roughly consistent with the first stage temperature measured on the DR insert).

A third-order polynomial was fitted to the published cooling power data, such that the total power load (background plus heater) could be fitted for a measured tem-

perature. The applied heater power is then subtracted, leaving an estimate for the background power. From this calculation, the background power loading was estimated (from the average of the fitted points) to be 190 mW.

An estimate of the load on the second stage due to the circulating $^3$He during normal operation may also be obtained in the same way. A PTC temperature of 3.65 K was measured when circulating mixture during DRF_CD15, consistent with a load of 610 mW on the second stage. This gives an estimated load of 420 mW due to the circulation of helium.

With the DR in continuous operation, measurements were taken of the refrigerator characteristics for different still heater powers, between 0 and 32 mW. Dilution refrigerators are inherently slow systems due to the interaction between the different temperature stages and the large heat capacity of the liquified helium mixture. After the still heater was set, the DR was left for several hours to stabilise before values were recorded.

The cooling capacity of the still is depicted in Fig. 5.3. The values of $T_{still}$ were measured using the calibrated Lake Shore RX-102A ruthenium oxide thermometer, rather than the uncalibrated Leiden Cryogenics ruthenium oxide sensor used for diagnostics during normal operation. For this range of still heater powers, $T_{still}$ varied from 910 mK up to 1160 mK. This is outside the specification for the still that with 5 mW load, the still temperature should not exceed 900 mK.

The consequence of the elevated still temperature is two-fold. Firstly, the temperature of the circulating $^3$He leaving the still heat exchanger will be higher than optimal, increasing the background loading on the mixing chamber. Secondly, the $^4$He content of the circulating mixture will be slightly increased due to the higher $^4$He vapour pressure, $P_{vp}(^4\text{He})$, at 1 K than at 700 mK (as in a conventional DR). The vapour pressure of $^3$He and $^4$He as functions of temperature are shown in Fig. 5.4. At 700 mK, $P_{vp}(^4\text{He})$ is negligible, increasing to $\sim$0.26 mbar at 1 K. $P_{vp}(^3\text{He})$ at 700 mK is $\sim$1.9 mbar, increasing to $\sim$11.9 mbar at 1 K. The percentage $^4$He content in the circulating mixture is obtained by taking the ratio of the $^4$He vapour pressure to the sum of the vapour pressures of the two isotopes at a given temperature. At 700 mK, the circulant is effectively pure $^3$He, while at 1 K the mixture is 2% $^4$He.

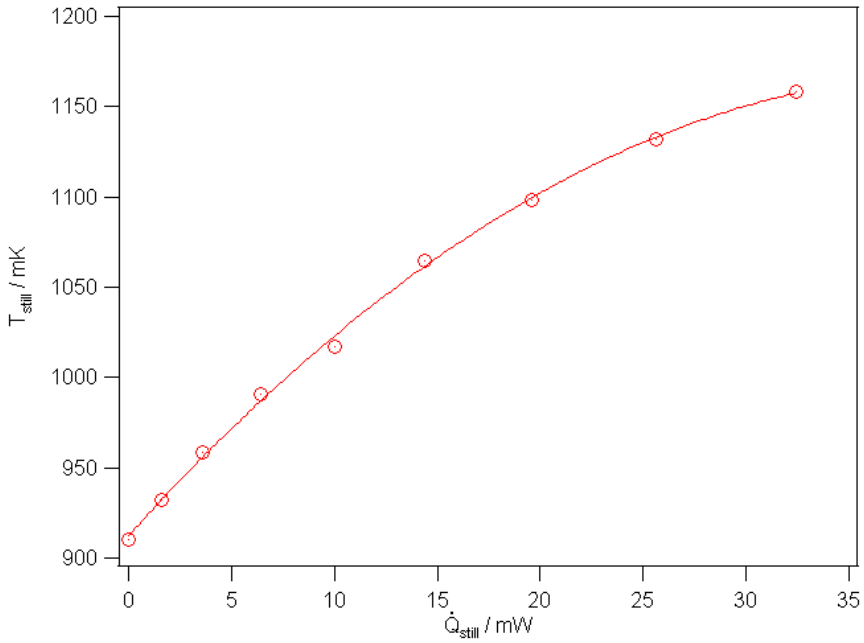


**Figure 5.3:** Cooling capacity of the dilution refrigerator still.

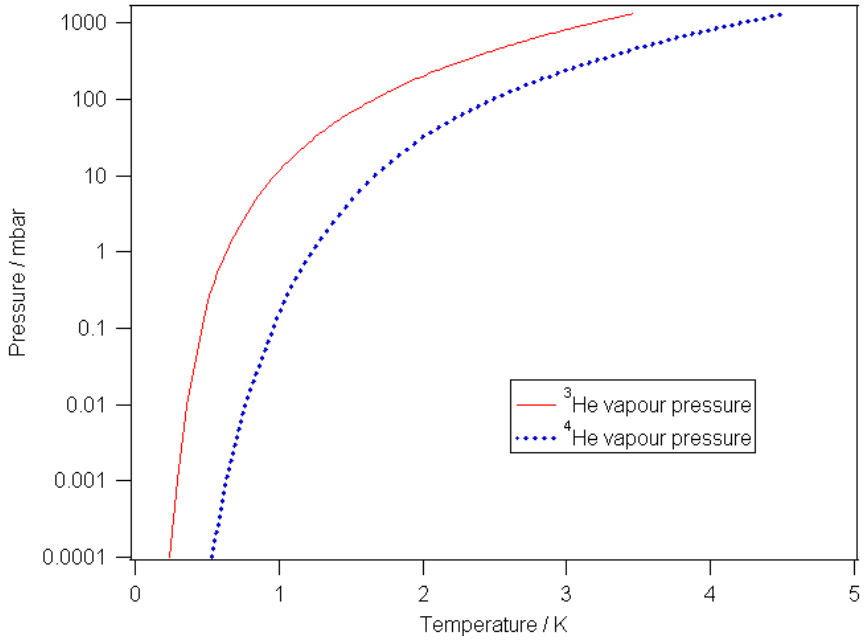


**Figure 5.4:** Vapour pressure of $^3$He and $^4$He as functions of temperature.

There are several effects due to the $^4$He content of the circulated mixture. Firstly, the $^3$He circulation rate may be degraded since the pumping system will have a constant total volume flow rate. Additional load will also be placed on the heat exchangers since the specific heat of $^3$He in a mixture can be substantially greater than for pure $^3$He. Furthermore, separation of the two isotopes can occur in pockets in the concentrated phase column, particularly in counterflow heat exchangers, resulting in a series of phase boundaries that produce alternate heating and cooling of the $^3$He, so wasting the enthalpy of the returning liquid.

The poor still performance is likely to be a result of the poor performance of the Joule-Thomson stage. The JT input temperature is measured to be ∼3.5 K, while the output temperature is ∼3 K, rather than at 1–2 K as would be desirable following the JT expansion [132]. In this DR, the gas is cooled and condensed in the still heat exchanger, placing additional load on the still since the circulating $^3$He must be cooled from 3 K to $T_{still}$ as well as condensed. Taking the heat capacity of $^3$He at ∼2 K as 10 J/mol [121] and a typical $^3$He circulation rate of 500 $\mu$mol/s, the additional load on the still due to the elevated JT temperature is ∼8 mW. This is not an inconsiderable heat load, given the measured still cooling capacity.

There are a number of possible causes for the poor performance of the Joule-Thomson stage. The first, and probably the most straightforward, of these is a direct heat leak onto the output of the stage. This possibility would not appear to be a good cause, since any leak would be from a temperature of ∼ 4 K around the second stage plate, making conduction of a significant amount of power onto the JT output difficult. Alternatively, it could be the design of the stage itself that is the cause, either through poor heat exchange between the instreaming $^3$He and the gas pumped from the still in the counterflow exchanger, resulting in minimal reduction in the enthalpy of the $^3$He, or incorrect impedances for the expansion of the gas at the output of the stage. The efficient function of the JT stage is reliant on sufficiently cooling the incoming $^3$He to reduce the enthalpy of the gas into the two-phase region of the enthalpy-pressure curve (see, for example, the $^3$He enthalpy measurements in Ref. [147]) so that following the isenthalpic expansion after the stage impedance, the $^3$He exists as a liquid-gas mixture at low pressure. If the enthalpy of the gas is not sufficiently reduced before the expan-

sion at the impedances, then the enthalpy must be reduced in the still heat exchanger, putting considerable load on that stage.

It is important to note that this argument assumes that the temperature of the $^3$He at the input to the counterflow exchanger in the JT stage is close to the temperature measured by the temperature sensor at the stage input. The RTD is mounted on a flange at the warm end of the outer tube of the JT stage, which is bolted to the second stage plate. To be precise, the measurement of the JT input temperature is actually the temperature of the gas outflowing from the still following the exchange of heat in the incoming $^3$He, rather than a direct measure of the incoming gas temperature. If the top of the heat exchanger capillary was decoupled from the pumping tube at this point, the true gas temperature could be considerably higher than 3.5 K. The heat sinking of the output capillary of the JT stage (following the expansion) to the flange on which the temperature sensor is mounted is considerably better than at the input. As such, the measured temperature of $\sim 3$ K at the output is considered reliable.

If the inflowing gas at the warm end of the JT stage is considerably hotter than expected, then it is conceivable that although the counterflow heat exchanger is working correctly, the incoming gas simply has too much enthalpy to be effectively removed, making the expansion at the outlet of the JT stage less effective than intended. The evidence against this explanation is that the measured temperature of the second stage, which is approximately that of the measured JT input temperature, is believed to be a better reflection of the instreaming $^3$He temperature. As discussed in §4.2, the input capillaries pass through a sintered block heat exchanger bolted to the underside of the second stage plate. The contact area between the $^3$He flow and the sintered block, and the block and the copper plate on which the temperature sensor is mounted, would suggest that this is a reasonable measurement of the gas temperature.

Taking this information into account would imply that although the $^3$He is being precooled to $\sim$ 4 K reasonably well, there is a minimal $\Delta T$ through the JT stage. Regardless of the cause of the high output temperature, the performance at the JT stage is one of the limiting factors of this DR.

In addition to measurements of $T_{still}$ as a function of $\dot{Q}_{still}$, the condensing pressure $P_{cond}$ and flow rate, $\dot{n}_i$, were recorded. The data is shown in Fig. 5.5. These measure-

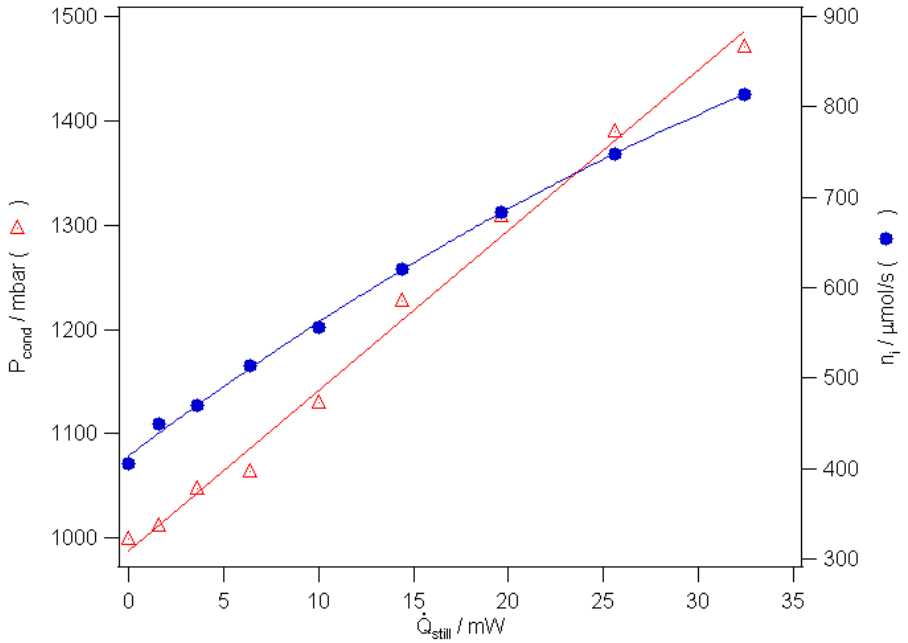


**Figure 5.5:** Condensing pressure, $P_{cond}$, and circulation rate, $\dot{n}_i$, as functions of $\dot{Q}_{still}$.

ments were made without the compressor running, and the helium circulating only on the main S3 scroll pump. $P_{cond}$ varied between 1 and 1.5 bar, while the circulation rate varied between 400 and 800 $\mu$mol/s. The circulation rate data in Fig. 5.5 is taken from the flow meter in the dilution circuit. The flow meter output requires calibration to convert the voltage reading to a flow rate. This calibration took the flow meter voltage reading as a percentage of full scale, which is equivalent to 5L/minute for this model. The voltage may be converted to a molar flow rate using the density of helium gas and the molar mass of $^3$He (the $^4$He content in the mixture is ignored).

The mixing chamber temperature as a function of the still power is shown in Fig. 5.6 for $\dot{Q}_{mc}$ values of 0, 49 and 100 $\mu$W. The shape of the three curves shows that there is a value of $\dot{Q}_{still}$ that minimises $T_{mc}$ (effectively balancing the circulation rate with the heat leak on to the mixing chamber and viscous heating, all of which increase with increasing still heater power). As $\dot{Q}_{mc}$ increases, there is a weak increase in the still power required to minimise the mixing chamber temperature. This effect is negligible, so for the majority of cooldowns with the DR in the test cryostat, $\dot{Q}_{still} = 14.4$ mW.

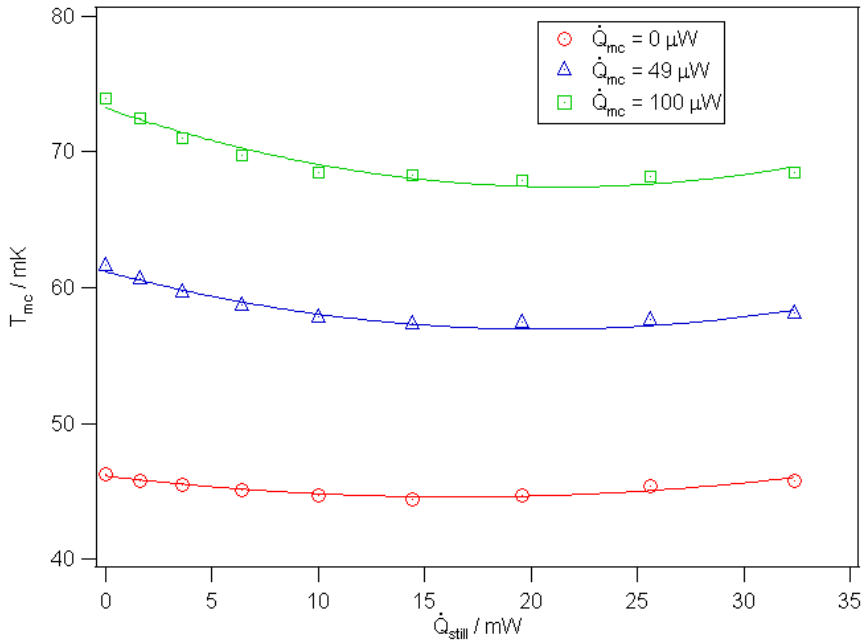


**Figure 5.6:** Mixing chamber temperature as a function of $\dot{Q}_{still}$ for three values of $\dot{Q}_{mc}$ between 0 and 100 $\mu$W.

Typically, and as discussed previously, the still temperature in a DR would be expected to be around 0.6–0.7 K. It is therefore somewhat surprising that for this DR, in which the still temperature is already running well above this "conventional" optimum, further increases of $T_{still}$ initially lowers the temperature (and increases the mixing chamber cooling power - see below). However, closer consideration of the behaviour of the fridge indicates that this should be the case. The limiting base temperature of the mixing chamber is a compromise between the heat load on the mixing chamber, and viscous heating effects due to the circulating mixture. If viscous heating were not present, it would be possible to make a fridge with an arbitrarily high cooling power simply by increasing the circulation rate. Tube sizes in a DR will typically be chosen to minimise viscous heating effects for a given circulation rate.

For a fixed heat load on the mixing chamber, the circulation rate increases (typically by increasing $T_{still}$ and hence the $^3$He vapour pressure), the mixing chamber temperature will initially decrease due to the increase in the $^3$He circulation rate (assuming that the circulation rate is not limited by the pumping system), even though the *fraction* of $^3$He

in the mixture decreases slightly due to the $^4$He content. At some circulation rate, a minimum in $T_{mc}$ will be reached. This is effectively a "heat leak limited" condition. If the circulation rate is increased further, viscous heating effects begin to dominate, increasing $T_{mc}$ (a "flow heating limited" condition) [148]. The behaviour is slightly more complex than this picture, since increasing the circulation rate by increasing $T_{still}$ will also increase the load on the mixing chamber, but such a change would not be expected to be large. Essentially, this implies that there will be an optimum circulation rate that minimises the mixing chamber base temperature for a given heat load, which will in turn depend on the design of the DR.

The cooling capacity of the mixing chamber is shown in Fig. 5.7 for the $\dot{Q}_{mc}$ range 0–100 $\mu$W, and in Fig. 5.8 for 0–400 $\mu$W. In both plots, the capacity was measured for two values of power input on the still, $\dot{Q}_{still}$. Since the power input at the still affects the circulation rate, it would be expected that a greater power input would give more cooling power on the mixing chamber due to the increased flow (up to a point, as discussed above), as is seen in this data.

The requirement that the mixing chamber provide a cooling capacity of 30 $\mu$W at 65 mK is easily met (with 14 mW input on the still, the mixing chamber has $>$80 $\mu$W capacity at 65 mK). The capacity of the mixing chamber at $\sim$120 mK was 400 $\mu$W compared to a specification of 500 $\mu$W capacity at that temperature.

As discussed in § 4.1, the cooling capacity of a dilution refrigerator, $\dot{Q}_{mc}$, at mixing chamber temperature $T_{mc}$ and with $^3$He throughput $\dot{n}_3$ is given by Eq. (4.14). The total cooling capacity is equal to the applied electrical heat, $\dot{Q}_{Elec}$, plus the permanently present heat leak, $\dot{Q}_{Leak}$, so that

$$\dot{Q}_{mc} = \dot{Q}_{Elec} + \dot{Q}_{Leak} = 12\dot{n}_3 t, \tag{5.1}$$

where

$$t = 8T_{mc}^2 - T_n^2. \tag{5.2}$$

As in Eq. (4.14), $T_n$ in Eq. (5.2) is the temperature of the helium streaming into the mixing chamber. A linear fit to a plot of the applied electrical power, $\dot{Q}_{Elec}$, as a function of $t$ would allow the $^3$He circulation rate and the magnitude of $\dot{Q}_{Leak}$ to be

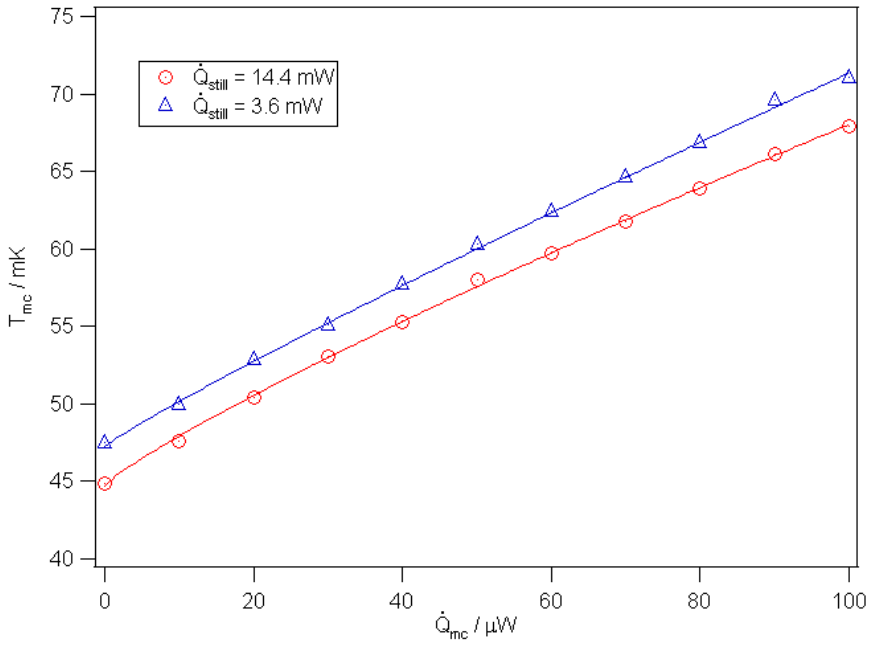


**Figure 5.7:** Measured cooling capacity of the mixing chamber, with applied loads of 0–100 $\mu$W. Data is shown for two different values of $\dot{Q}_{still}$, with a greater still heat load giving a higher circulation rate, and therefore a greater cooling capacity.

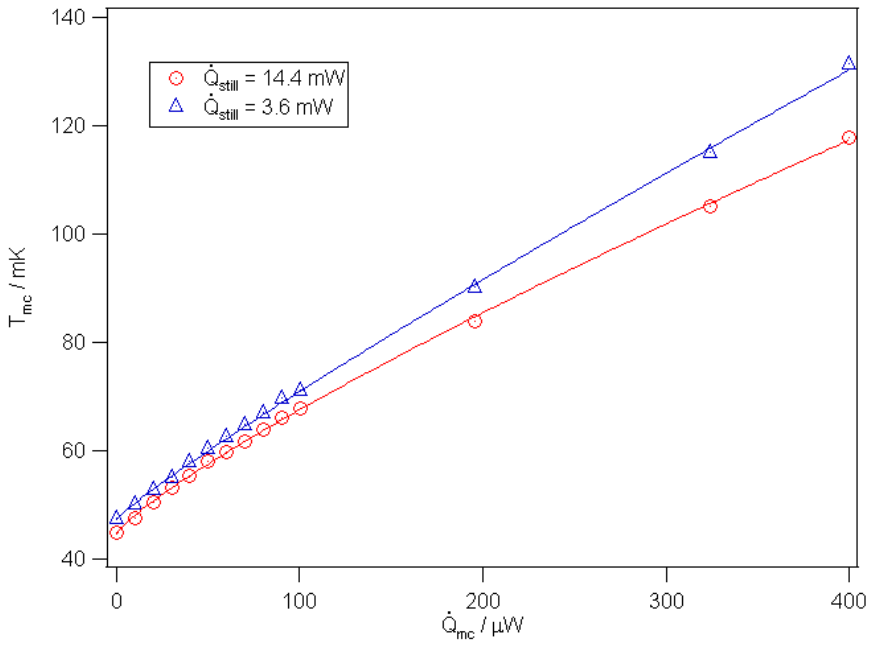


**Figure 5.8:** Measured cooling capacity of the mixing chamber, with applied loads of 0–400 $\mu$W. Data is shown for the two $\dot{Q}_{still}$ values in Fig. 5.7.

recovered from the gradient and intercept of the fitted function. Strictly, this analysis requires knowledge of the value of $T_n$ as well as $T_{mc}$, which is unavailable. However, we know that $T_n$ must be in the range $T_{mc} \leq T_n \leq \sqrt{8}\,T_{mc}$ from the discussion in §4.1, where the lower limit implies perfect precooling of the instreaming helium to the mixing chamber temperature. The upper limit is the case for no available cooling power on the mixing chamber after balancing the heat leak. This assumption is applied to the data plotted in Fig. 5.9. Although characterisation measurements of the mixing chamber capacity were generally made over the range 0–100 $\mu$W of applied power, the parameter $t$ is plotted for powers up to 50 $\mu$W only, since at higher power the measured flow rate was observed to change. This would result in the data deviating from the linear relationship in Eq. (5.1), since the flow rate is no longer constant. Furthermore, the derivation of the cooling power of the dilution process in Eqs. (4.12) and (4.14) use functions describing the enthalpy of the $^3$He and helium mixtures that are only valid at temperatures $\sim$ 60 mK and below. At higher applied powers, and therefore higher temperatures, the theoretical performance relationships begin to break down. The lines are linear fits to the data; the linear dependance is expected from Eq. (5.1). For the limit $T_n = T_{mc}$, a circulation rate of $(444 \pm 5)$ $\mu$mol/s and $\dot{Q}_{Leak} = (75 \pm 1)$ $\mu$W are recovered. For the limit $T_n = \sqrt{8}\,T_{mc}$, the same value of $\dot{Q}_{Leak}$ is found, with $\dot{n}_3 = (602 \pm 8)$ $\mu$mol/s. The intermediate case, with $T_n = 2T_{mc}$, $\dot{n}_3 = (518 \pm 6)$ $\mu$mol/s.

From the measured circulation rate as a function of still heater power (Fig. 5.5), the applied $\dot{Q}_{Still}$ of 14 mW gives a flow rate of 620 $\mu$mol/s. It is important to note that the measured flow rate will be the total flow of $^3$He and $^4$He, while the flow rates recovered from the method above will be the flow of $^3$He only, since the $^4$He flow contributes nothing to the available cooling power from dilution in the mixing chamber. Allowing for a few percent of the measured flow to be $^4$He, a ratio consistent with the vapour pressures of the two isotopes at $T_{still}$ (see Fig. 5.4 and associated discussion), the estimated $^3$He flow rate reduces to $\sim$600 $\mu$mol/s. This is more consistent with the recovered $\dot{n}_3$ value for the case $T_n = \sqrt{8}\,T_{mc}$. The value for the lower limit of $T_n$ implies a $\dot{n}_3$ value which is too low in comparison to the measured flow rates. This would imply that the temperature of the instreaming helium is close to the maximum limit of the temperature range, a result of poor heat exchange in the circuit.

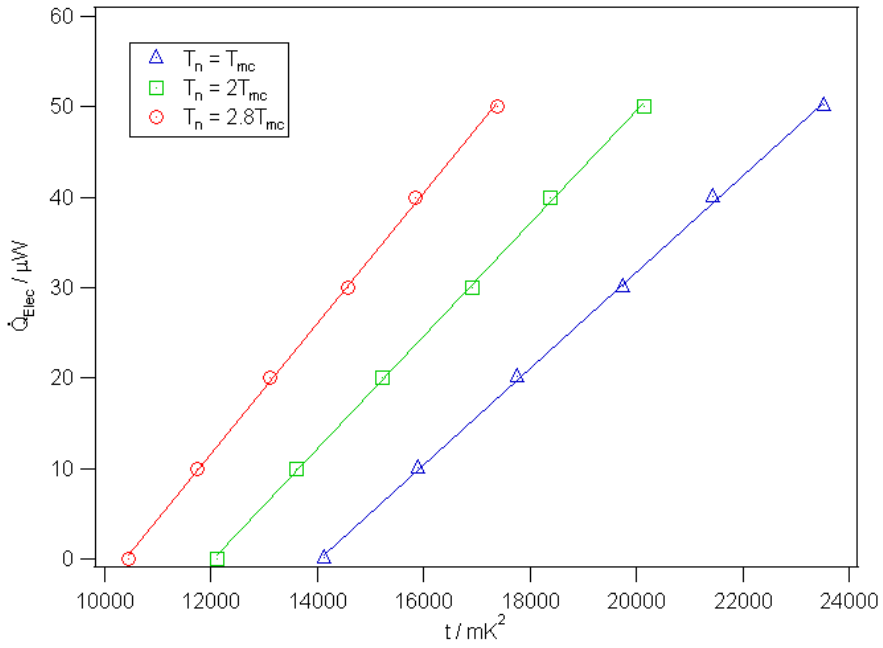


**Figure 5.9:** Cooling capacity of the dilution refrigerator as a function of the mixing chamber temperature and the $^3$He input temperature. For details, see text.

The magnitude of $\dot{Q}_{Leak}$ is very large. However, if we consider the nominal cooling capacity of a conventional MNK126-500 dilution refrigerator as published by Leiden Cryogenics (Fig. 5.10), a heat load of ∼75 $\mu$W equates to a temperature of ∼45 mK, which is consistent with the measured base temperature of this DR. The implication is that the value of $\dot{Q}_{Leak}$ is consistent with the measured performance figures.

A number of sources may contribute to the heat leak onto the mixing chamber. Some heat will be conducted from the higher temperature stages through the structure of the fridge. With the still in this DR operating at an elevated temperature in comparison to an ideal system, the level of conduction will be increased, but would still be expected to be at a low level due to the low thermal conductivities of the materials used in the fridge construction. Similarly, any accidental shorts to higher temperature or conduction through wiring would be expected to be at a low level. A potential major contributor to the background heat leak would be the presence of a quantity of $^4$He in the circulating mixture. As discussed previously, the elevated still temperature in this DR will increase the quantity of $^4$He in the mixture according to the ratio of the isotope vapour pressures

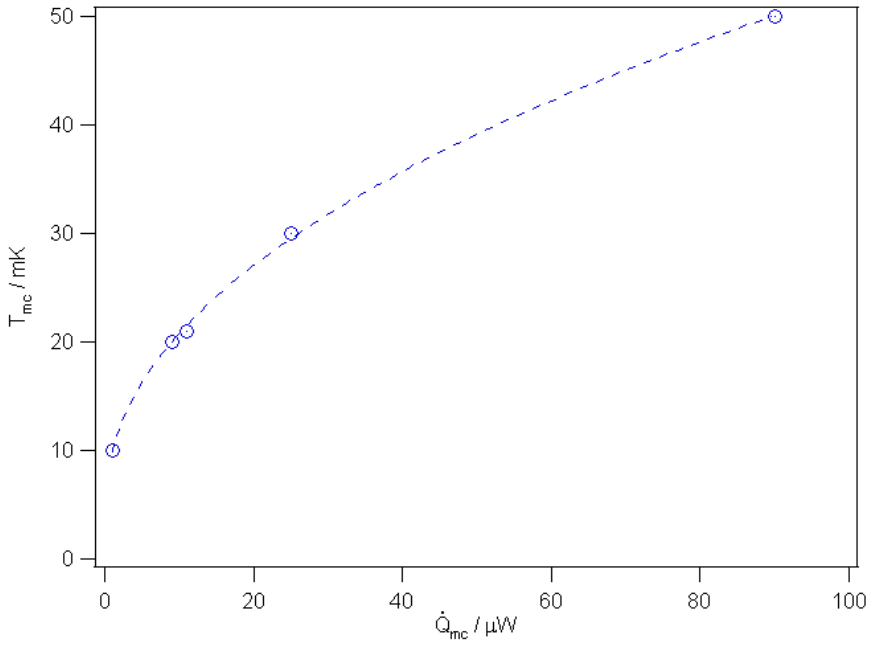


**Figure 5.10:** Published nominal cooling capacity of a Leiden Cryogenics MNK126-500 dilution refrigerator.

at $T_{still}$. While circulation of $^4$He contributes nothing to the available cooling power, removing the enthalpy of the $^4$He will degrade the performance of heat exchangers, and ultimately place additional load on the mixing chamber since the $^4$He must be cooled from the inlet temperature $T_n$ to $T_{mc}$. Note that the cooling of the $^3$He is already accounted for in the enthalpy balance when deriving the theoretical cooling power in Eq. (4.14).

A potential further source of heating in a DR is from mechanical vibration coupled to the mixing chamber. This may be a particular issue for a dry DR as a consequence of vibration associated with the mechanical cooler. Some work on the magnitude of the vibrational heat leak from cryocoolers has been described in the work on dry DRs by Uhlig, who reported heat leaks of up to 10 $\mu$W using Gifford-McMahon coolers [133]. Later work to improve vibration isolation of the cold head with bellows and flexible wicking reduced this vibration loading to 0.14 $\mu$W [136]. One of the advantages of pulse tube coolers over GM type is reduced vibration, although vibration is certainly not entirely eliminated. Later work by Uhlig with pulse tube cryocoolers indicated

heat leaks onto the mixing chamber of 75 nW [139]. It is important to note that the cryostats of Uhlig incorporated vibration isolation provisions to reduce the amplitude of vibration driven by the cold heads, while the SCUBA-2 DR does not. It is entirely feasible that vibrational heating contributes to the measured internal heat leak on the mixing chamber at the $\mu$W level.

Although it is difficult to draw any firm conclusions as to the cause or causes of the mixing chamber heat leak determined from this work, it is possible to infer some information as to the relative contributions of the discussed mechanisms. With the system in discontinuous operation (so-called "single shotting", with the return supply of $^3$He cut off from the concentrated phase), it was observed that only minimal cooling of the mixing chamber occurred. In a DR, it would be expected that the heat load on the mixing chamber is dominated by cooling of the circulating mixture. Therefore, when the return mixture supply is removed, the load on the mixing chamber will be greatly reduced and $T_{mc}$ will approach the theoretical minimum temperature for the $^3$He flow rate (as described by Eq. (4.12)). Given the minimal degree of cooling observed with the SCUBA-2 DR, it would imply that the load on the mixing chamber is dominated by another mechanism. Two of the discussed mechanisms, vibration and conduction, will still be present in continuous operation (although conduction would be slightly reduced since $T_{still}$ also reduces slightly in this operating mode). The implication of this observation is that the value of $\dot{Q}_{Leak}$ is dominated by either vibrational heating or the conduction load. Some investigation of fitting vibration isolation to the system was investigated, although with limited success, and is discussed in §5.6.

The data presented and discussed in this section represents the baseline performance for the dilution refrigerator. A key feature of these measurements is the implication that the performance of the DR is dominated by the elevated temperature at the output of the JT stage, and the apparent large background heat leak on the mixing chamber. The measured still temperatures are higher than would be expected in a conventional dilution refrigerator (generally $\sim$0.7 K with electrical heating, falling to $\sim$0.4 K with no applied heat [121]). The elevated still temperature would be consistent with greatly increased load due to the cooling and condensation of the relatively warm $^3$He outflowing from the JT stage.

## 5.5 Temperature Stability

The stability of the various temperature stages in the DR was explored using timestream data from the thermometers distributed through the system. A timestream was recorded at a sampling frequency of 10 Hz (this is the sampling frequency of the LS370 AC resistance bridge used to readout the sensor values, and is therefore the highest resolution possible) for a period (typically 5 minutes), and then Fourier transformed to produce a power spectrum.

The temperature of the second stage of the PTC is expected to show a periodic oscillation due to the cyclic nature of the cooling effect. The pressure wave in the PTC oscillates at a frequency of 1.4Hz. The pressure oscillation also causes a periodic elastic deformation of the stainless steel tubing, which is the main source of vibration from a PTC. The timestream data for the PTC second stage is shown in Fig. 5.11. The periodic oscillation may be clearly seen, with a peak-peak value of 75 mK. Although rigourous measurements were not carried out, the peak-peak variation was found to have some dependency on the second stage loading. With 0.25 W of additional applied power, the peak-peak variation was found to increase to 86 mK. These values are lower than measurements of the temperature stability of the lower cooling capacity Cryomech PT405 (0.5 W at 4.2 K), found to be 150mK peak-peak [138]. The power spectrum of this timestream, depicted in Fig. 5.12, shows the prominent feature at $\sim$1.4 Hz. Also present, although of smaller amplitude, are features at $\sim$0.3 Hz, $\sim$0.9 Hz and $\sim$2.1 Hz, with a series of smaller amplitude peaks up to 5 Hz. These features could be vibrational in origin as a result of the PTC oscillation driving other components in the insert. The oscillation of the PTC second stage temperature was also prominent in the timestream for the second stage plate of the DR insert, although the peak-peak variation is reduced to 18 mK. This is the result of the damping induced by the time constant of the joint between the PTC and the plate. The same was true for the input to the JT heat exchanger, although again the amplitude was reduced. The power spectrum of the second stage plate timestream (Fig. 5.13) shows the same discrete features as for the PTC, although the $\sim$1.4 Hz feature is at depressed amplitude.

The temperature at the input to the Joule-Thomson stage is coupled to the second stage plate, and show the same features at similar amplitude. The second trace in

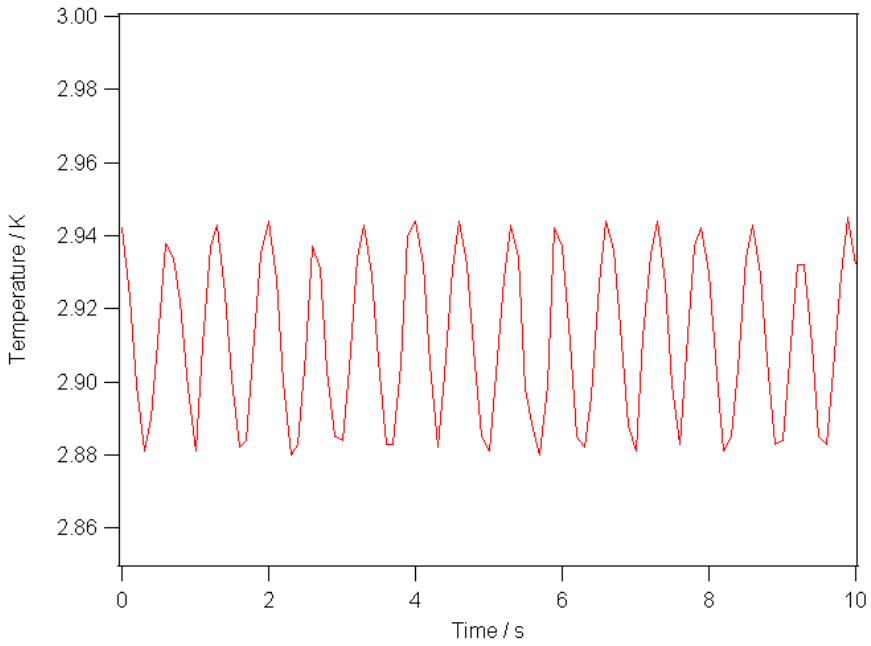


**Figure 5.11:** 10 second timestream of PTC second stage temperature.

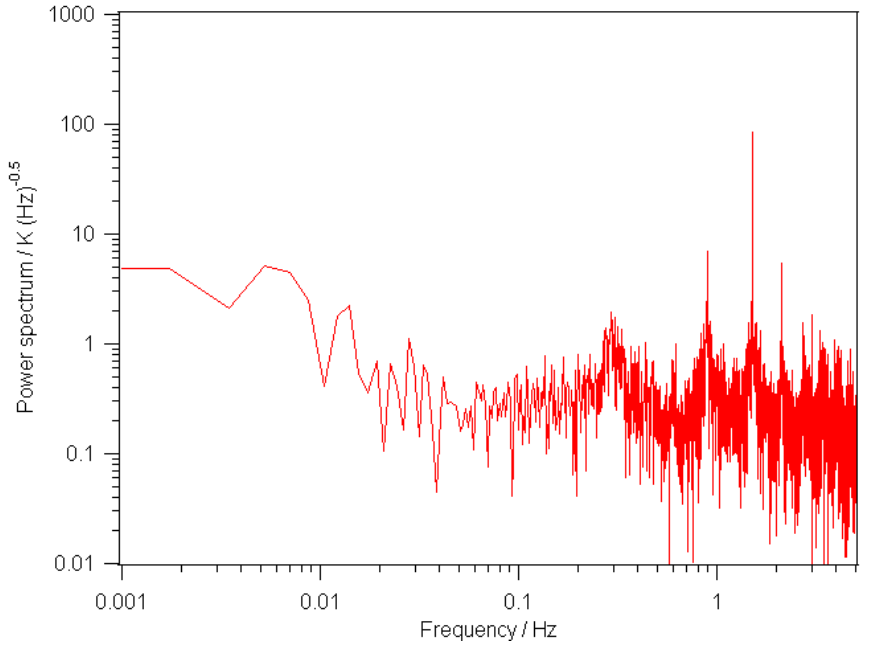


**Figure 5.12:** Power spectrum of PTC second stage temperature timestream.

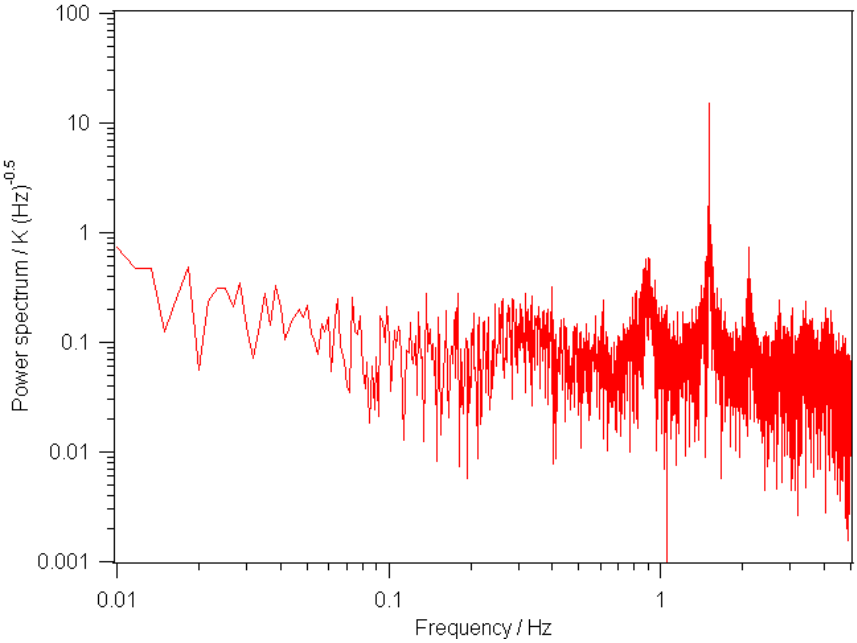


**Figure 5.13:** Power spectrum of DR second stage temperature timestream.

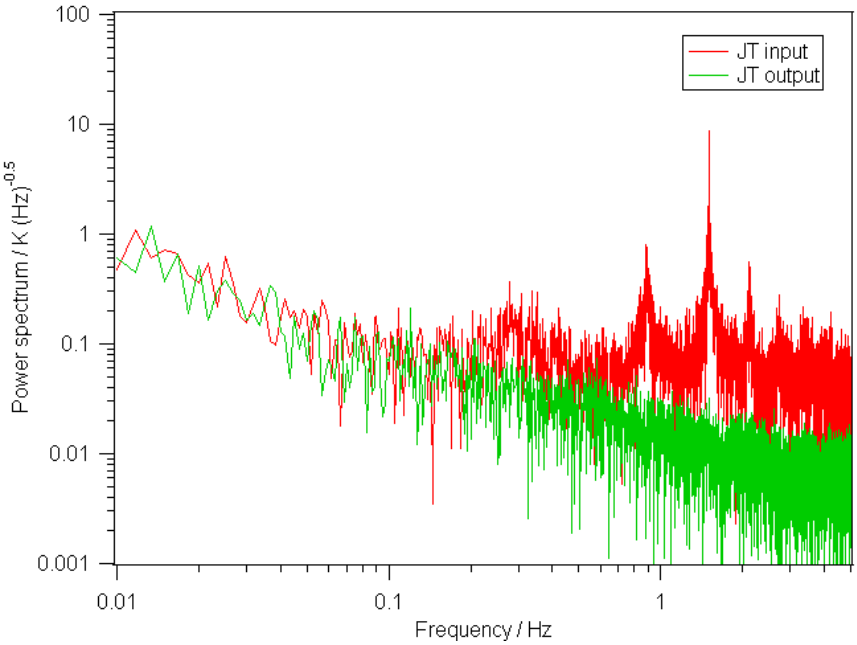


**Figure 5.14:** Power spectra of Joule-Thomson stage input and output temperatures.

Fig. 5.14 shows the power spectrum for the temperature of the output to the JT stage. Both spectra have similar profiles at low frequency (<0.1 Hz), but the output does not show the discrete frequencies associated with the PTC second stage that are present at the JT input. In addition, the floor of the output spectrum is approximately an order of magnitude lower above 1 Hz than at the input. This apparent stability at the JT output may be explained by the differences between the cooling processes at the input and output. While the cooling at the input is cyclic, since the input to the heat exchanger is coupled to the PTC, the output temperature is governed by the flow of gas through the heat exchanger, which is a continuous process. Although variations in the input temperature might be expected to have some low-level effect at the output, if such effects are present they are dominated by the $1/f$ profile in the power spectrum.

The temperature timestream for the still depicted in Fig. 5.15 shows considerable instability. It should be noted that the sample of the timestream in Fig. 5.15 is 100 seconds in length, whereas previous plots were only 10 seconds in length. The still temperature shows prominent longer period variations that are absent at the higher temperature stages. The Fourier transform of this timestream (Fig. 5.16) shows a $1/f$-type profile extending beyond 5 Hz, with no discrete features. The origin of these instabilities is not clear, although the variation could be the result of thermodynamic effects such as convection in the superfluid column between the mixing chamber and still. The mixing chamber temperature (Fig. 5.17) shows broadly similar variations to that on the still, indicating that the mixing chamber temperature is sensitive to the temperature of the still due to the effect on the instreaming $^3$He gas temperature.

There is a discrete signal at $\sim$ 1.4 Hz in the power spectrum of the mixing chamber. This feature appears to be associated with the PTC, and was first observed on the detector arrays themselves.

The mixing chamber temperature over a period of $\sim$8 hours is shown in Fig. 5.18, illustrating the long term stability of $T_{mc}$. The temperature exhibits a maximum peak-peak variation of 1.4 mK over this period. Such long period fluctuations are common in dilution refrigerators due to small variations in the $^3$He circulation rate, but can be smoothed using closed-loop temperature control. This technique was implemented for the DR during later cooldowns.

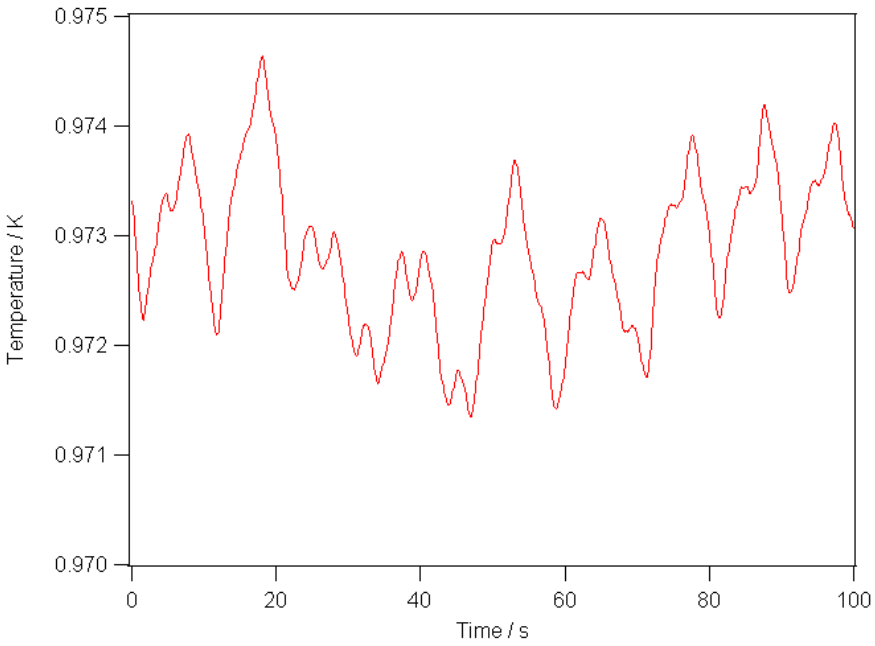


**Figure 5.15:** 100 second timestream of still temperature.

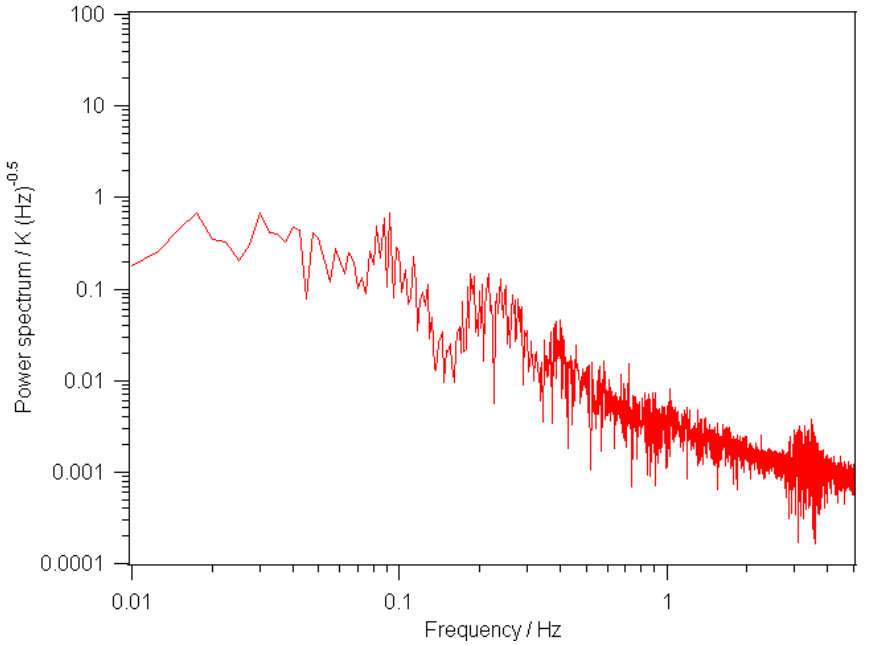


**Figure 5.16:** Power spectrum of still temperature timestream.

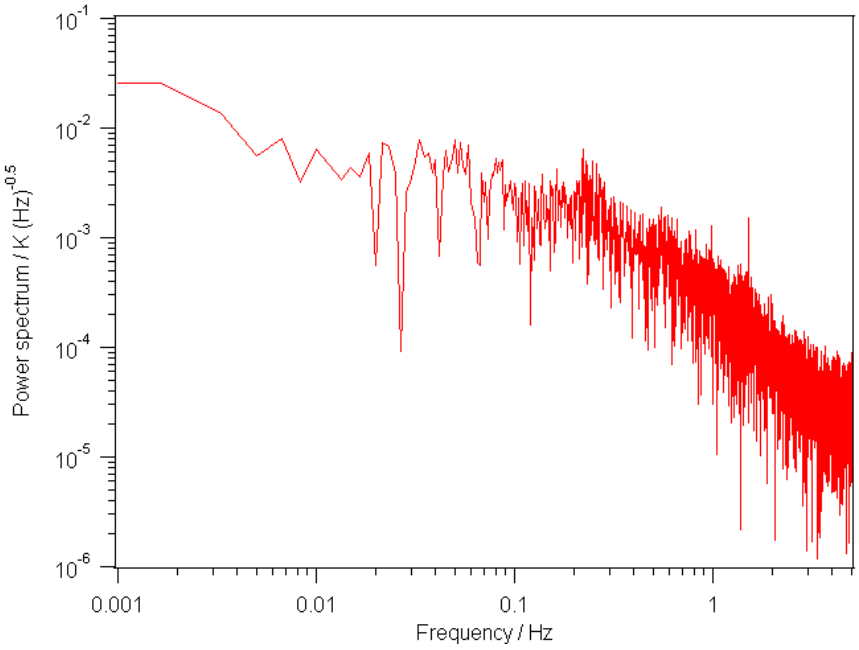


**Figure 5.17:** Power spectrum of mixing chamber temperature timestream.

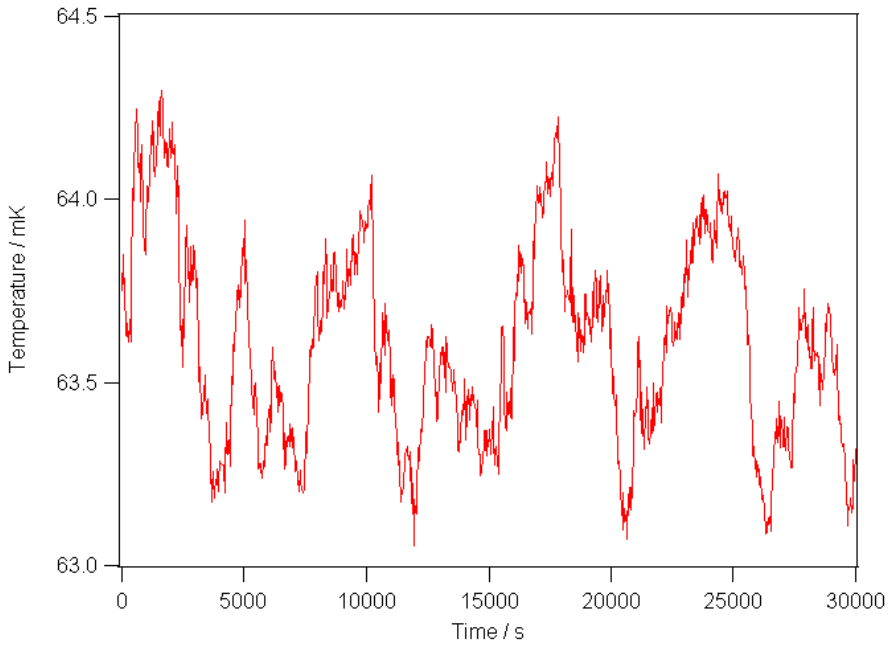


**Figure 5.18:** Stability of the DR mixing chamber temperature over a period of approximately 8 hours.

## 5.6 Cold head Replacement

During later detector testing in the instrument cryostat, a noise feature was identified at a discrete frequency of ∼1.4 Hz. This is the same frequency as the pressure oscillation in the pulse tube cooler, implying that the two oscillations were connected. Two possible mechanisms were identified for the detector noise feature. The first was microphonic, with the elastic deformation of the PTC regenerator and pulse tube due to the pressure oscillation causing vibration on the mixing chamber that was then transmitted to the focal planes. The second mechanism was the temperature oscillation on the PTC second stage causing an oscillation at the same frequency on the mixing chamber and hence on the detectors themselves. Investigation of the noise feature did not provide any strong evidence to support one mechanism over the other.

An identified possible solution was rework of the interfaces between the PTC and DR insert plates to include flexible wicks in place of the existing hard contact. This would serve to provide some isolation of the DR from the elastic deformation of the PTC tubes. Furthermore, the additional interfaces would reduce the conductance of the link, lessening the effect from temperature oscillations of the PTC on the second stage plate. The interface between the PTC cold head and the insert was such that the necessary changes to accommodate flexible wicks (raising the pulse tube cold head) could not be carried out due to a clash with a flange on the top of the still pumping tube. To overcome this, the original PT410 cold head was substitute for a newer "remote motor" (RM) cold head, with a reduced profile above the vacuum flange. The new cold head design separates the valve motor from the top of the regenerator and pulse tubes in order to reduce the transmission of high frequency vibration from the motor to the cold finger. It was not believed that high frequency vibration was being transmitted to the cold stages in the DR insert, so this feature was superfluous and simply a way to overcome the interface problems[1].

As part of the determination of the feasibility of these modifications, the effect of a higher second stage temperature on the mixing chamber temperature was investigated during INS_CD7. Heat was applied to the second stage plate during normal circulation,

[1]Other accessories to isolate the PTC cold head from the experiment are available from Cryomech, but these could not be interfaced to the DR insert.

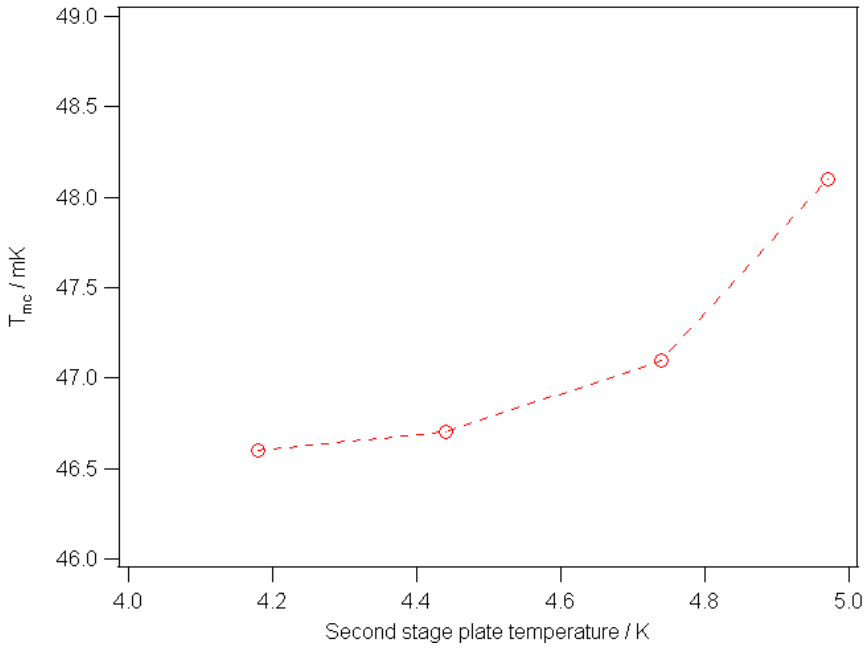


**Figure 5.19:** Mixing chamber temperature as a function of elevated second stage plate temperature.

and $T_{mc}$ measured. These measurements are depicted in Fig. 5.19. The measurements indicate that the change in $T_{mc}$ is negligible even if the second stage temperature is increased to ∼5 K. Taking this as the maximum allowable temperature for operation and assuming a typical temperature of 3.6 K on the second stage of the PTC, an upper limit of 1.4 K for the temperature drop along the PTC wick is obtained.

### 5.6.1 Wick Design

The design of the flexible wicks was complicated by the need to fit within the footprint of the existing interfaces. The outline design for both wicks was comprised of six flexible sections bolted to an interface plate. The interface plate would then be bolted to the existing faces. The six parallel links were intended to maximise the cross-sectional area of material through the wick assembly. Although this approach introduced two additional bolted contacts on each interface, the intermediate plates allowed the contacts to the flexible sections to be designed to maximise the contact force by using more bolts than would be possible if the flexible sections contacted directly to the original faces.

**Figure 5.20:** Flexible thermal wicks for the dilution refrigerator pulse tube cooler. The first stage wick is on the left, with the second stage wick on the right. See text for details.

The completed wicks are shown in Fig. 5.20. The interface plates for the first stage wick consist of a 10 mm thick annulus of 135 mm outside diameter and 95 mm inside diameter, allowing the second stage pulse tube and regenerator of the PTC to pass through the wick. The interface components are manufactured from commercial electrolytic tough pitch (ETP) copper, and gold plated. The flexible links are of 5N (99.999% pure) copper foil, also gold plated, and diffusion bonded at the ends to form a solid section for the bolted contact. The links are 50 mm in length, with 15 0.1 mm thick foils in each link. Contacts to the interface plates are made with two M4 screws per joint. A stainless steel plate is used under the screw heads to clamp the foil to the interface plate. The flexible links for the second stage wick are identical. The interface plates are 10 mm thick gold plated copper discs with a diameter of 98 mm. The wick performance was predicted from thermal modelling, described below, before the design was finalised and the components manufactured.

### 5.6.2 Thermal Model

The performance of the modified DR was expected to be dominated by the performance of the wick to the second stage of the PTC. The behaviour of this wick was modelled using the same approach as for the models of the overall instrument cryogenic design. The thermal modelling process is discussed in more detail in Chapter 6. The temperature drop across each stage of the wick is dependant on the conductance of the contact or link. The conductance of contacts has been measured by a number of groups in different temperature ranges. The data used for this modelling came from Refs. [149,150]. To account for increased conductance across a joint with large surface area and better clamping force than the samples measured, the modelled conductances are scaled. In this model, $\alpha$ is the scaling factor for the contacts between the foil sections and interface plates, and $\beta$ the scaling factor for the interface plates to the PTC cold finger and DR insert plate. The temperature drop across each stage was explored for different values of $\beta$, and for wicks of 15 and 20 foils. The joints between the foil sections and the interface plates are broadly similar to the joints measured in the referenced papers, so the value of $\alpha$ was not initially varied since no improvement was expected. Fig. 5.21 shows a block diagram of the input model, with the various contacts comprising the wick assembly indicated. In this model, there is assumed to be a negligible temperature gradient along the bulk components comprising the wick assembly, so the temperature drop is calculated for the four contacts and along the foil link sections. Strap 1 is one of six identical links; the power flowing across the contacts and along S1 is adjusted appropriately to account for this.

The model used a cooling curve profile based on measurements of the PTC performance during DRF_CD13, and an estimated load of 0.5W (in addition to the background load). Although the stated performance of the RM PTC was >90% of the standard version, modelling the performance based on the standard PTC was considered sufficiently accurate.

The model outputs for $\alpha = 1$ are shown in Table 5.5. From these results, it is apparent that the temperature profile is not strongly dependant on the number of foils, since in both cases there is only a small temperature drop along the link. The performance of the wick is dominated by the conductance of the bolted contacts. The

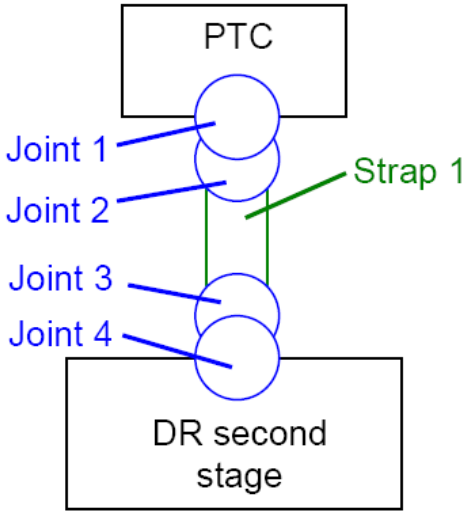


**Figure 5.21:** Block diagram for the pulse tube cooler wick thermal model.

first set of model outputs with $\beta = 1$ represents a worst case limit in which there is no improvement in the joints due to the large contact area between the interface plates and the existing structures. For this parameter value, the $\Delta T$ is too large. A small enhancement in these joints ($\beta = 2$) brings the $\Delta T$ much closer to the specification. Hence, assuming that it is not possible to improve the joints to the foil wicks, the required $\Delta T$ may be achieved by careful assembly of the joints between the interface plates and the PTC and DR plate.

For completeness, the modelling was repeated for the same values of $\beta$, but with $\alpha = 2$. The model outputs are listed in Table 5.6 using $n = 15$. Comparing the two sets of data, it may be seen that the model outputs are less sensitive to changes in $\alpha$ than to $\beta$. This is as expected, since less power passes through the joints J2 and J3 than J1 and J4 to account for the multiple links.

The modelling results indicated that the wick design should have a sufficiently small $\Delta T$ for the DR to operate with negligible change in the mixing chamber base temperature.

**Table 5.5:** Thermal model outputs for $\alpha = 1$. For the components J1–J4 and S1, the listed figure is the temperature of the warm side of the joint or link. For each $\beta$ value, results are listed for two values of $n$, the number of foils in the flexible links.

| | $\beta = 1$ | | $\beta = 2$ | | $\beta = 5$ | | $\beta = 10$ | |
|---|---|---|---|---|---|---|---|---|
| | $n$=15 | $n$=20 | $n$=15 | $n$=20 | $n$=15 | $n$=20 | $n$=15 | $n$=20 |
| PTC2 | 3.668 | 3.668 | 3.668 | 3.668 | 3.668 | 3.668 | 3.668 | 3.668 |
| J1 | 5.0091 | 5.0091 | 4.3898 | 4.3898 | 3.9723 | 3.9723 | 3.8231 | 3.8231 |
| J2 | 5.1985 | 5.1985 | 4.6046 | 4.6046 | 4.2085 | 4.2085 | 4.0679 | 4.0679 |
| S1 | 5.217 | 5.2124 | 4.6254 | 4.6202 | 4.2312 | 4.2255 | 4.0913 | 4.0855 |
| J3 | 5.3992 | 5.3947 | 4.8298 | 4.8248 | 4.4536 | 4.4482 | 4.321 | 4.3154 |
| J4 | 6.3884 | 6.3846 | 5.3991 | 5.3947 | 4.7077 | 4.7026 | 4.4536 | 4.4482 |
| $\Delta T$ | 2.7204 | 2.7166 | 1.7311 | 1.7267 | 1.0397 | 1.0346 | 0.7856 | 0.7802 |

**Table 5.6:** Thermal model outputs for $\alpha = 2$. As in Table 5.5, the temperatures are for the warm side of the joint or link. All results use $n = 15$.

| | $\beta = 1$ | $\beta = 2$ | $\beta = 5$ | $\beta = 10$ |
|---|---|---|---|---|
| PTC2 | 3.668 | 3.668 | 3.668 | 3.668 |
| J1 | 5.0091 | 4.3898 | 3.9723 | 3.8231 |
| J2 | 5.1047 | 4.4985 | 4.0921 | 3.9474 |
| S1 | 5.1235 | 4.5198 | 4.1154 | 3.9715 |
| J3 | 5.217 | 4.6254 | 4.2311 | 4.0913 |
| J4 | 6.2349 | 5.2169 | 4.4978 | 4.2311 |
| $\Delta T$ | 2.5669 | 1.5489 | 0.8298 | 0.5631 |

### 5.6.3 Test Results

Work with the remote motor PTC and flexible wicks was carried out between 28-03-2007 and 09-07-2007 during 9 cooldowns.

An issue with the rigidity of the DR insert with the flexible wicks installed was identified. Previously, the first and second stage plates of the insert were supported by both the still pumping tube and the cold stages of the PTC. However, with the flexible wicks fitted, the pumping tube did not have sufficient stiffness to support the plates, particularly with the radiation shields attached.

At the completion of the first precool, measurements of the cooling capacity of the new PTC were taken for comparison to the standard cold head. This comparison is depicted in Fig. 5.22. There is a small measurable difference between the capacities of the two coolers, as expected from information provided by Cryomech. The measured temperature difference between the second stage of the PTC and the second stage plate was $\sim 1$ K, which is consistent with the predicted performance.

Initial attempts to condense and circulate the helium mash resulted in an elevated base temperature of 90 mK during DRF_CD17 and CD18. It was suspected at first that the reduced rigidity of the insert discussed above was allowing a level of vibrational heating of the mixing chamber, even with the flexible wicks. Although early leak checking after a system failure during INS_CD7 (causing an over pressure and loss of mixture) had been negative, another possibility was that there had been some loss of mixture. On recovery of the mash, this proved to be correct, although it was not possible to establish the presence of a leak (at room temperature or cold) other than the loss of mixture. In a series of runs to investigate other aspects of the DR behaviour, the RM PTC was replaced with the standard cold head. During these cooldowns, the DR was operated successfully with base temperatures $<$60 mK.

The RM cold head was refitted for DRF_CD22. Performance on the second stage consistent with the earlier cooldowns was observed, but the DR achieved a base temperature of only 120 mK. Again, vibrational heating was identified as a possible cause. An analysis of time series data from the mixing chamber thermometry in this state, as shown in Fig. 5.23, shows broad, large amplitude features in the power spectrum at $\sim$0.12 Hz and $\sim$0.26 Hz. The second trace in Fig. 5.23 shows the power spectrum for the

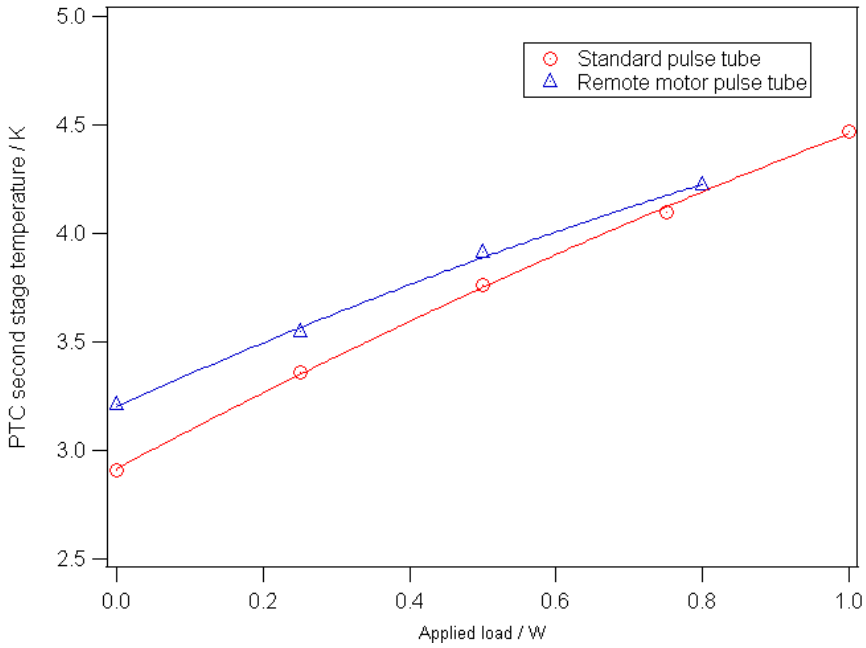


**Figure 5.22:** Cooling capacity of remote motor and conventional PT410 pulse tube coolers.

mixing chamber during DRF_CD14 with the standard PT410 cold head for comparison. The only distinct feature in the spectrum for the standard cold head is the signal at 1.4 Hz, although the $1/f$ profile is at a higher amplitude over most of the frequency range. The presence of the broad features in the remote motor PTC power spectrum may be the result of vibration transmitted to the mixing chamber as a consequence of the reduced rigidity of the insert, as discussed above. It should also be noted that the 1.4 Hz signal appears to be absent from the RM cold head spectrum.

Further consideration of the data from earlier runs indicated that a consistent feature of the cooldowns with both PTC cold heads was an elevated temperature on the output of the JT stage. This elevated temperature was higher for the RM PTC due to the $\Delta T$ down the wick elevating the temperature of the second stage plate and hence the input to the JT heat exchanger. The temperature at the output of the JT was $\sim$4.5 K during the RM PTC cooldowns, potentially increasing both the still and the mixing chamber temperatures. This effect was not observed during the earlier measurements of the DR performance with elevated second stage temperatures. This implies a change in the performance of the JT stage.

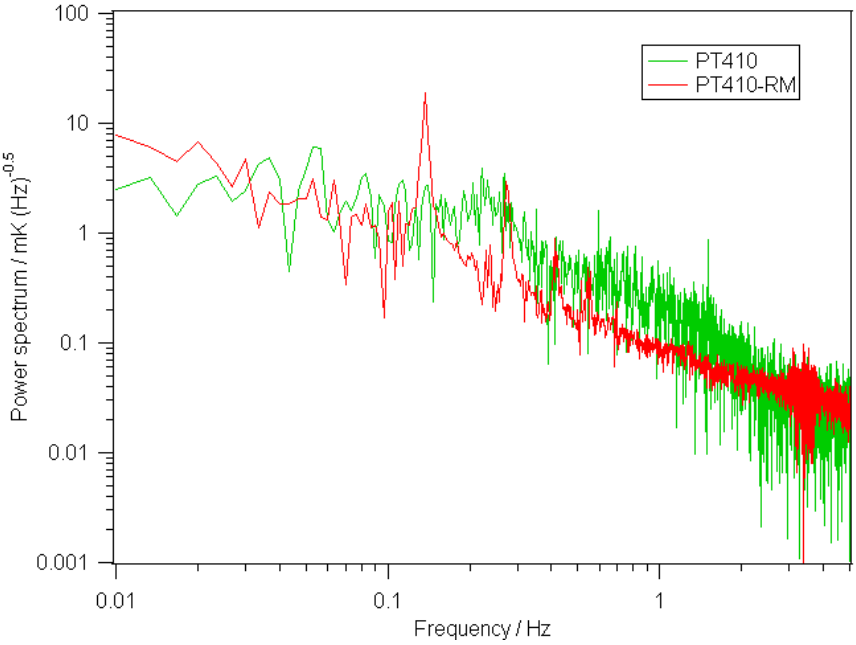


**Figure 5.23:** Power spectra comparing the stability of the mixing chamber temperature with the remote motor PTC cold head, and the standard PT410 cold head from an earlier cooldown.

Even though the cause of the elevated $T_{mc}$ values was not established conclusively, operation of the DR with the flexible wicking had not been demonstrated successfully and the work was abandoned. The RM PTC was refitted to the insert, but without the flexible wicks. It had also been observed that the quality of the original joint between the PTC and the second stage plate was not ideal due to the poor surface quality of the copper plate. Before the PTC cold head was refitted, the surface was cleaned and polished as well as possible in situ, and the 1 mm spacer plate in the joint was gold plated to further improve the contact. A final cooldown in this configuration showed that the $\Delta T$ across this joint had been reduced from 0.55 K before the contact was broken originally to 0.35 K. With adjustment of the PTC helium pressure to improve performance, the second stage of the PTC was running at 2.85 K, with the second stage plate at 3.2 K. The output of the JT stage was at 3 K, and the DR achieved a base temperature of 43 mK.

## 5.7 Summary

The performance of the SCUBA-2 DR has been measured and discussed, and was found to be sufficient for use in the instrument cryostat, although the base temperature of the DR was not as low as initially specified. The baseline performance achieved during this work was a base temperature of 44 mK, with a measured cooling capacity of 30 $\mu$W at 53 mK and 100 $\mu$W at 68 mK. This was against a specified performance of 30 $\mu$W capacity at 65 mK and a goal of 30 $\mu$W at 35 mK. Despite the elevated base temperature, the DR does meet the cooling capacity specification. The still was found to have a minimum temperature of 0.91 K, with a cooling capacity of 10 mW at 1.02 K. The measured temperatures are higher than would be expected for a conventional dilution refrigerator (the still would normally operate at 0.7 K due to electrical heating to maintain the circulation rate [121]). The specified performance of the still was a temperature of $<$0.9 K with $>$5 mW load. The measured still performance does not meet this specification.

More detailed analysis of the mixing chamber performance indicated the presence of an internal heat leak of 75 $\mu$W, which is a considerable load. Comparison with the nominal performance of a Leiden Cryogenics DR of this type indicates that the measured elevated base temperature is consistent with a heat load of this size. The origin of this heat leak is not clear, although is believed to be the result of a combination of elevated conduction loading due to the poor performance of higher temperature stages and vibrational heating from the pulse tube cooler.

The rms temperature stability of the various temperature stages in the DR was also considered, with oscillations at $\sim$1.4 Hz observed on the stages coupled to the pulse tube cooler. This oscillation is expected in the use of a PTC due to the cyclic nature of the cooling method. The lower temperature stages showed low-frequency instability with a typical $1/f$ profile.

Work to replace the pulse tube cooler with a lower vibration assembly was described, although ultimately this was only partially successful due to the large temperature difference along the thermal wicking degrading performance.

The characterisation data presented in this chapter is used as a baseline for comparison to the performance of the instrument cryostat, described in the next chapter.

# Chapter 6

# Cryogenics III: The Instrument Cryostat

This chapter describes the performance of the SCUBA-2 cryostat, with particular emphasis on the 1-K and millikelvin stages cooled by the dilution refrigerator. Performance data for each temperature stage is presented and compared to the values predicted from thermal modelling. The static thermal models for the 1-K and millikelvin stages are described and evaluated in detail. Performance data at the telescope is also described for comparison to the data collected during integration and testing.

The work described in this chapter builds on earlier work carried out during the design phase of the instrument development. Use is made of static thermal models for the cryogenic stages of the instrument, including predicted power loading and temperature distributions. This author has updated many aspects of the thermal models, particularly those for the 1-K and millikelvin stages of the cryostat, to reflect subsequent changes to the design and make the comparisons to measurement more realistic. The experimental measurements presented and analysis and model comparisons described are the work of this author.

## 6.1 Operation of the Cryostat

The cooldown of the cryostat takes places in two stages. Firstly, the precool phase cools the first and second stages of the instrument to base temperature, and the third and fourth stages to approximately 4 K. Although the cryostat is designed as a dry cryogenic system, the cool down of the large masses of the aluminium radiation shields would take a prohibitive length of time using the PTCs alone, due to the relatively low cooling power of cryocoolers at high temperatures compared to liquid cryogens. To reduce the time needed to cool the cryostat, liquid nitrogen (LN) tanks were included in the design on the 60-K and 4-K radiation shields. Cooling of the second, third and fourth stages of the cryostat to 4 K takes approximately 170 hours (7 days). LN is transferred to the precool tanks for approximately 20 hours in the early stages of the precool, using ∼400 litres of liquid. After this time, the tanks are evacuated to prevent a high conductive load on the stages from liquid or solid nitrogen. From this point, the PTCs cool the shields to base temperature. The third and fourth stages are precooled by the pulse tube cooler integral to the DR insert, with the DR heat switch providing a cooling path from the 1-K stage to the second stage of the PTC. A plot of a typical precool from ambient temperature is shown in Fig. 6.1. The curves in the plot depict the precool of the four temperature stages. In the case of the 60-K and 4-K structures, curves for the points nearest to and furthest from the interface to the PTC stages are plotted to illustrate the temperature gradient across the large structures.

Once the precool is complete, the dilution refrigerator is started following the same procedure described in Chapter 4. The main difference between the operation of the DR in the instrument cryostat is that additional heat is not supplied to the still. There is sufficient load from the 1-K stage of the cryostat to provide this power.

Since the masses sunk to the still and mixing chamber are greater in the instrument cryostat, cooling to base temperature takes longer in the instrument cryostat. A plot of the DR startup is shown in Fig. 6.2, with the temperature of the mixing chamber, still and 1-K box depicted. Cooling of the DR to base temperature takes approximately 6 hours, although the cryostat is generally allowed a further 24 hours for the components on the third and fourth stages to better thermalise.

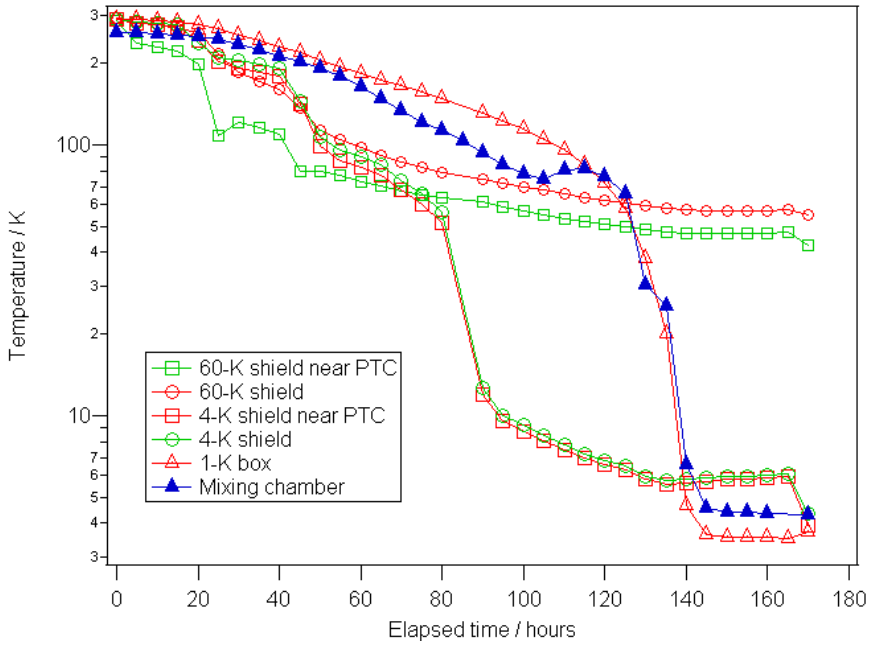


**Figure 6.1:** Graph of the cryostat cooldown from ambient to 4 K. See text for more details.

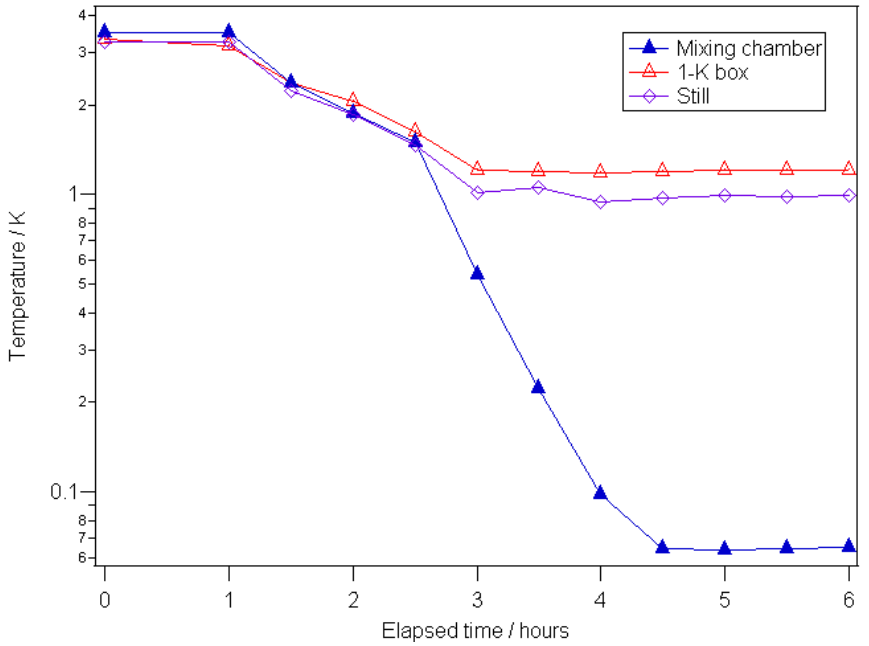


**Figure 6.2:** Graph of the cooldown of the 1-K and millikelvin stages from 4 K to base temperature. See text for more details.

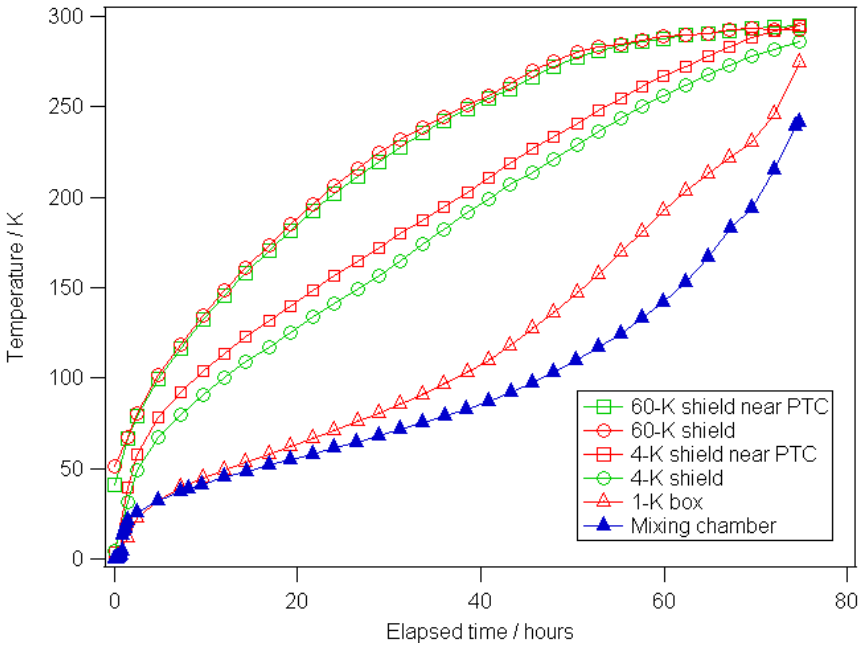


**Figure 6.3:** Graph of the warm up of the cryostat to ambient temperature.

Warm up of a dry cryostat can be achieved simply by switching off the mechanical coolers. In the case of the SCUBA-2 cryostat, heaters are fitted to the stages to increase the rate of warming. Once the helium mash is safely recovered from the DR, the PTCs are shut down and the heaters switched on. These provide 1 W of power to the millikelvin stage; 2 W to the 1-K stage; and 340 W to each of the first and second stages. Warming to ambient may be completed in approximately 70 hours. The progress of a warm up is depicted in Fig. 6.3.

Dynamic thermal models were prepared to predict the cooldown and warmup behaviour of the cryostat. It was predicted that the 4-K stage would reach base temperature in ∼66 hours, while the 1-K and millikelvin stages would cool to 4 K in ∼44 hours, and reach base temperature after a further 24 hours [94]. Warmup would be completed in 96 hours, with 300 W of power on the first stage and 200 W on the second stage. The extended cooldown time measured for the instrument in driven primarily by the time to cool the 1-K box to 4 K to allow the startup of the DR. The main cooling path for the 1-K box is through the third stage wick to the still of the DR, and then to the insert PTC through the precool link to the second stage plate. The effectiveness of the pre-

cool system is considerably less than that incorporated into the model. The increased warmup rate is the result of a greater heat input on the second stage compared to the model.

## 6.2 Thermal Modelling

An important aspect in the design of cryostats is an understanding of how heat is transferred to a stage from connected stages at higher temperature. The physical principles of heat transfer are well understood, allowing models of a cryogenic system to be constructed. Static thermal modelling is used to predict the thermal load on a stage and hence its temperature, or for modelling temperature distributions through a system. Such thermal models are used extensively in the following sections of this chapter, so the modelling process will be discussed here before proceeding. Dynamic thermal modelling may also be used to model cryostat cooldown times, however discussion here will be limited thermal modelling of steady state systems. Since cryostats operate under vacuum conditions, the effects of conduction through the gas phase may be ignored. The two heat transfer mechanisms with which we are concerned are conduction through solids and radiation.

### 6.2.1 Modelling Conduction

Models of conduction describe the power conducted through a component or a joint between two components. In general, the heat flow, $Q$, through a component of conductance $G(T)$ with one surface at a temperature $T_1$ and the second surface at a higher temperature $T_2$, is given by

$$Q = \int_{T_1}^{T_2} G(T)\mathrm{d}T. \tag{6.1}$$

For a component of cross-sectional area $A$ and length $l$, $G(T)$ is given by

$$G(T) = \frac{A}{l}\kappa(T), \tag{6.2}$$

where $\kappa(T)$ is the thermal conductivity of the material as a function of temperature, discussed in more detail below. If the temperatures $T_1$ and $T_2$ are known, then Eq. (6.1)

may be used to calculate the power flowing through the component. This may be used to predict the conduction loading on one stage of a cryostat from a higher temperature. Eq. (6.1) may also be expressed in terms of integrated thermal conductivity, $K(T)$, where

$$K(T) = \int_0^T \kappa(T)\mathrm{d}T. \tag{6.3}$$

In which instance, the heat flow is

$$Q = \frac{A}{l}\left(K(T_2) - K(T_1)\right) \tag{6.4}$$

after combining with Eq. (6.2).

Alternatively, if we wish to calculate the temperature profile for a given heat flow, then for each integral the unknown term is $T_2$, the temperature of the warm side of the component. This may be found since the integral term of Eq. (6.1) must be equal to the power flowing through a component. The temperature is found by solving Eq. (6.5) for $T_2$.

$$\int_{T_1}^{T_2} G(T)\mathrm{d}T - Q = 0. \tag{6.5}$$

Extensive tabulations for thermal conductivity values are available for many common materials. However, such measurements often extend to liquid helium temperatures only, and therefore any modelling of sub-kelvin performance must be based on specific measurement or from extrapolation from 4 K. It is also possible to estimate and extrapolate the thermal conductivity from measurements of the electrical conductivity of a sample at 4 K (the Wiedemann-Franz Law [121]). It should be noted that such extrapolation can be inaccurate, since thermal conductivity is very sensitive to impurities and defects in the sample. Furthermore, the low temperature properties of some materials which are useful, although not designed, for cryogenic use can also vary wildly from sample to sample. Many of the $\kappa$ measurements for the SCUBA-2 models were based on specific measurements made for the project. The conductivity of standard materials can be found in many texts on low temperature physics (e.g. Refs. [121, 122]), and the referenced literature therein.

The conductance of demountable joints is also difficult to predict, particularly at low temperatures. Due to the strict requirements on the performance of the third and fourth stages of the SCUBA-2 cryostat, careful consideration was given to the performance of the pressed contacts in the design. The data used for the modelling work presented herein come from measurements in Ref. [150]. The work found that the conductance of the joints around 1 K varied approximately linearly. These models used the lower end of the reported conductance range, which was 0.086 $\mathrm{WK}^{-1}$. A factor 5 increase was used for some contacts to account for the SCUBA-2 joints being larger and made with more screws than the samples tested. The temperature dependance of the joints was assumed to vary in the same way as for the joint material (ETP copper). In keeping with the work reported in Refs. [149, 150], no interposing materials were to used in the joints.

### 6.2.2 Modelling Radiation

The heat flow, $Q$, between two plane parallel surfaces of area $A$ and at temperature $T_1$ and $T_2$ due to radiation is given by

$$Q = A\epsilon\sigma \left(T_1^4 - T_2^4\right). \tag{6.6}$$

where $\epsilon$ is the emissivity of the surface, and $\sigma$ is Stefan's constant.

The emissivity of a material is dependant on the wavelength of incident radiation, and the physical state of the surface (an oxidised surface can have an emissivity 10 or more times that of a polished surface). A perfect blackbody has an emissivity of 1. Non-metallic surfaces such as glass and polymers have emissivities of $\sim$0.9. Calculations of radiation transfer between metallic surfaces are more problematic, since $\epsilon$ may be anywhere between 0.01 and 1 [120]. Most of the surfaces of interest in the thermal models discussed here are taken to be polished aluminium, with an emissivity of 0.05.

As discussed in Appendix A, a radiation shield at some intermediate temperature between ambient and the experimental volume is commonly used to decrease the heat load due to radiation. A multilayer insulation (MLI) blanket may also be used, consisting of layers of a low emissivity material such as aluminium foil or aluminised Mylar, spaced with a low thermal conductivity material (such as dacron, nylon or silk) to minimise

conduction between the layers. The effect of MLI blanket in the cryostat is incorporated as a low emissivity. Based on previous experience with instrument cryostats (specifically the widefield camera and the UIST spectrometer), the emissivity of the MLI is taken to be 0.0137. Radiation along cryogen fill pipes or wiring feedthroughs may be reduced by blackening the tubes to reduce reflections, or by using baffles.

## 6.3 First and Second Stage Performance

The performance of the four temperature stages of the instrument was modelled early in the design process. This section deals with the first and second stages of the instrument cryostat, outlining the thermal models and the predicted performance. The measured performance of the first and second stages described, and compared to the predicted performance. The modelling results for the first and second stages are taken from work carried out by D. Gostick at the design review stage [94]. The data analysis and comparison to the modelled data is work carried out by this author during the integration and verification of the instrument.

### 6.3.1 Pulse tube cooler capacity

The nominal cooling capacity of the PT410 PTCs is 1 W at 4.2 K on the second stage with 40 W at 45 K on the first stage. The variation of the cooling capacity of the two stages for modelling and comparison is available from Cryomech [143]. The cooling capacity of the first stage for loads up to 45 W is shown in Fig. 6.4. Similarly, the capacity of the second stage for loads up to 2 W is depicted in Fig. 6.5. Polynomial fits are shown for both profiles, allowing the stage temperature for a given load to be determined, or the load for a given stage temperature.

### 6.3.2 Thermal model data

The models used to predict the power loads on the first and second stages of the cryostat are summarised in the network diagrams shown in Figs. 6.6 and 6.7. The radiation and conduction loads were calculated using Eqs. (6.1–6.6). For structures such as shield supports and wiring, dimensions and materials are listed in the thermal networks. The power load due to each component is also listed. For the first stage network in Fig. 6.6,

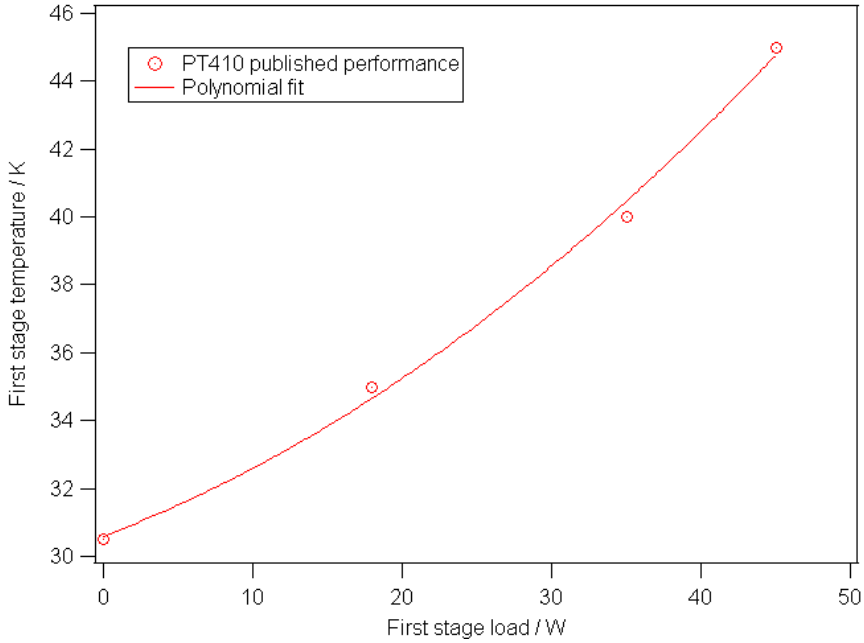


**Figure 6.4:** Cooling capacity of the first stage of the PT410 pulse tube cooler.

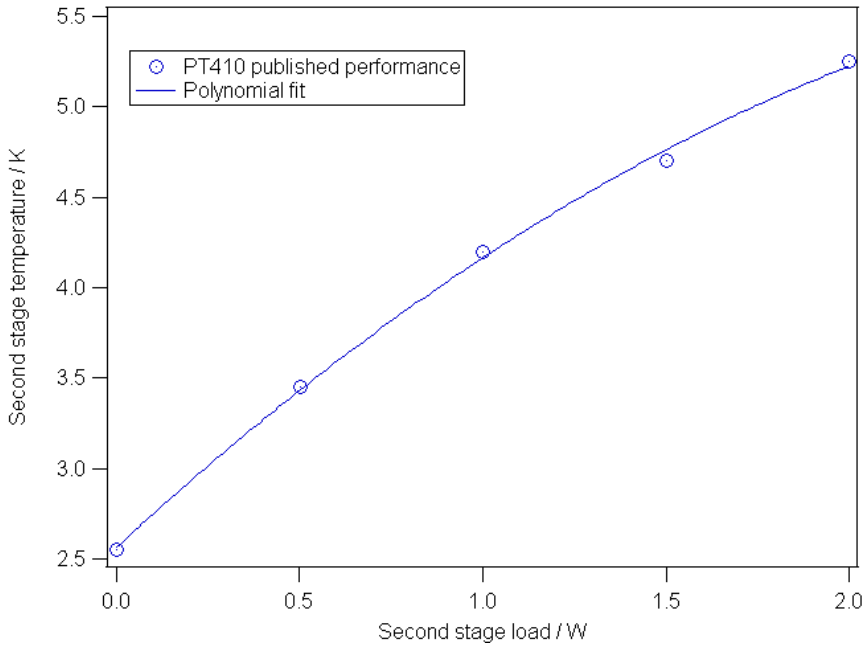


**Figure 6.5:** Cooling capacity of the second stage of the PT410 pulse tube cooler.

**Table 6.1:** Predicted thermal loads on the cryostat first (60-K) and second (4-K) stage.

| Element | Power / W | |
|---|---|---|
| | First stage | Second stage |
| Radiation | 84.9 | 1.1 |
| Radiation shield supports | 11.2 | 0.943 |
| Wiring | 1.54 | 0.5 |
| LN precool tank tubes | 0.52 | 0.032 |
| Total | 98.2 | 2.56 |

ambient temperature is taken to be 300 K, and the first stage is shown as 75 K as predicted from the model. In the second stage network, Fig. 6.7, the second stage temperature is 7.4 K.

The predicted heat loads for the first stage from the cryostat thermal models are summarised in Table 6.1. The primary contributor to the heat load on the first stage is radiation, although this is mitigated by the use of multilayer insulation blankets. The radiation contribution includes the power coming through the window. The next largest contributor is the heat leak along the G10 frames supporting the radiation shield on the vacuum vessel. The remaining load is due to the wiring and conduction along the fill tubes for the liquid nitrogen precool tanks (the tubes for the second stage tanks are sunk on the first stage to reduce the conductive load to the lower temperature stage). The total predicted load on the first stage is 98.2 W. With two PT410s providing cooling, the capacity at 60 K is approximately 100 W. The predicted base temperature of the 60-K radiation shield was 59 K, with a maximum temperature of 75 K at the furthest point.

The modelled loads for the second stage are summarised in Table 6.1. The total predicted heat load was found to be 2.56 W, against a total capacity of approximately 2.7 W at 4.5 K. The predicted heat load is primarily radiation and the heat leak along the shield supports. The second stage also provides cooling for the motor driving the cold shutter. The predicted base temperature for the 4-K shield was 5.34 K, with a maximum temperature of 7.44 K at the furthest point.

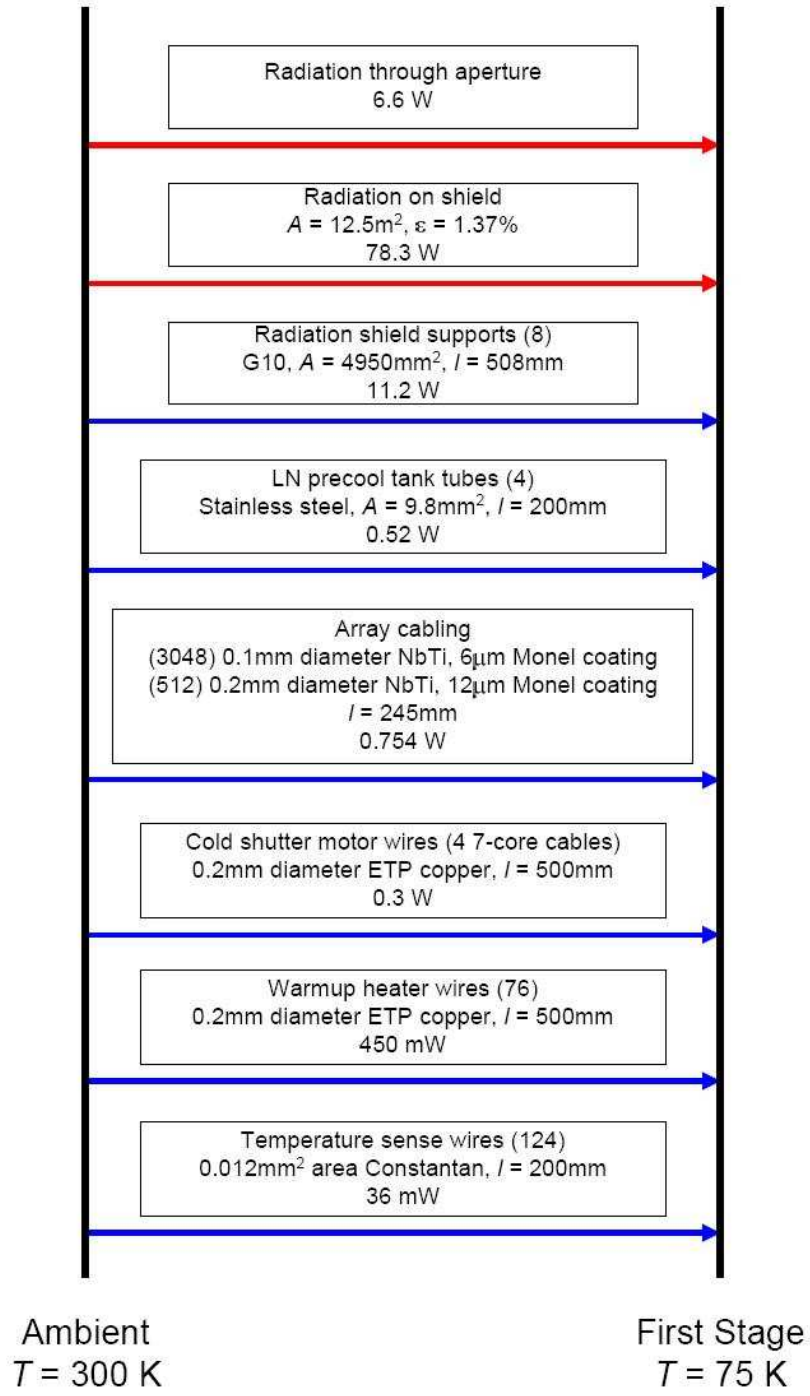


**Figure 6.6:** Network diagram summarising the inputs to the first stage thermal model. Relevant input parameters are listed for each component (area and emissivity for radiation, material and dimensions for conduction loads). The load due to each component is also listed.

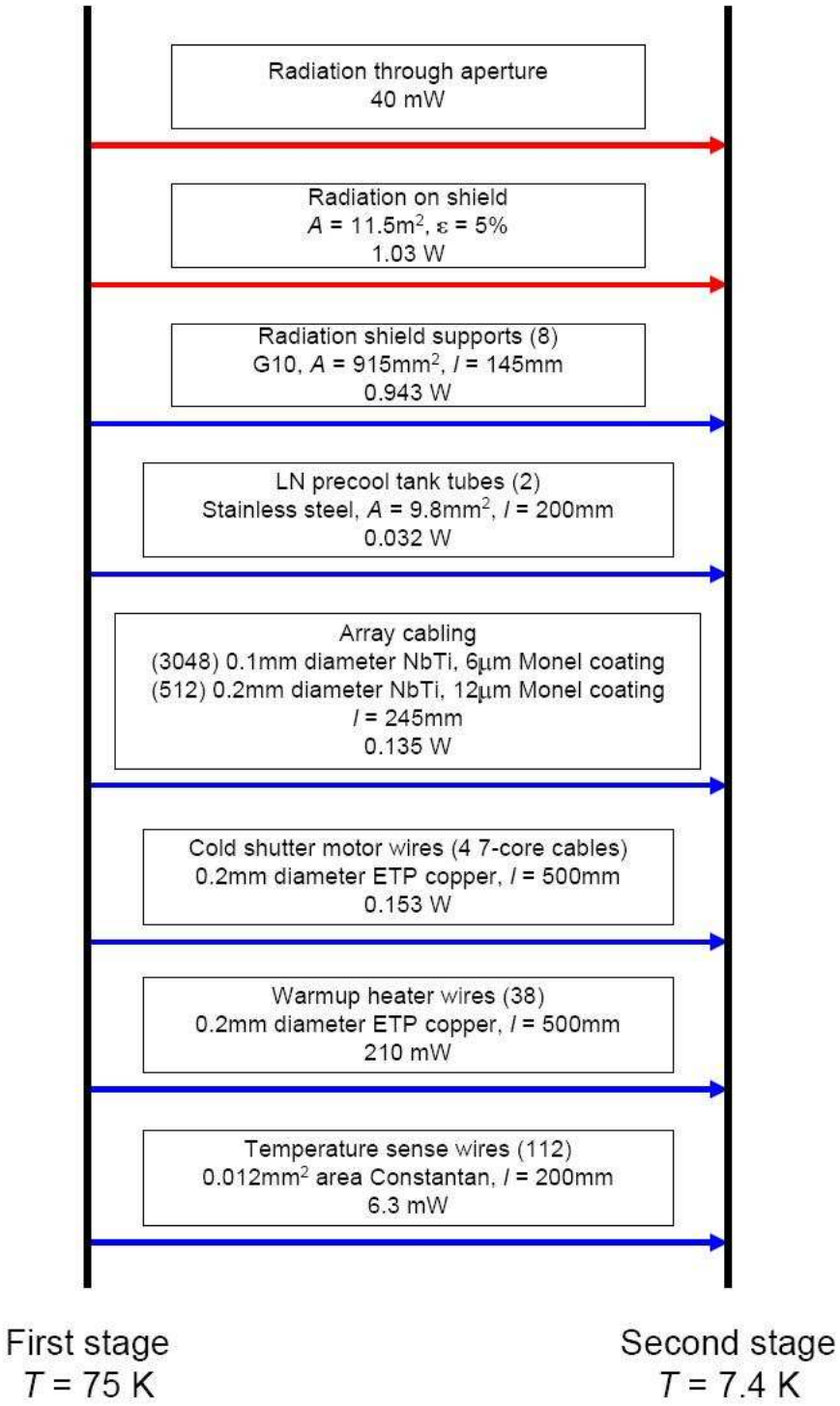


**Figure 6.7:** Network diagram summarising the inputs to the second stage thermal model. Relevant input parameters are listed for each component (area and emissivity for radiation, material and dimensions for conduction loads). The load due to each component is also listed.

**Table 6.2:** Predicted performance of the first and second stage wicks. The data listed is the temperature on the warm side of each joint.

| Element | Temperature / K | |
|---|---|---|
| | First stage wick | Second stage wick |
| PTC stage | 52.6 | 4.45 |
| PTC stage interface | 53.54 | 4.546 |
| Upper flange | 54.46 | 4.549 |
| Weld | 54.46 | 4.549 |
| Link | 57.24 | 4.699 |
| Weld | 57.24 | 4.699 |
| Lower flange | 58.27 | 4.701 |
| Shield | 59.07 | 4.803 |
| $\Delta T$ | 6.47 | 0.353 |

The performance of the wicks from the 60-K and 4-K shields to the first and second stages of the PTCs were also modelled. The model assumed that Apiezon vacuum grease was applied to the interfaces between the upper wick flange and the PTC, and between the lower flange and the radiation shield. The flanges and the welds in both models were assumed to be ETP copper. The links between the flanges on the first stage wicks were also ETP copper, while the links for the second stage wicks were 5N copper. Note that only half of the predicted power passes through each wick. The temperature drops predicted by the model for the wicks are summarised in Table 6.2. The modelled $\Delta T$ for the first stage wicks was 6.47 K, and 0.353 K for the second stage.

### 6.3.3 Results and model comparison

During INS_CD1, additional thermometry was fitted to the instrument in order to characterise the performance of the first and second stage. The major additions were silicon diode RTDs (Lake Shore DT-470-CU) on the first and second stage of one of the PTCs to allow the $\Delta T$ across the wicks to be measured.

The measured temperatures for the first stage are shown in Table 6.3. The temper-

**Table 6.3:** Measured temperature distribution across the first stage. Data was taken during INS_CD1 with additional diagnostic thermometry.

| Location | Temperature / K |
|---|---|
| PTC first stage | 35.2 |
| 60-K radiation shield at wick interface | 36.8 |
| 60-K radiation shield furthest from PTCs | 45.9 |
| $\Delta T$ across first stage wick | 1.6 |
| $\Delta T$ across radiation shield | 9.2 |

ature of the first stage of the PTC was found to be 36.8 K, significantly lower than the 52.6 K predicted from the thermal model. The temperature on the radiation shield side of the wicks was 36.8 K, increasing to 45.9 K at the far side of the shield. This gives a $\Delta T$ across the wick of 1.6 K (compared to 6.47 K from the model), and a temperature difference across the structure of 9.2 K (16 K predicted).

From the polynomial fit to the first stage cooling capacity of the PTC,[1] a temperature of 35.15 K is consistent with a load of 19.2 W. Assuming that the PTCs and interfaces are identical, this gives a total heat load of 38.4 W. This is more than a factor 2 lower than the load predicted from the model. Given that the conduction of heat through the cryostat materials is well understood, the likely explanation is that the performance of the MLI blankets was underestimated, resulting in a considerably lower radiation load on the first stage than predicted in the model. It should be noted that the full number of array cable harnesses were not installed in the cryostat at the time of this measurement, although this would only account for $\sim$1 W of the difference between the measured and predicted loading.

The low $\Delta T$ across the wick to the PTC can be explained by the reduced power flowing across the joints. If the parameters in the original wick thermal model are altered to be consistent with the measured data (PTC temperature 35.2 K and heat load 19.2 W for each wick), the modelled $\Delta T$ reduces to 2.33 K, which is more consistent

[1]The equation of the polynomial fit is $P = -0.104T^2 + 10.985T - 238.45$ for a power $P$ and temperature $T$.

**Table 6.4:** Measured temperature distribution across the second stage. Data was taken during INS_CD1 with additional diagnostic thermometry.

| Location | Temperature / K |
|---|---|
| PTC second stage | 2.96 |
| 4-K radiation shield at wick interface | 3.65 |
| 4-K radiation shield furthest from PTCs | 4.10 |
| $\Delta T$ across second stage wick | 0.69 |
| $\Delta T$ across radiation shield | 0.45 |

with the experimental values. The difference between the model and measured values is likely the result of the safety margins included in the models.

The measured temperature distribution for the second stage is shown in Table 6.4. Again, the PTC second stage temperature is lower than predicted (2.96 K compared to 4.45 K from the model), with the radiation shield temperatures at 3.65 K near the wick interface, rising to 4.10 K at the furthest point. The temperature gradient across the shield of 0.45 K is smaller than the predicted value of 2.1 K. The $\Delta T$ across the wick was measured to be 0.69 K.

The measured pulse tube second stage temperature can again be fitted to the nominal curve.[2] A temperature of 2.96 K is consistent with a heat load of 0.198 W for each cooler, or 0.396 W total for the second stage (compared to 2.56 W predicted). Some of this difference may be explained by the reduced first stage temperature. Changing the thermal model to include a first stage temperature of 40 K (average temperature of the 60-K shield), revised heat load figures for the second stage may be obtained. These are summarised in Table 6.5. The major change in loading is that of radiation. This is to be expected, since heat transfer by radiation has a fourth-power dependance on temperature, and is therefore very sensitive to the temperature difference between the two surfaces. Heat transfer by conduction has an approximately linear dependance.

There is still a factor 2 difference between the modelled load of 0.727 W and the fitted loading of 0.396 W. In the revised heat load model, the greatest contribution now

[2] $P = 0.117T^2 - 0.174T - 0.309$ for a power $P$ and temperature $T$.

**Table 6.5:** Revised thermal loads on the cryostat second stage, assuming a first stage temperature of 40 K, which is consistent with the measured data.

| Element | Power / W |
|---|---|
| Radiation | 0.086 |
| Radiation shield supports | 0.387 |
| Wiring | 0.245 |
| LN precool tank tubes | 0.009 |
| Total | 0.727 |

comes from the radiation shield supports. It is possible that the conductive load along the supports is overestimated, since the thermal conductivity of G10 could vary wildly at cryogenic temperatures (G10 is actually a standard for the electrical properties of the material, and specifies nothing about the thermal properties). As with the first stage modelling, some difference in the modelled loading could originate in the safety factors included in the model. The reduced temperature gradient across the radiation shield is expected since there is less power passing through the structure.

The measured temperature difference along the wick of 0.69 K is considerably larger than the predicted 0.353 K. If the revised figures for the PTC temperature and heat load are included, the predicted $\Delta T$ is only 0.1 K. This may be partially explained since at the time these measurements were made, the second stage wicks used bolted contacts between the foil link and interface flanges rather than the welded joints as in the model. This difference was due to problems with the welding process delaying availability of the production wicks. In fact, the model assumes that the welded joints are effectively lossless, which is not the case for even a very good bolted joint. Furthermore, the effect of Apiezon grease as an interposer at helium temperatures is not well understood. For these reasons, the large $\Delta T$ measured across the wick is not unreasonable since the accuracy of the model may be questioned.

The measured temperature data from the first and second stages of the cryostat are broadly consistent with the modelled performance. The major differences appear to result from a low radiation load on the first stage due to very effective MLI blanketing

of the 60-K radiation shield. Taking this into account in the models improves the agreement between the model predictions and the measurements. The performance of the first and second stages are well within the instrument specifications.

## 6.4 Third and Fourth Stage Performance

The models and design for the third and fourth stages of the cryostat were originally developed by A. L. Woodcraft [95]. The models were subsequently updated by W. S. Holland and this author based on changes to the cryogenics design and modelling inputs such as cooling capacities and power dissipation figures. The data presented here are from the updated models. The analysis and comparison to measured data described in Sect. 6.5 and 6.6 are the work of this author.

### 6.4.1 Third Stage Thermal Model

The predicted heat loads on the third stage of the cryostat are summarised in Table 6.6. The thermal model is summarised in the network schematic in Fig. 6.8. Note that these models use a second stage temperature of 4 K, rather than the temperature of 7.4 K as in the original models, to account for the reduced loading on that stage from the lower operating temperature of the first stage. The greatest contribution to the loading comes from the power dissipated in the 1-K electronics. There are 256 SQUID series arrays in the complete instrument (1 per column of detectors, 32 per subarray), each dissipating approximately 1 $\mu$W of power [103]. Note that there is also a bias resistor for each second stage SQUID dissipating power at 1 K, but each resistor only dissipates 0.7 nW and is therefore a negligible contribution.

The conductive loading from the 4-K radiation shield along the 1-K box supports is only 0.054 mW, smaller by a factor 2 than the load conducted along the wiring. The load carried along the wiring harnesses to the subarray modules is relatively low despite the high wire count since the NbTi cores should be superconducting at these temperatures. Heat from the cold shutter motor is conducted to the 1-K stage through the isolating supports in the motor mount and via the cold shutter. These loads total 0.088 mW for the two paths. Radiative loading from the second stage at 4K is negligible. The total heat load on the third stage is 0.586 mW.

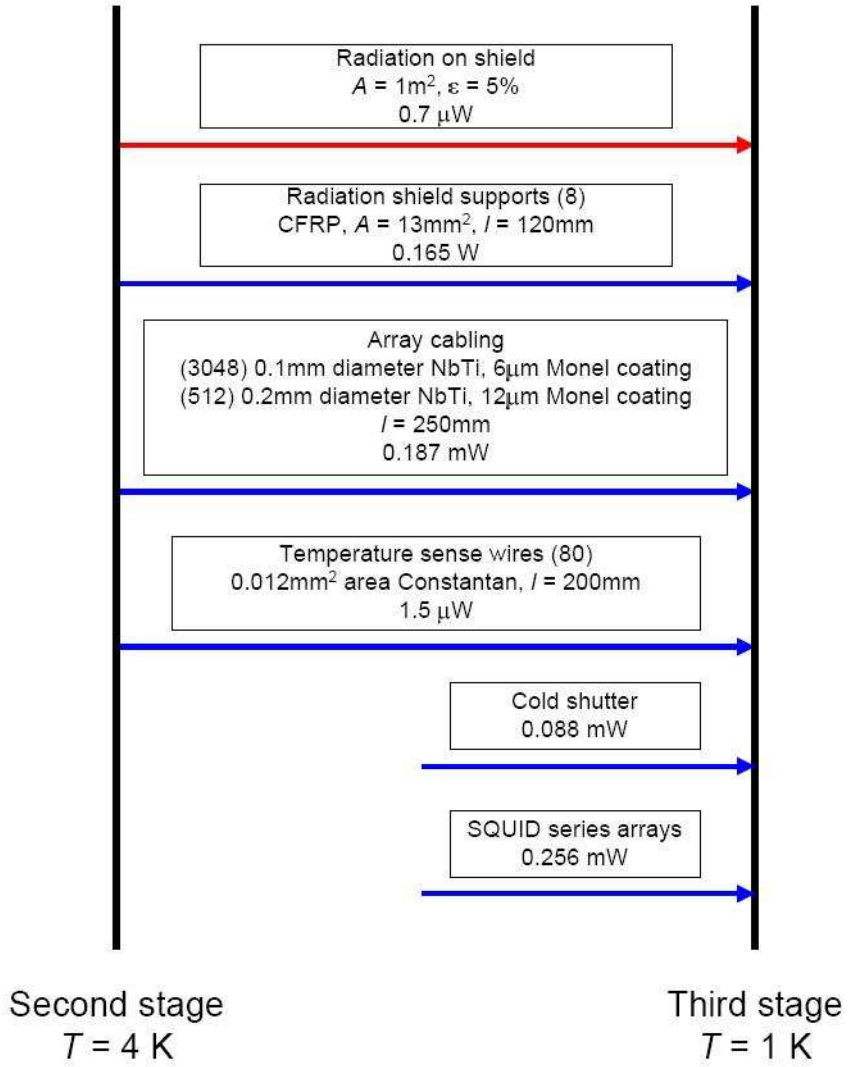


**Figure 6.8:** Network diagram summarising the inputs to the third stage thermal model. Relevant input parameters are listed for each component (area and emissivity for radiation, material and dimensions for conduction loads). The load due to each component is also listed. Note that this model assumes a revised second stage temperature to account for the reduced loading on that stage.

**Table 6.6:** Predicted thermal loads on the cryostat third (1-K) stage.

| Element | Power / mW |
|---|---|
| Radiation shield supports | 0.054 |
| Wiring | 0.189 |
| SQUIDs (1-K electronics) | 0.256 |
| Cold shutter motor | 0.088 |
| Radiation | 0.0007 |
| Optical | $4\times10^{-6}$ |
| Total | 0.588 |

The block diagram for the model of the cryostat third stage is shown in Fig. 6.9. Contact to the DR still is made through a double bolted joint (1 and 1a in the block diagram). The component between the two joints is a solid ETP copper block, and it is assumed (reasonably) that there is no temperature gradient across the bulk block. Strap 1 is composed of four stacks of 50 0.1 mm-thick 5N copper foils in parallel, diffusion bonded at each end to give a solid cross-section. The foils are annealed to increase the thermal conductivity. The interface from the copper straps and the ETP copper end pieces is a welded and bolted joint, as for the second stage wicks to the PTCs. It is assumed that these joints behave as the bulk material, and therefore that there is no temperature drop across the interface. The straps each have an effective cross-sectional area of 160 $mm^2$ and are 410 mm in length.

The ETP copper end piece interfaces to a gold-plated ETP plate on the 1-K box (joint 2 in Fig. 6.9). This plate is attached to the side of the 1-K box by an epoxy joint (joint 3). Making contact to aluminium surfaces is problematic due to the ready formation of an oxide layer. Reliable gold plating of aluminium is difficult, and an oxide layer will often be trapped under the plating. Furthermore, joints between dissimilar materials may be unreliable during thermal cycling due to differential contraction. Although the use of epoxy to make the joint to the 1-K structure has a lower thermal conductance than a pressed contact, the approach was considered more reliable. The joint is made with a pattern of aluminium screws into the side panel of the 1-K box,

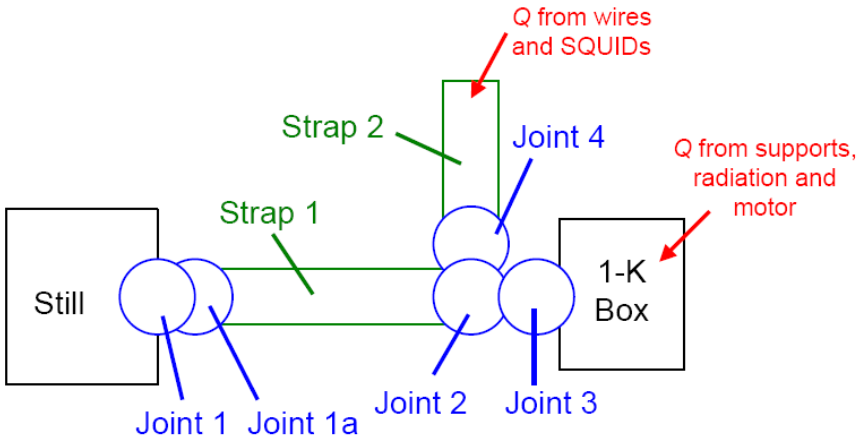


**Figure 6.9:** Thermal model block diagram of the cryostat third stage. See text for details

and using Stycast 1266 epoxy.[3] In this design, it is the copper-copper joint (joint 2) that is broken to remove the 1-K box from the instrument.

Rather than relying on the conductivity of the aluminium structure to cool the heat sinks of the cold shutter and wiring, further copper links provide a direct cooling path. These wicks also provide a path to the heat sinks of the 1-K electronics in each subarray module. These links are represented by joint 4 and strap 2 in the model block diagram.

The temperature profile predicted from the model is summarised in Table 6.7, with the temperature drop ($\Delta T$) and absolute temperature of the warm side of each joint listed. The value of $T_{still}$ was taken as 910 mK, consistent with the predicted power load and the measured still cooling capacity (see Fig. 5.3).

The thermal path to the still has a number of branches, with not all of the heat load passing across every joint. The power from the 1-K supports, the heat from the motor, and the 4 K and optical radiation load pass through the box, the epoxy joint (joint 3) and then to the still. However, the power from the wiring, 1-K electronics and cold shutter does not pass through the box and epoxy joint, but does pass joint 2 and along strap 1 to the still. The power flowing across each joint is also listed in Table 6.7.

The predicted $\Delta T$ from the still to the 1-K box structure is 5.6 mK. The temperature drop is not dominated by any single component. The temperature distribution across the box structure itself is more difficult to model, although the inclusion of further

[3]Emerson and Cuming, http://www.emersoncuming.com.

**Table 6.7:** Predicted temperature profile of the 1-K path. The temperature drop ($\Delta T$) for each element is listed, along with the temperature of the warm side of the joint or strap. The power flowing across the joint is also listed.

| Element | $\Delta T$ / mK | Temperature at warm side / mK | Power / mW |
|---|---|---|---|
| Still | - | 910 | 0.588 |
| Joint 1 | 1.5 | 911.5 | 0.588 |
| Joint 1a | 1.5 | 913.0 | 0.588 |
| Strap 1 | 0.5 | 913.5 | 0.588 |
| Joint 2 | 1.5 | 915.0 | 0.588 |
| Joint 3 | 0.6 | 915.6 | 0.099 |

wicking from the copper plate after joint 2 to similar plates with epoxy joints distributed around the aluminium structure would indicate that there will not be any "hotspots" in the structure due to the multiple cooling paths.

### 6.4.2 Fourth Stage Thermal Model

A summary of the predicted power loading on the fourth stage of the instrument is shown in Table 6.8. The design of the cryostat is such that the mK cooling system has two branches, one cooling each focal plane. The contributions to the fourth stage load are divided into the contribution from each of the focal plane channels, and the contribution of the common section of the cooling path. The design of the system is described in more detail below.

The fourth stage load is dominated by the heat leaks along the support structures from the third stage, illustrating the importance of careful design of low temperature systems. The conduction load along the array wiring to the 1-K electronics is also a major contributor. The power dissipation figures for the detector and multiplexer arrays for each wavelength are for full focal planes (4 subarrays at each wavelength) The figures for the contribution of the MUX are maximum power dissipation. Typical power dissipation figures are lower by a factor of $\sim$2 for the 850 $\mu$m arrays and $\sim$3 for the 450 $\mu$m arrays.

**Table 6.8:** Predicted thermal loads on the cryostat fourth (mK) stage. The power loads are divided into the contribution from each focal plane and the contribution of the common sections of the system. See text for more details.

| Element | Power / $\mu$W | | |
|---|---|---|---|
| | 850 $\mu$m channel | 450 $\mu$m channel | Common |
| Detectors (8 subarrays) | 0.2304 | 1.024 | n/a |
| MUX (8 subarrays) | 2.3766 | 2.8332 | n/a |
| Supports | 7.4 | 7.4 | 0.4 |
| Array wiring (8 subarrays) | 2.1 | 2.1 | n/a |
| Radiation | n/a | n/a | $1.4\times10^{-4}$ |
| Total | 12.107 | 13.357 | 0.4 |
| Total load | | 25.864 | |

A block diagram for the fourth stage thermal model is shown in Fig. 6.10. The contact to the DR mixing chamber is made via a plate (gold-plated commercial copper) with a protruding cylinder bolted to the mixing chamber plate (joint 1). The strap to the 1-K box (strap 1) clamps onto the cylinder (joint 1a), removing the need for accurate orientation of the mixing chamber plate relative to the strap. The attachment of strap 1 to the DR mixing chamber is shown in the CAD model image in Fig. 6.11. Strap 1 is composed of two stacks of 50 0.1 mm-thick annealed 5N copper foils, as for the 1-K strap, welded and bolted to commercial copper end pieces. The strap runs through the bellows section of the 1-K radiation shielding to a manifold plate at the box end (see Fig. 6.12). Strap 1 connects to the manifold at joint 2. The manifold plate is supported and isolated from the 1-K box structure by two Kevlar® thread assemblies (see Fig. 6.13). Kevlar has a low thermal conductivity at low temperature and a high tensile strength, allowing small cross-sections to be used for mechanical supports. Supports may be therefore be designed with extremely low thermal conductance [151, 152].

From the manifold, the cooling paths split to go to each focal plane separately. The cooling path to the 450$\mu$m focal plane is described by the model, since the power load on this channel is slightly higher than for the 850$\mu$m focal plane. Joint 2a is a

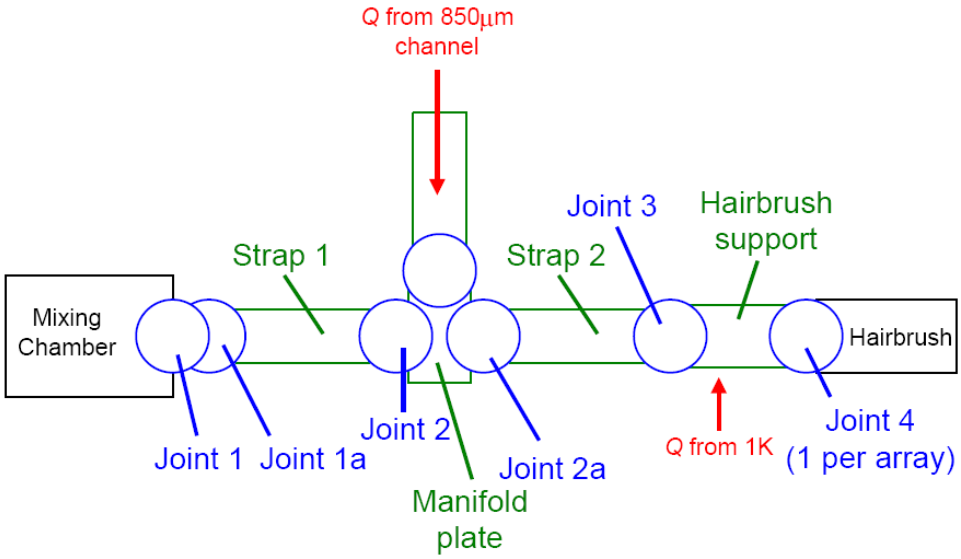


**Figure 6.10:** Thermal model block diagram of the cryostat fourth stage. See text for details

further demountable contact, broken to remove the focal plane unit from the 1-K box. Strap 2 is composed of three lengths of solid commercial copper bar, e-beam welded to produce a U-shaped cold bar running from the manifold to the focal plane, with a total length of 840mm (see cross-section of the focal plane units in Fig. 6.14). The cold bar is supported by two further Kevlar wheel assemblies identical to those described above for the manifold plate. The cold bar terminates at a circular plate welded to the bar. The plate bolts (joint 3) to a commercial copper platform. Finally, the array heat sinks (known as "hairbrushes") bolt to the platform (joint 4). The platform is also referred to as the "hairbrush support".

The focal plane is supported by a rigid thermal isolation support, shown in Fig. 6.15. The support assembly uses four isolation joints comprised of copper components separated by diamond powder sandwiched between sapphire discs. A high thermal resistance across the joint is achieved since the true contact area between the discs is very small. Use of a hard material such as sapphire is important since soft materials will tend to deform to some degree, increasing the contact area. The powder further decreases the contact area. Kevlar isolation supports were not judged to be suitable since movement during thermal cycling and over time had to be minimised to allow for accurate align-

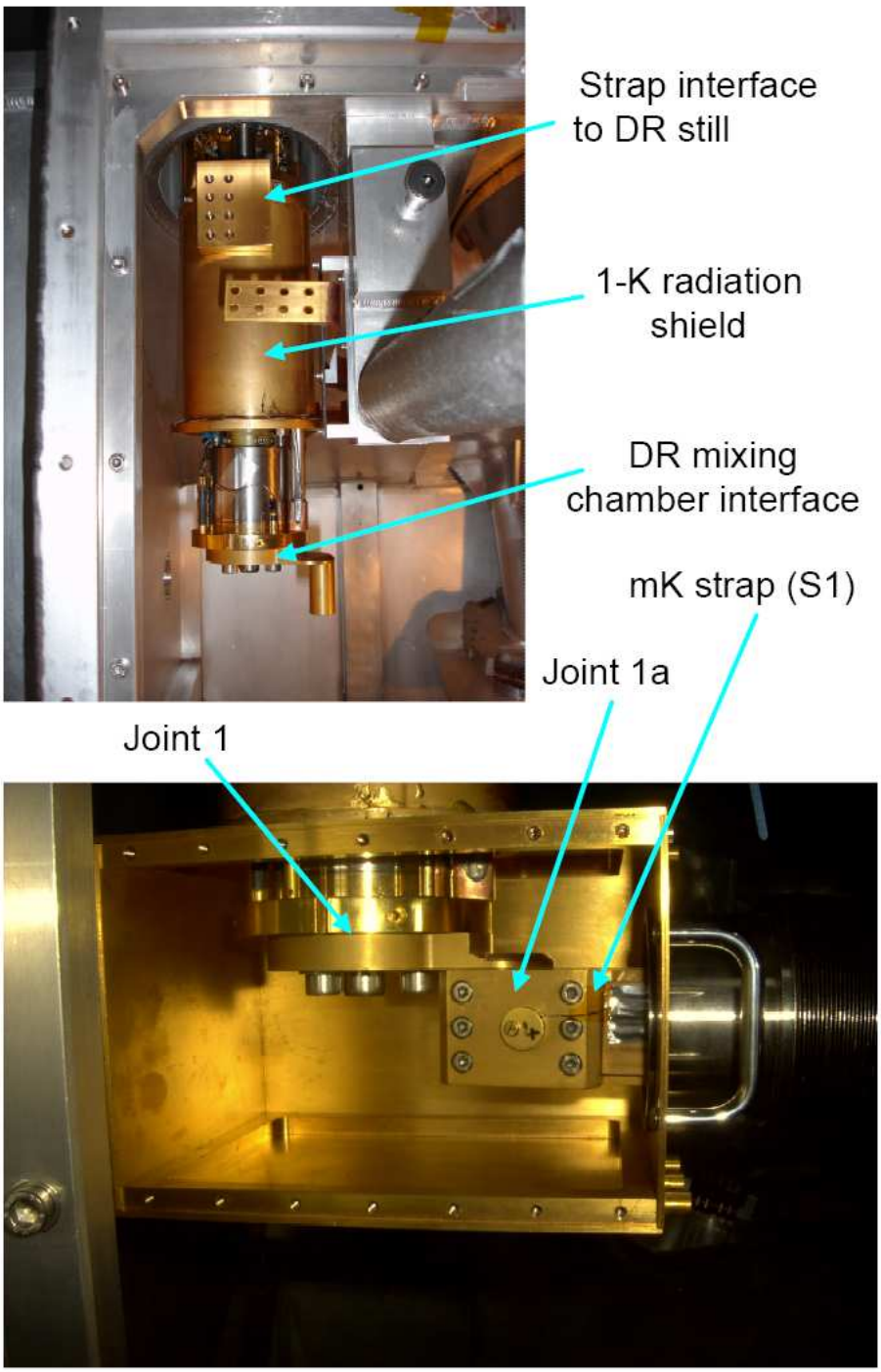


**Figure 6.11:** Interface between the millikelvin strap (strap 1) and the dilution refrigerator. Top: DR insert in the instrument cryostat with the upper section of the 1-K radiation shield and the mK strap interface plate fitted. Bottom: Lower section of the 1-K radiation shield and the mK strap.

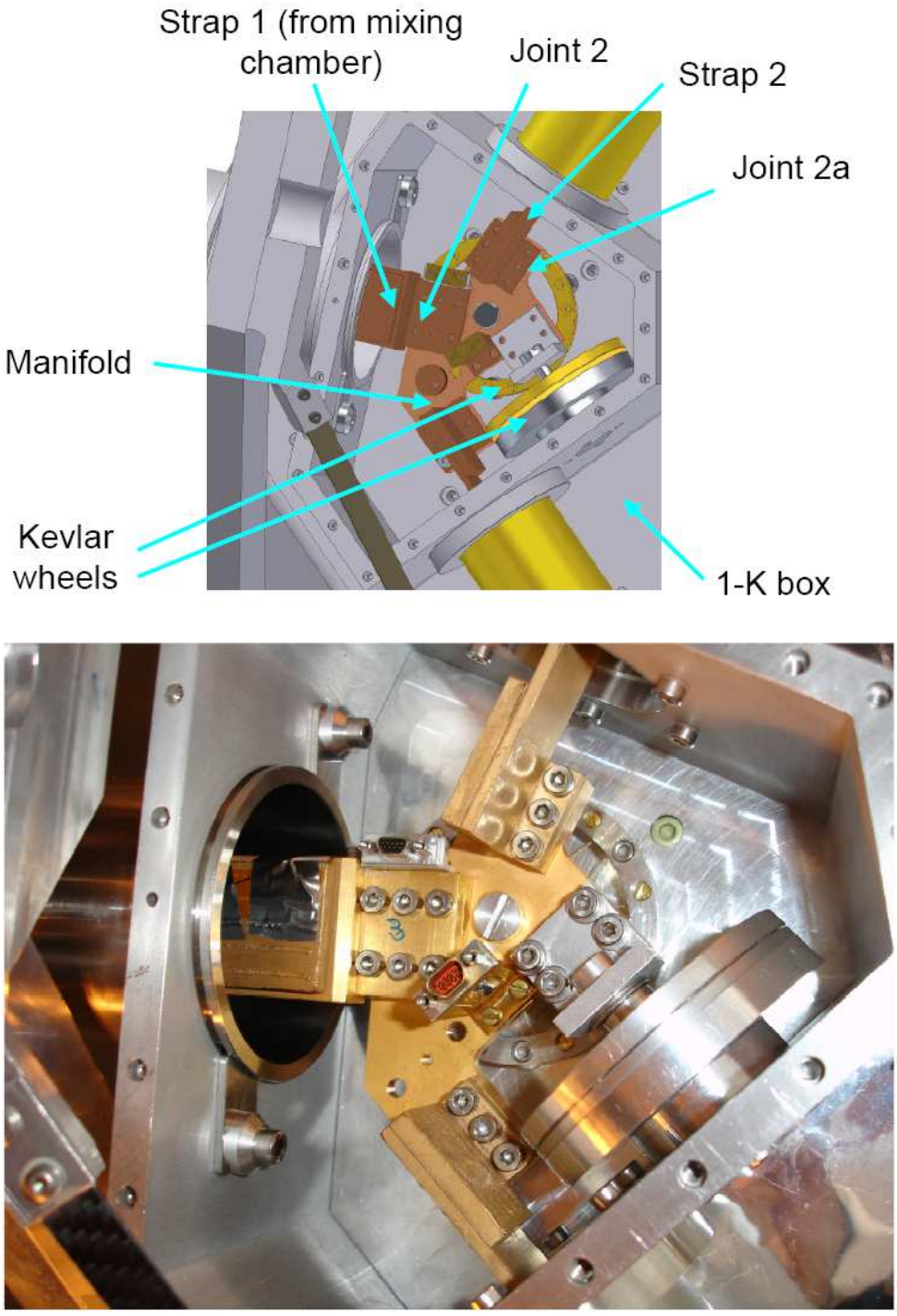


**Figure 6.12:** The millikelvin manifold plate. Top: CAD model of the manifold with the components and interfaces indicated. Bottom: photograph of the manifold plate.

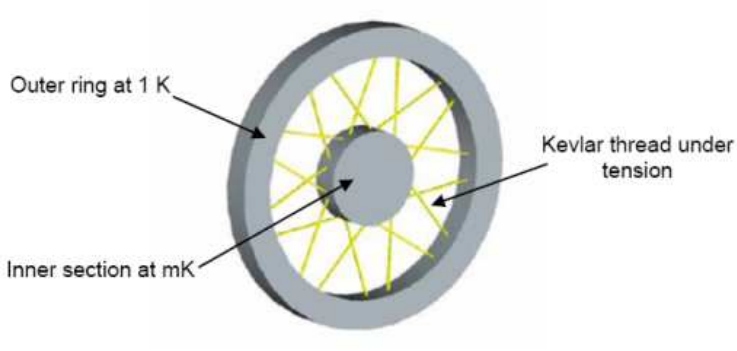


**Figure 6.13:** CAD model of an isolation support using Kevlar® thread. Adapted from Ref. [95].

ment of the focal planes. Kevlar thread will creep, and expands as the temperature is decreased. The sapphire isolation joints are described in more detail in Ref. [153].

The predicted temperature profile for the millikelvin cooling path is summarised in Table 6.9. As for the profile of the 1-K system described above, the temperature drop across each component and the temperature of the warm side of the component is listed, along with the power flowing through the joint or strap. The power figures used here are the full figures listed in Table 6.8 (fully populated focal planes and using the maximum power dissipation figures for the arrays). Although most of the thermal measurements for characterisation of the system were made with the arrays switched off (and therefore dissipating no power), the stage power dissipation is dominated by conduction loads, and therefore the temperature profile does not differ greatly whether the arrays are powered up or not. This temperature profile is for the 450 $\mu$m channel. The power dissipation for the 450 $\mu$m arrays is marginally higher than for the 850 $\mu$m arrays. Hence, the 850 $\mu$m channel should run slightly colder than the figures predicted here. The contributions from conduction loads are the same for both channels.

For the fully populated focal plane model, the predicted temperature drop from the mixing chamber to the hairbrush supports is 6.7mK, falling to 4.7mK for the partially populated model. This is consistent with the model inputs, since from the power load data in Table 6.8, the heat input is dominated by the support structures. This load is present regardless of the number of subarray modules. The temperature profile is not dominated by a single component.

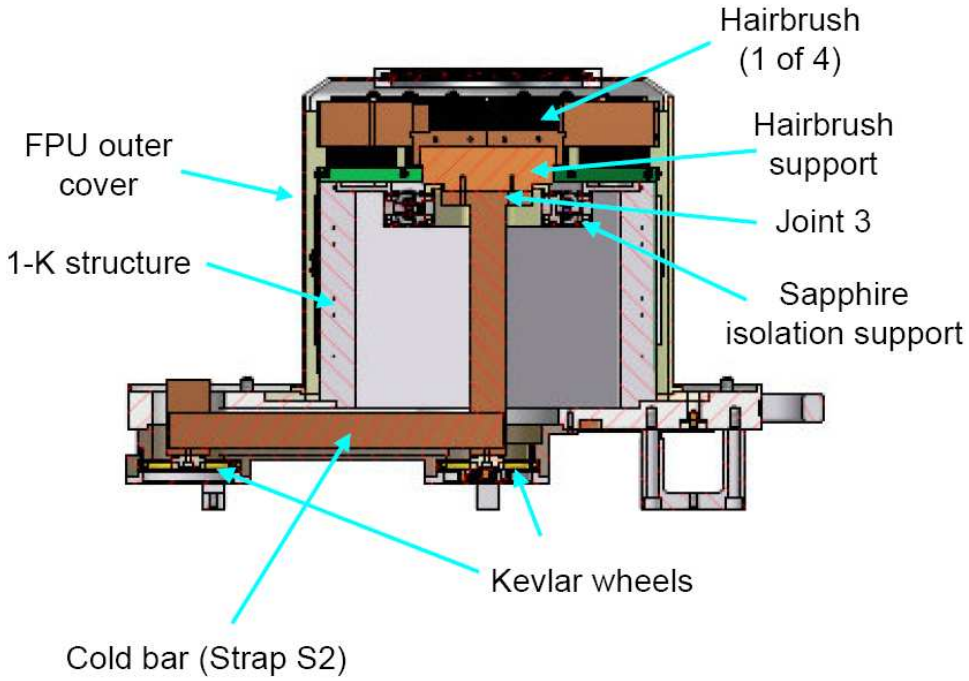


**Figure 6.14:** CAD model cross-section of the focal plane unit, showing the cold bar and thermal interfaces.

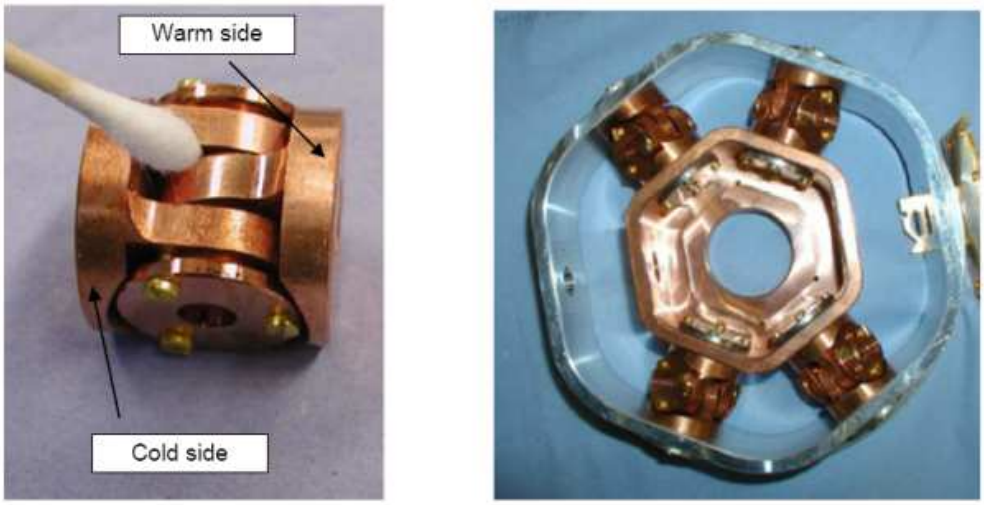


**Figure 6.15:** Thermal isolation support for the millikelvin stage using contact resistance between sapphire discs. Left: a single thermal isolation joint. Right: thermal isolation structure using four joints. Adapted from Ref. [95].

**Table 6.9:** Predicted temperature profile of the millikelvin cooling path along the 450 $\mu$m channel. The temperature drop ($\Delta T$) for each element is listed, along with the temperature of the warm side of the joint or strap. The power flowing across the joint is also listed. The profile is given both for 4 subarrays on each focal plane, and for a single array on each focal plane.

| Element | $\Delta T$ / mK | Temperature at warm side / mK | Power / $\mu$W |
|---|---|---|---|
| *4 subarrays on each focal plane.* | | | |
| Mixing chamber | - | 52.6 | 25.74 |
| Joint 1 | 1.1 | 53.7 | 25.74 |
| Joint 1a | 1.1 | 54.8 | 25.74 |
| Strap 1 | 1.1 | 55.9 | 25.74 |
| Joint 2 | 1.1 | 57.0 | 25.74 |
| Joint 2a | 0.5 | 57.5 | 13.30 |
| Strap 2 | 1.3 | 58.8 | 13.30 |
| Joint 3 | 0.5 | 59.3 | 13.30 |
| Joint 4 | 0.1 | 59.4 | 1.48 |
| *1 subarray on each focal plane.* | | | |
| Mixing chamber | - | 50.5 | 17.84 |
| Joint 1 | 0.8 | 51.3 | 17.84 |
| Joint 1a | 0.8 | 52.1 | 17.84 |
| Strap 1 | 0.8 | 52.9 | 17.84 |
| Joint 2 | 0.8 | 53.7 | 17.84 |
| Joint 2a | 0.3 | 54.0 | 8.87 |
| Strap 2 | 0.9 | 54.9 | 8.87 |
| Joint 3 | 0.3 | 55.2 | 8.87 |
| Joint 4 | 0.0 | 55.2 | 0.37 |

## 6.5 Third Stage Performance

The performance of the 1-K stage of the instrument was found to be broadly consistent during the test cooldowns of the instrument. A typical temperature profile for the third stage is summarised in Table 6.10. The still temperature, with no additional heat on the still, was found to be 1.03 K. This is considerably higher than the expected 0.91 K for the predicted power loading. The $\Delta T$ along to the interface plate (warm side of joint 2) was measured to be 130 mK, again considerably higher than the value of 5 mK predicted from the model. The temperature of the focal plane unit outer covers was found to be around 1.3 K. Note that the temperature gradient through the 1-K box was not specifically included in the model, but a large $\Delta T$ is not entirely unexpected, since there are two low-pressure aluminium-aluminium joints between the two points of measurement that are likely to have a poor conductance.

Since the still temperature is higher than expected, there must be a greater power loading on the third stage than anticipated. From measurements of the still cooling capacity detailed in Chapter 5, a temperature of 1030 mK is consistent with a power loading of $\sim$10 mW. The predicted loading in the model was only 0.588 mW with power to the 1-K electronics, which accounting for approximately half of the power dissipation. The measurements were taken with the SQUID amplifiers turned off, and therefore contributing nothing to the dissipated power.

Other possible sources of the excess power are the radiation shield supports and the array wiring. The array cables, composed of niobium-titanium with a transition temperature of 12 K, are nominally superconducting between the second and third stage heat sinks. However, measurements of the temperature distribution along the array cables indicated temperatures as high as 10–20 K at the second stage heat sinks, implying the superconducting transition point is closer to the 1-K box than intended by the design. If this effect is modelled, the change in power loading on the third stage is minimal since unlike many superconductors, the thermal conductivity of NbTi does not undergo a drastic change between the normal and superconducting states. Using pessimistic values of $\kappa$ for NbTi and the wire cladding, the conduction load from the wiring is of the order of 0.5mW from a cable temperature of 20 K.

**Table 6.10:** Measured temperature distribution through the third stage system. The location of the measurements refers to the block diagram of the third stage shown in Fig. 6.9.

| Location | Temperature / mK |
|---|---|
| Still | 1030 |
| 1-K radiation shield (warm side of joint 2) | 1160 |
| 850$\mu$m focal plane unit outer cover | 1340 |
| $\Delta T$ across third stage wick | 130 |

The calculated conduction load along the 1-K box carbon fibre supports are based on measurements carried out for the project on samples of the same batch of material as that used to produce the real supports. As discussed in §6.2, the low temperature properties of materials can vary wildly between batches, since the materials are not specifically design for use in cryogenic environments. Measurements of samples from the same batch were intended to mitigate this effect. While it is not inconceivable that there is some variation between the test samples and the actual support material, it would be unlikely that the variation would be large enough (orders of magnitude) to account for the additional conduction load.

A further possibility for the conduction load is a short between the third and second stage. Many of the structures on the 1-K stage are in close proximity to the second stage, so it may be possible that a short develops at low temperature due to differential contraction of the structures. However, the conduction through any short would be expected to be small, since the temperature gradient across any contact would only be $\sim$3 K, and the contact area would be small. Given the small number of temperature sensors across the third stage, it would be difficult to diagnose the presence of a short.

There is no clear explanation for the excess power loading on the third stage. If a value of 10 mW for the power dissipation is used in the third stage thermal model, the predicted temperature profile is that summarised in Table 6.11. The $\Delta T$ to the interface plate on the warm side of joint 2 is 73 mK, a factor 2 lower than the measured 130 mK. Although it is possible that one of the demountable joints was a bad contact at the time of measurement, this is believed unlikely to be a contributing factor since measurements

**Table 6.11:** Revised prediction for the temperature profile of the 1-K path, using power values consistent with the measured data. The temperature drop ($\Delta T$) for each element is listed, along with the temperature of the warm side of the joint or strap. The epoxy joint (joint 3) is omitted.

| Element | $\Delta T$ /mK | Temperature at warm side / mK |
|---|---|---|
| Still | - | 1030 |
| Joint 1 | 21 | 1052 |
| Joint 1a | 21 | 1074 |
| Strap 1 | 5 | 1081 |
| Joint 2 | 21 | 1103 |

on separate cooldowns, between which the joints were broken and remade, are largely consistent. It would be expected that there would be considerable variation in joint conductance between being broken and remade. A more likely explanation is that there is a temperature drop across the welded joints between the flexible foil sections of the wick and the solid ETP components at the ends (as with the wick models for the second stage, this model assumes lossless welded interfaces between the foil and solid sections). However, given the difficulty in predicting the behaviour of bolted joints at low temperatures, a factor 2 difference is very good.

## 6.6 Fourth Stage Performance

The measured temperature distribution through the fourth stage wick system for a typical cooldown is summarised in Table 6.12. The measurements described in this section were made with one subarray on each focal plane. The mixing chamber temperature was measured using the same carbon resistor temperature sensor as that used for previous work with the DR, while the other sensors are ruthenium oxide (Lake Shore RX-102A-CD) sensors. As with the ruthenium oxide sensors used in the evaluation of the DR performance, the sensors used in the instrument were calibrated independently against a Lake Shore germanium RTD.

**Table 6.12:** Measured temperature distribution through the fourth stage system. The location of the measurements refers to the block diagram of the fourth stage shown in Fig. 6.10.

| Location | Temperature / mK |
|---|---|
| Mixing chamber | 52.7 |
| Millikelvin strap (warm side of joint 1a) | 53.5 |
| Millikelvin manifold (warm side of joint 2) | 55.0 |
| 450$\mu$m focal plane (warm side of joint 3) | 56.3 |
| 850$\mu$m focal plane (warm side of joint 3) | 72.9 |

The mixing chamber temperature was found to be 52.5 mK. The temperature at the cold end of the millikelvin strap (strap 1 in Fig. 6.10) was measured as 53.5 mK, while the manifold plate after joint 2 was measured as 55.0 mK. This compares well to the predicted $\Delta T$ of 1.6 mK across joints 1 and 1a, and 1.6 mK along strap 1 and across joint 2. The temperature at the 450 $\mu$m focal plane in this case was measured as 56.3 mK, a $\Delta T$ of 1.3 mK (compared to a predicted 1.5 mK). However, the 850 $\mu$m focal plane was found to be at a temperature of 72.9 mK. It had been observed that there was considerable variation in the focal plane temperatures between cooldowns. This is believed to be the result of a bad joint between the manifold plate and the focal plane. When the FPUs are removed from the 1-K box (as occurred between each cooldown), joint 2a is broken. Also, as part of disassembly of the FPUs, joint 3 was broken frequently. Although precautions were taken on reassembly to clean the joints, some variation is to be expected. The difference between the two focal plane temperatures is also likely not as extreme as it appears. The sensor on the 850 $\mu$m focal plane consistently reads higher than the 450 $\mu$m sensors, implying a problem with the sensor calibration.

The cooling capacity of the DR mixing chamber was measured in the instrument cryostat. Typical data is illustrated in Fig. 6.16. Also shown is the baseline cooling capacity for the DR operating in the test cryostat, with $\dot{Q}_{still} = 14.4$ mW (a similar load on the still to the background load in the instrument cryostat) for comparison. The measured capacity of the DR in the instrument was 10 $\mu$W at 55 mK and 100 $\mu$W at

76 mK. 10 $\mu$W is the expected additional load on the fourth stage from a full compliment of detector arrays. These measurements indicated that there should be no issues associated with increasing the number of detector arrays in the instrument during subsequent operation.

The background load on the fourth stage due to conduction down supports and wiring can be estimated by comparison of the measured cooling capacity in the instrument cryostat to the baseline measurements. Using a polynomial fitted to the baseline cooling power measurements, the value of the mixing chamber load, $\dot{Q}_{mc}$, can be calculated for the measurements of the DR capacity in the instrument cryostat. If this is done for $T_{mc} = 52.5$ mK, the mixing chamber temperature with no additional electrical power, a value of the background power, $\dot{Q}_{bkg}$, of 28 $\mu$W is obtained. This is higher than the expected load listed in Table 6.9 of 17.84 $\mu$W for two subarrays, but is not an unreasonable value.

If this calculation is repeated for the full range of cooling power measurements and the applied electrical power subtracted, a constant value of $\dot{Q}_{bkg}$ should be obtained. This is not the case, as shown in Fig. 6.17. The background load estimated from this method is found to increase as a function of $\dot{Q}_{Elec}$. The estimated values of $\dot{Q}_{bkg}$ range from 28 $\mu$W for no additional load to 47 $\mu$W for $\dot{Q}_{Elec} = 100$ $\mu$W. The explanation for this effect is the difference in the cooling capacity due to the different load on the still. As observed in the analysis of the DR performance data in §5.4, a small difference in the load on the still will affect the cooling capacity of the mixing chamber. For this DR, temperature differences of a few millikelvin due to the difference in still power equates to changes of tens of microwatts in $\dot{Q}_{mc}$ values estimated using this method.

An alternative method for estimation of $\dot{Q}_{bkg}$ is the analysis using Eqs. (5.1) and (5.2) to determine the internal heat leak on the mixing chamber. The plot and fit of $t$ against $\dot{Q}_{Elec}$ for the cooling capacity measurements in the instrument cryostat is shown in Fig. 6.18. For this analysis, it has been assumed that the mixing chamber temperature equals the input temperature. As seen in the analysis carried out in Chapter 5, this assumption has no effect on the recovered value of $\dot{Q}_{Leak}$. The intercept of the linear fit to the data is $(87 \pm 2)$ $\mu$W, which is the sum of $\dot{Q}_{Leak}$, the internal heat leak of the DR, and $\dot{Q}_{bkg}$.

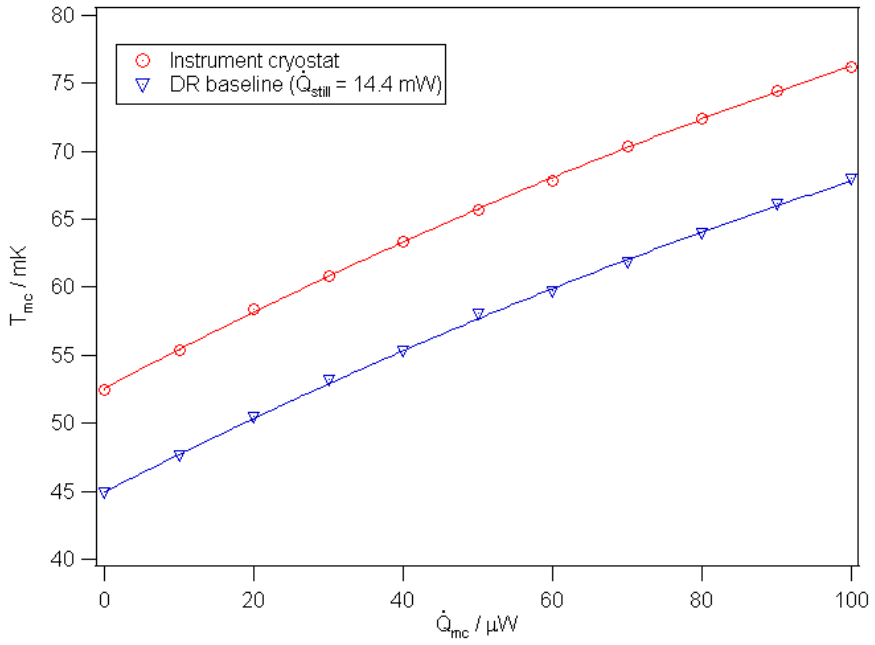


**Figure 6.16:** Measured cooling capacity of the dilution refrigerator in the instrument cryostat. Also shown is a capacity measurement for the DR in the test cryostat, with $\dot{Q}_{still} = 14.4$ mW.

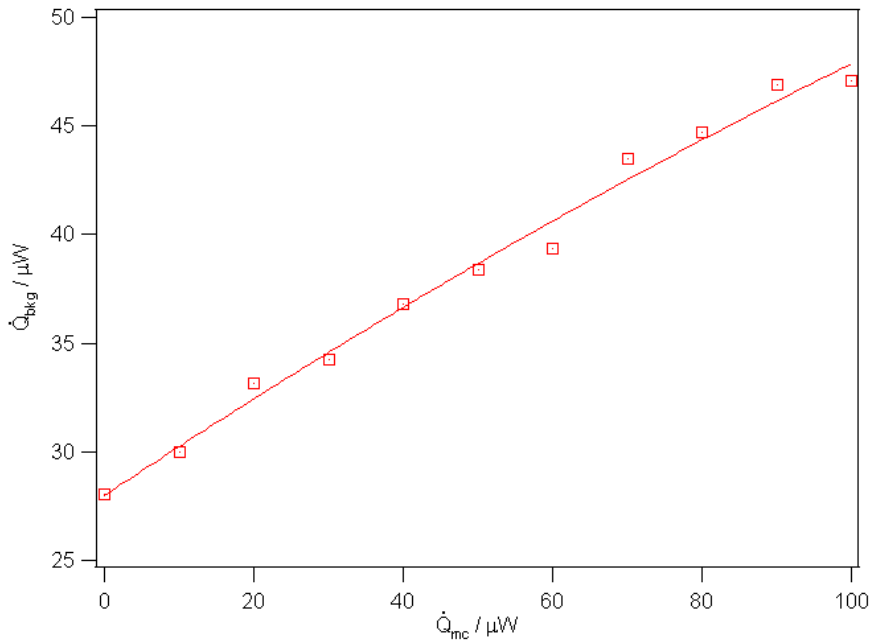


**Figure 6.17:** Estimated background power load on the fourth stage as a function of applied electrical power. See text for discussion.

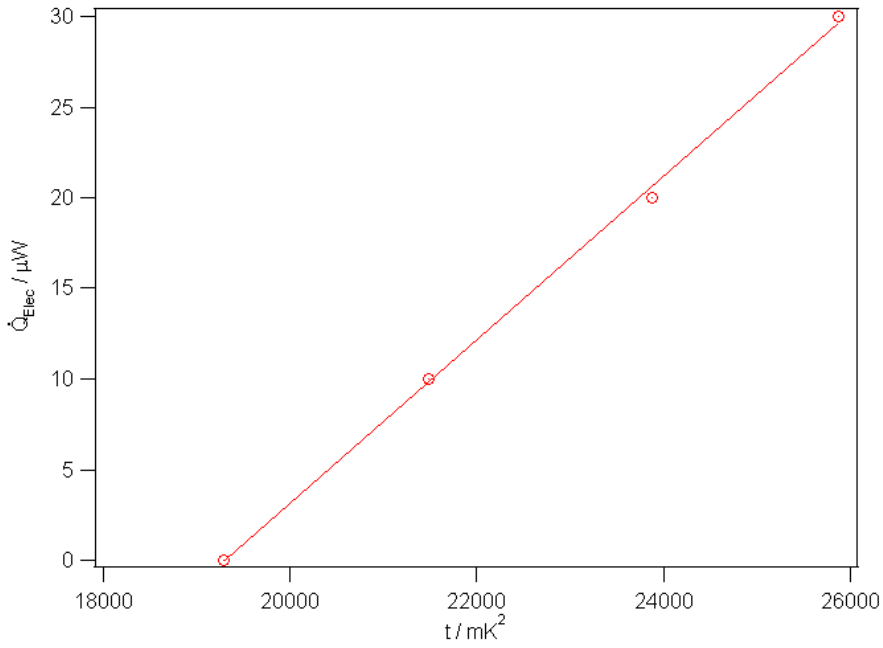


**Figure 6.18:** Mixing chamber temperature in the instrument cryostat as a function of the instreaming $^3$He temperature and applied electrical power.

The value of $\dot{Q}_{Leak}$ has some dependency on the value of $\dot{Q}_{still}$, as in the previous analysis. However, the effect of using a value of $\dot{Q}_{Leak}$ for a different $\dot{Q}_{still}$ is not as great. Using the cooling power measurements for the DR in the test cryostat discussed in Chapter 5, a value of $\dot{Q}_{Leak}$ of $(75 \pm 1)$ $\mu$W is recovered for $\dot{Q}_{still} = 14.4$ mW, and $\dot{Q}_{Leak} = (80 \pm 2)$ $\mu$W for $\dot{Q}_{still} = 3.6$ mW. Since the still load is nearer the top of this range in the instrument cryostat, it is not unreasonable to obtain an estimate of $\dot{Q}_{bkg}$ using $\dot{Q}_{Leak} = (75 \pm 1)$ $\mu$W. Making this assumption, it is found that $\dot{Q}_{bkg} = (12 \pm 2)$ $\mu$W, which is consistent with the heat load on the fourth stage expected from the thermal model.

### 6.6.1 Array Power Dissipation

In addition to the background heat load on the DR from the fourth stage system, an important aspect of the fourth stage behaviour is the effect of power dissipation from the detector arrays. Data supplied by NIST indicated that typical detector subarrays would dissipate 1.1 $\mu$W for the 850 $\mu$m arrays, and 2.2 $\mu$W for the 450 $\mu$m arrays.

**Table 6.13:** Summary of expected detector array power dissipation. Figures are for 4 subarrays at each focal plane.

| Element | Typical Power | | Maximum Power | |
|---|---|---|---|---|
| | 850 $\mu$m | 450 $\mu$m | 850 $\mu$m | 450 $\mu$m |
| Sky | 20 pW | 150 pW | 20 pW | 150 pW |
| Heater | 10 pW | 20 pW | 10 pW | 20 pW |
| Bias | 15 pW | 30 pW | 15 pW | 30 pW |
| **Total per pixel** | 45 pW | 200 pW | 45 pW | 200 pW |
| **Total per detector** | 0.2304 $\mu$W | 1.024 $\mu$W | 0.2304 $\mu$W | 1.024 $\mu$W |
| Heater shunt resistor | 0.0157 $\mu$W | 0.0315 $\mu$W | 0.0192 $\mu$W | 0.0385 $\mu$W |
| Bias shunt resistor | 0.3936 $\mu$W | 0.7872 $\mu$W | 0.4373 $\mu$W | 0.8747 $\mu$W |
| SQUIDs (per column)[a] | 3.3 nW[b] | 3.3 nW[b] | 15 nW[c] | 15 nW[c] |
| **Total SQUIDs** | 0.4224 $\mu$W | 0.4224 $\mu$W | 1.92 $\mu$W | 1.92 $\mu$W |
| **Total per MUX** | 0.8317 $\mu$W | 1.2411 $\mu$W | 2.3766 $\mu$W | 2.8332 $\mu$W |
| **Total per subarray** | 1.0679 $\mu$W | 2.2411 $\mu$W | 2.6127 $\mu$W | 3.8828 $\mu$W |

[a] A multiplexer column consists of one first stage SQUID, an address resistor and a second-stage SQUID.

[b] SQUID power dissipation figures from Ref. [103].

[c] Estimated figures at maximum bias and feedback with engineering margin.

Maximum power dissipation was estimated to be 2.6 $\mu$W and 3.9 $\mu$W, respectively. At 850 $\mu$m, the dissipation figures are dominated by the multiplexer, divided between the SQUIDs and detector bias shunt resistor. At 450 $\mu$m, the greater sky background results in a larger contribution from the TES pixels to the overall power dissipation. A summary of the contributions to the total is given in Table 6.13.

Initial measurements were made using the first production subarrays at each wavelength, classified as commissioning grade (or CG) arrays due to functionality problems. Measurements were made using scripts to power up each stage of the readout chain in turn while monitoring the mixing chamber temperature, $T_{mc}$. The values of $T_{mc}$ were then calibrated to a power scale using measurements of the DR cooling capacity. The

test was later repeated with a second-generation commissioning grade (CG2) subarray, following changes to the design of the MUX.

A summary of the commands issued during the test sequences are shown in Table 6.14. Slightly different scripts were used for the two generations of subarray. After each change was made, the system was left to stabilise for 1–2 hours before $T_{mc}$ was logged. Although the SQUID series array amplifiers dissipate power at the third stage rather than the fourth, some earlier observations had been made that the fourth stage temperature was affected by turning on the SSAs due to the changing heat leak along the isolation supports. 60000 DAC units on the SSA bias and 32000 on the SSA feedback are effectively full range. For the test on the CG subarray, the second stage SQUID (SQ2) bias was stepped through three values, the typical range at which the SQ2s are operated, and the SQ2 feedback was turned fully on. The first stage SQUIDs were turned on with bias and feedback values again simulating normal operating ranges. Finally, the pixel heater and detector bias were turned on at 50000 DAC units, at the high end of the typical operating range. For the CG2 test, the SQ2 bias was set at a typical mid-range value rather than being stepped in order to reduce the time required to run the test script.

Some columns on each array were not functional due to electrical open circuits. A large number of columns on the 450 $\mu$m CG subarray were masked during this testing since some channels caused excess heating on the focal plane, driving the TESs above the transition point. As a consequence of the small number of functional columns on the 450 $\mu$m array, the temperature changes as each element was turned on were effectively too small to distinguish from background fluctuations of the mixing chamber temperature. Sensible results could only be obtained for the 850 $\mu$m CG subarray, as illustrated in Fig. 6.19. In this plot, the step numbers refer to the commands issued in the test sequence (see Table 6.14), with the DR mixing chamber temperature plotted for each change. From measurements of the cooling capacity, the mixing chamber temperature may be calibrated to give an approximate power dissipation for each step in the sequence.

The clear result of this measurement is that the subarray is dissipating a considerable amount of power, far more than expected from even the maximum dissipation

**Table 6.14:** Summary of array power dissipation test sequences for the 850 $\mu$m and 450 $\mu$m commissioning grade arrays. The step number is used to identify the measured power dissipation in the results. Values associated with each command are DAC units. See text for explanation of the individual steps. The first sequence was used to test the original CG subarrays, and the second to test the second-generation 850 $\mu$m CG subarray.

| Step Number | CG subarray | CG2 subarray |
|---|---|---|
| 1 | SSA bias 60000 | SSA bias 60000, feedback 32000 |
| 2 | SSA feedback 32000 | SQ2 bias 32000 |
| 3 | SQ2 bias 15000 | SQ2 feedback 32000 |
| 4 | SQ2 bias 30000 | SQ1 bias 10000 |
| 5 | SQ2 bias 45000 | SQ1 bias 15000 |
| 6 | SQ2 feedback 32000 | SQ1 feedback 8000 |
| 7 | SQ1 bias 10000 | Pixel heater 65000 |
| 8 | SQ1 bias 15000 | Detector bias 65000 |
| 9 | SQ1 feedback 8000 | ... |
| 10 | Pixel heater 50000 | ... |
| 11 | Detector bias 50000 | ... |

figures listed in Table 6.13. Fully switched on, the subarray was found to dissipate approximately 17 $\mu$W, rather than 2.6 $\mu$W as anticipated for the maximum power levels. The power dissipation was dominated by the first stage SQUID feedback. A summary of the expected and measured power levels is shown in Table 6.15.

The initial explanation for the anomalously high power dissipation on the commissioning grade arrays was contamination in the multiplexer vias from the fabrication process. During the fabrication of niobium wafers, the formation of niobium pentoxide, which does not undergo a superconducting transition, is common. The consequence of this is that there will be resistive sections of the array, greatly increasing the dissipated power due to Joule heating. Changes were subsequently made to the MUX fabrication process, greatly decreasing the number of vias on the wafer. The new generation multiplexers were used to produce the second batch of arrays.

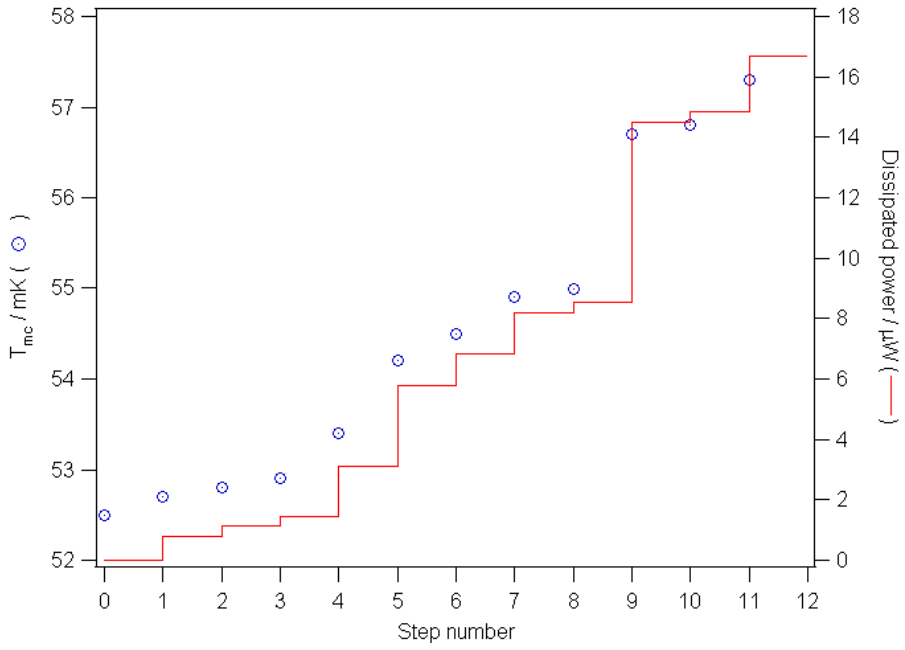


**Figure 6.19:** Plot of the mixing chamber temperature for the first-generation commissioning grade 850 $\mu$m subarray following the command script described in Table 6.14. A calibrated power dissipation scale is also shown.

Tests of the second-generation 850 $\mu$m subarray indicated similar problems, despite the redesign work (see Fig. 6.20). However, the behaviour of the second-generation subarray was different than that observed with the first-generation device. The power dissipation was dominated by the SQ1 bias and the pixel heater, rather than the SQ1 feedback. The subarray was found to dissipate a maximum of $\sim$10 $\mu$W. The contributions of the various stages are also summarised in Table 6.15.

From Table 6.15, it may be seen that the two arrays display different behaviour as the stages of the subarray are powered up. In the case of the first and second stage SQUIDs, this would be expected since the MUX wafer design was altered between the two array generations. However, the pixel heaters and SSAs were nominally identical. This suggested that the problem was not associated with the subarray itself. Unrelated work on the resistance of the array cabling indicated anomalously high resistance values on some of the wires connected to the subarrays rather than the cables fitted with shorts at the cold end. Probing of the subarrays at room temperature revealed the presence of parasitic resistances across the niobium flexes connecting the batwing circuit board to

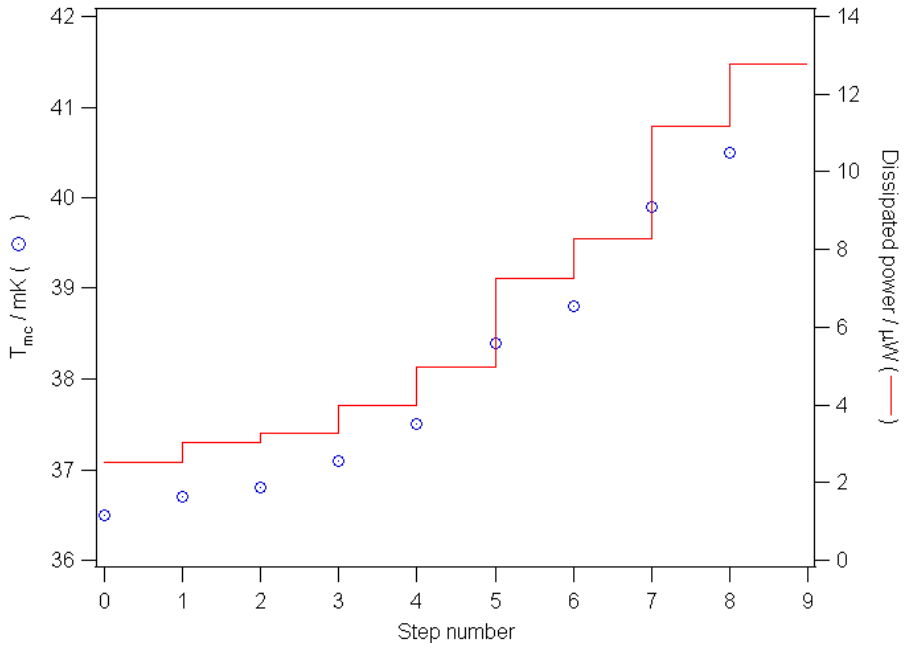


**Figure 6.20:** Plot of the mixing chamber temperature for the second-generation 850 $\mu$m commissioning grade subarray following the command script described in Table 6.14.

the 1-K PCB on certain tracks. It was found that there was a good correlation between the tracks showing high resistance and those causing excess heating. Given that testing of the niobium flexes following fabrication indicated good uniformity across individual flexes, the cause of the parasitic resistance must have been in the post-processing of the electronics modules, specifically the hotbar reflow process used to connect the Nb flexes to the circuit boards at each end. Nominally, the flex should be superconducting for the full length. However, it would appear that the reflow joints were remaining resistive when cold, causing addition power dissipation due to Joule heating effects.

A temporary solution to the problem was to mask columns showing particularly high levels of heating. A longer-term solution was implemented to redesign the electronics module to replace the Nb flexes and the hotbar reflow joints ready for the first science grade detectors. This work is described in more detail in Chapter 9.

The measured figures listed in Table 6.15 are essentially the maximum power dissipation for the subarrays. Using values closer to the typical operating conditions for the subarrays, a dissipated power of $\sim$5 $\mu$W per subarray is obtained for the original cold

**Table 6.15:** Summary of expected and measured array power dissipation figures for the first- and second-generation 850 $\mu$m subarray. Expected figures are based on the maximum power dissipation figures from Table 6.13.

| Element | Power / $\mu$W | | |
|---|---|---|---|
| | Expected | First measurement | Second measurement |
| SQUID series arrays | 0 | 1.13 | 0.48 |
| SQ2 + SQ1 | 0.48 | 13.37 | 5.27 |
| Pixel heater | 0.018 | 0.36 | 2.89 |
| Detector bias | 0.129 | 1.81 | 1.61 |
| Total | 0.627 | 16.67 | 10.25 |

electronics modules. The total power dissipation for 8 subarrays is ∼40 $\mu$W. From the measured cooling capacity of the DR, a load of 40 $\mu$W gives a mixing chamber temperature of $\sim$ 61 mK. Considering the thermal model with appropriate modification to allow for the higher power levels flowing across the bolted joints, the focal planes are predicted to be at a temperature of $\sim$ 73 mK, which is sufficiently cold for operation of the detectors at both wavelengths.

## 6.7 Cryostat Performance Operating at 22°

At the telescope, as a consequence of the optics design, the cryostat is actually orientated at 22° from the vertical. A known limitation with pulse tube coolers, unlike other types of cryocooler, is that the cooling effect is dependant on the gravity vector, and so the coolers must be orientated close to vertical to avoid loss of cooling power. The manufacturers information states that there will be no significant loss of the cooling power at up to 30° from the vertical. As part of the instrument test program prior to delivery, the cryostat was tested in the correct orientation. Cooldowns INS_CD7 to INS_CD10 were all conducted with the cryostat orientated at 22°.

It was observed that there was a slight increase in the temperature of the second stage, although any associated increase in the first stage temperature was marginal. The measurement of the temperature on the 4-K radiation shield at the interface from

the PTC wicks indicated a temperature of 3.8 K with the cryostat tilted, compared to a temperature of 3.65 K with the cryostat vertical. The temperatures of the DR still and mixing chamber were not observed to change significantly, with any variation in performance due to the system being tilted being at the level of normal variations between cooldowns.

The performance of the PTCs in the two positions may be compared used the polynomial fits to the nominal performance data of the second stage. In the same way as the load on the PTC was determined previously, an "effective load" may be calculated for the higher operating temperature. This assumes that the true power load has not changed between the two measurements, which is not unreasonable. Since the power flowing along the wicks are the same, the $\Delta T$ for the link to the PTCs listed in Table 6.4 will be the same, giving a PTC temperature of 3.1 K (compared to 2.96 K in INS_CD1). From the polynomial fit, this is an effective load of 270 mW on the PTC. Comparison of this value to the 198 mW determined previously, this is approximately a 27% loss of cooling capacity.

Measurements of the base temperature of the PTC integrated with the dilution refrigerator in the test cryostat as a function of orientation are shown in Fig. 6.21. The DR test cryostat was mounted on a flexure rig and cooled to $\sim$ 4 K with no helium mixture in the system. After allowing time for the base temperature to settle, the cryostat was rotated incrementally (in the same direction as the DR insert is mounted in the instrument cryostat), and the base temperature of the PTC second stage recorded. The PTC second stage temperature in the vertical orientation was 3.21 K, increasing to 3.34 K at 22° and 3.39 K at 25°. Comparison of these measurements using the polynomial fits to the nominal second stage cooling power (§6.3) indicates a reduction in cooling capacity of $\sim$ 23% at 22°. This would imply that the reduction in cooling capacity determined previously for the coolers on the instrument cryostat is consistent with that measured from the DR pulse tube, allowing for variations in the performance of individual systems.

This analysis indicates that there is no significant issue with the performance of the instrument cryostat in the tilted orientation.

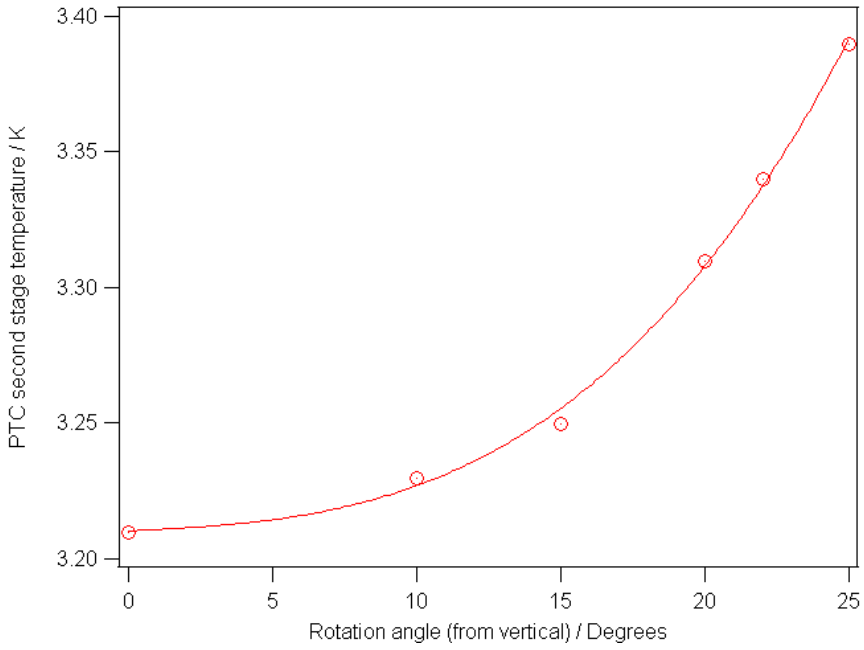


**Figure 6.21:** Measured pulse tube second stage base temperature in the DR test cryostat, as a function of rotation angle.

## 6.8 Anomalous Performance During Cooldown 9 and 10

At the start of INS_CD9, problems were experienced with the startup of the dilution refrigerator. The issue was diagnosed as a blockage in the dilution circuit due to mixture contamination and a buildup of frozen gas in the cold traps, both resulting from a leaking O-ring. The blockage in the circuit was cleared by partially warming the system to ∼90 K while pumping, followed by cooling back to 4 K. To avoid further problems, the helium mixture was dumped and replaced. Following startup, it was found that the DR achieved lower base temperatures than had been recorded on previous cooldowns. Similar performance was achieved during INS_CD10. The measurements described were taken during cooldown 10.

The temperature distribution of the third stage is summarised in Table 6.16. The still temperature with no additional heat load was 880 mK, compared to 1030 mK on earlier cooldowns. The temperature of the 1-K box was measured as 954 mK, rising to 1000 mK on the outer cover of the 850 $\mu$m focal plane unit.

**Table 6.16:** Measured temperature distribution through the third stage system during INS_CD10.

| Location | Temperature / mK |
|---|---|
| Still | 880 |
| 1-K radiation shield (warm side of joint 2) | 954 |
| 850 $\mu$m focal plane unit outer cover | 1000 |

**Table 6.17:** Measured temperature distribution through the fourth stage system during INS_CD10. The location of the measurements refers to the block diagram of the fourth stage shown in Fig. 6.10.

| Location | Temperature / mK |
|---|---|
| Mixing chamber | 35.1 |
| Millikelvin strap (warm side of joint 1a) | 35.8 |
| 450 $\mu$m focal plane (warm side of joint 3) | 37.2 |
| 850 $\mu$m focal plane (warm side of joint 3) | 38.6 |
| $\Delta T$ to 450 $\mu$m focal plane | 2.1 |
| $\Delta T$ to 850 $\mu$m focal plane | 3.5 |

The temperature distribution of the fourth stage is summarised in Table 6.17. The mixing chamber temperature with no additional load was 35.1 mK, rising to 37.2 mK on the 450 $\mu$m focal plane and 38.6 mK on the 850 $\mu$m focal plane. The temperature changes along the mK system are broadly consistent with those measured on previous cooldowns, implying no major change in the power flowing across the joints. The major difference is that the difference in temperatures between the 450 $\mu$m and 850 $\mu$m channels is considerably reduced compared to earlier measurements. This would imply that the bad joint causing the large temperature drop along the 850 $\mu$m channel was improved during reassembly. A measurement of the cooling capacity of the DR is illustrated in Fig. 6.22. The mixing chamber was found to have a cooling power of 30 $\mu$W at 47 mK and 100 $\mu$W at 65 mK.

The explanation for this change in performance is not clear. The change is not connected to the operation of the cryostat tilted at 22° since the previous two cooldowns were conducted in the tilted orientation with no noticeable change in the DR performance. Changes in the mixture ratio would be one obvious possibility, but this is unlikely since the parameter space of mixture volume and ratio had been covered extensively throughout the run time of the DR. A further possible cause would be the removal of a short or other heat leak in the DR system. However, the DR insert was not removed from the instrument cryostat between INS_CD8 and CD9, making the removal of a short due to wiring or other hardware unlikely. The most likely explanation is believed to be that there was some form of contamination in the DR capillaries or 4-K traps causing a flow restriction or internal conduction short. Following the helium charge being dumped and the insert flushed with clean $^4$He, such contamination could have been cleared.

If we consider a $t$-function analysis for the DR performance, illustrated in Fig. 6.23, a value of $\dot{Q}_{Leak} = (35.5 \pm 0.8)$ $\mu$W is recovered from the fit, with a $^3$He circulation rate similar to that from the earlier analysis for the DR performance in the instrument cryostat. Given that the new value of $\dot{Q}_{Leak}$ is lower by a factor 2 over the value recovered for the DR in the test cryostat, it is implied that the cause is internal to the DR insert, rather than a result of a change associated with the instrument cryostat. The reduction in the still temperature would result in better cooling of the $^3$He flow on the concentrated side of the dilution circuit, which would explain the lower value of $\dot{Q}_{Leak}$, with the reduced value of $T_{still}$ caused by the removal of a heat leak higher up in the DR.

Given the higher than expected power dissipation figures from the subarrays, the improvement in the DR performance is a considerable advantage since the lower bath temperature gives more overhead for load on the fourth stage. Based on the cooling power measurement depicted in Fig. 6.22 and assuming the power dissipation figures for each subarray used in Sect. 6.6.1, an operating temperature of $<$50 mK would be expected.

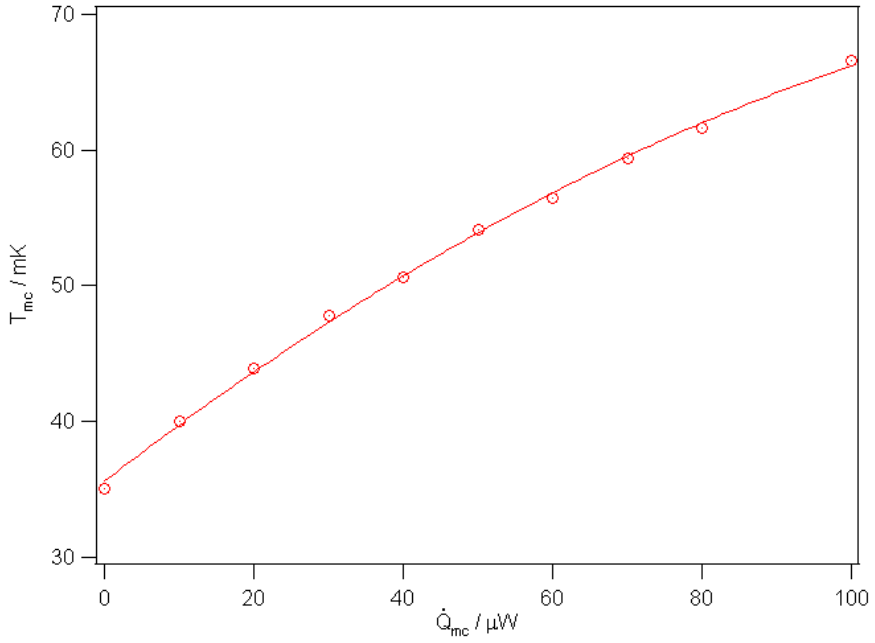


**Figure 6.22:** Measured cooling capacity of the dilution refrigerator mixing chamber during INS_CD10.

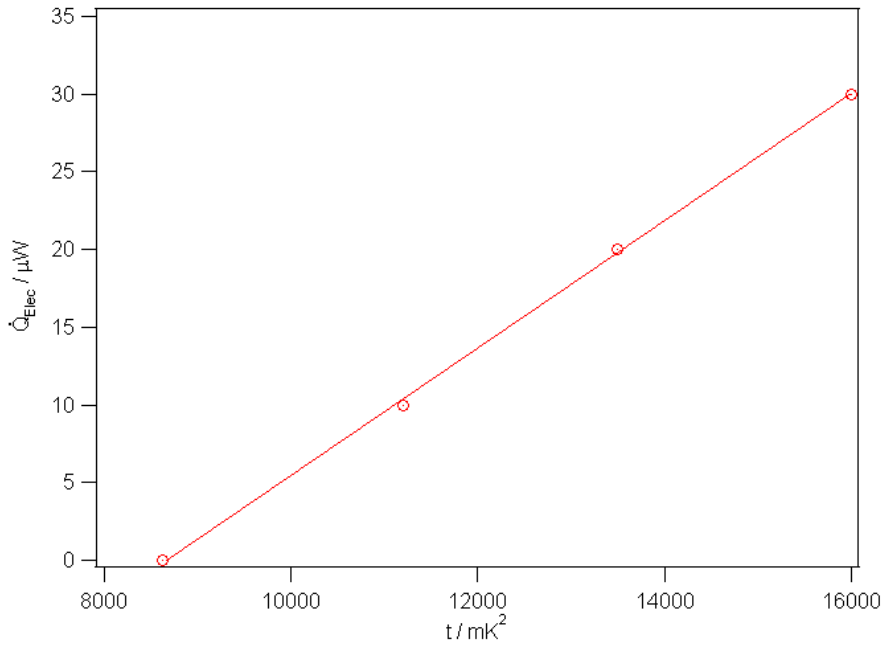


**Figure 6.23:** Measured mixing chamber temperature plotted as the $t$-function (assuming $^3$He input temperature is equal to the mixing chamber temperature) plotted as a function of applied electrical power. Data collected during INS_CD10.

## 6.9 Instrument Cryogenic Performance at the JCMT

Following installation of the instrument at the JCMT, the first cooldown at the summit (JCMT_CD1) started on 02 June 2008, with precool completed on 27 May, followed by start up of the dilution refrigerator. The DR started successfully on the first attempt with only minor issues associated with the loading on the circulation turbo pumps.

The base temperatures of the 60-K and 4-K shields were found to be consistent with the performance measured on previous cooldowns, and described in §6.3. Unlike cryogenic systems using liquid cryogen baths, the behaviour of cryocoolers would not be expected to be affected by operation in reduced atmospheric pressure. The temperatures of the first and second stages were consistent with those measured in the lab with the cryostat in the tilted orientation prior to delivery to the telescope.

The performance of the dilution refrigerator was found to be consistent with the performance measured during INS_CD4–CD8, rather than the improved performance achieved during INS_CD9 and CD10. The base temperature achieved after optimisation of the mixture was 48 mK. Although the reversion to the earlier performance levels on replacement of the helium charge is unfortunate, as noted previously operation of a full complement of detector arrays is perfectly possible even at the elevated temperature.

## 6.10 Summary

The design and performance of the main SCUBA-2 cryostat has been described in this chapter, including the predicted performance of the stages from thermal modelling and measurement data collected during operation of the cryostat, with comparison between the predicted and measured performance.

The base temperature of the first instrument stage was found to range between 36.8 and 47.9 K, with a temperature on the PTC of 35.2 K. This operating temperature is consistent with a power load of ∼38 W, considerably lower than the predicted power loading of ∼100 W. It is likely that the difference in the power loading is due to the effectiveness of the multilayer insulation on the 60-K radiation shield being better than anticipated in the thermal model, thus reducing the radiated power load from 300 K. The temperature gradient across the shield and across the wick to the PTCs are consistent with this reduced power loading. The instrument second stage was found to have a

temperature range of 3.65 to 4.10 K, and a temperature on the PTC cold finger of 2.96 K. This is consistent with a power load of ∼0.4 W. Again, this is lower than the predicted power figures, but is consistent with the reduced conductive and radiative loading from the lower temperature of the first stage.

The power loading on the DR still from the 1-K instrument stage was found to be ∼10 mW, considerably higher that the expected loading of ∼0.6 mW. The origin of the excess power loading is not clear. The resulting still temperature is 1.03 K, with a temperature at the 1-K box of 1.16 K and ∼1.34 K at the focal plane units.

The base temperature of the mixing chamber in the instrument was found to be ∼53 mK. Analysis of the cooling power of the system in the instrument indicated a load of (87±2) $\mu$W. Assuming an internal heat leak due to the DR system of 75 $\mu$W, as recovered from the analysis carried out in Chapter 5, a background power loading from the millikelvin thermal system of (12±2) $\mu$W. Analysis of the power loading on the fourth stage from early generation detector arrays was also presented, indicating that the current detectors dissipate considerably more power than originally intended (∼5 $\mu$W, compared to 1–2 $\mu$W). The excess power dissipation was found to be connected with a structural issue that is currently undergoing redesign.

Discussion of the performance changes with the cryostat in a tilted orientation for mounting on the telescope was presented, with the only significant change being the cooling capacity of the second stage of the pulse tube. This was shown to be consistent with measurement of the PTC performance change using the DR pulse tube in the small test cryostat. The behaviour of the instrument during the first commissioning cooldown at the summit was described briefly. As anticipated, the base temperatures and performance of the system was found to be consistent with that measured in the lab at sea level.

# Chapter 7

# Magnetic Shielding I: Background and Finite-element Modelling

Superconductivity and magnetism are two physical phenomena that have always been closely linked. The behaviour of superconducting materials alters in the presence of magnetic fields, hence magnetic fields around superconducting devices such as SQUIDs must be controlled to a level where the devices will behave as required. In the case of detector arrays such as those used in SCUBA-2, the arrays must be well shielded against magnetic fields in order that the transition edge sensors maintain the required sensitivity, and for the SQUID-based multiplexers and amplifiers to function.

This chapter discusses the interaction of magnetic fields with the superconducting devices in SCUBA-2, and the methods by which these fields can be controlled. The results of the design and finite-element modelling process for the shielding are presented. The finite-element modelling described builds on earlier work carried out as part of the design process of the instrument. The work of this author extends the original work to a detailed design and performance model. In addition to the presented review of techniques for control of magnetic fields, the modelling work described is the work of this author.

Details of the finite-element electromagnetic modelling work presented in this chapter has previously appeared in the *Proceedings of the SPIE* as "Finite-element Modelling of Magnetic Shielding for SCUBA-2" [154].

## 7.1 Motivation and Background

### 7.1.1 The Effects of Magnetic Fields on the SCUBA-2 Detectors

The behaviour of both the TES devices and SQUIDs will be affected by the presence of magnetic fields. SQUIDs are extremely sensitive magnetometers. The presence of a strong AC magnetic field will modulate the current flowing in the SQUIDs. For weak fields, this would appear as an additional modulation in the output from the devices, which would be indistinguishable from a science signal. In a stronger field, the modulation could have an amplitude large enough to exceed the critical current for part of the cycle and drive the SQUIDs into the normal state, effectively rendering the devices useless. A DC field will change the output level from the devices, again appearing as an additional signal on the readout. The SQUID series array amplifiers are more sensitive to the field effects than the SQUID multiplexers as the presence of a strong field could induce phase differences along the series chain of SQUIDs in the array, impairing the signal amplification.

The TESs operate in a mixed superconducting state, and a strong field will prevent the devices going superconducting. The presence of magnetic flux at the detectors could lead to problems with flux becoming pinned in the TES bilayer as the devices moves between the normal and superconducting states. Furthermore, one of the factors that control the sensitivity of the TES detectors is the width of the transition region. The presence of an AC or DC magnetic field will broaden this transition, reducing the sensitivity of the pixels. The TES devices also have some susceptibility to noise from moving flux vortices threading through the superconducting layer.

### 7.1.2 Magnetic Field Requirements

The design of the SQUIDs used for the SCUBA-2 detectors offers a number of advantages in terms of shielding from magnetic fields. Firstly, noise caused by moving flux vortices trapped in the superconducting loops is not an issue for niobium SQUIDs,

since the niobium efficiently pins the flux. Furthermore, planar SQUIDs are insensitive to tangential magnetic fields due to the negligible area of the SQUID loop and input coils in the plane of the device, so only the normal component of the field will have a significant effect on the device behaviour.

The magnetic field requirements at the detector arrays are based upon modelled performance for shielding used in TES and SQUID test cryostats at the National Institute of Standards and Technology. The broadening effect on the TES superconducting transition width is estimated to be negligible for a DC magnetic field of up to 1 mT, and for an AC field of up to 3 $\mu$T. Critical current modulation in the SQUIDs is only an issue for AC fields greater than 1 $\mu$T. The output of the SQUIDs in the multiplexer is linearised using an operating mode known as flux locking, in which a feedback loop is established from the output of the series array amplifiers to the multiplexer. There was particular concern that strong fields at the 60 Hz mains frequency and harmonics could cause the readout electronics to lose flux lock, and hence the multiplexer SQUIDs to behave non-linearly.

The effect of AC fields with frequencies much greater than the detector time response may be disregarded. As discussed in Chapter 3, the maximum time constants of the SCUBA-2 detectors are 1.5 and 2.8 ms at the short and long wavelength respectively, giving a 3 dB frequency roll-of of 100 and 50 Hz. Including a reasonable margin on the frequency response, and taking the other field information into account, the baseline requirement for the magnetic field at the SCUBA-2 detectors was that the normal field component over the frequency range 0–200 Hz must not exceed 100 nT [155].

### 7.1.3 Principles of Magnetic Field Control

There are essentially two methods by which magnetic fields can be controlled in an experimental volume. Either a magnetic field can be applied such that the field resulting from the geomagnetic field or other sources in the vicinity is reduced, or the experimental space can be shielded by materials that exclude magnetic flux from the enclosed volume. The same principle can be used to contain flux around a localised field source such as a motor. These techniques are discussed in more detail in the following sections.

### Field Cancellation

It is possible to cancel the effects of a magnetic field by generating an equal strength field in the opposite direction, leaving a zero overall sum. Such a field may be generated by a simple solenoid. This approach is most effective for a static field, or a field that changes in a well-understood way, such as the field from a ramping electromagnet in an adiabatic or nuclear demagnetisation refrigerator [130]. Such systems have been designed for use with TES microcalorimeters and SQUID electronics, such as for the ATSSI (Advanced Technology Solar Spectroscopic Imager) sounding rocket experiment [156].

### Shielding

Magnetic shielding can be provided by either superconducting shields, or by materials with a high magnetic permeability (mu-metals). The two materials interact with magnetic fields in different ways. Superconducting shields exclude magnetic flux, while mu-metals attract flux by providing a low-reluctance path. The properties of the two types of shielding materials are discussed below.

**Superconductors** All systems of particles will tend to occupy the ground state unless excited by an external source of energy. In certain materials, it is possible for electrons to achieve a lower energy state than the normal single particle ground state by forming pairs, called Cooper Pairs. The Cooper Pairs will all have the same net momentum and hence be described by the same wavefunction (although with different phases). This is known as the superconducting state, the origin of the name being the zero resistance properties of the particle state. Superconducting materials are useful for shielding against magnetic fields since superconductors effectively display perfect diamagnetism.

It can be shown that if a magnetic field is applied to the surface of a superconductor, then a screening current will be generated at the surface to oppose the applied field. Both the magnetic field and the screening current density will decay exponentially with depth into the material, described by

$$B(x) = B_0 \exp\left[-\frac{x}{\lambda}\right], \tag{7.1}$$

where $B_0$ is the field at the surface and $\lambda$ the London penetration depth. As a su-

perconductor cools through the transition (or critical) temperature, $T_c$, any magnetic field in the material will be expelled by the generation of screening currents (an effect first observed by Meissner and Ochsenfeld in 1933 (see Ref. [157] for a translation of the original work), and generally known as the Meissner effect). Depending on the geometry of the superconductor, this can lead to the trapping of magnetic flux in normal regions in the material, or in space enclosed by superconducting regions (for example, the space enclosed by a ring of superconductor). Superconductors also have a critical field, $B_c$, above which the screening currents will break down and the superconductivity quenched. It can be shown from free energy arguments that that when $B = B_c$, the normal state is energetically favourable to the superconducting state, and a phase transition occurs. As the screening currents break down, flux will penetrate the material.

Superconducting materials are classified as either type I or type II based on the characteristics of the superconducting-normal interface for the material. The two types display different responses to an applied magnetic field. Type I superconductors, which behave exactly as described above, are all elemental, with low transition temperatures (lead having the highest transition temperature of a type I superconductor, 7.19K). Type II superconductors are predominantly alloys and ceramic materials (with the exception of niobium, vanadium and technetium). Type II materials have higher transition temperatures (up to $\sim$190 K), but have two critical fields. If the applied field is greater than the lower critical value, $B_c$, vortices of magnetic flux can thread through the material. However, unlike the type I superconductors, the screening currents in a type II material do not break down completely, but rather the superconductor enters a mixed state. If the applied field exceeds the higher critical field, $B_{c2}$ then the superconductivity is completely quenched as in type I materials. The existence of this mixed state allows type II materials to carry very large supercurrents without destroying the superconductivity.

The behaviour of superconductors can be described by four main parameters. These are the critical temperature, $T_c$, the critical field, $B_c$, the penetration depth, $\lambda$, and the coherence length,[1] $\xi$. Table 7.1 shows the properties of several representative superconducting materials (both type I and II) at a temperature of $T \to 0$ K.

[1]The coherence length is a parameter that comes out of the wavefunction used to describe the Cooper Pairs in BCS theory, but in qualitative terms can be interpreted as the size of a Cooper Pair in the superconducting region.

However, the critical field, penetration depth and coherence length are all functions of temperature, as described for a general temperature $T$ by Eqs. (7.2– 7.4). Here, the subscript zero denotes the value of the parameter at $T = 0$ K. Table 7.2 shows the properties of the elemental superconductors listed in Table 7.1 at a temperature of 1 K.

$$B_c(T) \approx B_{c0}\left[1 - \left(\frac{T}{T_c}\right)^2\right], \tag{7.2}$$

$$\lambda(T) = \frac{\lambda_0}{\sqrt{\left[1 - \left(\frac{T}{T_c}\right)^4\right]}}, \tag{7.3}$$

$$\xi(T) \sim \frac{\xi_0}{\sqrt{\left[1 - \left(\frac{T}{T_c}\right)\right]}}. \tag{7.4}$$

**Mu-metals** The high magnetic permeability of mu-metals provides a low-reluctance path for magnetic flux. Mu-metal is generally an alloy of iron and nickel (although some variations exist between manufacturers). If a high permeability material is placed in a magnetic field, then the magnetic flux will become concentrated in the material, effectively attenuating the field strength around the material. The higher the value of the magnetic permeability, the more effective the material is at channelling flux. The other important parameter that characterises the behaviour of mu-metals is the saturation field. Once the applied magnetic field exceeds the saturation field, the material ceases to offer a low reluctance path for the flux and the mu-metal is no longer effective as a shield. The nickel content of the alloy is adjusted to vary the properties of the mu-metal, producing either an alloy with a high permeability at the expense of a reduced saturation field (typically 75–80% nickel), or a high saturation alloy with a reduced permeability (40–50% nickel).

The value of magnetic permeability, and therefore the effectiveness of mu-metal as a shielding material, is strongly temperature-dependant. “Ordinary” mu-metals at 4 K are only ∼10% as effective as at 300 K. While ordinary mu-metal will be suitable for shielding on the inside or outside surfaces of the vacuum vessel, it would not be suitable for use on the lower-temperature stages. As an alternative, specialist mu-metals are

**Table 7.1:** Properties of selected superconducting materials as $T \to 0$ K. For the Type II superconductors, $B_c(0)$ is the first critical field.

| Material | Type | $T_c$ /K | $\lambda_0$ /nm | $\xi_0$ /nm | $B_c(0)$ /mT |
|---|---|---|---|---|---|
| *Non-transition elements* | | | | | |
| Al | I | 1.18 | 50 | 1600 | 10 |
| In | I | 3.41 | 64 | 440 | 28 |
| Sn | I | 3.72 | 51 | 230 | 30 |
| Pb | I | 7.19 | 39 | 83 | 80 |
| *Transition elements* | | | | | |
| V | II | 5.4 | ··· | ··· | 125 |
| Nb | II | 9.25 | 44 | 40 | 127 |
| *Ceramic cuprates* | | | | | |
| (La/Sr)$CuO_4$ | II | 36 | 100 | 2.5 | 900 |
| $YBa_2Cu_3O_{7-\delta}$ | II | 93 | 130 | 1.5 | 1000 |

**Table 7.2:** Properties of the elemental superconductors from Table 7.1 at $T = 1$ K. For the Type II superconductors, $B_c(0)$ is the first critical field.

| Material | Type | $T/T_c$ /K | $\lambda$ /nm | $\xi$ /nm | $B_c$ /mT |
|---|---|---|---|---|---|
| *Non-transition elements* | | | | | |
| Al | I | 0.85 | 72.3 | 4130 | 2.78 |
| In | I | 0.29 | 63.8 | 522.2 | 25.6 |
| Sn | I | 0.27 | 51.1 | 269.2 | 27.8 |
| Pb | I | 0.14 | 39 | 89.5 | 78.4 |
| *Transition elements* | | | | | |
| V | II | 0.19 | ··· | ··· | 120.5 |
| Nb | II | 0.11 | 44 | 42.4 | 125.5 |

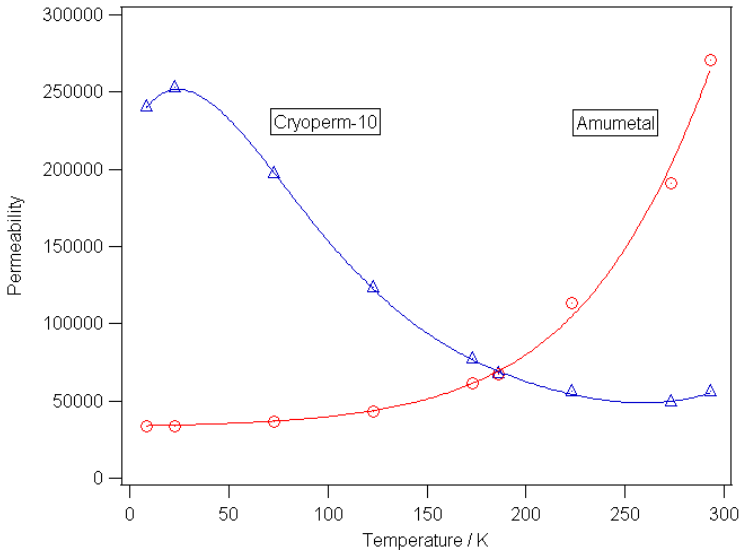


**Figure 7.1:** Plot of the magnetic permeability of Cryoperm-10 (annealed for use at 4 K) and the magnetic permeability of a representative "ordinary" mu-metal as a function of temperature.

available that are optimised for cryogenic uses. Cryoperm-10[2] is available optimised for either 77 K or 4 K, and is produced as a sheet material. Metglas[3] is a metallic-glass foil with a permeability that is only weakly dependant on temperature, and is therefore effective for cryogenic applications. The magnetic permeability of 4 K Cryoperm-10 and a generic ordinary mu-metal as functions of temperature is shown in Fig. 7.1.

The magnetic properties of selected mu-metals are summarised in Table 7.3. Metglas 2605SA1 is an iron-based high-permeability alloy, with properties listed for both the annealed and unannealed states. CO-NETIC AA and CO-NETIC B are trade names of shielding materials produced by the Magnetic Shielding Corp. and are included as examples of ordinary mu-metals.

The effectiveness of mu-metal shielding can be estimated by approximating the shield to an infinitely long cylinder. For such a geometry with diameter $d$, wall thickness $t$, and composed of a shielding material with magnetic permeability $\mu$, an applied field perpendicular to the cylinder axis will be attenuated by a factor $A$, given by Eq. (7.5). For large values of $\mu t/d$ and small $t/d$, this reduces to Eq. (7.6) [121].

[2]Amuneal Manufacturing Corp., http://www.amuneal.com.

[3]Metglas Inc., http://www.metglas.com.

**Table 7.3:** Properties of selected high-permeability shielding materials at 300 K (unless otherwise stated).

| Material | Maximum (dc) permeability | Saturation field /T |
|---|---|---|
| Metglas 2605SA1 (as cast) | 45000 | 1.56 |
| Metglas 2605SA1 (annealed) | 600000 | 1.56 |
| Cryoperm-10 (at 77 K or 4 K) | 250000 | 0.90 |
| CO-NETIC AA | 450000 | 0.80 |
| CO-NETIC B | 150000 | 1.50 |

Considering the approximation given in Eq. (7.6), the shielding factor is proportional to the thickness of the shield and its permeability, but inversely proportional to the shield diameter. Hence, for a given thickness of material, a small shield is more effective than a large shield. The figure of merit for the effectiveness of a shield geometry is $t/d$, where $d$ is either the diameter of a cylindrical shield, or the longest dimension of a rectangular shield. From this, it may be concluded that foils (such as Metglas) are unsuitable for shielding large volumes.

$$A = \frac{\mu}{4}\left[1 - \left(\frac{d}{d+2t}\right)^2\right] + 1, \tag{7.5}$$

$$A \approx \frac{\mu t}{d}. \tag{7.6}$$

There are a number of factors that must be considered during the design of mu-metal shielding. Theoretical magnetic shielding formulae tend to describe geometries of either a sphere or an infinitely long cylinder, since these forms have a high degree of symmetry and are therefore easy to model. Such shielding arrangements are not practical to construct, but ideally these geometries should be approximated as closely as possible. The preference for curved rather than angular shapes is due to the ease with which magnetic flux in mu-metal will follow gentle radii, whereas sharp corners are less effective at containing channelled flux. As discussed previously, the volume enclosed by the shielding should be kept to a minimum, since the effectiveness of a shielding layer

varies approximately as the inverse of the largest dimension enclosed. This approach also offers advantages in terms of reducing material consumption.

To ensure that flux entrapped in the shielding material is contained, shielding should be closed on all sides. If the shield is composed of separate elements, then the continuity of the shield should be maintained through contact of the components. Such an arrangement creates a closed magnetic circuit, and more closely approximates a sphere. This allows flux trapped in the material to more easily follow a continuous, low-reluctance path. For an opening in a shield face of diameter $r$, the field along the axis of the opening will decay as [121]

$$A(x) = \frac{3\pi x^3}{2r^3}. \tag{7.7}$$

Shielding design principals indicate that magnetic fields can penetrate to a distance equal to five times the diameter of the opening [158].[4] Tubular shielding can be used to prevent penetration of the fields through openings, although to be effective the length of the cylinders should be at least five times the diameter.

Attenuation of magnetic fields can be increased through the use of multi-layer, or "nested" shields. Two or more layers of high-permeability material as concentric shells, with gaps between the layers, are more effective than a single layer equivalent to the total thickness. Literature provided by the manufacturers of shielding material indicates that the spacing of the shield layers should be at least equal to the thickness of the shielding material used, although spacings of up to four thicknesses will provide a more efficient use of material. The spacing can be either free space, or provided by a magnetically "inert" material. It is vital that the nested layers are not touching at any point, otherwise the magnetic flux can "short" from one layer to another, destroying the effectiveness of the multiple shield layers.

### 7.1.4 Shielding Requirements

The major sources of magnetic fields that can affect the detector arrays are external to the instrument, namely the geomagnetic field and fields due to the telescope structure

[4]This figure is consistent with an attenuation of 5000 on the applied field. The choice of this value is empirical.

and enclosure drive motors. Measurements made at the JCMT indicated a field strength in the region of the SCUBA-2 mount of approximately 0.15 mT when the telescope drive motors are running, falling to 0.07 mT when these motors are not operating.

The two ancillary instruments associated with SCUBA-2, the polarimeter and FTS, both include a number of motors. The FTS is mounted several metres away from the main cryostat, and the polarimeter is attached to a moveable mount immediately in front of the cryostat window. Also mounted in this position is the retractable blackbody calibration source with associated drive motor and mechanism. It was specified in the design requirements of these instruments that the magnetic field strength at the main instrument cryostat does not exceed the Earth field strength. The polarimeter will be the greater issue due to the instruments proximity to the main cryostat.

Magnetic field sources within the instrument are more difficult to quantify. Although these fields are likely to be of low magnitude, the close proximity to the detector arrays may be problematic if the fields are not properly controlled. Fields generated by currents flowing in the arrays and wiring are likely to be too small to affect the array performance. Currents due to RF pickup and ground loops could be significant although it is intended that screening outside the cryostat will control these effects. Furthermore, the field due to the cold shutter motor must be considered.

In order to meet the field requirement at the detector arrays of 100 nT, the magnetic shielding must provide a total attenuation factor of 1500 for fields external to the instrument. Since it is necessary to leave apertures in the shielding to allow light to reach the detectors, the effectiveness of the shielding will have some dependance on the direction of the magnetic field relative to the instrument. Therefore, the shielding design must provide at least this attenuation factor for fields in all directions.

Concerns over the effects of magnetic flux trapped by the superconducting shielding at the 1-K stage of the instrument lead to the additional requirement that the magnetic field at the superconducting shield be reduced to $<5$ $\mu$T (10% of the Earth's magnetic field strength) when the superconducting transition of the shield occurs. The instrument can be cooled in a controlled manner, in the reduced field strength, and in an optimum orientation relative to the field. Therefore, the high-permeability shielding must be able to provide an attenuation factor of at least 15 during this time.

### 7.1.5 The Shielding Strategy for SCUBA-2

The basic shielding approach for SCUBA-2 was composed of several stages. Firstly, superconducting shielding at the 1-K stage was intended to provide the majority of the required magnetic field attenuation at the detectors. Any flux trapped by the superconducting layers would be a potential problem, so mu-metal shielding would be added to the vacuum vessel and radiation shields as necessary to reduce the field strength in the volume enclosed by the superconducting shield when the transition temperature is reached. Shielding at ambient temperature on the vacuum vessel was the primary choice, since this would minimise the impact on the instrument cold structures. The baseline shielding design is summarised in Table 7.4 and the block diagram in Fig. 7.2, and is discussed here in more detail.

Shielding at ambient temperature on or external to the vacuum vessel may be provided by any of the available "ordinary" mu-metal alloys. The magnetic environment at the JCMT is such that the instrument will not be exposed to a strong field, so the mu-metal alloy does not require a high saturation field. This will allow an alloy with high magnetic permeability to be used, providing a more effective shield. However, as discussed previously, the permeability of these alloys would be greatly reduced if used on any of the cryogenic stages of the instrument. Two candidate materials for cryogenic shielding were identified, Cryoperm-10 and Metglas. Metglas is a thin foil material, making it unsuitable for shielding large volumes due to the number of layers required and the difficultly in covering large areas. As a result, Cryoperm was selected as the best material for shielding on the 60-K and 4-K stages if this proved to be necessary.

Although the 1-K stage of the instrument is composed of aluminium, the transition temperature of the alloy used in the manufacture (aluminium 6082 T6) was expected to be lower than the 1.1 K critical temperature of the pure metal, and so could not be relied upon to cool into the superconducting state. A measurement of the 6082 $T_c$ gave a value of 0.97 K [159], which at the expected operating temperature of the 1-K box would make the structure entering the superconducting state marginal. Additional material with a higher transition temperature was therefore to be added to the 1-K stage to provide a superconducting shield. To reduce the effects of any magnetic flux trapped by the superconducting shielding, further high-permeability shielding would be

**Table 7.4:** Summary of the baseline magnetic shielding design for SCUBA-2. At each stage, the approximate composition of the shielding is described with nominal values for the thickness of the shielding layers.

| Structure | Shielding | Approximate thickness |
|---|---|---|
| Focal plane | Superconducting groundplane behind detector array | 5 $\mu$m molybdenum |
| SQUID series arrays | Outer superconducting can over high-permeability shield | 1 mm thick niobium, 0.5 mm Cryoperm-10 |
| Focal plane units | Superconducting shield over Metglas foil | $\sim$ 100 $\mu$m s/conductor $\sim$ 100 $\mu$m Metglas |
| 1-K box | Superconducting shield over Metglas foil | $\sim$ 100 $\mu$m s/conductor $\sim$ 100 $\mu$m Metglas |
| Cold shutter motor | High-permeability shield | $\sim$ 100 $\mu$m Metglas or Cryoperm |
| 4-K optics box | Cryoperm high-permeability shielding (if required) | $\sim$ 1 mm Cryoperm |
| 60-K radiation shield | Cryoperm high-permeability shielding (if required) | $\sim$ 1 mm Cryoperm |
| Vacuum vessel | Mu-metal high-permeability shielding inside vessel | $\sim$ mm mu-metal |

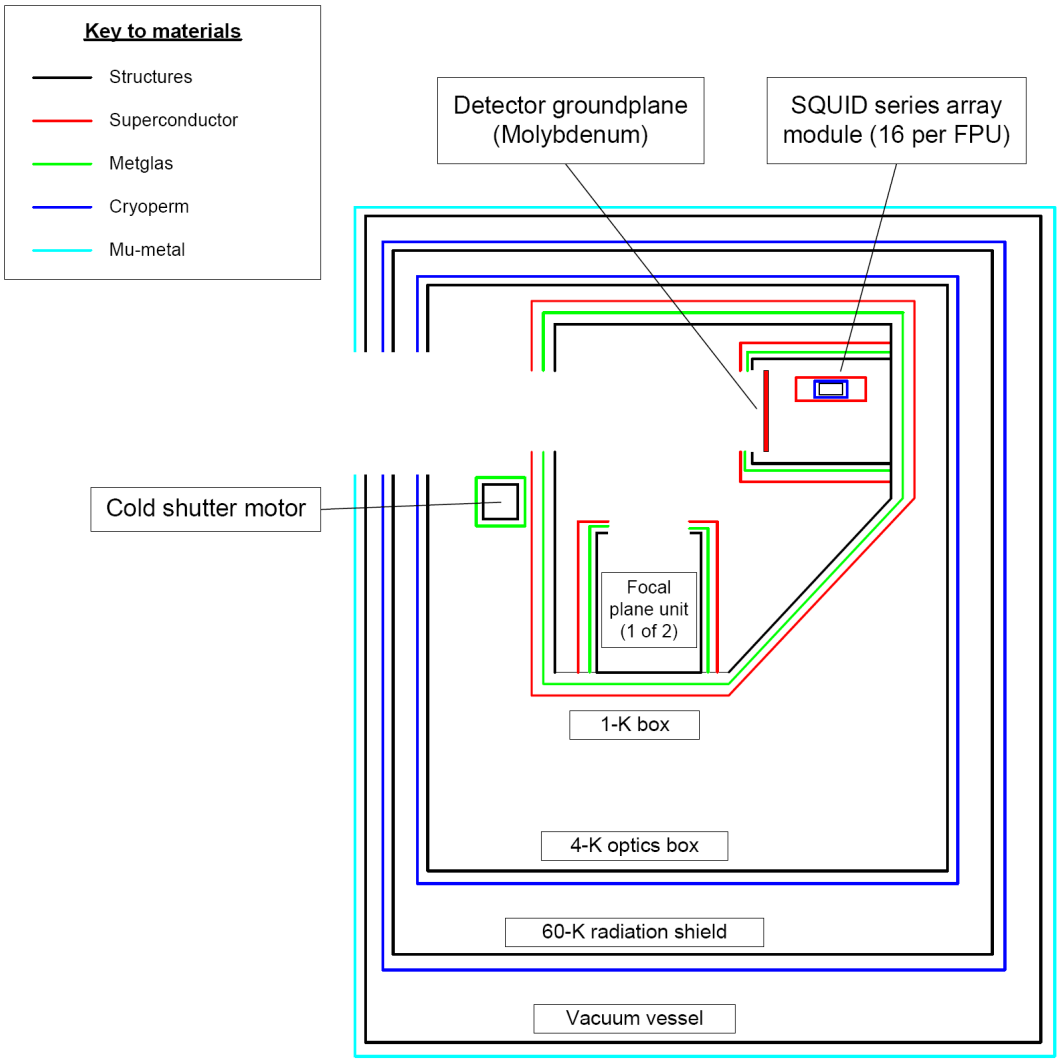


**Figure 7.2:** Block diagram of the SCUBA-2 outline shielding design indicating the main structures and associated shield layers. Nominal dimensions for the proposed shield layers are included in Table 7.4.

included inside the superconducting shield. Data from testing of the multiplexer devices suggest that Metglas shielding is useful for reducing low frequency noise in the SQUID circuits [155], making Metglas foil the obvious choice for this additional shielding.

If availability of material is taken as the first consideration for the selection of the superconductor to use in the shielding, then any of the elemental superconductors are readily available either for application by direct deposition (for example, sputtering onto aluminium) or in the form of foils. The properties of these candidate materials are listed in Table 7.1. If it is assumed that the shielding layer will be well heatsunk to the 1-K box, then the material properties at $T = 1\text{K}$ are given in Table 7.2.

The use of type II superconductors as shielding materials can be seen as problematic due to the mixed superconducting state allowing penetration of magnetic flux. However, to avoid the potential for trapping significant flux in the niobium SQUIDs as the devices enter the superconducting state, it was judged that the magnetic shielding should pass through the superconducting transition before the SQUIDs did so, making niobium the best choice for shielding. Lead was selected as a second choice material in case of fabrication issues with niobium since, although suitable, the slightly lower transition temperature (7.19 K, compared to 9.25 K for niobium) would make meeting this cooldown requirement more problematic. Issues associated with the Type II behaviour of niobium were judged to be a secondary consideration since the expected field strengths inside the cryostat were well below the critical field.

Superconductors do not completely exclude magnetic flux lines, but rather cause them to decay exponentially in a surface skin, defined by the penetration depth. Generally, for a shielding layer to be effective, the layer must be more than three penetration depths in thickness. Furthermore, if the thickness of the layer is of the order of or less than one coherence length, the Cooper pairs will overlap significantly with the normal state material outside the superconducting layer, leading to different properties from those of a "pure" layer. This is called the proximity effect. In general, a proximitised layer will have a lower critical field than a pure layer, while the transition temperature may be enhanced or suppressed depending upon the properties of the normal metal. Therefore, the penetration depth and coherence length dictate the minimum thickness for a superconducting shielding layer. Although the direct deposition of a suitable

shielding layer onto the aluminium structure of the 1-K box was considered, this approach was rejected due to the need for special equipment for the process. The thinnest available foils are thick enough to avoid the proximity effect.

The characteristics of the available Metglas alloys are summarised in Table 7.5, in each case with the annealed and unannealed (as cast) values. Due to the need to apply the Metglas foil to the structure of the 1-K box, it was judged impractical to anneal the shielding. As is the case for the mu-metal on the vacuum vessel, the cryogenic shielding will not be subject to strong magnetic fields, and hence a high saturation induction is not necessary. Metglas 2705M, a cobalt-based alloy, was identified as the best candidate for the 1-K box shielding since this alloy has the highest magnetic permeability without annealing, and so will provide the most effective shield.

Some shielding is further provided by components already integrated into the instrument design. In the subarray module design, a layer of molybdenum on the back of the multiplexer wafers acts as a superconducting ground plane behind the arrays. This is particularly important for shielding the detectors from fields generated by Johnson noise currents in the copper array supports. Other superconducting layers and components present in the subarray module design, such as superconducting flexes around the edges of the arrays, will add to the shielding effect.

## 7.2 Finite-Element Modelling

### 7.2.1 Method and Modelling Inputs

To develop and demonstrate the design of the magnetic shielding for SCUBA-2, a three-dimensional finite-element magnetic modelling method was employed. A commercial software package,[5] Ansoft® Maxwell 3D™, was selected for the modelling work.

#### Description of the Modelling Software

The modelling was carried out initially using Maxwell 3D version 6, and later version 10. Maxwell 3D calculates the magnetic field inside a volume given user-specified boundary conditions. The software package includes a drawing application to construct three-

[5] Ansoft Corporation, http://www.ansort.com.

**Table 7.5:** Properties of Metglas alloys.

| Material | Maximum permeability | Saturation induction /T |
|---|---|---|
| *As cast* | | |
| 2605SA1 | 45000 | 1.57 |
| 2605CO | 120000 | 1.80 |
| 2605S3A | >20000 | 1.41 |
| 2605SC | >40000 | 1.61 |
| 2826MB | >50000 | 0.88 |
| 2705M | 290000 | 0.77 |
| 2714A | >80000 | 0.57 |
| *Annealed* | | |
| 2605SA1 | 600000 | 1.57 |
| 2605CO | 400000 | 1.80 |
| 2605S3A | 35000 | 1.41 |
| 2605SC | 300000 | 1.61 |
| 2826MB | 800000 | 0.88 |
| 2705M | 600000 | 0.77 |
| 2714A | 1000000 | 0.57 |

dimensional models, for which the user can then specify material properties, boundary conditions and excitations. The finite-element magnetic modelling method divides the volume of the model into a tetrahedral mesh and solves for the electric field on the mesh in the frequency domain. The problem is converted into a set of linear equations in the form of a matrix, and a field solution is obtained by inverting the matrix for the initial mesh. The mesh is then refined based on the local field strength, and the refined field solution is compared with the previous solution. This process is iterated until user-specified convergence criteria are satisfied. The software also includes tools for visualising the field solutions on planes or in volumes as required.

### Shield Models

The shielding geometries in the models were produced by mapping flat surfaces onto existing 3D models of the instrument vacuum vessel and radiation shield structures. For the vacuum vessel, 60-K and 4-K radiation shields, each surface was modelled as a continuous section of material, with apertures positioned as appropriate. This basic shield design was then modified to change the thickness of the surfaces, the number of layers and the separation of the layers.

The shielding layers on the vacuum vessel and radiation shields were of the order of 1 mm in thickness. Since the overall shield models were large (of the order of 1 metre) compared to this thickness, the models were approaching the maximum aspect ratio that can be handled by Maxwell 3D (documented as $10^4$). Even the basic shielding geometries required large mesh sizes to achieve accurate solutions. Problems were encountered in the modelling process as more concentric shield layers were added to the geometries and the mesh size exceeded the available 32-bit address space. In a number of instances, it was necessary to model the vacuum vessel and cryogenic stage shields separately to overcome this limitation.

Modelling of the 1-K stage shielding comprised separate models for the 1-K box and the focal plane units, each solved for Metglas and superconducting shielding.

### Material Models

A large number of materials are modelled in the Maxwell 3D package, although only a generic "ordinary" mu-metal model is included. The $B$-$H$ characteristics of the more specialised shielding materials differ sufficiently from the generic behaviour that models for Cryoperm and the Metglas alloys were derived from the basic model by modifying the existing $B$-$H$ behaviour for the generic mu-metal using information from the material data sheets for the different alloys. Superconducting materials in the designs were modelled as volumes of vacuum when the materials were in the normal state, and as an idealised perfect conductor when in the superconducting state.

#### Model Excitation

Excitation was provided as a uniform applied field in one of the three axial directions of the models. Early modelling of the vacuum vessel shielding was based on an applied $H$-field of 40 A/m, equal to the strength of the Earth's field, although this was later increased to 120 A/m as more information on the magnetic environment at the telescope became available. Models of the shielding on the 1-K instrument stages used an applied field of 40 A/m.

It is important to note that the modelling software did not allow the application of AC fields - all of the work described herein concerns DC fields only. However, this was not considered to be a serious issue since this application is concerned only with relatively low frequency AC fields (as discussed previously, up to 200 Hz). The properties of the materials used for these models did not vary significantly over this frequency range, nor did measurements of the AC fields at the telescope indicate any increases in field strength over this range. A necessary assumption was made that the DC behaviour of the shielding models would also describe the AC behaviour with reasonable confidence.

#### Modelling the Cold Shutter Motor

The effect of the cold shutter motor on the magnetic environment around the 1-K box, and the effectiveness of any shielding present, was difficult to include in the main shielding models, since the magnetic field from the motor will not behave as a uniform field. The motor was modelled in isolation as a current loop with a magnetic moment equal to the published value for the selected motor model, and the effectiveness of a number of local shielding geometries investigated.

### 7.2.2 Modelling Results

Once field solutions were obtained for the models, the results were plotted on a plane bisecting the model geometry and normal to the applied field direction. The quantity used to evaluate the effectiveness of the shielding was the magnitude of the $H$-field. The attenuation factor for each shield combination was taken to be the ratio of the applied field strength to the upper limit of the field strength in the area of interest in the model (such as the space occupied by the 1-K box for the larger instrument structures, or the

approximate position of the focal plane in the models of the 1-K stage shielding). The effectiveness of adding shielding to different temperature stages of the instrument was modelled and evaluated as the shielding design developed. This section discusses the modelling results for shielding on the different instrument structures, and goes on to consider the overall effectiveness of the shielding design against uniform external fields.

**Vacuum Vessel**

The initial concept for the vacuum vessel magnetic shielding was a single shell of 1.5 mm thick mu-metal attached to the inside of the vessel, with provision for fitting additional shielding to the outside of the vessel if required. Attaching shielding on the external surface of the vessel was rejected early in the design process since large gaps would be required in the shield for service connections, so disrupting the continuity of the layer.

The main results of the vacuum vessel shield modelling are summarised in Table 7.6. The initial model for the vacuum vessel shielding consisted of a single 2 mm mu-metal shell. The attenuation provided by this geometry was low, but it was immediately apparent that the effectiveness of the shield was dependant on the direction of the applied field. It was found that for fields applied normal to the cryostat window, the shielding was less effective by a factor of approximately 2 than for fields tangential to the window, as illustrated by the results in Fig. 7.3. This was initially believed to be the result of flux penetrating the window aperture. The 2 mm shield design provided an attenuation factor of 1.7 for fields normal to the window and 3.3 for fields tangential to the aperture.

Since the use of a thicker single layer shield was not considered practical, the next design used two 1.5 mm shields spaced by 1.5 mm of vacuum. This geometry was found to improve the attenuation of fields normal to the window, but had no discernable effect for tangential fields. A further model increased the shielding to three 1 mm layers, giving an attenuation factor of 2 for fields normal to the window, and 5 for tangential fields. Due to concerns over the available space envelope and mass limitations, it was unfeasible to add any additional layers of mu-metal.

Since only small improvements to the shielding attenuation appeared possible by adding additional layers, it was believed that the shielding effectiveness was dominated

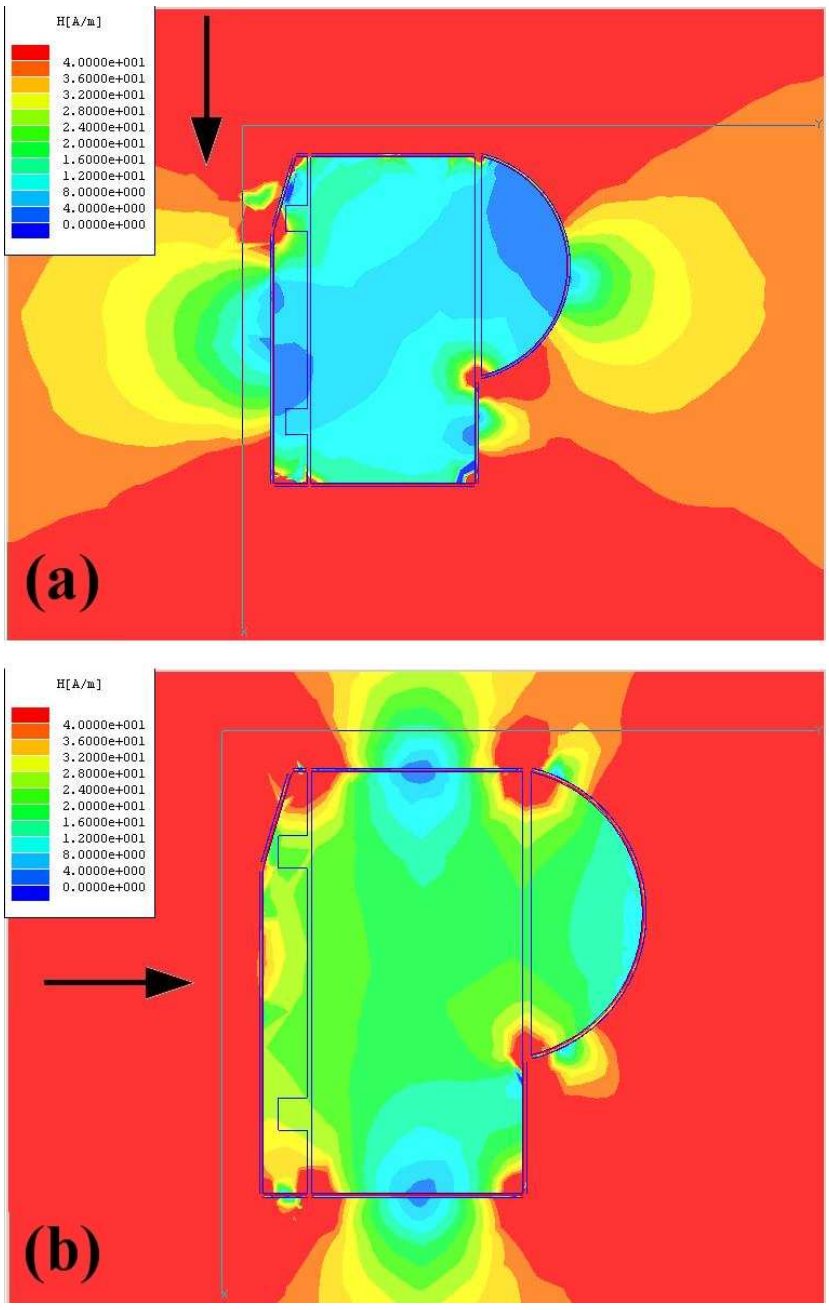


**Figure 7.3:** Plot of the $H$-field magnitude for a representative vacuum vessel shield model. The arrow indicates the direction of the 40 A/m applied field in each case, with the field in (a) normal to the top plate of the cryostat and (b) normal to the cryostat window aperture. The full magnitude scale is 4 A/m (0.4 A/m per division). The reduced attenuation of the shielding for the field normal to the window aperture (b) may be seen.

**Table 7.6:** Summary of modelling results for shielding on the vacuum vessel.

| Shielding | Attenuation factor for applied field | |
|---|---|---|
| | Tangential to cryostat window | Normal to cryostat window |
| Single 2 mm mu-metal | 3.3 | 1.7 |
| Double 1.5 mm mu-metal, 1.5 mm spacing | 3.3 | 2 |
| Triple 1 mm mu-metal, 2 mm spacing | 5 | 2 |
| Triple 1 mm mu-metal, 6 mm spacing | 5 | 2.5 |
| Double 1 mm mu-metal, 10 mm spacing | 5 | 2.5 |

by the gaps and apertures in the shields. An established method for reducing the penetration of flux through apertures in magnetic shielding is to fit cylindrical baffles along the normal of the aperture. A number of geometries with baffles on the window aperture and other penetrations through the shields were modelled, but no significant improvement was achieved. Locally increasing the shielding around the apertures using annular baffles also had no effect. It was subsequently found that the reduced effectiveness of the shielding for fields normal to the cryostat window was not primarily the result of flux penetrating the aperture, since the attenuation for this applied field direction was still significantly lower even when the window aperture was removed from the model completely. An alternative explanation was that the number of apertures in the top plate of the cryostat for wiring and other services reduced the effectiveness of that shielding section as a low-reluctance path. Substituting the top sections of shielding with plates that had a reduced number of apertures improved the attenuation factor for fields normal to the cryostat window, to the extreme case where an uninterrupted shield section resulted in a negligible difference in attenuation for the two field orientations.

The vacuum vessel shielding models were composed of separate panels rather than a single continuous shell, since the actual shielding would need to fit into the tolerances of the existing vacuum vessel structure and it was not believed feasible to attempt to fit shielding to the required tolerance to produce a continuous shell. Early models had a poor fit tolerance (of the order of 20–30 mm diagonal separation). Decreasing

the gaps between adjacent panels to a maximum of 10 mm diagonal separation did not significantly increase the overall attenuation of the shielding, but did increase the uniformity of the internal field.

To increase the effectiveness of the shielding design without adding additional material, a series of geometries with larger spacings between the three concentric mu-metal shields were modelled. It was found that small improvements to the attenuation and uniformity of the field strength in the region of the 1-K box could be achieved with gaps of up to 6 mm between shields giving good results. A final iteration of geometries found that removal of the middle of the three shielding layers, so comparing a model of three 1 mm shield layers with 6 mm spacing to a two layer model with 13 mm spacing, made no difference to the overall attenuation of the design, indicating that the same level of shielding could be achieved with less material. This result is shown in Fig. 7.4 for a single field direction.

The optimum design of the vacuum vessel shielding, taking into account limitations on space and mass, was identified as two 1 mm mu-metal shields with a vacuum gap of 10 mm. This geometry gave an attenuation factor of 2.5 for applied fields normal to the window aperture, and a factor of 5 for tangential fields. $H$-field magnitude plots for the three axial directions are shown in Fig. 7.5.

The vacuum vessel shield geometries were modelled with applied fields up to five times the Earth's field strength. It was found that the internal field strengths scaled linearly with the applied field, implying that the shielding materials were not close to saturation. Over the range of field strengths the instrument is expected to be exposed to, the attenuation factors listed will remain constant.

### 60-K and 4-K Radiation Shields

From the early stages of modelling the shielding designs for the vacuum vessel, it was clear that shielding on this stage alone would be insufficient to meet the magnetic field requirements at the 1-K box. Fitting shielding to the cryogenic stages of the instrument would have been problematic. The thermal performance of the 60-K stage would not be greatly affected by the additional mass of shielding, since considerable cooling power is available on the first stage. However, the 60-K radiation shield has limited mechanical

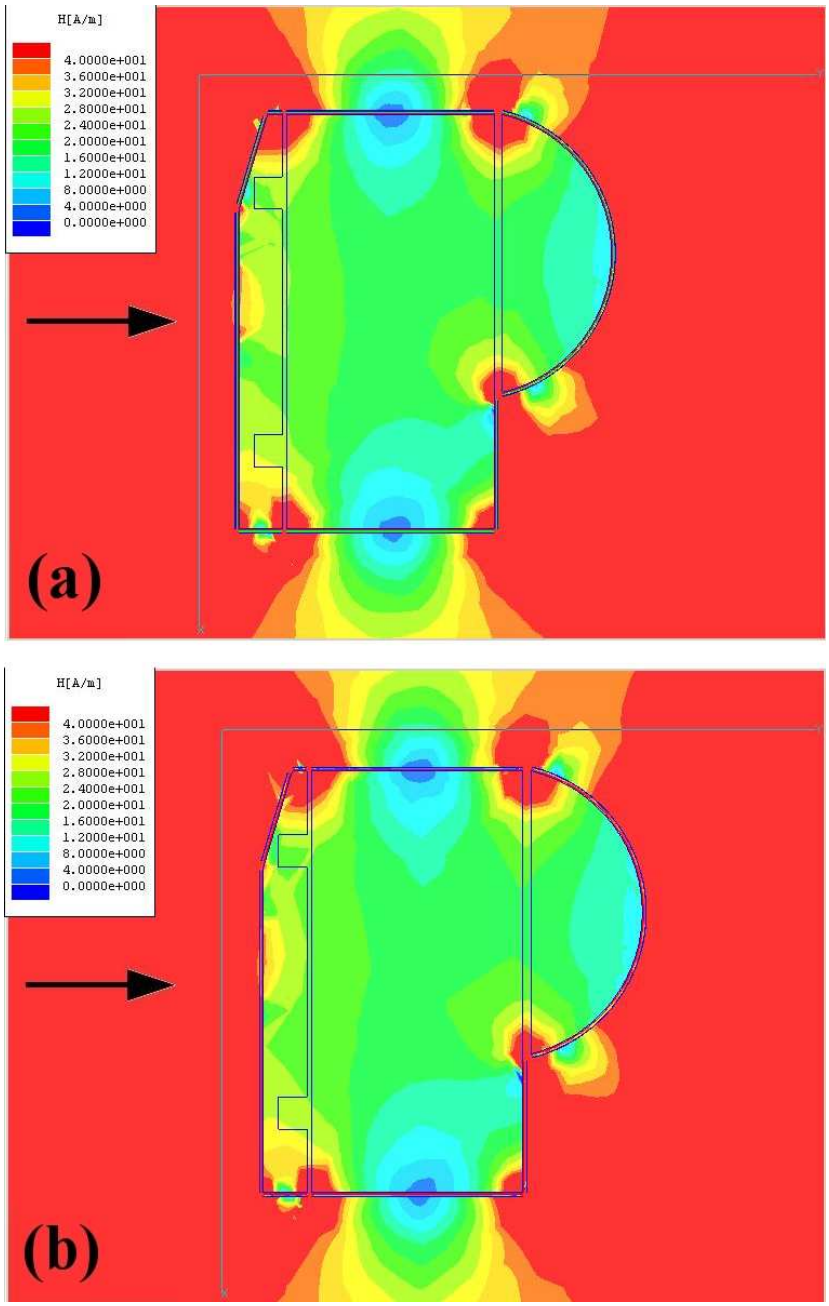


**Figure 7.4:** Plot of the $H$-field magnitude for two vacuum vessel shield models. The arrow indicates the direction of the 40 A/m applied field in both cases normal to the cryostat window aperture. The shield model in (a) has three 1 mm shield layers, while the model in (b) has the centre of the three layers removed but without changing the separation of the outer two layers. The full magnitude scale is 4 A/m (0.4 A/m per division). Very little change in the attenuation of the magnetic field is seen between the two models.

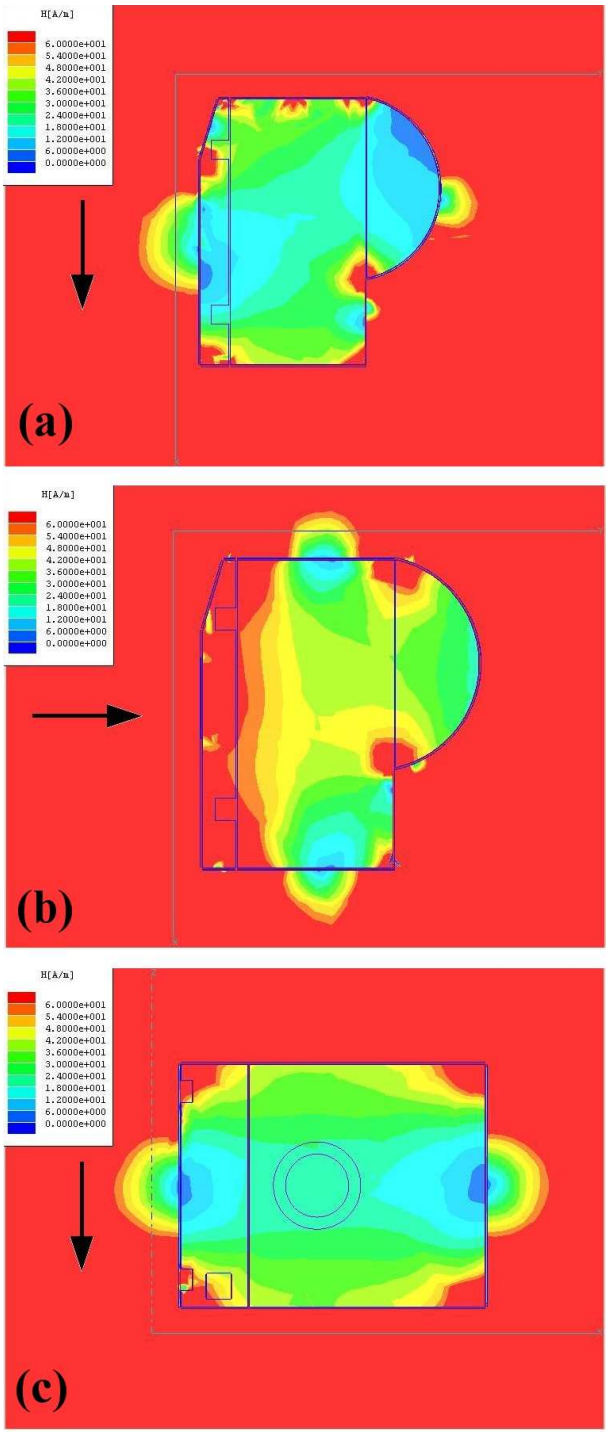


**Figure 7.5:** Plot of the $H$-field magnitude for the optimised shield vacuum vessel shield model. The arrow indicates the direction of the 120 A/m applied field in each case, with the field in (a) normal to the top plate of the cryostat, (b) normal to the cryostat window aperture, and (c) normal to the side of the cryostat. The full magnitude scale is 6 A/m (0.6 A/m per division).

strength, and would be unable to support a significant quantity of mu-metal. Conversely, the 4-K optics box would be able to mechanically support more mu-metal shielding, but would suffer thermally from the additional mass since the cooling power on the 4-K stage is limited.

Initially, it was assumed that 1 mm Cryoperm shielding would be added to the 60-K and 4-K stages of the instrument, either as a single layer, or a two layer nested shield as for the vacuum vessel shielding design. The attenuation factors provided by different shield combinations are summarised in Table 7.7, both for the cryogenic shielding modelled in isolation, and as part of the overall model with the vacuum vessel shielding included. The vacuum vessel shielding used consisted of two 1 mm mu-metal layers spaced by 10 mm of vacuum. It should be noted that the total attenuation of a combination of shielding elements is not necessarily the product of the attenuation of the individual elements, since the close proximity of the concentric shielding layers in these models leads to some interaction between the individual elements. Further, the attenuation factors quoted for each model are for the magnetic field strength in the region of the 1K box. When different shields are combined, the inner layers may have a stronger applied field since there will be variation in the field strength through the volume of the model.

Fig. 7.6 shows $H$-field magnitude plots for three models of the cryogenic stage shielding, initially with a single 1 mm Cryoperm shield on the 60-K stage, then a double shield on the 60-K stage, and finally a double shield on the 60-K stage with a single Cryoperm layer on the 4-K radiation shield. All three models are isolated from the vacuum vessel shielding due to solution limitations, as discussed previously. The three example plots in this figure are for solutions with an applied magnetic field of 48 A/m normal to the window aperture, as in each plot. It may be seen that there is a gradual decrease in the $H$-field magnitude in the enclosed volume as the additional shielding layers are added to the model.

From these modelling results, the addition of Cryoperm shielding on the 60-K and 4-K stages of the instrument appears to be very effective. However, the quantity of shielding material that must be added to the instrument to achieve this attenuation is considerable. Each 1 mm layer of material added to the cryogenic stages of the

**Table 7.7:** Summary of modelling results for shielding on the 60-K and 4-K instrument stages. The upper set of data lists the attenuation factors for the 60-K and 4-K shields in isolation, while the lower set includes the contribution from the optimum vacuum vessel magnetic shielding in addition to the 60-K and 4-K shielding.

| Shielding | Attenuation factor for field | |
|---|---|---|
| | Tangential to window | Normal to window |
| *Cryogenic shielding in isolation:* | | |
| One 1 mm Cryoperm layer on 60-K stage | 5 | 2.5 |
| Two 1 mm Cryoperm layers on 60-K stage | 5 | 3.2 |
| One 1 mm Cryoperm layer on 4-K stage | 3.5 | 4.5 |
| Two 1 mm Cryoperm layers on 4-K stage | 4.5 | 7 |
| Two 1 mm Cryoperm layers on 60-K stage and one 1 mm Cryoperm layer on 4-K stage | 9 | 5 |
| *Combined with vacuum vessel shielding:* | | |
| One 1 mm Cryoperm layer on 60-K stage | 17 | 4.3 |
| Two 1 mm Cryoperm layers on 60-K stage | 17 | 6 |
| One 1 mm Cryoperm layer on 4-K stage | 12 | 7.7 |
| Two 1 mm Cryoperm layers on 4-K stage | ... | ... |
| Two 1 mm Cryoperm layers on 60-K stage and one 1 mm Cryoperm layer on 4-K stage | 30 | 8.6 |

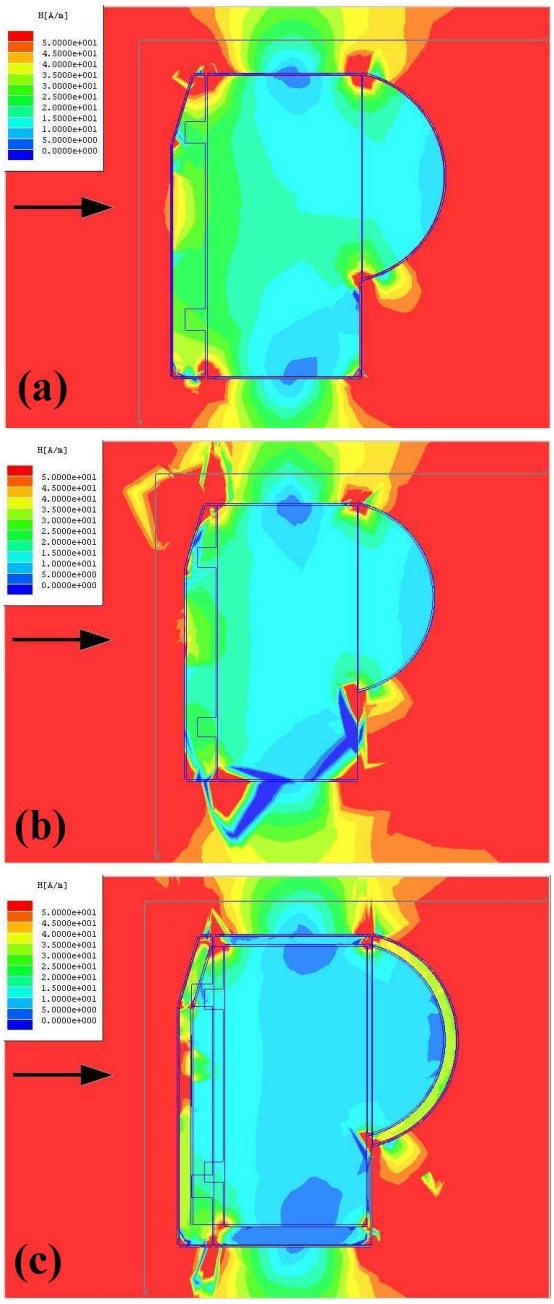


**Figure 7.6:** *H*-field plots showing reducing field strength inside the shielded volume of the 60-K radiation shield as more shielding layers are added. (a) Single 1 mm Cryoperm layer on the 60-K structure, (b) 2 1 mm Cyroperm layers on the 60-K shield, and (c) 2 1 mm shields on the 60-K stage and a 1 mm layer on the 4-K structure. In each case, the shielding is modelled in isolation from the vacuum vessel shielding. The arrow indicates the direction of the 48 A/m applied field in each case. The full magnitude scale is 5 A/m (0.5 A/m per division). A reduction in internal field strength can be seen (a) to (c).

instrument would increase the cold mass of the structures by approximately 100 kg, so impacting the thermal performance and cooldown times of the system. Alternative approaches for shielding the cold stages of the instrument were explored. The use of Metglas foil was considered, and it was found that in principle the same attenuation factors for the Cryoperm shielding could be achieved using nested shields of Metlgas and an inert filler material of similar total thickness, but considerably lower mass than the sheet shielding materials. Due to the quantity of material needed to produce layers of significant thickness on the large cryogenic structures, and difficulties associated with the attachment of the foil shields, this solution was rejected. The use of a superconducting shield on the 4-K structure, using a material with a relatively high transition temperature such as niobium or lead, was also considered. Although this approach appeared promising, issues with attachment of material to the 4-K structure were considered too great for this to be a reasonable solution.

**1-K Stage**

The approach to the shielding design on the 1-K stage differed slightly from the development of the vacuum vessel shielding in that insufficient time was available for rigorous modelling of the designs. Furthermore, the available space envelopes for shielding layers on the 1-K stage imposed a serious restriction on the amount of shielding material that could be attached. The thickness of the superconducting shield was dictated by the available material, while consideration of the design of the 1-K stage allowed a reasonable thickness of Metglas shielding to be estimated.

Test geometries modelled previously indicated that nested shields of thin foil materials behaved in a similar manner to the results for the sheet materials on the vacuum vessel. In principle, relatively substantial Metglas shields could be produced by layering Metglas foil with an inert filler up to ten times the thickness of the high-permeability material. Ultimately, the thickness of the shield for the focal plane units (FPUs) nested in the 1-K box was modelled as 70 $\mu$m (approximately 3 layers of Metglas foil without nesting), while the shield on the 1-K box was modelled as 200 $\mu$m. Both the 1-K box and FPU models incorporated the appropriate apertures for the light path to the detectors.

**Table 7.8:** Summary of modelling results for shielding on the 1-K instrument stage.

| Shielding | Attenuation factor for applied field | |
|---|---|---|
| | Tangential to aperture | Normal to aperture |
| *1-K Box:* | | |
| Metglas high-permeability shield | 30 | 10 |
| Superconducting shield | 4 | 40 |
| *Focal plane units:* | | |
| Metglas high-permeability shield | 10 | 4 |
| Superconducting shield | 2 | 10 |

The results for the Metglas and superconducting shields on the 1-K box and the FPUs are summarised in Table 7.8. It may be seen that there is a strong directional dependance on the effectiveness of the shielding, more so than for the vacuum vessel shielding. For fields applied normal to the cold stop aperture on the 1-K box, the attenuation of the Metglas high-permeability shielding is lower by a factor of 3 than for fields tangential to the aperture, as shown by the results in Fig. 7.7. The same is true for the FPUs, although the attenuation for the two field directions differs by a factor of 2.5. The results for the high-permeability shielding on the FPUs are shown in Fig. 7.8.

The superconducting shield on the 1-K box indicated an attenuation factor of 4 for fields tangential to the cold stop, and a factor of 40 for fields normal to the aperture. The superconducting shield on the FPUs gave an attenuation factor of 2 for fields tangential to the aperture, and a factor of 10 for fields normal to the aperture.

The design of the 1-K box orientates the two focal planes at right-angles. It is possible that for a given applied field direction, one focal plane unit will be in a field tangential to the FPU aperture, while the other has an applied field normal to this aperture. Hence, the overall attenuation factor will be different for the two focal planes, which complicates the analysis. The 1-K box and FPU shielding effectiveness can be determined for each focal plane for field directions relative to the cold stop aperture on the 1-K box. The focal plane in the "straight through" position (the path transmitted by the dichroic) is the 850 $\mu$m array, while the focal plane at 90° is the 450 $\mu$m array.

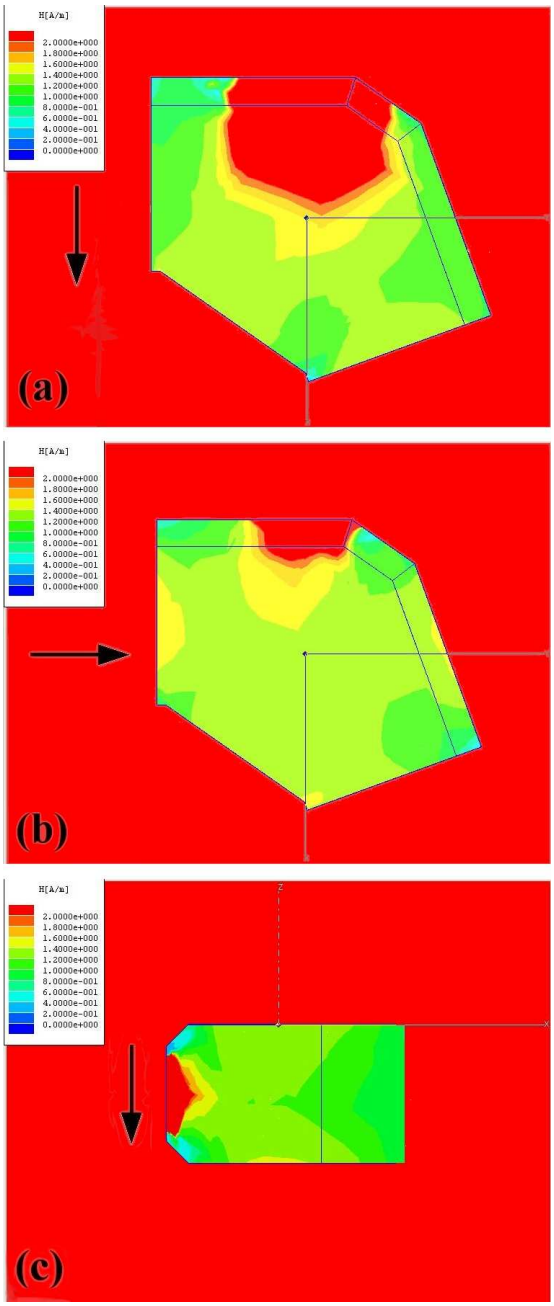


**Figure 7.7:** Plot of the $H$-field magnitude for 200 $\mu$m high-permeability shield on the 1-K box. The arrow indicates the direction of the 40 A/m applied field in each case, with the field in (a) normal to the 1-K cold stop, (b) and (c) tangential to the cold stop. The full magnitude scale is 2 A/m (0.2 A/m per division).

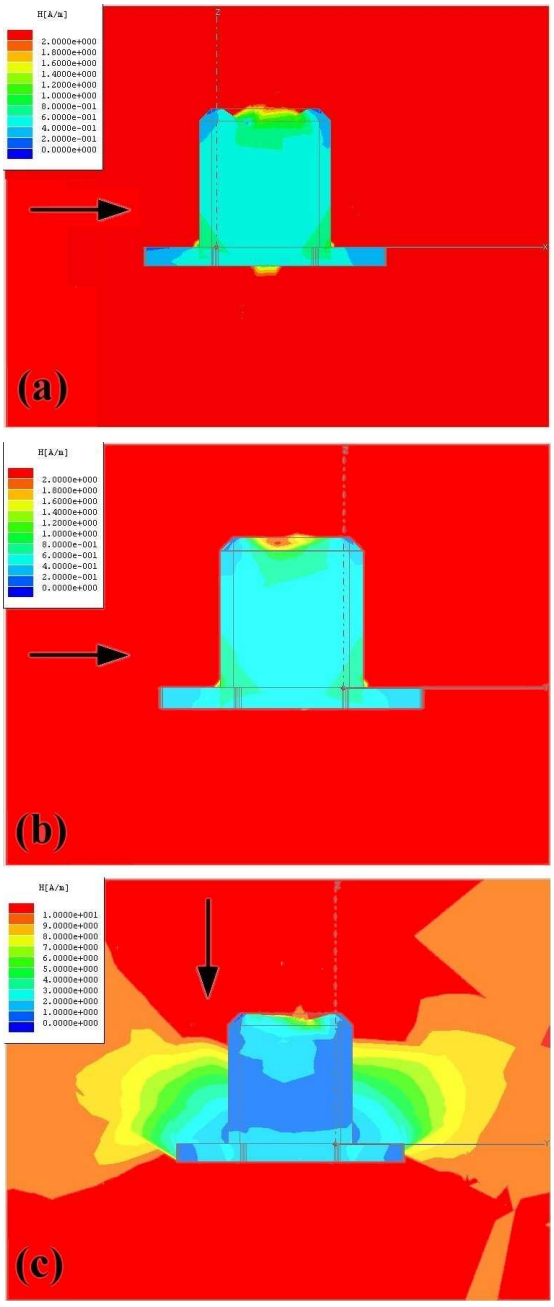


**Figure 7.8:** Plot of the $H$-field magnitude for 70 $\mu$m high-permeability shield on the focal plane units. The arrow indicates the direction of the 10 A/m applied field in each case, with the field in (a) and (b) tangential to the aperture, and (c) normal to the aperture. The full magnitude scale is 2 A/m (0.2 A/m per division).

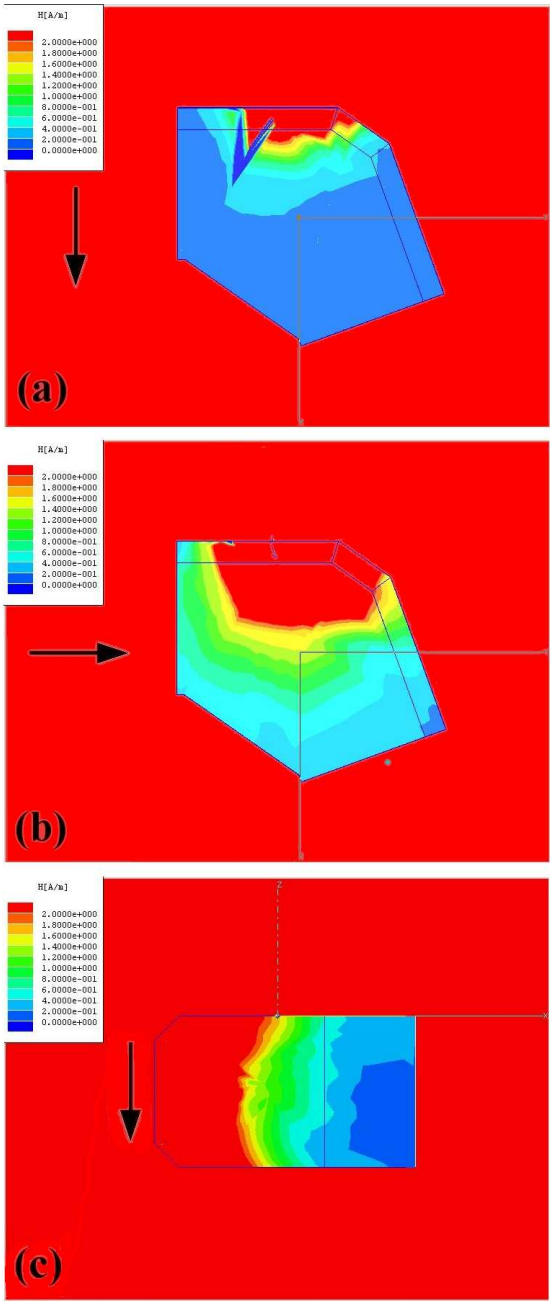


**Figure 7.9:** Plot of the $H$-field magnitude for 200 $\mu$m superconducting shield on the 1-K box. The arrow indicates the direction of the 40 A/m applied field in each case, with the field in (a) normal to the 1-K cold stop, (b) and (c) tangential to the cold stop. The full magnitude scale is 2 A/m (0.2 A/m per division).

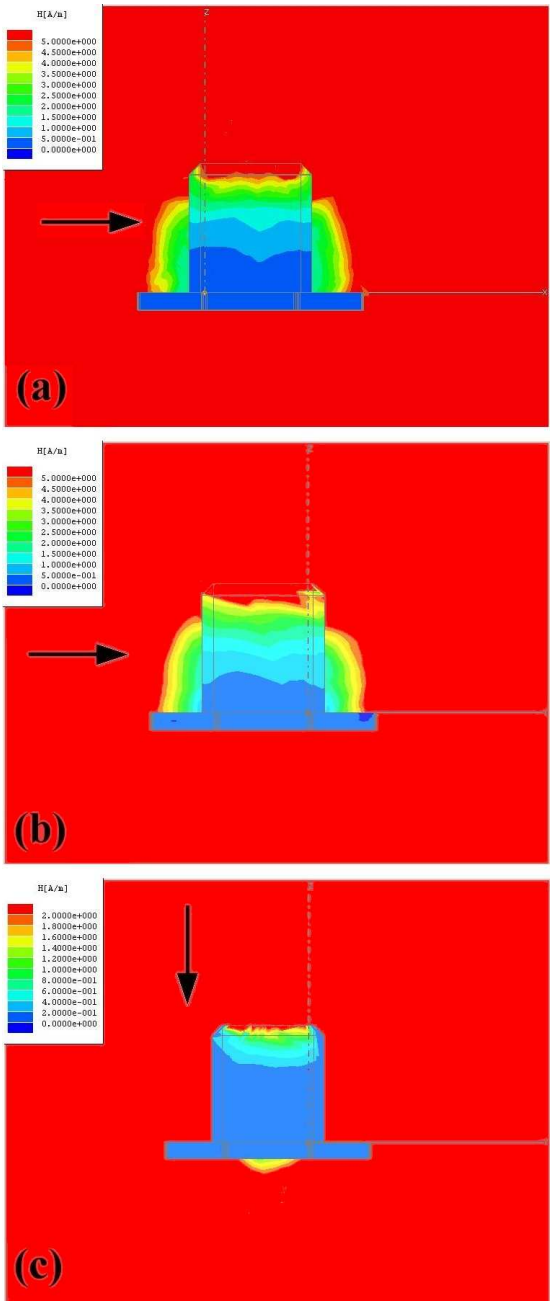


**Figure 7.10:** Plot of the $H$-field magnitude for 70 $\mu$m superconducting shield on the focal plane units. The arrow indicates the direction of the 10 A/m applied field in each case, with the field in (a) and (b) tangential to the aperture, and (c) normal to the aperture. The full magnitude scale is 5 A/m (0.5 A/m per division) in (a) and (b), and 2 A/m (0.2 A/m per division) in (c).

For an applied field normal to the cold stop, the field will be normal to the 850 $\mu$m focal plane position and tangential to the 450 $\mu$m focal plane. An applied field tangential to the cold stop will also be tangential to the 850 $\mu$m focal plane, but could be tangential or normal to the 450 $\mu$m focal plane. Table 7.9 summarises the contribution of each shielding stage to the total attenuation at the two focal planes for field directions relative to the cold stop.

### 7.2.3 Analysis and Final Shielding Design

The final shielding design for the radiation shields and vacuum vessel recommended as a result of the modelling process consisted of a double 1 mm mu-metal shield on the vacuum vessel, combined with a Metglas shield of 200 $\mu$m thickness on the 1-K box and Metglas shielding of 70 $\mu$m thickness on the focal plane units, in addition to the superconducting shields on the 1-K structures. This layout is summarised in Table 7.10. Note that although the thickness of the superconducting shields in the FE models were the same as the high-permeability shields for convenience, the effectiveness of the superconducting layer is independent of the shield thickness (see, for example, discussion in Ref. [121]), to a minimum thickness taken to be three times the penetration depth, $\xi$. The thickness of the superconducting layers listed in Table 7.10 are ten times the penetration depth of niobium (the first choice material for the superconducting shielding) at 1 K in order to satisfy the minimum depth requirement with a reasonable margin. The second choice material, lead, has a smaller penetration depth than niobium, and so will also satisfy the requirement with this thickness. Details of the penetration depths are given in Tables 7.1 and 7.2.

Definition of the overall shielding effectiveness is complicated by the orientation of the 1-K instrument stage relative to the cryostat window. It may be seen by comparison between the 1-K and cryostat shielding that it is the high-permeability and superconducting shielding on the 1-K box and FPUs that dominates the overall shielding effectiveness, with a small contribution from the mu-metal shielding on the cryostat. A "worst case" attenuation factor is calculated by assuming that the direction of the field is normal to the cryostat window aperture and normal to the cold stop aperture while the 1-K stage is above the transition temperature of the superconducting shield.

**Table 7.9:** Summary of predicted shielding effectiveness on the 1-K instrument stage for the 850 and 450 $\mu$m focal planes. For the 450 $\mu$m focal plane results, the figures in parentheses give the results for the case where the applied field is tangential to the cold stop, but normal to the 450 $\mu$m focal plane unit.

| Shielding | Attenuation factor for applied field | |
|---|---|---|
| | Tangential to cold stop | Normal to cold stop |
| *850 $\mu$m focal plane:* | | |
| 1-K box Metglas shield | 30 | 10 |
| 1-K box superconducting shield | 4 | 40 |
| FPU Metglas shield | 10 | 4 |
| FPU superconducting shield | 2 | 10 |
| Total attenuation without superconducting shield | 300 | 40 |
| Total attenuation with superconducting shield | 2400 | 16000 |
| *450 $\mu$m focal plane:* | | |
| 1-K box Metglas shield | 30 | 10 |
| 1-K box superconducting shield | 4 | 40 |
| FPU Metglas shield | 10 (4) | 10 |
| FPU superconducting shield | 2 (10) | 2 |
| Total attenuation without superconducting shield | 300 (120) | 100 |
| Total attenuation with superconducting shield | 2400 (4800) | 8000 |

**Table 7.10:** Summary of shield design recommended following the FE modelling process. Although not included in the design process, the superconducting groundplane on the mulitplexer wafer and the shielded cans surrounding the SQUID series arrays are included for completeness.

| Location | Shielding |
|---|---|
| Focal plane | 5 $\mu$m molybdenum layer on multiplexer wafer |
| SQUID series arrays | 1 mm niobium shield with inner 0.5 mm Cryoperm-10 shield |
| Focal plane units | 0.5 $\mu$m niobium shield[a] over 70 $\mu$m Metglas[b] |
| 1-K box | 0.5 $\mu$m niobium shield[a] over 200 $\mu$m Metglas[b] |
| Vacuum vessel | Two 1 mm nested mu-metal shields, $\sim$10 mm vacuum gap |

[a] Thickness stated is 10 times the penetration depth of niobium at 1 K as a minimum value. Shielding effectiveness is independent of shield thickness above this value.

[b] Minimum thickness, including nesting of shield.

The predicted attenuation provided by each shielding component for the 850 and 450 $\mu$m focal planes are summarised in Table 7.11. The attenuation factor of 15 needed to meet the requirement for trapped flux in the superconducting shield volume is easily met for both focal planes, and the total attenuation factor exceeds the requirement by a large margin. Alternatively, the worst case field direction for the superconducting shielding may be considered as a field normal to the cryostat window, but tangential to the cold stop and both FPU apertures. The attenuation contributions for this field configuration are shown in Table 7.12. Also in this case, both the high-permeability shield attenuation and total attenuation requirements are easily met.

### 7.2.4 Shielding for Internal Field Sources

The effects of magnetic field sources internal to the instrument are more difficult to model and quantify. However, some investigation was carried out on the magnetic field from the cold shutter motor on the 1-K box, and the effects of uniform fields on the detector arrays.

**Table 7.11:** Summary of contributions from components of the shielding design to the overall attenuation of external magnetic fields. The quoted figures represent a "worst case" field direction for the high-permeability shielding.

| Shielding | Attenuation factor | |
|---|---|---|
| | 850 $\mu$m FP | 450 $\mu$m FP |
| Vacuum vessel mu-metal shield | 2.5 | 2.5 |
| 1-K box high-permeability shield | 10 | 10 |
| *1-K box superconducting shield* | 40 | 40 |
| Focal plane unit high-permeability shield | 4 | 10 |
| *Focal plane unit superconducting shield* | 10 | 2 |
| Attenuation without superconducting shield | 100 | 250 |
| Attenuation with superconducting shield | 40000 | 20000 |

**Table 7.12:** Summary of contributions from components of the shielding design to the overall attenuation of external magnetic fields. The quoted figures represent a "worst case" field direction for the superconducting shielding.

| Shielding | Attenuation factor | |
|---|---|---|
| | 850 $\mu$m FP | 450 $\mu$m FP |
| Vacuum vessel mu-metal shield | 2.5 | 2.5 |
| 1-K box high-permeability shield | 30 | 30 |
| *1-K box superconducting shield* | 4 | 4 |
| Focal plane unit high-permeability shield | 10 | 10 |
| *Focal plane unit superconducting shield* | 2 | 2 |
| Attenuation without superconducting shield | 750 | 750 |
| Attenuation with superconducting shield | 6000 | 6000 |

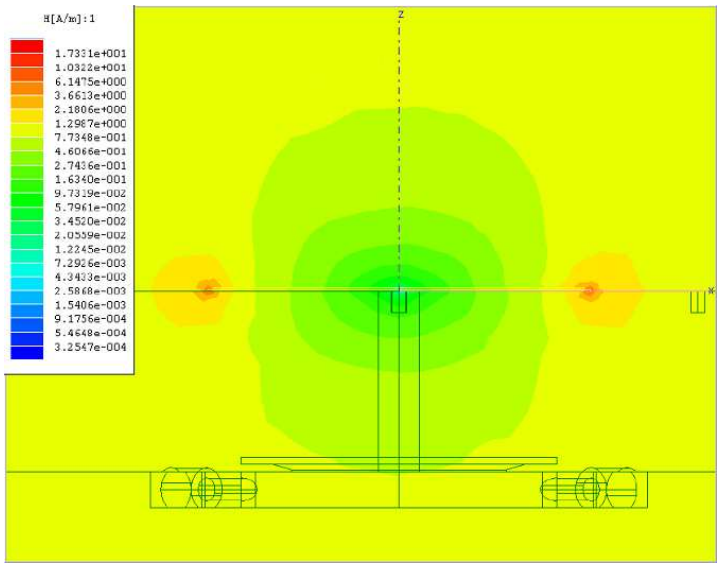


**Figure 7.11:** Focal plane with superconducting backplane, showing field gradient and fringing effects in an applied field normal to the array.

### Shutter Motor

A number of possible shield designs for the cold shutter motor were explored, primarily based around the concept of enclosing the motor assembly in a box of high-permeability or superconducting foil. However, this line of the development was abandoned since due to the design of the motor assembly, fitting a shielded box was judged too problematic. Some basic shielding was fitted to the motor as part of the shielding integration process, as described in Chapter 8, but this construction bore no resemblance to the basic designs that were modelled.

### Detector Array Groundplane

The superconducting layer on the backplane of the detector arrays was modelled for uniform fields perpendicular to the arrays. The resulting $H$-field pattern is illustrated in Fig. 7.11, with decreasing attenuation towards the edges of the focal plane. Of particular note are the fringing effects at the edges of the array. These results indicate that there is likely to be a gradient in the magnetic field strength across the array due to the groundplane, and that there will be a concentration in the field towards the outermost columns.

Two possible solutions were initially identified to compensate for this fringing effect. Either increase the size of the superconducting layer so that the groundplane is larger than the active pixel area, or place pieces of mu-metal at the edges of the focal plane. Extending the groundplane beyond the active area was not considered practical. However, due to problems with Joule heating a subsequent change in the design of the subarray module included a coating of tin on the PCB carrying the array connections out of the detector. The tin coating would be in the superconducting state at the array temperature, and although not forming a continuous layer, will correct for at least some of the fringing effects seen in these models.

The presence of a gradient in field strength across the array could have implications for the operation of the detectors, even if the overall field strength requirements are met. As an extreme case, it is possible that a gradient in the field strength across the array could prevent some areas of the detector going superconducting, or that pixels will be at different points in the resistance-temperature characteristic for a given temperature, so causing a gradient in pixel sensitivity across the focal plane. The presence of additional superconducting elements around the edges of the detector array, such as the tin layer on the array PCBs described above, may be sufficient to minimise or remove any field gradient present across the detectors.

If later testing indicates that there is a gradient effect impairing the operation of the arrays, then it may be necessary to further remove the field gradient by placing additional high-permeability or superconducting material on the focal plane.

## 7.3 Summary

This chapter has discussed the effects of magnetic fields on the devices that compose the SCUBA-2 detectors, specifically a loss of sensitivity due to the broadening of the superconducting transition of the TESs, and additional signals on the multiplexer SQUIDs. The principles of magnetic field control were discussed, as were the properties of various shielding materials. This background information allowed an outline shield design to be devised. The design was further developed and optimised through a process of electromagnetic modelling using a finite-element method. The results of the modelling work were analysed to provide a predicted field attenuation for the final shielding design.

The final recommended shield layout was composed of a high-permeability mu-metal shield on the inner surface of the vacuum vessel, combined with superconducting and high-permeability shields on the 1-K box and the focal plane units. Use of further cryogenic shielding on the 4-K and 60-K stages of the cryostat was rejected due to concerns over increasing the thermal mass and the expense of material. The layout of the shielding layers is summarised in Table 7.10. This shielding design fed into a practical design and implementation discussed in the next chapter.

# Chapter 8

# Magnetic Shielding II: Shielding Design, Construction and Verification

Although an outline design for the magnetic shielding was produced from the results of the finite-element modelling presented in the previous chapter, this outline still required development into a practical shielding design. In order to achieve this, a number of obstacles needed to be surmounted, particularly in relation to the cryogenic shields. Details of the practical design, and the construction of the shielding, are discussed in this chapter. In order to determine the effectiveness of the final shielding design, measurements of the detector response to an external magnetic field source were made and compared to the predicted attenuation from the modelling results.

Details of the design of the cryogenic shielding for the 1-K stage of the instrument, and the verification test data, appeared as "Cryogenic Magnetic Shielding for SCUBA-2" in the *Proceedings of the SPIE* [160].

## 8.1 Shielding Design and Construction

The finite-element modelling results produced a recommended shield layout for the instrument. It was then necessary to develop practical shielding designs based on the optimised shielding models. The major instrument structures were complete or had fixed designs prior to the completion of the shield modelling, and so the magnetic shield designs developed during the process had to be retrofitted to the instrument. This presented challenging restrictions on the shielding design which required a number of novel approaches and solutions to be adopted.

In the following section, the design of the shielding for each of the major structures is discussed separately, including the problems presented by the existing structures and how these issues were overcome.

### 8.1.1 Vacuum Vessel Shielding

A number of issues related to the existing design of the outer vacuum vessel required solutions for the successful integration of the magnetic shielding. The first of these was the available space envelope between the vacuum vessel inner wall and the 60-K radiation shield. The space was restricted by by structural features such as the truss system supporting the radiation shield and the precool tanks, and the space required for the multilayer insulation blanket between the two temperature stages. Further problems were anticipated due to the uneven welds on the inside surface of the vacuum vessel.

The vacuum vessel is composed of three separate sections, allowing for different degrees of instrument disassembly. The rear section specifically was intended for frequent removal to allow access to the 1-K stage and detectors. The mid-section, the largest of the three, includes the mounting ports for the cryostat services and cabling feed throughs, while the front section supports the 60-K radiation shield via a truss system. It was judged to be too great a challenge to design a self-supporting mu-metal shield; the alternative option was to design the shield around the three vessel sections and attach the mu-metal to the existing aluminium structure, in such a way that the shielding could be split in the same positions as the vessel. This requirement had already been anticipated in the earlier FE modelling work, and the model geometries were design as a series of separate sections.

The detailed design, construction and installation of the vacuum vessel shielding was contracted out to a specialist shielding company.[1] The material used for the shielding was 80% Nickel-Iron alloy with a high magnetic permeability (as opposed to a a high saturation field - see Chapter 7 for discussion). The maximum mu-metal panel size available from this source (defined by the capacity of the ovens used to anneal the material after machining) was 1.0 by 0.5 metres. In order to shield the large area of the vacuum vessel sections, a number of plates would be fitted together. Continuity would be maintained by fitting strips of mu-metal along the joints, overlapping adjacent panels by 20 mm. A similar approach was used at right-angle joints.

The shielding ultimately fitted to the vacuum vessel was broadly similar to the modelled designed described in the previous section, although with a number of important differences. The use of an aluminium frame to attach the shielding to the vacuum vessel (discussed below), rather than direct mounting to the inside wall of the vessel, reduced the available space between the wall and the 60-K radiation shield for the mu-metal. The separation of the two mu-metal layers was therefore reduced from 10 mm in the models to 4 mm. Furthermore, the small size of the available mu-metal panels introduced a number of potential discontinuities in the shielding layers, although this was largely controlled by joining the panels with overlapping mu-metal strips. Conversely, the continuity of the shielding was better than that of the models since the modelled geometries used distinct panels with significant gaps to tile the inside of the vacuum vessel, a feature that is known to have contributed significantly to the penetration of the flux into the shielded volume. The final shielding improved on this situation by maintaining the continuity through the whole shield by using further overlapping strips and appropriate demountable joints.

The small panel size and the need to avoid warping over the area of each panel (potentially causing shorts between the two shield layers) would have required a large number of holes to be drilled and tapped into the vacuum vessel. The potential for loss of vacuum from such a large number of holes was considered unreasonable, so as an alternative approach an inner frame of aluminium alloy, pre-drilled with tapped holes to match the pattern of mu-metal panels, was attached to the inside surface of

[1] Magnetic Shields Ltd., http://www.magneticshields.co.uk.

the vacuum vessel using a relatively small number of screws. The two layers of mu-metal were attached to this frame using threaded aluminium studs. This approach also overcame the problems associated with uneven welding on the inside of the vessel since the 6 mm thick aluminium frame was deeper than the welds, giving a better uniformity for attachment of the mu-metal panels. Fig. 8.1 shows a section of the aluminium frame attached to the inside of the vacuum vessel centre section. A mu-metal panel is also shown fitted to the frame. The spacing between the two shells is maintained using stacks of Tufnol washers, and non-conducting collars were placed over the studs to prevent shorts between the mu-metal layers. Fig. 8.2 shows a side plate of the vacuum vessel centre section with the complete shielding fitted.

It was necessary to allow clearance holes in the shielding layers for a number of instrument services. The cryostat window assembly required an aperture of 600 mm diameter approximately in the centre of the front section. The upper face of the centre section required a number of clearance holes, including ports for the dilution refrigerator insert, cryocoolers, turbomolecular pump and service cabling. A series of eight clearance holes were required down one side of the centre section as feedthroughs for the detector array readout cables. Additional apertures was left in the shielding layers behind the access panel in the vessel front section, although since this aperture were substantial, a removable shielding panel (3 mm mu-metal, screwed onto the outer shielding layer) was included in the design. Fig. 8.3 shows the apertures left in the upper shielding panels for the cryostat services.

The shielding attached to each of the three vacuum vessel sections was designed with a mating joint that would maintain full continuity in the shield, but still allow the vessel sections to be separated without the need to remove additional bolts. The two layers of shielding on one half of the joint were splayed outwards, allowing the layers on the opposite half to lock into the gap. This gave two continuous layers of mu-metal around the entire volume of the vessel. Fig. 8.4 shows a section of shielding on the vessel centre section, illustrating the splayed mu-metal panels.

**Figure 8.1:** Aluminium frame attached to the inside of the vacuum vessel during the early stages of assembly of the shielding. A single mu-metal panel is shown in place. The feed throughs in the vacuum vessel wall are for the detector array cable harnesses.

**Figure 8.2:** Completed installation of shielding on one side section of the vacuum vessel. The pattern of fixing studs and the overlapping mu-metal strips to maintain continuity between adjacent panels can be seen.

**Figure 8.3:** Fully installed upper section of the shielding showing the cryostat service apertures for the dilution refrigerator insert (circular aperture top left), pulse tube cooler cold heads (twin apertures lower centre) and the service wiring panel (rectangular aperture on the right).

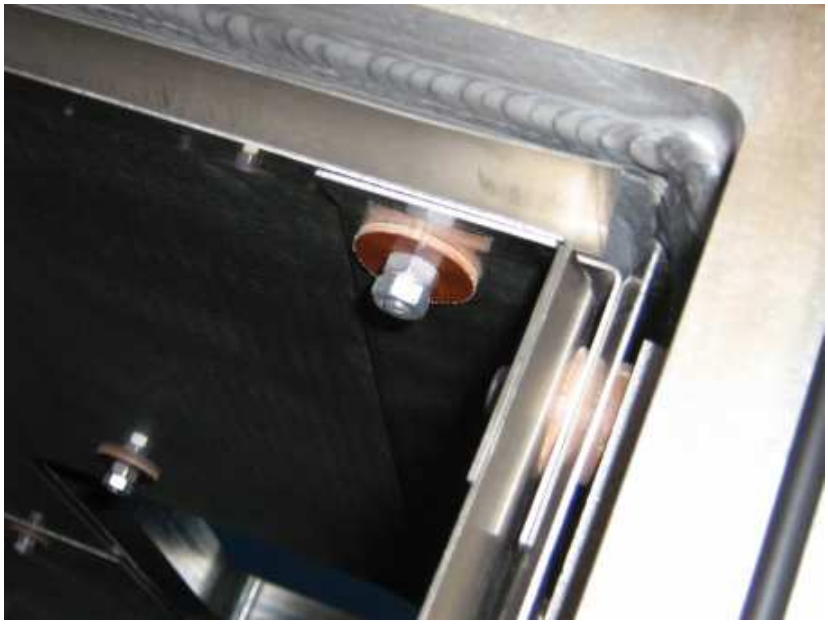

**Figure 8.4:** Detail view of the shielding joint between two sections of the vacuum vessel structure. The splayed mu-metal panels can be seen.

### 8.1.2 1-K Box and Focal Plane units

The structure of the 1-K stage is composed of aluminium (6082 T6), with thermal paths and contacts of gold-plated copper. Due to the magnetic field requirements, it was specified that no magnetic materials (other than shielding materials) should be used in the construction of the detector enclosure. As such, screws and other fastenings in the structure are of brass or aluminium rather than steel. The only exception to this are the screws used to make the copper-copper joints for the thermal straps. The need to produce a good contact force on these joints required stainless steel screws rather than softer metals. To minimise the effect of the presence of steel in the structure, A2 grade (non-magnetic) stainless screws were used.

The key challenges in the construction of the shielding for the 1-K box were how to efficiently cover the large area of the box with Metglas and niobium foil, how to attach the small sections of foil to the aluminium structure, and, to a lesser extent, how to produce a nested Metglas shield.

The nominal dimensions of Metglas 2705M foil are 2 inches (50.8 mm) wide and 0.85 mil (21.6 $\mu$m) thick. Attachment of the large number of Metglas foil strips required to cover the box area would be impossible with a physical fixing such as screws due to the large number of holes that would be required. Metglas foil had already been used extensively to shield the SCUBA-2 subarray test cryostat at Cardiff University [161], the method of attachment used for the foil strips was a combination of Kapton and Mylar tape. Concerns over the long-term reliability of this method made this an unsuitable approach for the instrument shielding. The method ultimately selected to attach the shielding was to bond the Metglas foil onto a backing material, such that the completed sheets could be cut to size and shape. Use of epoxy was also a useful way to thermally sink the shielding material to ensure the layers cooled to the stage temperature.

The FE modelling results for the 1-K box required a Metglas shield of at least 200 $\mu$m total thickness. The method recommended by the manufacturers for foil shields suggests that foil layers are spaced by 3 to 4 thicknesses of an inert material, although FE modelling of nested foil shields had previously indicated that shields are effective with up to 10 thicknesses of space between layers. The backing sheet used for the majority of the shielding was aluminised Mylar with a thickness of 127 $\mu$m, or approxi-

**Figure 8.5:** Section of Metglas composite sheet. Approximately 10 strips of Metglas are bonded to a backing sheet of 15 $\mu$m thick aluminised Mylar using Stycast 2850FT epoxy.

mately 5 thicknesses of Metglas. Mylar was selected as a backing material due to ready availability in a number of different thicknesses, and suitability for use in a vacuum. The shielding could in principle be made as a single sheet and attached to the 1-K box using a small number of screw fixings. Tests carried out during development identified Stycast[2] 2850FT as a suitable adhesive to bond the Metglas foil to Mylar sheets. A test section of the composite shielding is shown in Fig. 8.5.

The composition of the shielding for the 1-K box is shown in cross section in Fig. 8.6. An inner Metglas layer is bonded with Stycast to a 15 $\mu$m aluminised Mylar backing. The middle sheet of Metglas is bonded to a 127 $\mu$m Mylar backing, as is the outer layer of Metglas, which also incorporates the niobium shield. This outermost layer was composed of a 127 $\mu$m Mylar backing sheet with Metglas foil, then tiles of 0.25 mm niobium[3] bonded to the Metglas with Stycast epoxy, and then a final layer of 127 $\mu$m Mylar bonded to the niobium. The thickness of the Mylar sheets defines the separation

[2]Emerson and Cuming, http://www.emersoncuming.com.

[3]The thickness of the niobium sheet was selected based on what could be easily sourced. A thinner layer would have been as effective, and would have been preferable in many respects due to the decreased mass. However, thinner material would have been considerably more expensive.

of the nested Metglas, in this case approximately 5 thicknesses of high-permeability foil. A thinner sheet of Mylar is used to back the innermost Metglas layer since it is not necessary to space this layer from the aluminium, allowing a slight reduction in the overall thickness of the finished composite.

These shielding layers were produced as oversized sheets, then cut to size using a flat projections of the 1-K box structure generated from the computer models of assembly. Screw holes matching the pattern in the aluminium structure were pre-drilled. Larger apertures for thermal contacts were cut either by hand or using hole saws. The shielding sheets were attached to the aluminium box primarily by a pattern of M3 brass screws around the edges of the shielding. The pre-cut through-holes for the screws were intentionally made oversized, so stacks of brass washers were used to ensure a good contact between the screw heads and shielding layers. Only a small number of screw fixings were used for the layers to reduce the number of holes required in the 1-K box, so to improve the thermal contact between the shielding and aluminium strips of 19 mm wide, double-sided adhesive copper tape were placed between each of the three foil layers and between the innermost layer and the aluminium box. Finally, the loose edges of the shielding were sealed with Mylar tape.

The original intention had been to fold the majority of each shielding layer onto the aluminium structure as a single section, but due to limited flexibility of the thicker sheets, this proved difficult. To overcome this, the two outermost layers were separated into a series of flat panels, which were then attached independently to the 1-K box. Continuity between the panels was maintained by taping additional strips of Metglas along the joints using copper and Mylar tape, again maintaining a minimum overlap of 20 mm.

Thermal contact to the 1-K box structure consists of four large copper plates attached to the aluminium panels by a pattern of screws and a large-area epoxy joint, as described in Chapter 6. The need to make the contact between the copper and the aluminium forced large gaps to be left in the shielding layers. To reduce the penetration of flux through the the shielding, in particular the superconducting layer, oversized panels of niobium foil were attached inside the box to approximately cover the area of the copper plates.

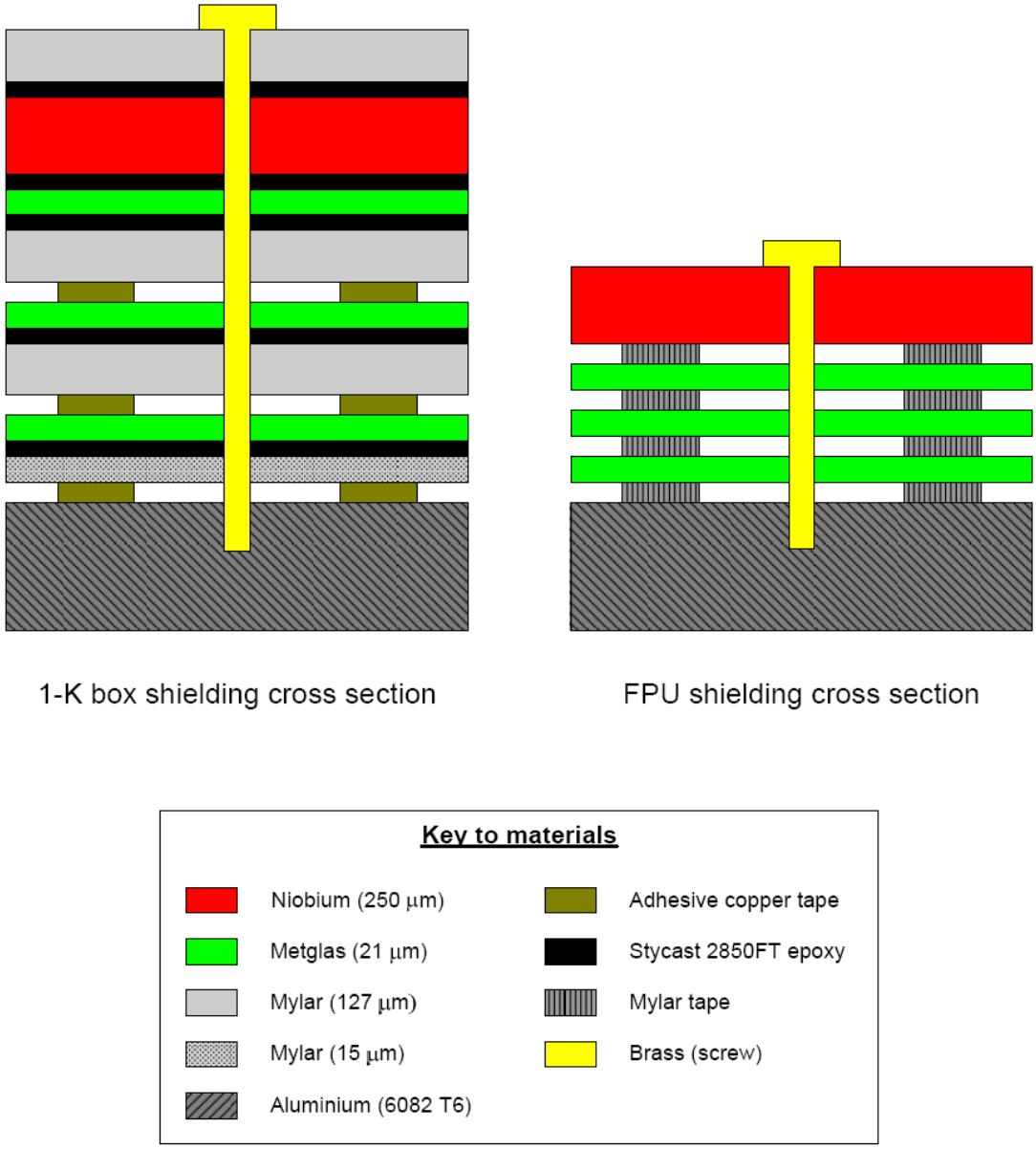


**Figure 8.6:** Cross section schematics of the foil shielding for the 1-K box and focal plane units. The different foils are indicated by the colour coding in the figure.

The shielding on the focal plane units was attached to the removable outer covers that fit over the detector subarrays. The shielding, shown in cross section in Fig. 8.6, consisted of three layers of Metglas foil attached by adhesive Mylar tape to the aluminium covers. Sections of 0.25 mm thick niobium foil were then fitted over the Metglas using tape and M2.5 brass screws. Finally, joints between the niobium foil sections and the edges of the layer were sealed with aluminium adhesive tape. Fig. 8.7 shows one of the focal planes with the outer cover in place over the detectors.

The modelled shields for the FPUs were composed of a minimum 70 $\mu$m of Metglas under a superconducting shield. The three layers of Metglas foil used in this assembly produces a layer of approximately this thickness, with no inert spacer as on the 1-K foil shields. However, the final shielding differed from the models in that the structure of the FPUs forced more discontinuities in the shielding than had originally been anticipated. The need to allow access for wiring in particular heavily restricted the areas to which shielding could be attached. Ultimately, it was only possible to attach Metglas as an open-ended box around the detectors, with niobium foil extending slightly over the edges of the outer cover. The approximate coverage of the Metglas and niobium is illustrated schematically in Fig. 8.8. This differs significantly from the modelled shield geometries, since this final shielding design no longer forms completely enclosed shells. It is likely that this has a detrimental effect on the shielding performance by allowing flux to leak into the enclosed volume.

### 8.1.3 Cold Shutter Motor

A definite design for shielding the cold shutter motor was not developed as part of the FE modelling process. The motor used for the shutter mechanism (Phytron[4] USS 42.200.2.5-NSSN-UHVC) has a reduced magnetic moment due to coil alignment, but to supplement this additional shielding was fitted to the motor casing. Ten layers of Metglas 2705M foil were wrapped onto the housing to form a cylindrical shield coaxial with the motor. The foil sections were wrapped individually around the motor and secured with Mylar tape with each foil strip overlapped by 20 mm to form a continuous cylindrical shell. Since the overlap of each layer represents a weak point in the shield

[4]Phytron, Inc., http://www.phytron.com.

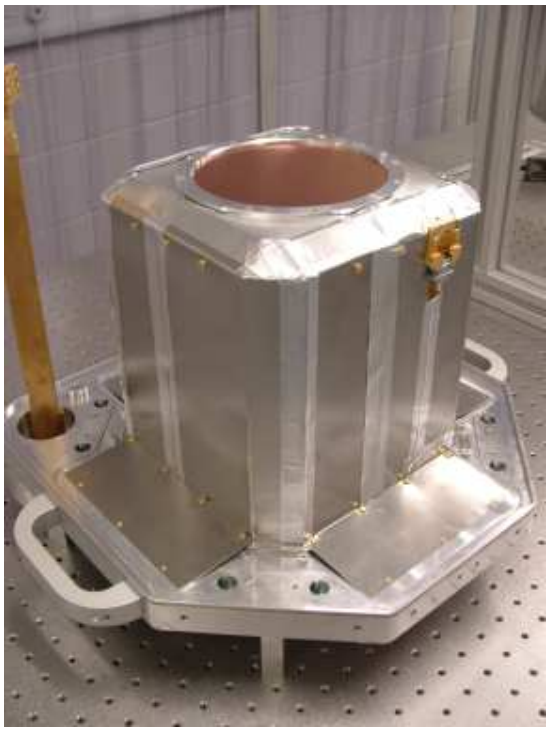

**Figure 8.7:** Focal plane unit with the shielded outer cover in place.

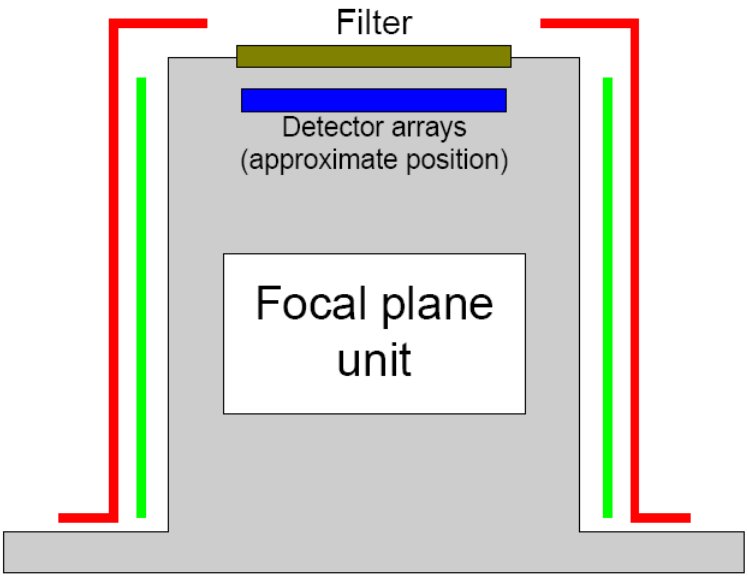


**Figure 8.8:** Schematic cross section of the focal plane unit magnetic shielding, showing the coverage of the Metglas foil in green, and the niobium foil in red.

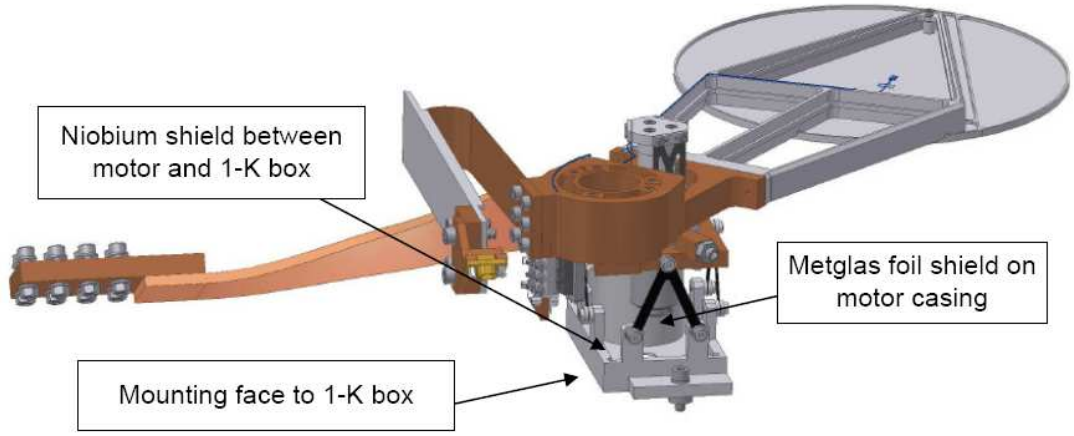


**Figure 8.9:** Computer model of the cold shutter motor and the 1-K box, with the location of the Metglas and superconducting shielding around the motor indicated.

that could allow flux to penetrate, the position of the join of each layer was offset 180° from the overlap of the previous layer to reduce this effect. In addition, a 0.25 mm section of niobium foil was fitted between the motor and the 1-K box, perpendicular to the axis of the motor. These sections of shielding are indicated in Fig. 8.9.

### 8.1.4 SSA Cans

As noted in Chapter 7, the SQUID series array amplifiers are more sensitive to interference from magnetic fields than the multiplexer devices. To overcome this problem, the SSAs are enclosed by dedicated shielding consisting of an outer niobium can to provide a superconducting shield, supplemented by an inner, high-permeability shield. An SSA module is shown in Fig. 8.10 with the outer niobium can removed to expose the series array boards and the inner shield. This design has been used successfully to shield this type of device. The only change for the SCUBA-2 modules is that the inner mu-metal shield is made from Cryoperm-10, in place of the CONETIC-AA alloy used in NIST modules.

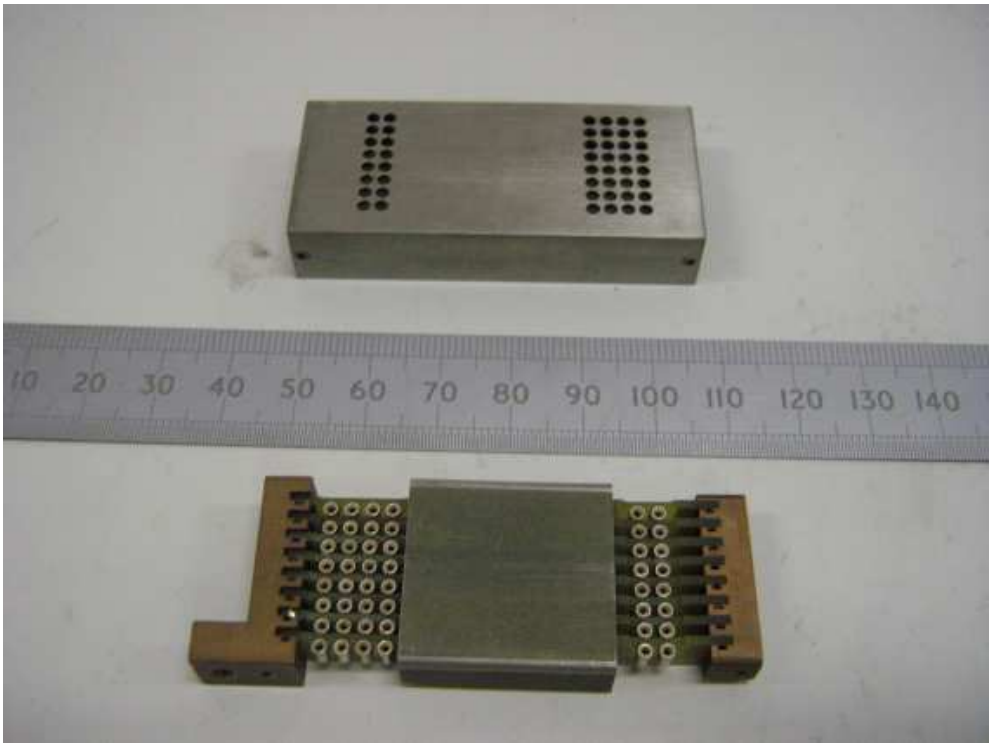


**Figure 8.10:** Photograph of a disassembled SQUID series array module. The niobium superconducting can is shown at the top of the image (above the length scale) The eight SSA boards are shown below the length scale fitted to the copper heat sinks and enclosed by the inner Cryoperm-10 magnetic shield.

### 8.1.5 Shielding for Ancillary Instruments

Measurements of the magnetic fields from the two ancillary instruments (the FTS and polarimeter) to estimate the field from the instruments at the approximate location of the instrument cryostat. The requirement that the field at the cryostat window should not exceed the Earth's field was easily met by the FTS module, since this instrument uses relatively small motors and is physically some distance from the main instrument. The polarimeter, which has continuously-operating motors to drive the waveplate, was found to exceed the field requirement. High-permeability foil was added to the motor assemblies in the same way as for the cold shutter motor to reduce the field.

### 8.1.6 Summary of Final Shield Design

Details of the final arrangement of the cryostat shielding are summarised in Table 8.1.

**Table 8.1:** Summary of the final cryostat shielding layout.

| Location | Shielding |
|---|---|
| Focal plane | 5 $\mu$m molybdenum layer on multiplexer wafer |
| SQUID series arrays | 1 mm niobium shield with inner 0.5 mm Cryoperm-10 shield |
| Focal plane units | 0.25 mm niobium shield over 70 $\mu$m Metglas, partial coverage only (see Fig. 8.8) |
| 1-K box | 0.25 mm niobium shield over $\sim$ 330 $\mu$m Metglas (including nesting with Mylar, see Fig. 8.6) |
| Cold shutter motor | 200 $\mu$m cylindrical Metglas shield on motor, 0.25 mm niobium shield on axis between motor and 1-K box |
| Vacuum vessel | Two 1 mm nested mu-metal shields, $\sim$5 mm vacuum gap |

## 8.2 Shielding Verification

Measurements of the magnetic field environment in the lab indicated a static field with a strength of the order of 0.1 mT, or twice Earth field strength, similar to that measured at the telescope. The dominate component of this field was in a horizontal orientation. It is suggested that this field originates from the presence of motors and other equipment in the laboratory building, since the dominant component of the Earth's magnetic field at a latitude of 56° North (the approximate latitude of Edinburgh) is in the vertical direction [162]. No issues with operation of the detectors in this static field were observed. The direction of the Earth's field would be expected to be different at the telescope due to the lower latitude. At a latitude of 20° North (Mauna Kea) and at altitude of 4000 metres, the dominant field direction is horizontal, although the Earth's field strength is weaker than the measured fields at the telescope due to the motors and steel structure.

The effectiveness of the magnetic shielding was determined by applying an external field from an electromagnet, and measuring the response of the second stage SQUIDs (SQ2s) to the field change. The SQ2s were used since, in principle, they should be the most sensitive part of the readout chain to changes in the magnetic environment. The first stage SQUIDs have additional shielding due to the presence of the superconduct-

ing detector ground plane, while the series array SQUIDs are shielded by independent superconducting and high-permeability cans. Furthermore, the output signal from the readout chain is actually a multiplication of the response of each device in the chain, complicating the interpretation and calibration of the response to an external field. By using the SQ2s, the output is a convolution of the SQ2 and the SSA response only. Making the reasonable assumption that the SSAs are unaffected by the external field, the output essentially is a measure of the SQ2 response. A similar approach was used for measurements on the TES arrays for ACT [163], which are similar to the SCUBA-2 multiplexers.[5] Measurements were made on the 850 $\mu$m array only; the behaviour of the short wave array in the instrument at the time was such that sensible data could not be taken.

Measurements of the response to an external field were made by applying an magnetic field with an electromagnet. A field was applied in different directions and at a number of locations around the cryostat. The strongest response was seen with the magnet at the backshell of the cryostat, in the location physically closest to the arrays, and with the field applied perpendicular to the 850 $\mu$m focal plane. With the magnet in other locations, little or no response was observed. With the magnet at this location, the field strength at the focal plane (a distance of $\sim$600 mm) without the presence of shielding was estimated as 10 $\mu$T. A change in the applied field was produced by switch the electromagnet on and then off again a short time later, and looking at the change in the SQUID response.

The response of a selection of SQ2s with the magnet close to the focal plane is shown in Fig. 8.11. The data is taken as a timestream, with the output measured in DAC units. The three plots shown are from columns 3, 16 and 30 (of 32 columns in a subarray); these were selected since the channels showed a clear response to the field change (some channels were very noisy, making the response harder to measure, or were simply not operational), and since the distribution of these channels indicates the change in response across the array. The times at which the magnetic was switched on and off are indicated on the diagram (approximately 560 and 620 seconds, respectively).

[5]The multiplexer SQUIDs are the same, as is the multiplexer scheme, although the ACT arrays use several one-dimensional multiplexers rather than a two-dimensional array as in SCUBA-2.

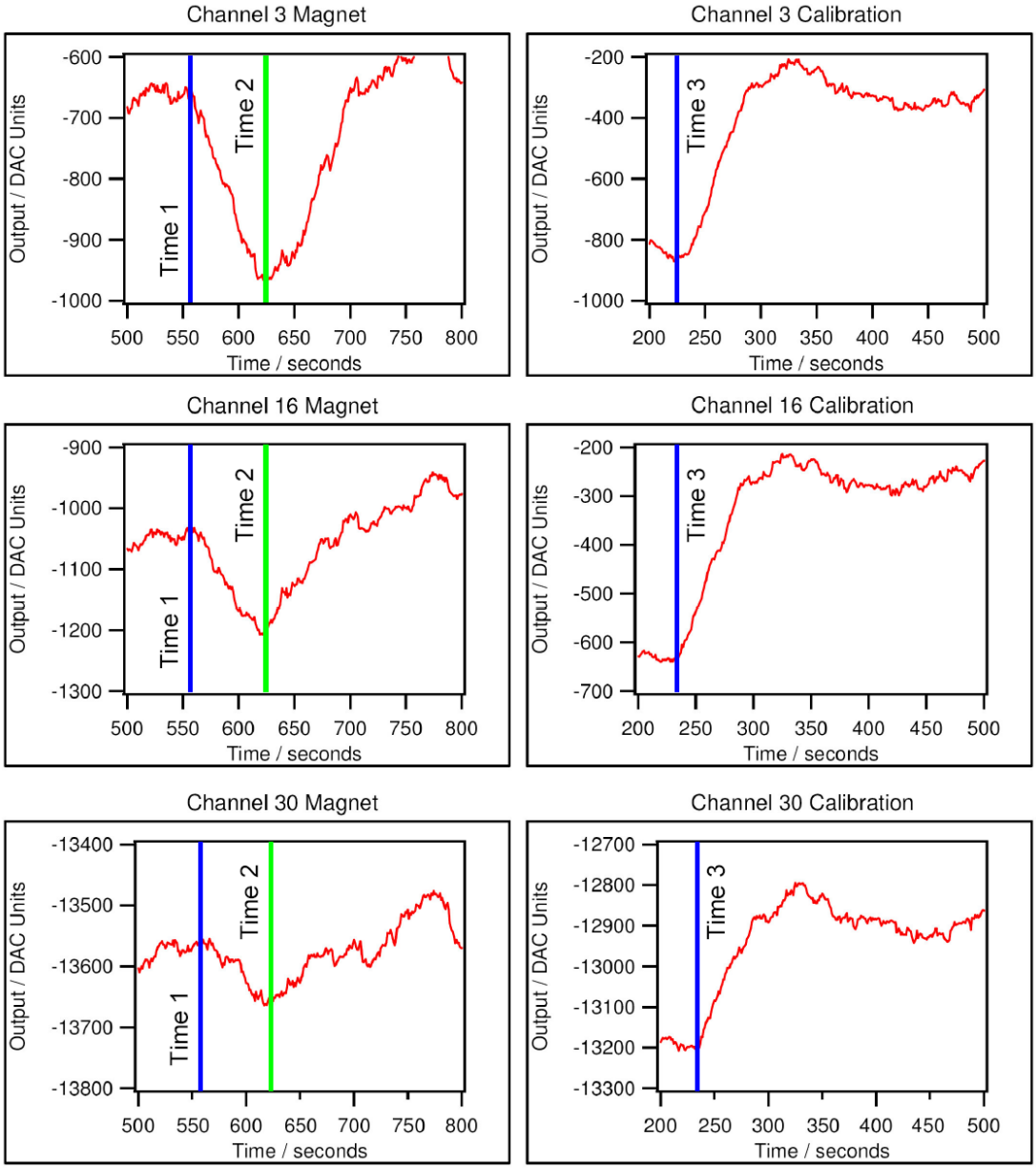


**Figure 8.11:** Time series plots of detector output on channels 3, 16 and 30 of an 850$\mu$m subarray. The plots in the left column show the response of the second stage SQUIDs to an applied field of $\sim$1 $\mu$T at the focal plane. The field change was produced by switching on an electromagnet at time 1 (approximately 560 seconds), and switching off the magnet again at time 2 (approximately 620 seconds). These points are indicated on the plots. The plots on the right show the response of the same SQUIDs to a change of 100 DAC units on the SQ2 feedback at time 3 (approximately 230 seconds), allowing calibration of the response to the external field. See text for discussion of the calibration method and the analysis of the response.

In the presence of a magnetic field, the SQUIDs behave the same as if the SQUID feedback current was changed. The response was calibrated by making a deliberate change of 100 DAC units to the SQ2 feedback, and measuring the change in output. Each SQUID will not have exactly the same response, so the same feedback change was made on all channels to give an independent calibration for each channel. The calibration for channels 3, 16 and 30 are also shown in Fig. 8.11, with the position of the feedback change (approximately 230 seconds) indicated.

The output change in response to the external field can be compared to the change in response to the change in feedback current, resulting in a feedback change equivalent to the change due to the field. The response to the SQUID to changes in feedback or magnetic field strength is periodic. The characteristic response (a $V$-$\phi$ curve) has a period of one flux quantum,[6] $\Phi_0$ (see Appendix B for a description of SQUID behaviour). The SQUIDs for the SCUBA-2 detectors are designed such that the full range of the feedback (65000 DAC units) sweeps out a $V(\phi)$ cycle. Hence, we can obtain the change in flux at the SQ2s, $\delta\Phi_s$, in units of $\Phi_0$, due to the external field by taking the feedback change equivalent to the presence of the external field, $\Delta$, as a fraction of the full range, such that

$$\delta\Phi_s = \frac{\Delta}{65000}\Phi_0. \tag{8.1}$$

Although SQUIDs have a high sensitivity to changes in magnetic flux, the small area of the devices ($\sim 10^{-10}$ m$^2$) means coupling magnetic fields directly to the SQUID can be problematic. The solution is to couple the field into the SQUID using an inductive coil. In the case of the SCUBA-2 multiplexer, this is a loop consisting of 41 gradiometrically-wound coils for the input from each SQ1, and a coil to couple flux into the SQ2. This arrangement, the SQ2 summing coil, is shown schematically in Fig. 8.12. The area of the coil is considerably larger than the area of the second stage SQUID.

According to flux quantisation (see Appendix B for further discussion of this phenomenon), the a change in flux through the closed superconducting circuit of the summing coil due to an applied field, $B$, will be opposed by a current, $I$, flowing in the coil, such that

[6] One flux quanta is equal to $2\times10^{-15}$ Tm$^2$.

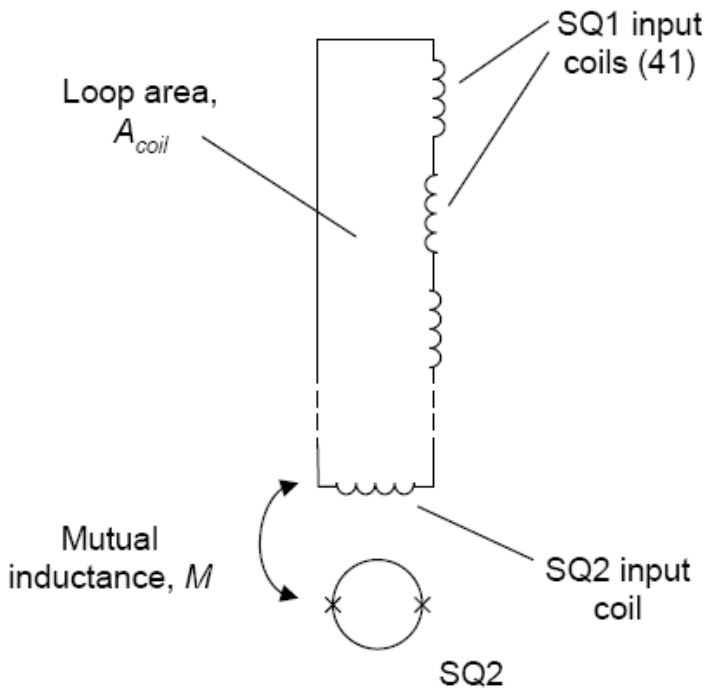


**Figure 8.12:** Schematic representation of the arrangement of the SQ2 input. The second stage SQUID couples to the summing coil, of area $A_{coil}$ and self inductance $L_{coil}$, with mutual inductance $M$.

$$IL_{coil} = BA_{coil}, \tag{8.2}$$

where $L_{coil}$ and $A_{coil}$ are the self inductance and enclosed area of the summing coil, respectively. Since the summing coil and the SQ2 are coupled circuits, the current in the summing coil will induce a change in the flux through the SQUID, $\delta\Phi_s$, described by

$$\delta\Phi_s = MI, \tag{8.3}$$

where $M$ is the mutual inductance between the summing coil and the SQUID. Hence, if we measure a change in flux through the SQUID, this is related to the applied field by

**Table 8.2:** Calculated external magnetic field attenuations for channels 3, 16 and 30 on an 850 $\mu$m commissioning grade subarray. The intermediate steps of the calculations following the method described in the text are also included.

| | Channel Number | | |
|---|---|---|---|
| | 3 | 16 | 30 |
| Response to external field / DAC units | 300 | 250 | 100 |
| Response to feedback change / DAC units | 600 | 400 | 400 |
| $\delta\Phi_s$ / $10^{-4}\Phi_0$ | 8 | 10 | 4 |
| $B$ /nT | 0.28 | 0.34 | 0.13 |
| Attenuation (10 $\mu$T applied field) | $4\times10^4$ | $3\times10^4$ | $8\times10^4$ |

$$B = \frac{\delta\Phi_s L_{coil}}{M A_{coil}}. \tag{8.4}$$

For this calculation, the self inductance of the summing coil is assumed to be ∼30 nH (41 SQ1 inputs plus the inductance of the SQ2 input coil), and the mutual inductance between the coil and the SQ2 to be ∼3 nH. This values are based in measurements for early prototype multiplexers described in Ref. [103]. Since the SQ1 coils are wound gradiometrically, the effective area of the summing coil is the area of one SQ1 coil plus the area enclosed by the SQ2 input coil ($5.7\times10^{-8}$ m$^2$) [164].

Using this data and Eq. (8.4), the change in flux at the SQUID, $\delta\Phi_s$, determined from the feedback measurement may be converted to a field at the detector array, $B$. Comparison to the applied field of ∼10 $\mu$T gives the attenuation factor. The calculation for the three channels in Fig. 8.11 using this method is summarised in Table 8.2.

The calculated attenuation factors for these channels range from 30000 to 80000. This is consistent with the high-end predicted attenuations from the FE models (see Tables 7.11 and 7.12), although the measured attenuations are slightly greater than the predicted figures. It would be expected that the measured performance would be lower than the modelled performance, since in many respects the models were idealised. In particularly, the FE models likely overestimated the effectiveness of the shielding on the 1-K box and focal plane units, since the final constructed shielding has considerably

more discontinuities than the geometries modelled. However, two major differences between the modelled and and final shielding that could have increased the shielding effectiveness are that the vacuum vessel shielding was constructed such that the mu-metal forms a complete shell, as opposed to the model which had gaps between shield sections, and that the high-permeability shielding on the 1-K box used larger spacing layers between the Metglas foil than included in the model. The modelled shielding for the 1-K stage had a total thickness of 200 $\mu$m, whereas the final shield was approximately 450 $\mu$m thick.

The attenuation factor for channels 3 and 16 are similar, increasing slightly for channel 30. With channel 3 on the outer edge and channel 30 at the centre of the focal plane, this may indicate a field gradient across the focal plane, as expected from the modelling of the detector array groundplane. This is not conclusive. The model results predict a change of approximately an order of magnitude in the field strength between the edge of the focal plane and the centre, whereas the measured results imply a factor 2 difference. Without data from other subarrays on the focal plane, the presence of a gradient can not be reliably shown. The high attenuation factor measured for these channels would indicate that even if there is a field gradient, it is sufficiently small that it will not affect the performance of the arrays.

While this analysis has produced a determination of the attenuation of external fields provided by the shielding, it does not provide any information on the response of the detector arrays to a field with a changing direction. Equally, the shielding requirements assume that the detector arrays are static with respect to the field. This distinction was not fully appreciated prior to the delivery of the instrument and start of commissioning at the telescope. It has subsequently been determined that although the shielding attenuation meets the requirements as defined, the level of shielding is insufficient to reduce the response of the detectors to changing fields to a sufficient degree. The performance of the system at the telescope, and the consequences of a changing field direction at the focal planes, are discussed in the next section.

## 8.3 Measured Response to Magnetic Fields at the JCMT

During commissioning of the instrument at the JCMT, it was observed that movement of the telescope antenna in azimuth causes a change in the signal level of the second stage SQUIDs. This change is well defined and repeatable, with an amplitude of $\sim$0.1 $\Phi_0$. Given the area of the SQ2 summing coil, it can be shown that a change of this magnitude in the SQ2 output is consistent with a field change of $\sim$ 2 nT at the focal planes. With shielding factors of $\sim$ 50000 as determined from the verification measurements described above and in Table 8.2, a 2 nT field change at the focal planes corresponds to a change of 100 $\mu$T outside the cryostat.

Subsequent measurements of the field environment at the JCMT using a three-axis magnetometer (a more accurate instrument than the gaussmeter originally used for the field measurements) mounted on the instrument cryostat showed that as the antenna completed a full revolution in azimuth the field perpendicular to the cryostat window varied by $\sim$ 100 $\mu$T with a sinusoidal variation (the variation in the other axial directions have amplitudes $\leq$ 10% of this) [165].

The observed variation in the detector output is therefore entirely consistent with what would be expected. The original shielding requirement took no account of the fact that the cryostat would be moving relative to the external field. Motion sensitivity has been reported for other instruments using SQUID-multiplexed TES arrays (e.g. Ref [110]), however, these other examples appear to be high frequency pickup from the telescope drive motors. This is not the effect seen in the SCUBA-2 data. To reduce this effect, it will be necessary to reduce the field changes at the focal plane. This could be achieved either by increasing the attenuation of the shielding, or through the application of a field at the SQUIDs to counter the changing external field.

The actual attenuation factor required for the cryostat shielding may be estimated by assuming that any changes in the SQ2 output must be less than the inherent noise of the cold electronics, which is $\sim$100 $\mu\Phi_0$. Since changes at the 0.1 $\Phi_0$ level are observed, the required attenuation is 1000 times better than that currently achieved, or a requirement of $10^7$. It would be difficult to add more shielding to the cryostat in order to achieve the additional attenuation. The available space at the 1-K stage is extremely limited, while adding material at the higher temperature stages would not offer major

improvements due to the large volumes enclosed. An additional attenuation factor of a few hundred would be achievable if the temperature of the 1-K box and focal plane units could be reduced such that the aluminium structure were to go superconducting, but this is unlikely to be achieved without major changes to the cryogenic design.

The alternative solution would be to implement a method of countering the field changes by applying a field at the focal planes. The possibility of fitting a cancellation coil at the focal planes or external to the cryostat has been considered. A further possibility is changing the SQ2 feedback to counter the changes in the flux threading the SQUIDs. This is a potentially more elegant solution on the grounds that it requires no additional hardware.

Work to develop this solution is ongoing. In parallel to this, some changes are to be made to the construction of the magnetic shielding at the focal plane units in an effort to increase the attenuation factor. The main change is to construct an FPU shield as a continuous, welded structure rather than building the shield from foil sections, which will, in principle, reduce the penetration of flux through any gaps in the superconducting shield.

## 8.4 Summary

This chapter has described the work carried out on the detailed design, construction and verification of magnetic shielding for the SCUBA-2 detector arrays. The development of the design derived from the finite-element modelling results presented in Chapter 7 into a practical design necessitated a number of changes, primarily since the shielding layers were retrofitted to the existing cryostat structures. The construction of the shielding layers was described, including details of a novel solution for the cryogenic shielding layers using a composite of Mylar, Metglas and niobium bonded with thermal epoxy. The final arrangement of the cryostat shielding is summarised in Table 8.1.

Measurements to determine the effectiveness of the final shielding design against external fields were detailed. The method used for these measurements used the second stage SQUIDs of a subarray, determining the response of the SQUIDs to a large external field. The response was calibrated by making a change to the SQUID feedback and comparing the change in output for the feedback change and that due to the external

field, allowing calculation of the field change at the SQUIDs. Measurements were made on three channels distributed across the array on the 850 $\mu$m focal plane, with calculated attenuation factors of between 30000 and 80000. This exceeds the attenuation requirement by a factor of at least 20, and also exceeds the predicted performance from the models. However, subsequent work with the instrument during commissioning at the JCMT revealed that effects are seen as the cryostat moves through the static field in the enclosure, to the level where a sinusoidal signal is observed in the detector output.

Further investigation of the field environment as a function of the antenna azimuth showed that the magnetic field changes by as much as 100 $\mu$T as the telescope moves through a full rotation, which is consistent with the detector response given the measured attenuation figures. It should be noted that although the attenuation figures measured prior to delivery of the instrument easily met the requirements, it may be seen that the requirements were incorrectly defined and the implication of the cryostat moving in a magnetic field were not fully appreciated prior to approval for delivery being given. The magnetic shielding as implemented is easily sufficient to deal with static fields, but not to reduce the device response to changing fields to a sufficiently low level. The observed behaviour is now better understood following further investigative work, and possible solutions are under development.

# Chapter 9

# Conclusions and Further Work

The work described in this thesis has dealt with a number of aspects of the design, testing and performance of the SCUBA-2 instrument. These areas included the design and performance of the bolometer arrays, the cryogenic performance of the instrument, with particular focus on the dilution refrigerator, and the design of shielding to attenuate the strength of magnetic fields at the focal planes. These topics are discussed individually in the following sections. The major results in each area are broadly summarised, and where appropriate discussion of potential improvements for future instrument designs is included. At the end of this chapter, future directions of development for submillimetre instrumentation and related technologies are considered.

## 9.1 Detectors and Arrays

The major problem experienced with the SCUBA-2 detector arrays so far has been low pixel yields, although this has generally been improving with each production generation. The reasons for pixels being non-operational is not solely due to pixels being electrically "dead" as a result of shorts or failed wire bonds, but have a number of sources of failure including physical parameters being out of specification, or individual columns on the array being masked out due to excessive power dissipation (as discussed in Chapter 6). Many of these problems are simply the result of the immaturity of the

technology, and are for the most part sufficiently well understood that the issues will be solved in future array batches.

Specific problems with the latest generation of arrays can be generally attributed to the variation of thermal conductance across the arrays, both due to variation of the deep etch trenches around the pixel absorbers, and the hybridisation error on the 850 $\mu$m array. While this effect will also increase the NEPs on these arrays, it does not explain the increased noise on the arrays at the JCMT compared to that measured prior to the delivery. It is currently believed that the most likely source of the higher noise levels is magnetic flux trapped at the focal planes causing large DC offsets in the multiplexer SQUIDs. This is one of a number of potential magnetic effects associated with operation at the telescope that have been identified, although the solution in this instance is potentially straightforward. The magnetic effects are discussed in more detail in §9.3.

Recent arrays have been observed to cause higher than expected levels of power dissipation, in extreme cases the level of heating when particular MUX columns are biased causing extreme temperature increases of several hundred millikelvin. To deal with this problem, a number of columns on all the arrays must be masked out. Although initially believed to be a result of niobium oxide contamination on the multiplexer wafers introducing normal state regions in the otherwise superconducting circuit, later investigation following a redesign of the multiplexer to mitigate this issue traced the problem to the cold electronics module rather than the array itself. In the current layout of the electronics module, connections between the SQUID amplifier arrays at 1 K and the millikelvin section of the module are made via Kapton flexes with deposited niobium tracks. Electrical connections to the flexes are made by a hot-bar reflow process with an interposing layer of epoxy embedded with conductive particles. Although such joints are intended to have very low resistance, a number of joints in the SCUBA-2 modules showed anomalous resistances, such that when current flows through certain tracks the Joule heating is sufficient to cause measurable heating at the focal planes. The origin of the increased resistance is unclear, although one possibility is a partial delamination of the joints. At the time of writing, the cold electronics modules are undergoing a redesign to replace the niobium flexes with woven NbTi ribbon cables, similar to those used for

the array wiring harnesses. Contacts can then be made by conventional soldering, which will provided superconducting joints. Other changes are being incorporated to increase the reliability of the wire bonding process to the detector wafer, which should reduce the number of broken bonds on thermal cycling.

In general, it has been demonstrated that this detector and array technology is a viable approach for filled focal planes with hundreds or thousands of pixels, both in SCUBA-2 and a number of similar instruments. As discussed previously, the majority of the problems experienced have resulted from the immaturity of the technology, and are now well understood. However, the array technologies used in the present generation of submillimetre instruments may have only limited usefulness for scaling to larger focal planes and higher pixel counts. While larger arrays may be fabricated, the practical size of arrays is limited by the numbers of wires going to the focal plane to instrument higher pixel counts, and issues with effectively cooling large wafers to avoid hot spots at the centre of arrays.

Although development for larger arrays is ongoing, construction of a megapixel-scale camera, a likely goal for astronomy at the shorter submillimetre wavelengths, would be difficult. Such high pixel counts would be excluded by the power dissipation at the focal plane from time-division multiplexing schemes used in the current generation of TES instruments, and the need to bring large numbers of wires out of the cryostat. The use of SQUID-based frequency-division multiplexing (FDM) has been demonstrated for TES detectors using low-frequency carriers [166]. FDM schemes with microwave carrier frequencies are more attractive due to larger signal bandwidth. Microwave SQUID multiplexers have also been demonstrated, potentially allowing hundreds of TES devices to be read out through a single coaxial cable [167]. However, as discussed in Chapter 1, at present the length of cabling from the focal planes is limited to a few hundred millimetres, otherwise the propagation time of signals along the wires is too long to allow feedback signals to be returned to the detector arrays.

Alternative detector technologies may offer better approaches in the future for the construction of large arrays. A device that has been receiving considerable attention is the kinetic inductance detector, the principle of which was outlined in Chapter 1. A test camera with 36 pixels operating at 850 $\mu$m and 1.25 mm was recently demonstrated

on the CSO [168], with plans to scale the instrument to a 576 pixel array. KIDs are a particularly useful detector, since multiple devices may be coupled to a single "pixel", in this case a phased-array of slot dipole antennae, in an array. The pixels in such a camera are therefore able to image at several wavelengths simultaneously, increasing observing efficiency. FDM for KIDs is easily achieved. The devices developed for the instrument described are generally referred to as distributed element KIDs. Such detectors use coplaner waveguide arrangements to form quarterwave resonators. The disadvantage with this approach is that the fabrication of the devices is impossible for shorter wavelengths due to the scale of the components. An alternative arrangement, the lumped-element KID, has seen development for use at THz frequencies [169]. Such devices likely offer the best option for future large arrays, although still need further development.

## 9.2 Instrument Cryogenics

Due to the low temperature operation of continuum detectors for submillimetre and millimetre astronomy, the cryogenics systems are of central importance to such instruments. Operation of focal planes at 100 mK and below is known to be particularly problematic, to the extent where despite the performance advantages of the lower base temperature, instrument designs often opt for a base at 300 mK in order to simplify operation. These issues were somewhat compounded in SCUBA-2 as a consequence of the large cryostat and the cryogen-free design. However, detailed performance measurements (described in Chapter 6) demonstrated cryostat performance predominantly within that required for operation.

The major area of risk for the cryogenics system was the dilution refrigerator. It should be noted that the concept of "dry" dilution refrigerators was relatively new in the early stages of the project, the development of such systems being limited to research projects such as the work of Uhlig (Refs. [133–136, 138, 139]). Such systems are now available commercially from a number of companies, including Leiden Cryogenics. Considerably more effort was required for commissioning of the DR than was originally anticipated, in addition to a programme of modification and upgrade to improve a number of operational features of the system. This work was described in more detail in

Chapter 4. Although the performance of this fridge is broadly acceptable for SCUBA-2, the behaviour and design of the DR are not ideal. Given concerns over the reliability of the system, steps have been taken to procure a spare dilution refrigerator, potentially a compatible system from a different supplier.

An issue with the cryogenics design that will be an important consideration for future instrument designs is the effect of power loading from the 1-K stage of the instrument on the still of the dilution refrigerator. As discussed in Chapter 6, characterisation of the instrument cryostat indicated a loading of ∼10 mW on the DR still from the 1-K stage, compared to an anticipated load of ∼0.5 mW. This additional loading could have had a potentially detrimental effect on the performance of the dilution refrigerator, degrading the base temperature for the focal planes. Fortunately, the behaviour of this DR was such that the optimal operating condition required a load of ∼14 mW on the still, much of which was provided by the ambient loading when operating in the main cryostat. The origin of the additional heat on the instrument third stage is not clear, although this serves to illustrate the potential problems associated with the design of cryogenic instruments, particularly the large cryostats that will be required for the next generation of widefield cameras.

Furthermore, the effects of the use of dry cryogenic systems with TES detectors must be considered. It has been known for some time that there are potential problems with the use of bolometers in dry cryostats due to microphonic sensitivity of the detectors. A number of studies have been carried out to this effect (e.g. Ref. [170]). High-impedance semiconductor bolometers are more susceptible to microphonic pickup. While the lower impedance of TES devices, combined with the considerably reduced levels of vibration from pulse tube cryocoolers compared to earlier types, has effectively eliminated this issue, work with SCUBA-2 has implied the presence of coupling via temperature oscillations of the PTC base temperature. There have been discrete noise features at the PTC oscillation frequency observed in the TES output, seemingly coupled to oscillation in the bath temperature either as a direct result of the oscillation of the higher temperature stages in the cryogenic system, or due to vibrational heating at the DR mixing chamber. This suggests that physical and thermal damping of links to the cryocoolers is still an issue due to the temperature-sensitive nature of the TES devices.

Experience with this DR and the problems associated with the behaviour of the JT stage and interaction with other temperatures stages prompted conceptual work on alternative designs for dry DRs. The reason for use of the JT stage in dry DR designs is primarily due to the sequence of development, and initial use of cryocoolers unable to reach 4 K. Although the practice has continued successfully, the availability of 4 K cryocoolers with high cooling capacity opens other possibilities, including the use of a separate condenser at ∼1 K as in the conventional dilution refrigerator design (the 1-K pot). A separate condenser offers advantages, such as heat sinking of electronics and radiation shields at approximately 1 K without placing large loads on the still, potentially affecting the operation of the DR. This work was accepted for publication in the journal *Cryogenics* as "Proposed designs for a "dry" dilution refrigerator with a 1 K condenser", and is described in more detail in Appendix C. Recent development of dry DR systems has produced designs that no long require JT stages. By greatly improving the heat exchange with the second stage of the pulse tube, it has been possible to produce a $\sim$ 3 K heatsink without an additional expansion stage, allowing the still to complete the condensation of the mixture [171–173]. However, this would not be a suitable solution for use in large cryostats, since as discussed above, such systems continue to rely on the still as a 1 K heatsink.

Designing an instrument cryostat around a dilution refrigerator is a problematic approach compared to the use of a 300 mK bath temperature, however, if a 100 mK base temperature is required, options are limited. A possibility for future instrument design, although one which requires further development, would be the application of normal-insulator-superconductor microcoolers [174]. These devices are discussed in more detail in Appendix A, but in brief are thermoelectric coolers that would be able to reach temperatures in the 100–200 mK range from a 300 mK bath. The use of such devices combined with a $^3$He sorption cooler would be far more reliable than dilution refrigerators for remote operation of instruments, and considerably less complex than either DRs or adiabatic demagnetisation refrigerators.

## 9.3 Magnetic Shielding

The need to magnetically shield instruments incorporating superconducting devices is a relatively new concept, although one which will reoccur in future instruments incorporating superconducting devices. The shielding design for SCUBA-2 proved to be considerably more involved than originally anticipated, largely due to a poorly defined shielding concept early in the design process. The size and geometry of the instrument were far from optimal from a shielding standpoint, while retrofitting shielding around the existing structures and components forced numerous compromises in the design that greatly reduced the effectiveness of the shielding. Although the design requirements were ultimately exceeded, experience with the operation of SCUBA-2 at the telescope has indicated that the initial specification was incorrectly defined.

The shielding requirements were based on an estimate that the Earth's field should be attenuated by 500 times at the focal planes. This figure included a factor 10 safety margin, and originated from the effects of static and alternating fields on the SQUIDs and TESs. The required attenuation for the cryostat shielding was 1500, since measurements at the JCMT indicated fields of order three times Earth's field in the region of the cryostat. Testing of the cryostat shielding prior to delivery indicated attenuations of $\sim 10^4$ had been achieved. Measurements of the shielding performance at the telescope revealed a changing output signal as the telescope antenna was rotated in azimuth. Further investigation indicated that the detectors were responding to the movement of the cryostat in the telescope field in a way entirely consistent with the shielding factor measured in the lab during verification. Simple calculations have shown that the required shielding attenuation is $\sim 10^7$.

The conclusion from this is that the shielding requirements were not correctly defined nor sufficiently understood at the time. Work on possible solutions, such as application of SQUID feedback to counter the effect or increasing the attenuation factor of the shielding, is ongoing.

As discussed previously, there is some evidence that a contributor to the noise levels measured from the arrays at the telescope is trapped flux. While this problem could be dealt with in a similar way to the motion sensitivity issue discussed above, either by applying a flux offset via a coil or by increasing the level of shielding, a far easier

solution is to ensure that the detector arrays are cooled into the superconducting state with the cryostat orientated such that the magnetic field is in the plane of the devices. This orientation may be identified from work already undertaken on investigating and more accurately mapping the telescope field environment.

Now that the first generation of instruments using TES detectors and SQUID multiplexing have been deployed, a much better understanding of the behaviour of such detector arrays in magnetic fields and in operating environments has been developed. The issues experienced with SCUBA-2 and with similar projects may be overcome in future instruments by adopting an integrated approach to the instrument design process that includes development of the magnetic shielding scheme. Inclusion of a cancellation coil at the focal plane from the outset would also be an advantageous provision. Furthermore, recent developments in the design of the SQUID multiplexer arrays at NIST has produced a new generation of MUX with reduced coupling to external fields. Much of this improvement has been achieved by replacing the summing and coupling coils for the first and second stage SQUIDs with gradiometric configurations.

## 9.4 The Status of SCUBA-2

At the time of writing, SCUBA-2 is undergoing commissioning at JCMT. This process has been hampered by a number of issues, including the non-science grade nature of the most recent detector arrays, and some reliability problems with the dilution refrigerator. Despite this, SCUBA-2 achieved "engineering" first light in August 2008 (Fig. 9.1), a major milestone for any instrument.

Currently, a new batch of detectors arrays (in principle, sufficient to fully populate both focal planes) are undergoing processing in preparation for an anticipated instrument upgrade in early 2009. Following recommissioning of the instrument and further on-sky commissioning time, SCUBA-2 will be released to the JCMT community. The first science results are expected in the second half of 2009.

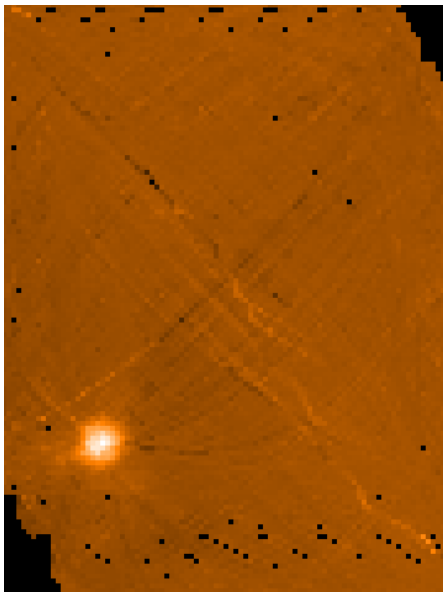

**Figure 9.1:** SCUBA-2 engineering first light image of Saturn.

## 9.5 A Brief Look Forward

Although submillimetre astronomy has come a long way since the earliest days of single-pixel photometric observation with infrared and optical telescopes, the field is only now starting to mature — as demonstrated by the recent explosion of development in sensitive detectors and instruments with large fields of view. Astronomy at these wavelengths still has a considerable way to go to be comparable to infrared astronomy, both in instrument capability and understanding of the astrophysical processes observed.

Current telescopes observing in the submillimetre, primarily the JCMT and CSO, have been operational for two decades and are reaching the end of their lifetimes. Development of new facilities is already well advanced, both for ground-based observation and telescopes above the atmosphere.

An imminent addition for submillimetre and far-IR astronomy is the Herschel space observatory, due for launch in 2009. Herschel, with a 3.5 m primary mirror and covering wavelengths between 60 and 500 $\mu$m with a number of spectroscopic and photometric continuum instruments, in addition to a heterodyne receiver instrument, will provide an unprecedented capability. Looking further ahead, SPICA, a collaborative project between Japan and the European Space Agency, will put a cooled 3.5 m telescope at the

L2 point [175]. With coverage between 5 and 200 $\mu$m, SPICA will give a major increase in sensitivity at the shortest submillimetre wavelengths by taking advantage of the lower photon noise offered by the actively cooled aperture. A further mission proposal, known as the far infrared interferometer (FIRI) [176], aims to combine the advantages of a cooled aperture in space to increase sensitivity and a high angular resolution through the use of an unfilled aperture. Considerable technological development will be required for these proposed missions, in particular the production of extremely low noise detectors in order to realise the full potential of such telescopes.

Despite many of the advantages offered by space-based submillimetre missions, ground-based facilities will continue to play a vital role since both larger apertures and higher angular resolution are available. The first generation of interferometers for the submillimetre and millimetre wavebands, the SMA in Hawaii and ALMA in Chile, are coming on line and offer huge potential for high-resolution imaging. Continued use of single dish telescopes will still be an important synergy for high-resolution observation since single dishes provide better sensitivity and mapping speeds. In the short term, facility instruments such as SCUBA-2 can provide much of this capability, but the lifetime of the JCMT is limited. The best future prospect for fulfilling this role is the Cornell-Caltech Attacama Telescope (CCAT) project [177], a 25 m dish on Cerro Chajnantor, above the ALMA site in Chile. Expected to achieve first light in 2013, a large telescope at such a good submillimetre site will provide excellent capabilities for survey astronomy across the full range of submillimetre wavelengths, including access to the shortest atmospheric transmission window at 200 $\mu$m. To take full advantage of the large field of view offered by such a telescope, advances in array technologies will be needed to provide filled focal planes for $\sim$10 000 pixel facility-class continuum instruments. The CCAT facility and its instruments represent a critical step forward in the development of submillimetre astronomy.

The development of instruments for the submillimetre has not so far been an easy task, and the difficulties are not likely to be lessened for the ambitious next generation of projects. However, as has been demonstrated by the tantalising glimpses of the submillimetre sky obtained in the last decades, the scientific returns offered more than justifies tackling the technological challenges.

# Appendix A

# Review of Cryogenic Technologies

As the demands on the performance of astronomical instruments have increased over the last century, it has became necessary to design instruments as cryogenic systems. For instruments operating in the visible and near-infrared regions of the spectrum, this generally involves operation of the detector elements and optical components at temperatures of 100–200 K, easily achievable with liquid nitrogen refrigeration. The development of instruments for longer wavelengths frequently required lower operational temperatures, approaching sub-kelvin and millikelvin temperatures for detectors working at far-infrared and submillimetre wavelengths, to achieve the required noise performance to detect small signals. Recent developments in detectors based on superconducting materials also require low operating temperatures, since superconductivity is a low-temperature phenomenon.

Cooling techniques capable of reaching sub-kelvin temperatures (i.e., below 1 K) have been developed in the field of low temperature physics to allow investigation of phenomena approaching absolute zero. Although techniques now exist that can cool samples into the $\mu$K and nK regimes, such technologies have no practical use in instrument development since these coolers would be impractical for cooling bulk structures such as detector arrays. Three techniques capable of reaching temperatures in the sub-kelvin region (pumped $^3$He cryostats, adiabatic demagnetisation cooling, and di-

lution refrigeration) have found application for astronomy and particle physics. The bolometers in the original SCUBA instrument operated at 100 mK, cooled by a dilution refrigerator (DR). Although a number of other instruments have operated at similar wavelengths using coolers at 300 mK, to achieve the desired sensitivity for the SCUBA-2 detectors, operation at ∼100 mK is required.

This chapter provides a background summary of the major methods of achieving low temperatures, with particular emphasis on refrigeration at and below liquid helium temperatures (4 K) and the development of mechanical coolers, both of which are relevant to submillimetre instrumentation. Sub-kelvin techniques, frequently used in millimetre and submillimetre continuum instruments such as SCUBA-2, are also discussed.

The process of refrigeration is essentially the reduction of entropy of a system. The most common methods of reducing system entropy in the context of cryogenic engineering are evaporation of a liquid (or sublimation of a solid) or the expansion of gas. Until relatively recently, the major method for achieving cryogenic temperatures was the use of baths of liquid cryogens, while expansion techniques were used to produce the cryogenic liquids. More recently, commercial mechanical coolers are capable to reaching liquid helium temperatures. Accounts of the historical progress and development of these techniques are available in the introductory sections of many textbooks on low temperature physics (e.g. White & Meeson [120] or Pobell [121]). Brief discussions of relevant cooling methods are included in this section.

## A.1 Refrigeration using Liquid $^4$He

Helium-4 was first liquified by Kammerlingh Onnes at Leiden in 1908, and has for many years been readily available from commercial suppliers, although at considerable expense compared to the price of liquid nitrogen. The use of liquid $^4$He is common in instruments operating at submillimetre and millimetre wavelengths, and receivers for radio astronomy, for a number of operational reasons. The high sensitivity requirements of astronomical observation necessitates the reduction of Johnson noise in instrument electronics and detectors. Also, for bolometer detectors, phonon noise in thermal links must be reduced. Both noise mechanisms are temperature dependant, and hence operation at low temperature is advantageous.

For bolometric instruments with low operating temperatures, it is necessary to reduce the radiative loading on instrument focal plane from fore-optics and other structural components. This is less of an issue for heterodyne detectors since mixers are essentially monochromatic, while the finite bandwidth of bolometer systems increases the optical power in the detection band. Radiation shields nominally at 4 K are therefore useful in such instruments as radiated power has a fourth-power dependency on temperature, and hence the power loading from a 4 K structure can be as much as seven orders of magnitude smaller than the loading from 300 K.

In low temperature refrigeration systems, such as those designed to achieve sub-kelvin temperatures (as discussed in more detail in Sect. A.4), liquid helium baths are used as intermediate temperature stages to cool radiation shields, reduce conduction loading on colder stages, and to precool or liquify circulating gases.

Cryostats using liquid $^4$He as a refrigerant are little more complex than a vessel from which the helium is allowed to boil off at atmospheric pressure. At atmospheric pressure, liquid $^4$He boils at 4.2 K, the lowest boiling point of any substance with the exception of the lighter $^3$He isotope. The vessel is designed such that conductive loads from ambient temperature are minimised, and may be surrounded by multilayer insulation blankets to reduce the radiative power loading. The helium vessel may also be enclosed by a higher temperature stage, such as a bath of liquid nitrogen, to provide further reductions in radiative and conductive loading.

## A.2 Mechanical Coolers

An alternative approach for the production of low temperatures without using liquid baths are mechanical cryocoolers circulating helium gas around a closed cycle. Essentially, these coolers are developments of the "expansion engines" used in the early stages of low-temperature research [120]. Modern commercial cryocoolers are capable of achieving temperatures down to 15 K on a single stage refrigerator, or less than 3 K with a two-stage system. Such coolers are useful since they can provide cooling continuously without replenishment of a cryogen bath (particularly useful in 4 K system due to the expense of liquid helium), but with associated disadvantages such as mechanical vibration and susceptibility to power failures.

In the construction of a refrigerator, it is necessary to make the machine as efficient as possible. The efficiency of any cyclic cooling process is very dependant on the exchange of heat between the flow of incoming gas and that returning from the region of cooling. Heat exchangers are broadly classified as continuous (or recuperative), in which incoming gas exchanges heat with a return flow in a continuous process, and regenerative exchangers. The latter type are essentially "cold reservoirs" for the discontinuous or pulsed flow processes used in some cycles, allowing the storage of energy from one stream and transferring the energy to a second stream. Regenerators typically take the form of a metal mesh or matrix of metal spheres.

### A.2.1 Continuous Heat Exchange Refrigerators

An example of a refrigerator using a recuperative heat exchanger is the Joule-Thomson cooler, based on an early observation that a gas will cool when expanded slowly through an orifice. Refrigerators working on this principle were originally designed as liquefiers, but later found application in cooling infrared detectors for scientific and military use. A working gas (typically nitrogen or argon) is compressed at room temperature, and the heat of compression is removed by heat exchange to ambient. The high pressure gas is precooled through recuperative heat exchangers by the counterflow gas from the cold finger, and then expands through a calibrated flow impedance (an orifice, valve, capillary or porous plug), with the intention of producing a two-phase mixture of liquid in equilibrium with its vapour at low pressure. Heat is removed by the evaporation of liquid, with the vapour then recycled through the heat exchanger and the compressor. When operated in a closed-cycle, the efficiency of JT coolers is low due to the high compression ratio required for the recycled gas. JT coolers may be used in an open-cycle mode, with a reservoir of compressed gas opened to the impedance, and the return component vented to atmosphere. Such coolers have a higher efficiency, since there is no need to recompress the gas as part of the cooling cycle, and can cool from ambient to 77 K in only a few seconds. However, the cooling effect lasts only as long as there is gas in the reservoir (typically no longer than a few minutes) [178].

Cryocoolers have also been developed based on the Brayton cycle (also called the "reverse Brayton cycle" to distinguish it from the expansion method used to liquify

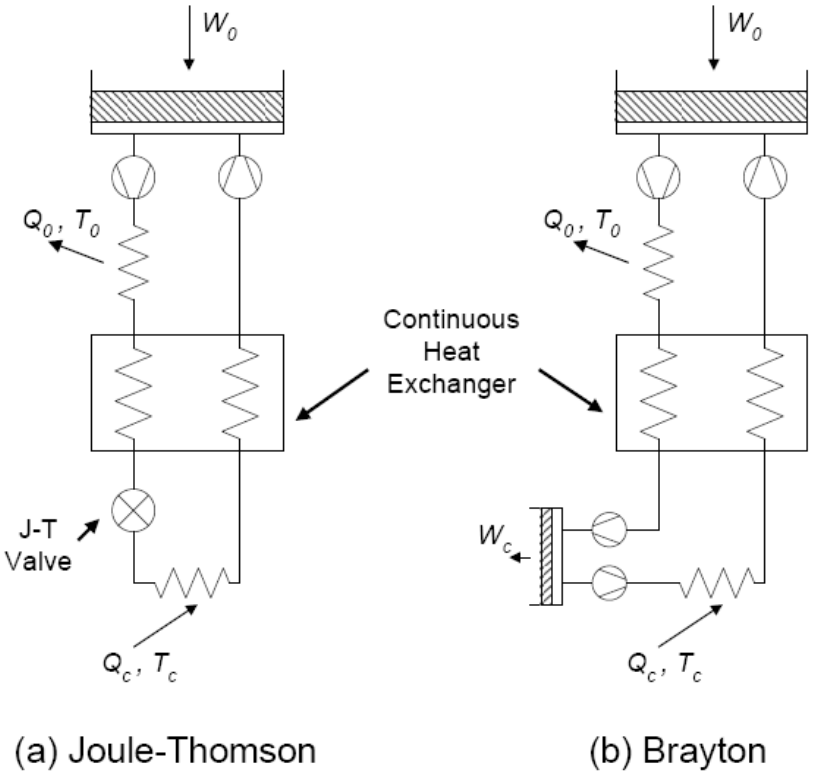


**Figure A.1:** Schematic representations of cryocoolers based on Joule-Thomson expansion and the Brayton cycle. For each case, $W_0$ is the work done at room temperature to compress the gas, with the heat of compression $Q_0$ expelled at the ambient temperature $T_0$. Heat $Q_c$ is absorbed from the cold environment at temperature $T_c$. For the Brayton cooler, the gas does work, $W_c$, as it expands in the engine, also at temperature $T_c$. Figure adapted from Ref. [178]. See text for more details.

gases), in which the cooling effect occurs as the expanding gas does work in an "engine" (usually a turbine). This process has a higher efficiency than simple J-T expansion, but is more complex and costly due to the inclusion of cold moving parts. Brayton cryocoolers have found application for detector cooling on space missions, such as the NICMOS instrument on the Hubble space telescope [179].

Schematic representations of refrigerators based on the Joule-Thomson and Brayton cycles are shown in Fig. A.1.

### A.2.2 Regenerative Heat Exchange Refrigerators

A number of different types of cryocooler based on regenerative heat exchangers have been developed since initial work in the 1950s resulted in the creation of the Stirling refrigerator. Presently, the two main types of cooler available are the Gifford-McMahon (GM) and the pulse tube cooler, or PTC.

#### Stirling Coolers

The Stirling cooler was first developed in 1954 [180] as an air liquefier based on the Stirling engine principle. An improved two-stage system, capable of reaching lower temperatures, was later developed. The Stirling cooler consists of an enclosed volume with two pistons mounted either side of a regenerative heat exchanger. The piston at the ambient temperature side compresses the gas isothermally (the heat of compression is rejected to ambient, usually by water cooling). The gas is transferred isochorically through the regenerator by moving both pistons, cooling from ambient to the expansion temperature and transferring heat to the regenerator matrix. The second piston (known as the displacer) then moves to expand the gas (theoretically at constant temperature), the work of expansion being used for cooling. Finally, the gas is again moved isochorically through the regenerator, warming to the ambient temperature and removing the heat previously transferred to the regenerator matrix during the first isochoric stage of the cycle.

Stirling cryocoolers have distinct advantages in that the coolers are compact and have good efficiency. Stirling coolers have found application in cooling of infrared sensors for military application (although not for missile guidance, since Stirling coolers cannot provide the fast cooldown times of JT systems), and for space operation [178].

#### Gifford-McMahon Coolers

Gifford-McMahon cryocoolers are similar in design and operation to Stirling coolers, although in this type of refrigerator, the compression of the working gas can be isolated from the cold head and the flow controlled by valves [181]. This separation of the processes overcomes many of the vibrational problems associated with Stirling coolers. Early versions of the cooler used a single displacer piston in parallel with a regenerator,

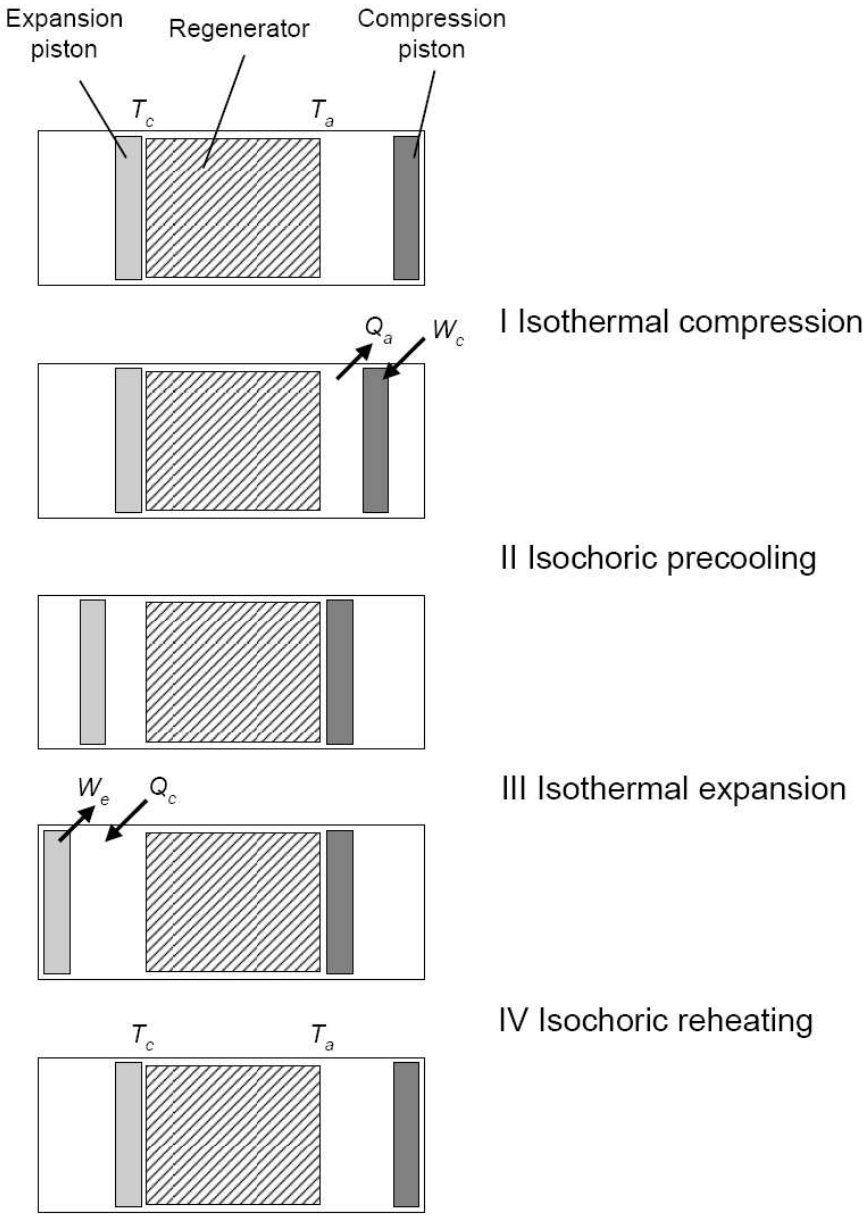


**Figure A.2:** Schematic operational cycle of a Stirling cooler. Stage I of the cycle is isothermal compression of the working gas at ambient temperature $T_a$ in the right-hand (compression) volume by moving the compression piston. The work of compression $W_c$ is transferred to the gas, and heat $q_a$ is rejected to ambient. In Stage II, the compressed gas is precooled through the regenerator isochorically by moving both pistons. Stage III is an isothermal expansion, with the work of expansion $W_e$ extracted from the gas and heat $q_c$ is removed from the environment. Finally, in stage IV the gas is reheated by moving both pistons to force the gas isochorically through the regenerator to the compression volume.

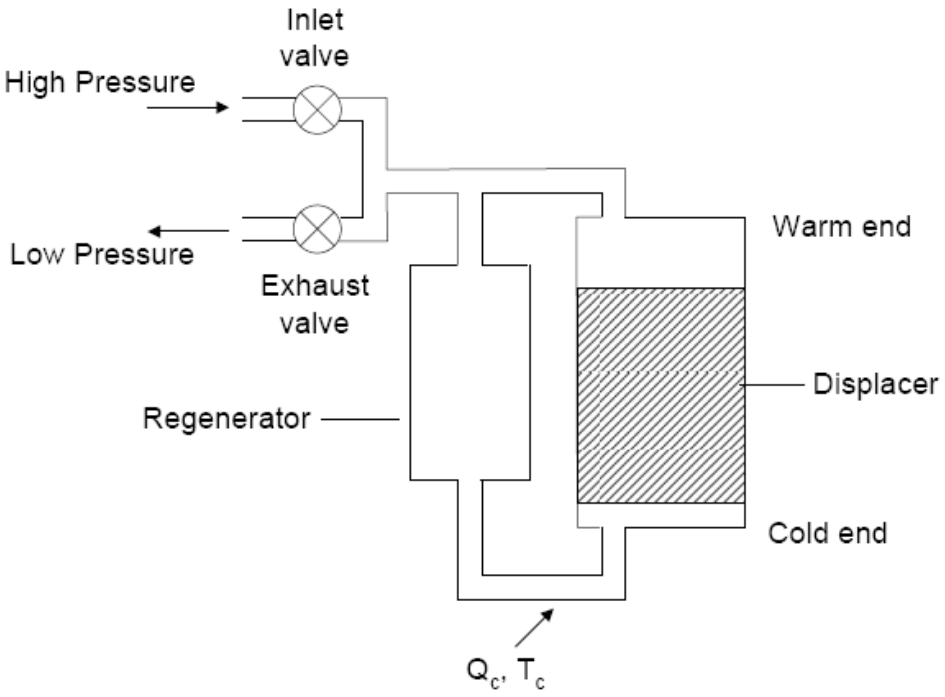


**Figure A.3:** Schematic of a single-stage Gifford-McMahon refrigerator with seperate regenerator and displacer. See text for details.

although the design was later improved to combine the displacer and regenerator as a single component. Fig. A.3 shows a schematic of a single-stage cooler with separated displacer and regenerator in order to illustrate the process. With the displacer at the cold end of the cylinder, high pressure gas enters through the inlet valve and fills the warm volume. With the intake valve open, the displacer moves upwards to enlarge the cold volume, drawing gas from the warm end through the regenerator matrix. The intake valve is then closed and the exhaust valve opened slowly, causing the gas to expand and produce cooling. Finally, the displacer moves downwards to drive the remaining cold gas through the regenerator.

Single- and two-stage GM coolers are readily available commercially. Modern single-stage GM coolers are capable of providing cooling powers of up to hundreds of watts in the 30–80 K temperature range, while two-stage coolers can reach temperatures down to 3 K with up to 1.5 W of cooling power at 4 K.

The performance of such cryocoolers is heavily dependant on the ability of the regenerator to hold heat during the cycle. Early GM and Stirling coolers were unable to cool below ∼10 K due to the unavailability of materials with a significant heat capacity in that temperature range, leading to large heat exchange inefficiencies. Investigation began in the early 1990s into the use of materials showing a specific heat anomaly leading to enhancement of the heat capacity in the temperature range of interest (e.g. Ref. [182]). A number of rare earth materials undergo magnetic ordering in the temperature range 4–15 K. Of these, $Er_3Ni$ was found to have a good compromise between thermodynamic behaviour and suitability for use as a regenerator material. Such materials are used to produce two-stage coolers, with an upper cylinder section containing a displacer-regenerator composed of ordinary metallic material attached to a displacer composed of the magnetic material in a second cylinder.

G-M coolers have been used for a large number of astronomical instrument applications, both at higher operating temperatures of >100 K at near-IR wavelengths, and for 4 K temperatures at mid-IR and radio wavelengths. Early two-stage coolers operating at 10–15 K on the second stage could be combined with a Joule-Thomson expansion stage using helium gas to reach temperatures around 4 K. Such an arrangement was used for the HARP spectrograph [183]. G-M coolers have generally not been used for bolometer instruments due to cold head vibration causing microphonic interference on the detectors.

### Pulse Tube Coolers

A basic version of the pulse tube cooler was described by Gifford and Longsworth in the early 1960s [184]. It had been observed that blanked pumping lines connected to gas compressors got hot at the closed end. Connecting such a line with a regenerator in series between the pipe and the compressor produced cooling at one end of the tube and heating at the other. Such a device achieved 150 K, with a two-stage version reaching 120 K. The coolers were highly inefficient and performed poorly, and further development was effectively abandoned. Interest was revived in the 1980s as the coolers showed potential for space applications. Such a refrigerator offered huge savings in mass and increased lifetime in comparison to stored cryogens, and the small number of moving

parts compared to other mechanical coolers enhanced lifetime. A key development came in 1983, when it was shown that the efficiency of coolers could be increased by inserting an orifice and reservoir volume at the hot end of the pulse tube, increasing the phase shift between the pressure and mass oscillation [185]. This implementation is known as the orifice pulse tube, and is now the standard design of pulse tube refrigerator.

A schematic for a single-stage orifice pulse tube cooler is shown in Fig. A.4. An acoustic pulse is produced in the gas at the warm end of the regenerator. In most commercial coolers, this pulse is generated by a compressor and rotary valve, as shown in the schematic, but could also be produced by a piston or thermoacoustic oscillator. In the case of the rotary valve system, the pulse is generated by the valve switching to the high pressure line from a remote compressor. The ambient temperature compressed gas is precooled in the regenerator, then flows through the orifice to the reservoir, exchanging heat to ambient at the warm end of the pulse tube. The rotary valve switches to the low pressure line, adiabatically expanding the gas in the pulse tube and producing cooling. The cooled, low-pressure gas in the pulse tube is forced to the cold end by the outflow from the reservoir. As the gas passes from the cold end of the tube to the cold end of the regenerator, it again picks up heat from the cold environment which is then deposited in the regenerator.

The arrangement shown in Fig. A.4 is generally referred to as a "U-tube" geometry, and is that used in the majority of commercial cold heads. Other possible arrangements are coaxial, in which the pulse tube is enclosed by the regenerator, and in-line, with the regenerator in series with the pulse tube and the cold station at the point of connection. The in-line arrangement has the highest efficiency, since there is no dead space between the cold end of the regenerator and pulse tube, although the practicality of the cold stage being in the middle of the layout is limited for most applications. The coaxial geometry has the smallest space envelope, but problems may arise with mismatched temperature profiles of the two components leading to a heat flow and reduced efficiency. This geometry is under development for use in applications where the small footprint is highly advantageous, such as for military sensors [178].

Many companies now commercially produce two-stage pulse tube refrigerators with cooling powers of up to 40 W at 45 K on the first stage and 1 W at 4.2 K on the

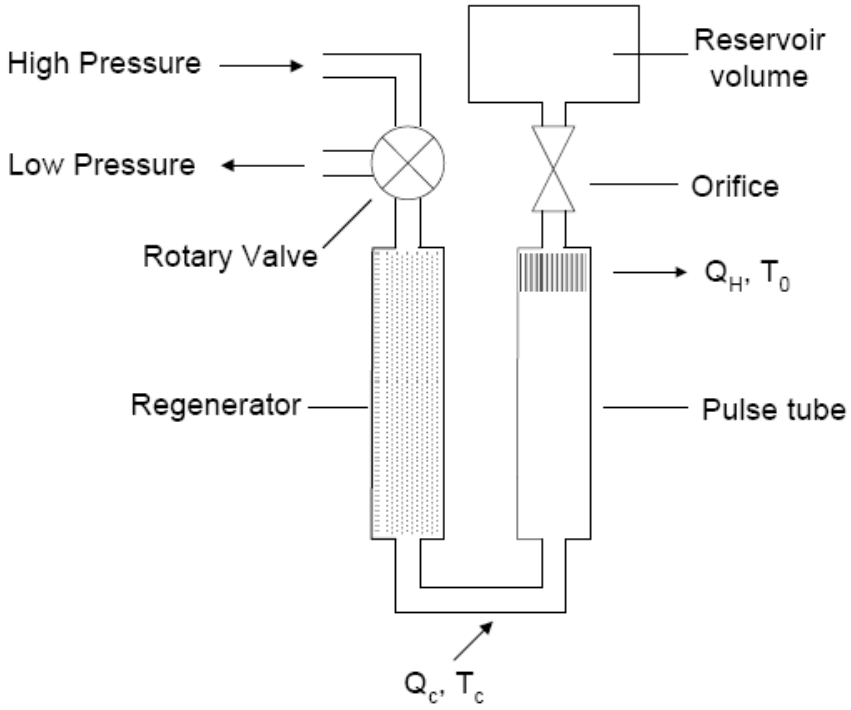


**Figure A.4:** Schematic of a single-stage pulse tube refrigerator. See text for details.

second stage, with unloaded base temperatures less than 3 K. Cryomech have recently produced a cooler model able to provide 1.5 W at 4.2 K.

Some work has been conducted on developing pulse tube coolers using $^3$He rather than $^4$He as the working gas. The refrigerator described in Ref. [186] is a two-stage system, but with two independent stages in parallel rather than two connected stages as in a normal two-stage cooler. With $^4$He in the first circuit and $^3$He in the second, the cooler achieved a minimum temperature of 1.27 K on the second stage, and a cooling power of 0.5 W at 4.2 K (greater than that achieved with $^4$He in both stages).

GM and pulse tube coolers are the most readily available types of regenerative refrigerator. PTC systems tend to be more expensive, but have the advantage of reduced vibration and longer service lifetimes than GM coolers since there are no moving displacers and cold seals. However, the performance of pulse tube coolers has a gravity dependance due to convective current effects in the gas column. The PTC cold heads must be mounted close to vertically in the cryostat to ensure no loss of cooling power, whereas GM coolers may be mounted in any orientation. GM coolers have generally

been preferred for astronomical instruments, since it is often necessary for cryostats to operate at changing orientations. However, as discussed above, the reduced vibration from pulse tube cold heads make this type attractive for bolometric instruments. PTCs are now finding use in a number of submillimetre and far-IR instruments.

## A.3 Cooling Below 4 K

Liquid helium has the lowest boiling point of any liquid (4.2 K at atmospheric pressure for $^4$He). To reach lower temperatures, other methods are required. A common approach is to use a pumped $^4$He cryostat, in which the vapour pressure above a volume of liquid $^4$He is reduced by pumping, and the liquid is then allowed to evaporate under reduced pressure. Such cryostats may be operated in a single-shot mode, in which a volume of liquid is pumped and boils until the liquid is depleted, or as a continuous flow system in which the liquid volume is replenished, often by allowing a small flow of helium from a non-pumped reservoir that also provides thermal buffering for the cold stage.

Reduction in the vapour pressure above the liquid can be achieved using a mechanical pump, or an adsorption pumps. Mechanical pumps allow cryostats to operate as continuous flow systems, in either an open- or closed-cycle, whereas sorp pump systems require periodic recycling. A common design is to use a self-contained cooler combining a sorption pump and an evaporator. Such a system requires a condensation point at 4.2 K or below to cycle the cooler. This may be provided by a liquid $^4$He bath, or by a closed-cycle mechanical cooler. Such systems are inexpensive, physically small since there are no room temperature pumps, and can provide long hold times (this is dependant on the volume of gas in the system and the load on the cold head, but generally of the order of tens of hours).

$^4$He undergoes a superfluid transition below 2.2 K. Additional heat leaks and pumping loads will occur due to heat transfer along and the evaporation of the superfluid film on the $^4$He volume. To suppress film flow, it is necessary to pump the helium bath through a narrow orifice, limiting the ultimate pressure achievable by a given pumping system. Well-designed coolers, with efficient pumping systems and minimised heat loads from superfluid film creep, can reach minimum temperatures of around 700 mK (e.g. [187]), although the nominal limit is taken to be around 1 K. Pumped $^4$He coolers

are commonly used as intermediate stages in a low-temperature system, such as the sub-kelvin coolers described in Sect. A.4.

## A.4 Sub-kelvin Cryogenic Systems

The sub-kelvin temperature region has been accessible since the early 1930s, initially through the adiabatic demagnetisation of paramagnetic salts. Competing techniques using $^3$He developed once the lighter helium isotope became readily available during the 1950s. Refrigeration using $^3$He has several advantages over paramagentic cooling, and so replaced this approach for many applications.

### A.4.1 Adiabatic Demagnetisation Refrigerators

The adiabatic demagnetisation refrigerator (ADR) was the first type of refrigerator capable of reaching temperatures significantly below 1 K. The technique was independently proposed by Debye in 1926 [188] and Giauque in 1927 [189], and first implemented by groups at the University of California [190], Leiden [191] and Oxford [192]. The outline approach to this cooling method is the ordering of dipoles in a pill of a paramagnetic salt by applying a magnetic field. This increases the entropy of the system, producing heat that is removed via a short to a cold stage (generally a 4 K or 1 K bath). The salt pill is then isolated from the cold stage and demagnetised adiabatically, decreasing the entropy of the dipoles and producing cooling.

The salt pill will warm over time due to the external heat leak. The amount of heat a salt pill can absorb will generally be several orders of magnitude smaller than the latent heat of evaporation of an equal volume of liquid helium, so great care must be taken to minimise the heat leak onto the salt pill. The major contribution to the heat leak will come from the salt pill supports, and the off conduction of the heat switch used to sink the pill to the cold bath during magnetisation. In some refrigerators, a second salt pill (the "guard pill") is used to buffer the heat leak onto the primary pill. This is able to increase the hold time of the pill, but has little effect on the base temperature. Such a system is described in Ref. [193]. An alternative approach is to use a two-stage ADR, essentially two ADRs in series, with the first salt pill and magnet pre-cooling the second salt pill to provide a lower starting temperature for the second stage. A

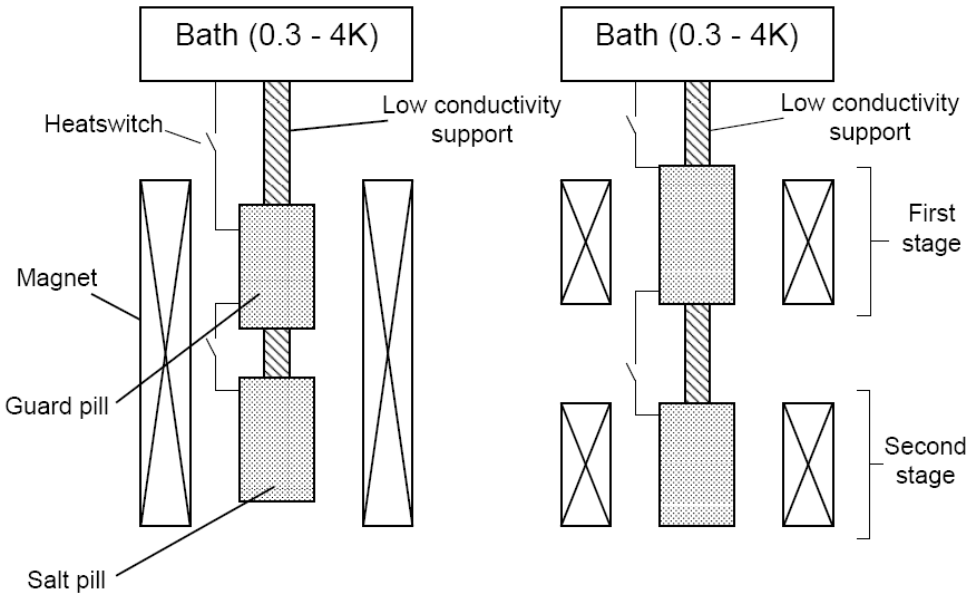


**Figure A.5:** Schematic of two ADR designs, as described in the text. Left: a single-stage ADR with a guard pill. Right: a two-stage ADR.

lower base temperature can be achieved, with the first stage then acting as a guard pill. The first practical demonstration of a refrigerator of this type is described in Ref. [194]. Schematics of these two designs are shown in Fig. A.5.

An early limitation on the base temperature of the ADRs was the power required to produce strong magnetic fields using normal coil magnets, and the maximum field that could be produced due to heat dissipation. However, with the introduction of superconducting magnets in the early 1960s, fields as strong as 20T may be generated with power consumption several orders of magnitude smaller than conventional solenoids. Control of the fields from the magnet in the experimental space must also be considered carefully for many applications. This issue may be dealt with through the use of cancelation coils and magnetic shielding to reduce the field in the experimental volume to an acceptable level. The major disadvantage of the method is that adiabatic demagnetisation is a one-shot process; although a number of "cyclic" refrigerators have been designed (such as that described in Ref. [195]), interest in the development of such coolers waned with the appearance of the dilution refrigerator, which is able to provide millikelvin temperatures continuously, although at the expense of being mechanically more complex.

The relative ease of operation of ADRs makes this technique attractive if continuous cooling is not required. ADRs are also a viable option for millikelvin cooling on balloon flights and sounding rocket experiments [37, 196], since dilution refrigerators generally require considerable gas handling at room temperature. The self-contained nature of ADRs is also an advantage for space missions, as is the gravity independence of the cooling. An ADR is planned for cooling the detector arrays for the SAFARI instrument on the future SPICA telescope to 50 mK [197]. In ground-based experiments, an ADR has been used to cool the bolometers and dispersive components of the submillimetre spectrometer instrument Z-Spec [198].

### A.4.2 Pumped $^3$He Cryostats

The most straightforward method of refrigeration using $^3$He is to pump on a volume of liquid to reduce the vapour pressure, in the same way as the pumped $^4$He systems described above. At atmospheric pressure, $^3$He boils at 3.19 K. The lower temperature limit that can be achieved by pumping is of the order of 0.3 K. The difference in performance between pumped $^3$He and $^4$He cryostats is the result of the different physical structure of the two isotopes. The lower mass of the $^3$He atom gives a larger zero point motion than $^4$He, and consequently the vapour pressure of $^3$He at all temperatures is greater than that of $^4$He, making the lighter isotope easier to pump. Furthermore, the behaviour of the two isotopes is described by different statistics ($^4$He is a boson, while $^3$He is a fermion). One consequence of this is that although both isotopes undergo a superfluid transition, this occurs below 2 mK for $^3$He. Since there are no issues associated with superfluid film creep, a $^3$He bath may be pumped via a wide tube rather than through an orifice as in $^4$He systems, giving higher effective pumping speeds.

The scarcity of $^3$He makes the light isotope around ten times as expensive per volume of gas as $^4$He. As such, $^3$He cryostats are invariably self-contained systems. There is a need to provide an intermediate temperature stage capable of condensing the $^3$He when the refrigerator is cycled. This stage is almost exclusively a pumped $^4$He bath, as described in the previous section. A common form of $^3$He refrigerator is a "dipstick" type placed in a $^4$He dewar, with a pumped volume fed from the 4 K bath (generally known as the "1-K pot") to condense the $^3$He. Such systems often use a charcoal sorption pump to

reduce the vapour pressure of the $^3$He rather than a mechanical pump, since the former design allows the assembly to be fully welded, as opposed to having O-ring connections as room temperature, reducing the possibility of leaks. The cryostat operates by first heating the sorp pump to drive out $^3$He, which condenses at the 1 K stage and flows into a bath. The sorb pump is then allowed to cool to 4 K, cold enough to absorb $^3$He gas and reduce the vapour pressure above the liquid. Once the liquid has been depleted, the cycle is repeated. Alternatively, the system may be operated as a continuous cycle cryostat with suitable return lines and a sealed pump at room temperature. Both types of system are described by Lounasmaa [122].

An alternative approach is to combine a self-contained, sorp-pumped $^4$He refrigerator with a $^3$He fridge in a single system. This allows operation directly from a 4 K plate cooled by either a liquid helium bath or a mechanical cooler, simplifying both design and operation. Such a refrigerator, coupled to a pulse tube cooler, was used for the TES detector array on the Greenbank radio telescope (and is described by Devlin et al. [187]). Commerically, such systems are available from Chase Cryogenics[1], and have been used in a number of other astronomical instruments (e.g. APEX-SZ [199] on the APEX telescope and BOLOCAM at the CSO [82]). Such systems are typically referred to as 'He-7 coolers', denoted a $^4$He and a $^3$He stage. Also available are He-10 coolers, with a second $^3$He stage to provide additional thermal buffering and allow a lower base temperature to be achieved. The limit for he-7 cooler is typically taken to be 300 mK, while a He-10 system may achieve 250 mK. With the move towards the use of dry cryogenic systems for instruments, these self-contained refrigerators will be a standard approach in future designs.

Since $^3$He cryostats are unable to reach millikelvin temperatures, they are not direct competitors for ADR systems, although $^3$He fridges have replaced ADRs at the higher temperature range of the sub-kelvin regime due to simplicity of operation. $^3$He cryostats are also useful in that a single system can be used from 0.3–3.2 K, more than a decade in temperature.

[1]Chase Research Cryogenics Ltd., (http://www.chasecryogenics.com).

### A.4.3 $^3$He-$^4$He Dilution Refrigerators

The concept of a millikelvin refrigerator based on the heat of mixing of $^3$He and $^4$He was first described by London, Clark and Mendoza in 1962 [124], based on an idea originally proposed by London in 1951. Such a refrigerator was first demonstrated in Leiden in 1965, achieving a temperature of 0.22 K. Improved designs followed, with Neganov, Borisov and Liburg achieving 25 mK a year later [200]. Modern refrigerators are able to achieve temperatures below 2 mK (e.g. Ref. [201]), close to the fundamental limit imposed by the $^3$He superfluid transition that prevents the dilution process occurring.

A detailed discussion of the operational and design principles of the dilution refrigerator (DR) is given in Chapter 4, but in brief the refrigeration effect makes use of the differing statistics describing the behaviour of $^4$He and $^3$He atoms, as discussed previously. At sufficiently low temperature a mixture of the two isotopes will separate into distinct phases, with the less dense, $^3$He-rich phase (essentially pure $^3$He) floating on the $^4$He-rich phase (superfluid $^4$He with $\sim$6.5% $^3$He). Cooling is achieved by $^3$He crossing the boundary between the two phases.

Although dilution refrigerators effectively replaced ADRs in low temperature research due to the ability to provide continuous, high cooling power refrigeration, there are disadvantages to such a refrigerator. An effective refrigerator requires very efficient heat exchangers, entailing the use of considerable lengths of delicate capillary tubing. Such tubing is difficult to handle, and can be prone to blockage during operation. Furthermore, dilution refrigerators require bulky room temperature pumping and gas handling systems, increasing complexity and expense.

### A.4.4 Normal-Insulating-Superconducting Coolers

A refrigeration technique that has seen considerable interest and development in recent years, although is still some way from a practical technology, is the use of normal-insulator-superconductor (NIS) tunnel junctions [174, 202]. In these devices, two superconducting contacts, one with an insulating layer, are made to a normal metal layer of $\sim$10–100 $\mu$m scale. A biasing voltage is applied to the normal metal to raise the Fermi energy of the metal to match the conduction band in the superconductor. Electrons with energies greater than the Fermi energy can tunnel through the insulating

layer to the superconductor, whilst electrons passing from the superconductor to the normal metal have on average the Fermi energy, so the electron temperature as a whole is lowered.

Such junctions can reach temperatures of the order of 200 mK from a 1 K or 300 mK bath temperature, but will individually provide only a few pW of cooling power. Multiple junctions may be fabricated in parallel to provide sufficient cooling power to bulk structures, such as detector arrays. Recent development of such system coupled to TES bolometers for instrumentation on the Greenbank Telescope has achieved cooling of individual TES devices [203], and more recently, arrays of devices [204]. Operating from a 300 mK bath temperature, the NIS coolers provide an additional cooling stage to bring the TES devices close to background limited performance, but without a complicated cryogenic system such as a dilution refrigerator. Although further development work is required, such as system shows excellent potential for both ground- and space-based cryogenic systems.

# Appendix B

# An Overview of Superconducting Quantum Interference Devices

The superconducting quantum interference device, or SQUID, is a superconducting circuit that has found extensive use in recent years for highly sensitive measurements of magnetic flux, and high resolution measurement of dc voltage and current. Many applications of the devices have been demonstrated. In SQUID-based multiplexer schemes for TES detectors, such as that used for SCUBA-2, SQUIDs are used for both current and voltage measurement, and cryogenic amplification.

This appendix is intended to provide an overview of the behaviour of the devices and the physics underlaying that behaviour. The description presented here is not rigorous. More complete discussions may be found elsewhere (e.g., Refs. [205, 206]). The basic quantum mechanics associated with the superconducting state will be described, the Josephson effect, centrally important to the operation of SQUIDs, will be introduced. The behaviour of the dc SQUID, the device used in the multiplexer scheme for SCUBA-2 and similar instruments, will then be described.

## B.1 Quantum Mechanics of the Superconducting State

All systems of particles will naturally seek to occupy a state of lowest energy, the ground state, unless excited by an external energy source. The phenomenon of superconductivity occurs since, in certain materials, it is possible for electrons to achieve a state of lower energy than the single particle ground state by forming "Cooper pairs", all of which have the same net momentum. In this ground state, all of the electrons are described by the same quantum mechanical wavefunction.

In the normal state, the wavefunctions of the electrons in a material are unrelated. For a material in the superconducting state, however, a single wavefunction describes the entire population of electron pairs, with the wavefunction in different parts of the superconductor related by a phase change. This long-range coherence of the wavefunction is central to a number of superconducting properties, including the concept of quantisation of flux.

Closed superconducting circuits may only contain discrete units of flux, known as "fluxons". The fundamental flux quantum, $\Phi_0$, is described by

$$\Phi_0 = \frac{h}{2e}, \tag{B.1}$$

where $h$ is Planck's constant and $e$ the charge on an electron. The factor 2 is introduced since in the superconducting state, the electrons are paired. A simple way to discuss flux quantisation is to consider the properties of a superconducting ring, the simplest example of a closed superconducting circuit.

Consider a superconducting ring cooled through the critical temperature, $T_c$, in a magnetic field such that one quantum of flux threads the ring. If the external field is removed, then according to Faraday's Law of Induction, the change in the field lines threading the ring will induce a current that opposes the field change. In a normal metal, this current would decay away rapidly, but in a superconductor this cannot happen. If the induced current were to decay, then the flux threading the ring would also decay, which is forbidden since the circuit may contain only discrete values of flux. The next permitted value would be zero, equivalent to the current ceasing abruptly. Since, as discussed above, the superconducting state is composed of a large number of electron pairs occupying the same quantum state, for the current to abruptly cease all of the

particles would be required to change state simultaneously, an event with such a small probability that in practical terms will never occur. Since the current flowing in the superconductor will continue indefinitely without decay, the electrical resistance of the material is zero. Hence, the phenomenon of flux quantisation is at the root of the zero resistance property of superconductors.

Flux quantisation itself is a consequence of the long-range coherence of the superconducting wavefunction. As discussed previously, the wavefunctions at any two points in a superconductor are related by a phase change. In a superconducting ring, the wavefunction at any given point must be the same as the wavefunction obtained by moving around the ring and returning to the same point - one circuit of the ring is equivalent to a $2\pi$ phase change.

Application of a magnetic field to a superconductor will induce a change in the phase of the wavefunction (a consequence of the quantum mechanical relationship between phase and canonical momentum). A given field creates a specific change in the wavefunction. Since the wavefunction going completely around the ring must be an integer multiple of $2\pi$, the amount of flux contained within the ring may only assume discrete values. This property is the origin of flux quantisation.

## B.2 The Josephson Effect and Josephson Junctions

A further consequence of the long-range coherence of the wavefunction in superconductors is the Josephson effect. The relationship between the phases in a single region of superconductor has already been discussed. Further to this, in two regions of superconductor separated by a thin insulating layer or narrow gap, the phases of the wavefunctions will also be related. The two regions effectively behave as a single superconductor. Electrical currents can flow between the two regions with zero resistance. These are referred to as Josephson currents; physical systems composed of two superconducting regions that exhibit this property are Josephson junctions. The resistanceless currents that flow in Josephson junctions are a manifestation of the dc Josephson effect. High-frequency oscillations of the current flowing in the junctions is called the ac Josephson effect.

Any weak coupling between two regions of superconductor — small constrictions, microscopic point contacts, or weakly-conducting layers — will exhibit the Josephson effect. All such structures can be referred to as Josephson junctions. The term "weak link" is also used, since the critical current of the Josephson junction (the maximum current that may flow without destroying the superconductivity) is lower than for the bulk superconductor. Such junctions are the basic active device in superconducting electronics, much as the transistor for semiconductor electronics. SQUIDs are some of the most useful superconductive circuits. A SQUID is a superconducting ring broken with either one or two Josephson junctions. A SQUID with a single junction is referred to as an rf SQUID, which will not be discussed here, while a two-junction circuit is referred to as a dc SQUID.

## B.3 The dc SQUID

The dc SQUID is a superconducting ring broken by two Josephson junctions, as discussed above. This is shown schematically in Fig. B.1(a). If a constant bias current, $I_{bias}$, is passed through the SQUID, then assuming the two junctions are identical, the current will split equally through the junctions ($I_1 = I_2 = 0.5I_{bias}$, where $I_1$ and $I_2$ are the currents in the junctions J1 and J2, respectively). A supercurrent will flow through the SQUID so long as the total current does not exceed the critical current, $I_c$, of the junctions (which is lower than the critical current of the bulk ring). For two identical junctions and zero magnetic field, both junctions will develop a voltage at the same time. The critical current of the SQUID is simply twice the critical current of one of the junctions.

If magnetic flux (of less than $0.5\Phi_0$) is applied to the SQUID, a screening current, $I_s$, is generated that creates a magnetic field equal and opposite to the applied field, canceling the flux threading the ring. This is shown schematically in Fig B.1(b). The currents flowing in the junctions are

$$I_1 = \frac{I_{bias}}{2} - I_s \tag{B.2}$$

$$I_2 = \frac{I_{bias}}{2} + I_s \tag{B.3}$$

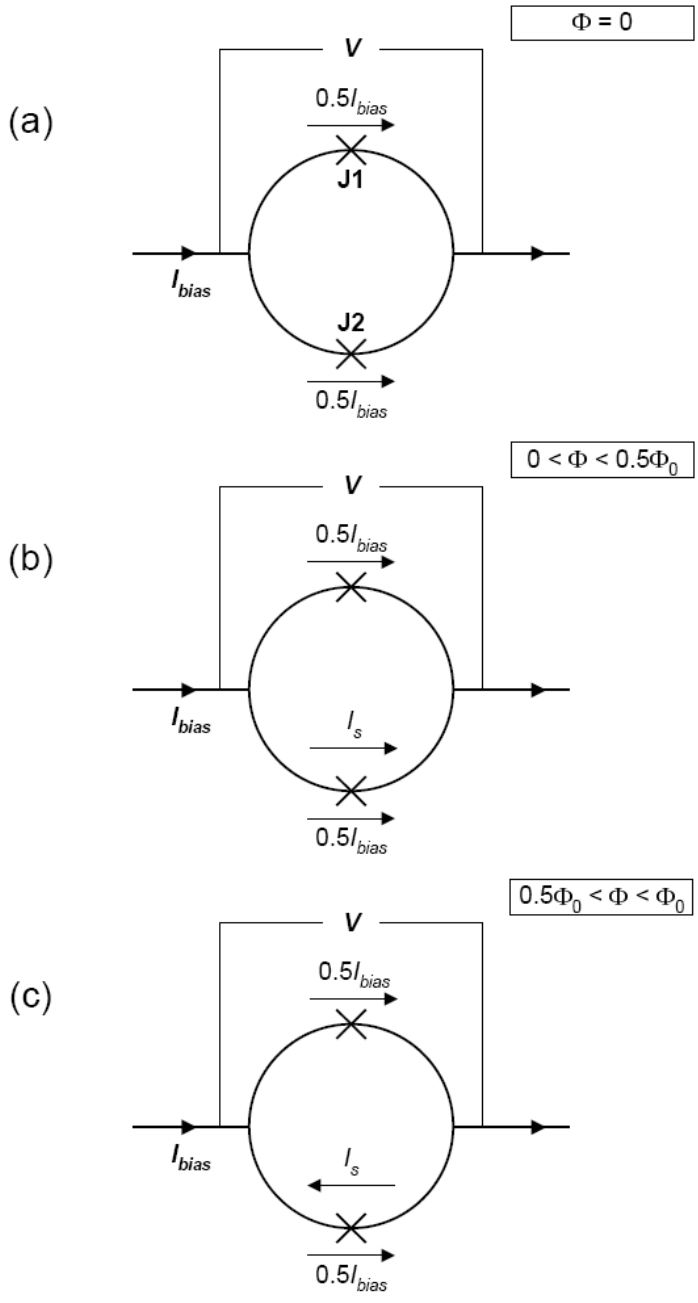


**Figure B.1:** Schematic representation of a SQUID with (a) zero applied flux, (b) applied flux of less than $0.5\Phi_0$, and (c) between $0.5\Phi_0$ and $\Phi_0$. Arrows indicate the direction of current flow. See text for full discussion.

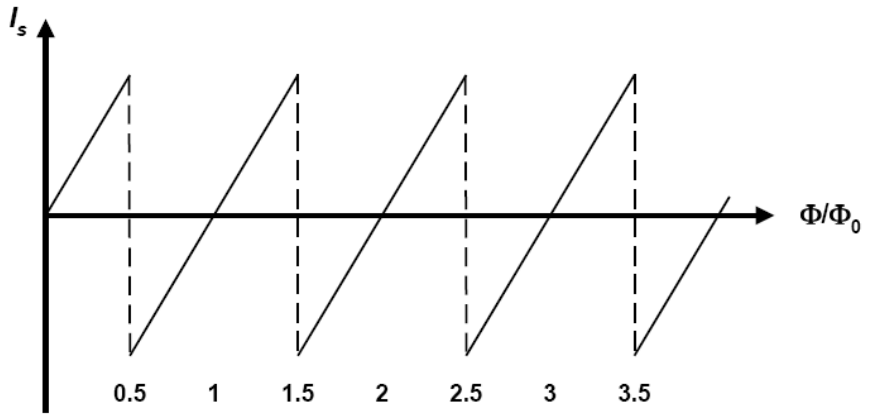


**Figure B.2:** The SQUID screening current, $I_s$, as a function of applied flux, $\Phi$.

The presence of the magnetic field has lowered the critical current of the SQUID, since the screening current is superimposed onto the fraction of the bias current passing through one junction (in this case, J2). If $I_{bias}$ were to be increased, $I_2$ will exceed $I_c$ at a lower bias current than if $I_s$ were zero. If J2 becomes resistive, then all of the bias current will pass through J1. This will exceed $I_c$ and cause J1 to develop a voltage as well. When both junctions are resistive, a voltage may be measured across the SQUID.

As the applied magnetic field is increased, the screening current also increases. When the applied flux reaches half a flux quantum ($0.5\Phi_0$), the junctions will momentarily go normal, destroying the continuity of the circuit and allowing one quantum of flux to thread the loop. This change is energetically favourable, since as the applied flux increases further, the screening current to maintain a net flux of $\Phi_0$ is less than that to maintain zero flux. The screening current must change direction to achieve this, as depicted in Fig. B.1(c). As the applied flux is increased to $\Phi_0$, $I_s$ will fall to zero again. The screening current is periodic in applied flux, with a period of one flux quantum, as illustrated in Fig. B.2.

Since the screening current is periodic in applied flux, the same must be true for the critical current. $I_c$ will be at a maxima when the applied flux is an integer multiple of $\Phi_0$, since the screening current will be zero. Similarly, $I_c$ will go through a minimum when the applied flux is a half integer multiple of $\Phi_0$, since this is when $I_s$ is largest.

This periodic relationship is depicted in Fig. B.3(a). The form of the critical current as a function of applied flux, $I_c(\Phi)$, is described by

$$I_c(\Phi) = I_c(0)\left[\cos\left(\frac{\pi\Phi}{\Phi_0}\right)\right]. \tag{B.4}$$

This periodicity of the critical current is analogous to the quantum interference of light diffracting through a double slit. This is the origin of the SQUID acronym.

To operate the SQUID as a practical magnetometer, the device is biased such that the bias current just exceeds the critical current and the SQUID is resistive. Since the critical current is periodic in applied flux, the voltage across the screen will also be periodic for a fixed bias current. The voltage will be a maximum when the critical current is a minimum, and vice versa. This is commonly known as a $V$-$\Phi$ curve, and is depicted in Fig. B.3(b).

The applied flux may therefore be measured by measuring the voltage across the SQUID. However, due to the periodicity of the $V$-$\Phi$ response, it is impossible to distinguish between zero applied field and a field that generates an integral number of flux quanta. This allows an essentially infinite dynamic range, but makes absolute measurements of the magnetic field problematic. It is often the case, however, that only *changes* in the field are of interest, and hence the field change may be obtained by "counting" the number of $V$-$\Phi$ cycles.

Although the SQUID acts as a flux-voltage converter, a common operating mode is "flux locking". In this scheme, an external coil (the "feedback" coil) is used to generate a magnetic field such that the total flux through the SQUID loop is constant. The SQUID is therefore operated as a nulling detector. This has a considerable advantage in that the SQUID voltage response is kept within a small range, typically a few $V$-$\Phi$ cycles. The current supplied to the coil is indicative of the applied flux being cancelled. Since the feedback current will likely have a limited range, the SQUID dynamic range may be increased by implementing a "flux jumping" scheme, such that if the SQUID moves to the upper limit of the feedback range, the operating point is relocked further down the $V$-$\Phi$ curve at the lower end of the feedback range. The SQUIDs for SCUBA-2 are operated in this manner.

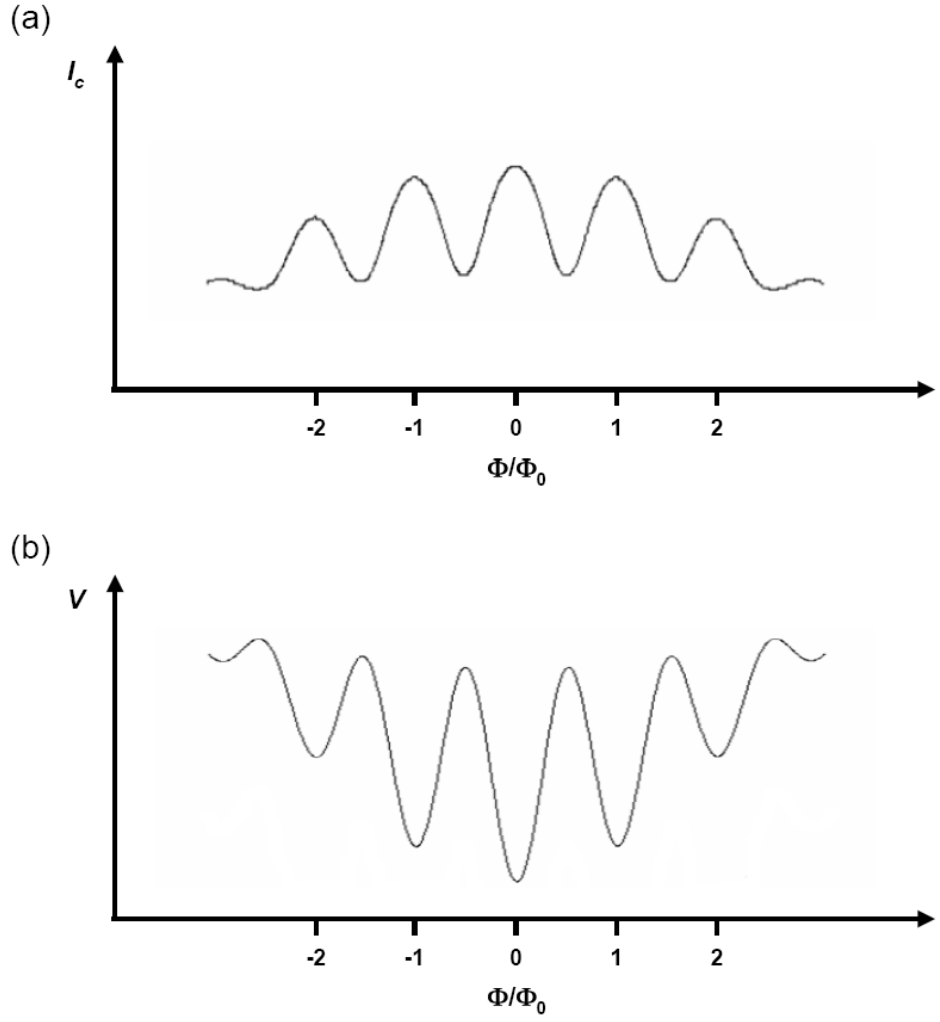


**Figure B.3:** Schematic representations of (a) the SQUID critical current, $I_c$, and (b) the voltage across the SQUID, as functions of applied flux, $\Phi$.

# Appendix C

# A Concept for a Dry Dilution Refrigerator with a 1 K Condenser

The work described herein concerns an alternative scheme for constructing dry dilution refrigerators, including an independent condenser at ∼1 K in place of the Joule-Thomson stage used in the current generation of systems. An outline of this proposal will appear in the journal *Cryogenics* as "Proposed designs for a "dry" dilution refrigerator with a 1 K condenser" [207].

## C.1 Introduction

The development of dry dilution refrigerators using mechanical coolers and Joule-Thomson expansion stages was discussed in Chapter 4. While early cryocoolers did not reach base temperatures of 4 K, this was not a problem for the dry dilution refrigerator designs, since the JT stage would cool the instreaming gas below the inversion temperature in the counterflow exchanger. As cryocoolers with greater cooling power and base temperatures below 4 K have become available, the practice of using a JT stage in the DR designs has continued.

There are disadvantages to the use of Joule-Thomson exchangers. Since the temperature at the output of the JT stage may be as high as 3 K, applications that require

a thermal sink at ∼1 K are required to utilise the cooling power of the still, since there is no pumped $^4$He stage. Use of JT stages already places greater demands on the still cooling capacity than in a conventional DR in order to fully liquify the $^3$He, and further loads due to the experiment may begin to degrade the performance of the mixing chamber. Furthermore, interaction between the JT and other temperature stages complicates the behaviour of the DR in comparison to refrigerators with separate condenser stages, where an unknown or varying heat load on the pumped $^4$He stage has little effect on the operation of the dilution circuit. DRs using JT stages and cryocoolers often operate with high condensing pressures during the early stages of circulation and condensation of the helium mixture, requiring the inclusion of a compressor in the circuit. Operation in this way is contrary to the usual practice of keeping the condensing pressure below 1 atmosphere to avoid leaks out of the DR.

The DR still was used in the SCUBA-2 design to cool radiation shielding and dissipate the power from the cryogenic amplifier arrays. However, as discussed in Chapter 6, the heat load on this stage was found to be considerably higher than that predicted from thermal modelling. While the origin of this additional load is not clear, it has not proved to be a serious issue since the heat load was close to the optimum operating load for the DR still. However, such a load could have been detrimental to the performance of the system.

Future instruments will potentially have higher demands for cooling capacity at 1 K. A useful arrangement for such systems would be to separate the role of the condenser and the still, allowing a 1 K heat sink with potentially high cooling power, analogous to the 1-K pot in conventional wet DRs, without interaction with the dilution circuit itself and enabling control of the circulation rate through electrical heating of the still alone.

To achieve this goal, but maintaining the dry design, two DR designs with a 1-K condenser are proposed. The first concept uses closed-cycle $^4$He adsorption pumped coolers, as is common to provide a condensation point in pumped $^3$He refrigerators, but with the goal in this case of providing a 1 K stage continuously. As an alternative to this, the second scheme uses a continuously-operating $^4$He refrigerator, with a room temperature pump circulating the gas and the returning $^4$He being liquified by the

cryocooler. These schemes are described in more detail § C.3 and § C.4. The next section estimates the cooling power required at the condenser stage in order to support dilution refrigerators with various circulation rates.

## C.2 Cooling Power of the Condenser

The cooling power required at the condenser stage may be estimated from the heat capacity and latent heat of vapourisation of $^3$He. Taking the temperature of the condenser, $T_{cond}$, to be 1 K (approximately the temperature at which the 1-K pot in a conventional DR would operate), then the latent heat of vaporisation[1] of $^3$He at the condenser temperature, $L_3(T_{cond})$, is 45 J/mol. Assuming also that the temperature of the previous stage in the system (provided by the second stage of a PTC) is 4 K, then the load on the condenser, $\dot{Q}_{cond}$, is given by the power required to cool $^3$He from 4 K to ∼1 K (a $\Delta T$ of 3 K ) and condense that helium at a flow rate of $\dot{n}_3$, as described by

$$\dot{Q}_{cond} = \dot{n}_3 L_3(T_{cond}) + \dot{n}_3 C_3 \Delta T. \tag{C.1}$$

In Eq. (C.1), $C_3$ is the heat capacity of $^3$He. Although the heat capacity is a function of temperature, since the temperature change is small a fixed value of $C_3$ at an intermediate temperature may be used. The heat capacity at 2 K, 5 J/molK, will be used. The condenser load for $^3$He circulation rates from 50–1000 $\mu$mol/s from Eq. (C.1) is plotted as the solid line in Fig. C.1. As an indication of the DR performance available for this range of $\dot{n}_3$ values, the maximum mixing chamber power, $\dot{Q}_{max}$ for three values of the mixing chamber temperature, $T_{mc}$, are also plotted in Fig. C.1. The maximum cooling power is calculated using Eq. (4.12).

## C.3 Sorption Cooled Condenser

A schematic of the proposed design is shown in Fig. C.2. The pulse tube cooler precools the incoming $^3$He gas to ≤4 K before the gas flows in to the condenser stage. The condenser is cooled to ∼1 K by a $^4$He sorption cooler. In order to provide continuous cooling to the condenser, a second sorption cooler is used, such that one cooler may be

[1] Unless otherwise stated, all helium data is taken from Ref. [121].

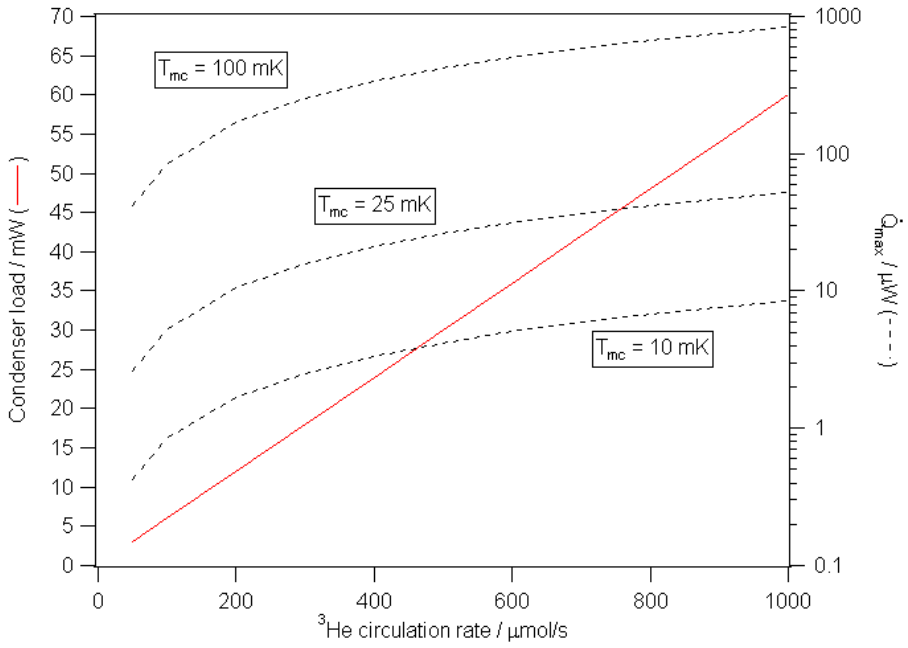


**Figure C.1:** Dilution refrigerator condenser load as a function of $^3$He circulation rate from Eq. (C.1) (solid line). Also plotted is the maximum mixing chamber cooling power, $\dot{Q}_{max}$, as a function of circulation rate for mixing chamber temperatures of $T_{mc}$ = 10, 25 and 100 mK (broken lines).

recycled while the other is operating. The operating cooler is shorted to the condenser via a heat switch (HS1b in Fig. C.2), while the recycling cooler is isolated by a similar switch in the off state (HS2b). Similarly, the charcoal pump of the operating cooler is connected to the second stage of the pulse tube cooler by a switch (HS1a), while the pump of the recycling cooler is isolated by opening the equivalent switch (HS2a). The recycling cooler uses the second stage of the pulse tube as a condensation point for the helium.

A conceptual cycle of the condenser stage could take the form of the following. Once one sorption cooler expends its liquid helium supply, the evaporator and the charcoal adsorption pump are isolated from the condenser and the 4 K plate respectively by opening the appropriate heat switches (for example, HS1b and HS1a), while the second cooler takes the load by closing the equivalent heat switches to maintain the condenser temperature. The exhausted cooler is then recycled by heating the charcoal pump to drive off the $^4$He, which condenses at the 4-K plate and collects in the evaporator. Once

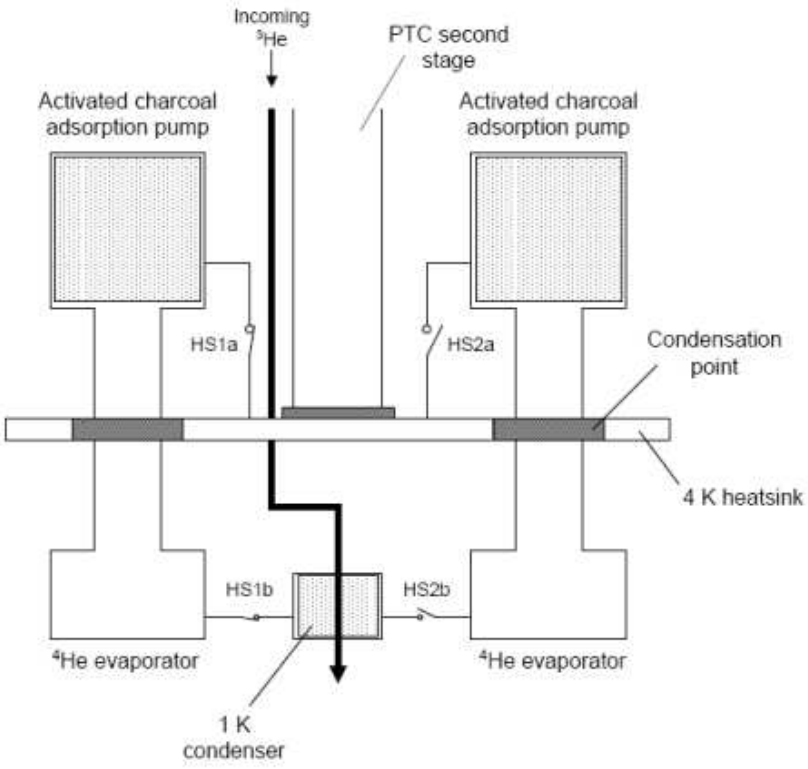


**Figure C.2:** Schematic for the proposed condenser stage with $^4$He sorption coolers. For details, see text.

the other sorption cooler is expended and isolated, the heat switch to the charcoal pump (HS1a) is closed, cooling the pump to 4 K and allowing helium to cryopump from the evaporator and cooling the evaporator to ∼1 K. Once the evaporator has cooled, the heat switch to the condenser (HS1b) is closed.

The best choice of heat switch for this system is a gap-gap design [208]. Switches of this type are typically composed of a thin-walled tube of stainless steel or another low conductivity material that may be pressurised with an exchange gas (hydrogen or helium being common choices) to turn the switch to the 'on' state. The switch volume is connected to a charcoal getter pump that is heated to close switch, or allowed to cryopump the exchange gas in order to open the switch. Such systems have a reasonable ratio of on and off conductances, but a disadvantage of this approach is that a small amount of power (typically ∼1–2 mW) must be supplied to keep the switch in the on state.

Alternative switch designs include mechanical or superconducting switches. Mechanical switches, in which the contact is made by pressing jaws together onto a tongue connected to the cold stage, have high on/off ratios (the off condition really is off, since there is no physical connection to the cold stage), but require large contact forces to achieve a good on conductance. The devices are also bulky, and require high-current wiring to drive the motor. Superconducting switches generally have low on conductances and high off conductances [121].

This approach has an advantage in that the condenser is a self-contained system, with no need for external fittings or pumps. However, given the potentially large load on the condenser (particularly for high circulation rates), construction of sorp coolers with a reasonable hold time might be problematic. Furthermore, the need for the heat switch system for recycling the coolers and connection to the condenser complicates the design.

## C.4 Continuous Flow Condenser

An alternative condenser stage could be provided by a continuously-operating $^4$He refrigerator, fed by a closed-circuit liquefaction system. A schematic of such a system is depicted in Fig. C.3. In addition to precooling the circulating $^3$He, the PTC second stage provides a condensation point for $^4$He in an independent circuit.

The required $^4$He circulation rate, $\dot{n}_4$, to support a given $^3$He circulation rate for the dilution circuit may be estimated using the relationship

$$\dot{Q}_c \approx 0.5 \dot{n}_4 L_4, \tag{C.2}$$

where $\dot{Q}_c$ is the cooling power available at the condenser and $L_4$ is the latent heat of evaporation of $^4$He [121]. In this case, the minimum value of $\dot{n}_4$ is found when the condenser cooling power balances the condenser load due to the circulation of $^3$He, as given by Eq. (C.1) and depicted in Fig. C.1, and the additional background load on the condenser from the experiment, $\dot{Q}_{bkg}$. $\dot{n}_4$ is shown as a function of $\dot{n}_3$ for two values of $\dot{Q}_{bkg}$ in Fig C.4, assuming operation at $T_{cond} = 1$ K. At this temperature, $L_4 = 84$ J/mol.

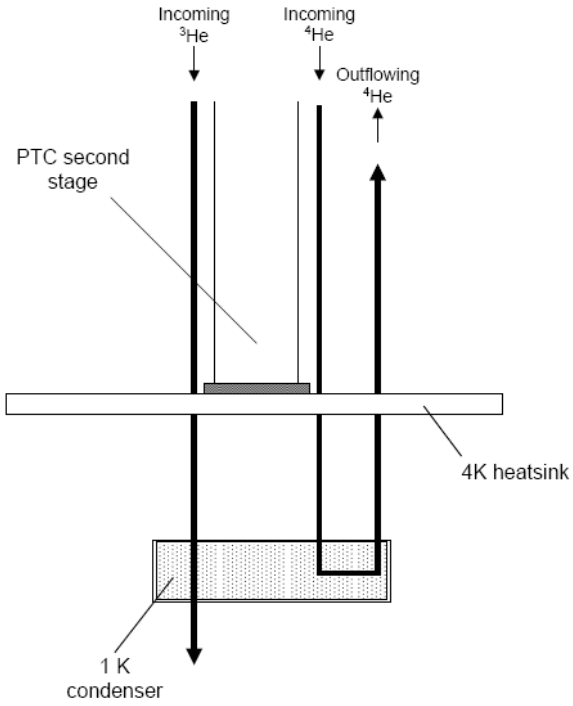


**Figure C.3:** Schematic for the proposed condenser stage cooled by a continuous-flow pumped $^4$He system. For details, see text.

Such $^4$He circulation rates are supportable with a simple mechanical pump at room temperature. An important consideration, however, is the effect of the circulating gases (both $^3$He and $^4$He) on the pulse tube cooler, particularly on the second stage where the temperature must be maintained close to 4 K to allow the $^4$He returning to the condenser to liquify. The loads on the two PTC stages may be estimated from enthalpy considerations for the cooling process.

The load on the first stage of the PTC, $\dot{Q}_1$, is due to cooling of the gas in the $^3$He and $^4$He circuits from 300 K to some lower temperature, plus a conduction and radiation load from 300 K due to the presence of structural components and an outer vacuum can. The load due to the circulating helium, for which the notation $\dot{q}_1$ will be used, is calculated by the difference in enthalpy, $H$, at the two temperatures multiplied by the mass flow of the helium. Hence,

$$\dot{q}_1 = \dot{n}_4(H_4(300\text{ K}) - H_4(T_1)) + \dot{n}_3(H_3(300\text{ K}) - H_3(T_1)) \tag{C.3}$$

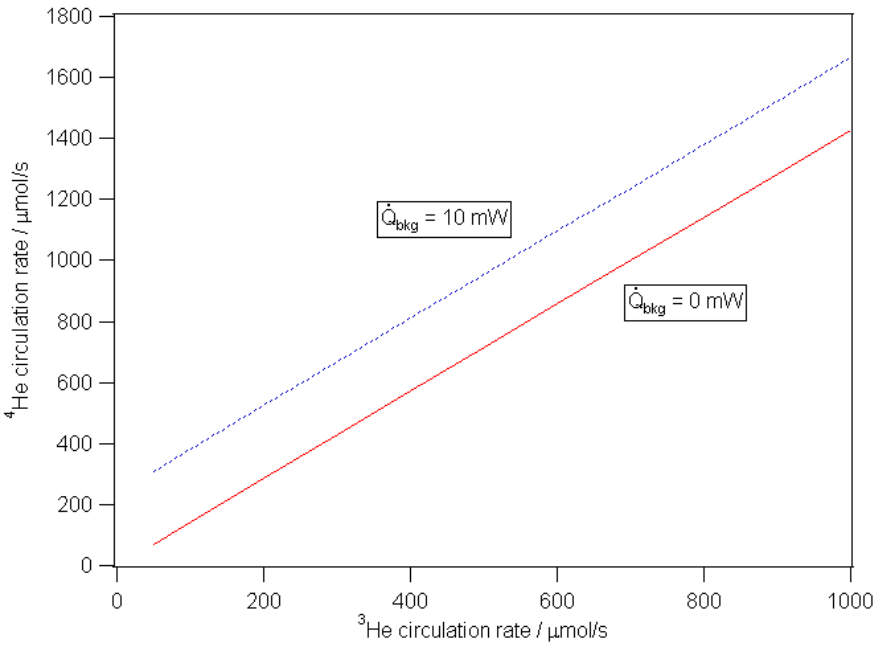


**Figure C.4:** Minimum required $^4$He circulation rate as a function of $^3$He circulation in the dilution circuit for condenser background loads, $\dot{Q}_{bkg}$, of 0 mW (solid line) and 10 mW (broken line).

where $\dot{n}_i$ and $H_i(T)$ are the molar flow rate and enthalpy at temperature $T$ of either $^3$He ($i = 3$) or $^4$He ($i = 4$), and $T_1$ is the temperature of the first stage. For the purpose of this calculation, $T_1$ will be taken as 36 K, which will be justified below. The enthalpy of $^4$He is taken from Ref. [209], while the enthalpy of $^3$He is estimated assuming an ideal gas [121]

$$H(T) = \frac{5}{2}RT, \tag{C.4}$$

where $R$ is the gas constant. The estimated load on the PTC first stage due to cooling the circulating $^3$He and $^4$He from ambient to 36 K is depicted in Fig. C.5, as before for two values of the background condenser load, $\dot{Q}_{bkg}$.

The temperature of the PTC may be estimated in the same way as for the thermal model analysis described in Chapter 6. From a polynomial fit to the published performance of a Cryomech PT410 pulse tube, the first stage temperature, $T_1$, for a given first stage load, $\dot{Q}_1$, is described by

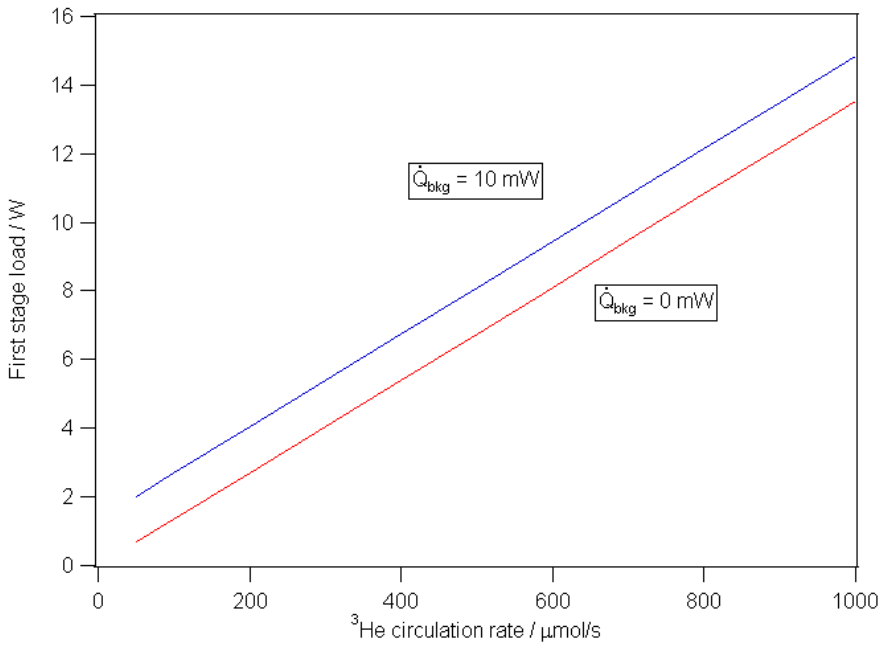


**Figure C.5:** Estimated load on the pulse tube first stage due to circulation of helium, assuming the first stage temperature $T_1 = 36$ K. Models are given for condenser background loads, $\dot{Q}_{bkg}$, of 0 and 10 mW. These data assume no conduction load on the first stage.

$$T_1 = 0.0033\dot{Q}_1^2 + 0.1665\dot{Q}_1 + 30.598. \tag{C.5}$$

Assuming now an additional load of 10 W due to conduction and radiation from ambient temperature added to the load $\dot{q}_1$ due to the circulation of helium, the predicted temperature of the first stage as a function of $^3$He circulation in the dilution circuit is depicted in Fig. C.6.

The predicted first stage temperatures depicted in Fig. C.6 lay in the range 33–36 K, a range that is insensitive to the value of $H_i(T_1)$ due to the relatively high cooling power available on the first stage. The value of 36 K chosen for $T_1$ in the initial calculations of the first stage load was selected since it lay at the upper limit of the predicted temperature range. The results do not differ greatly if a different value of $T_1$ is selected.

The first stage temperature is important for the estimation of the load on the second stage of the PTC, $q_2$, since this load will depend on the value of $H_i(T_1)$. In addition to cooling the flow of $^3$He and $^4$He from $T_1$ to ∼4 K, the second stage must also condense

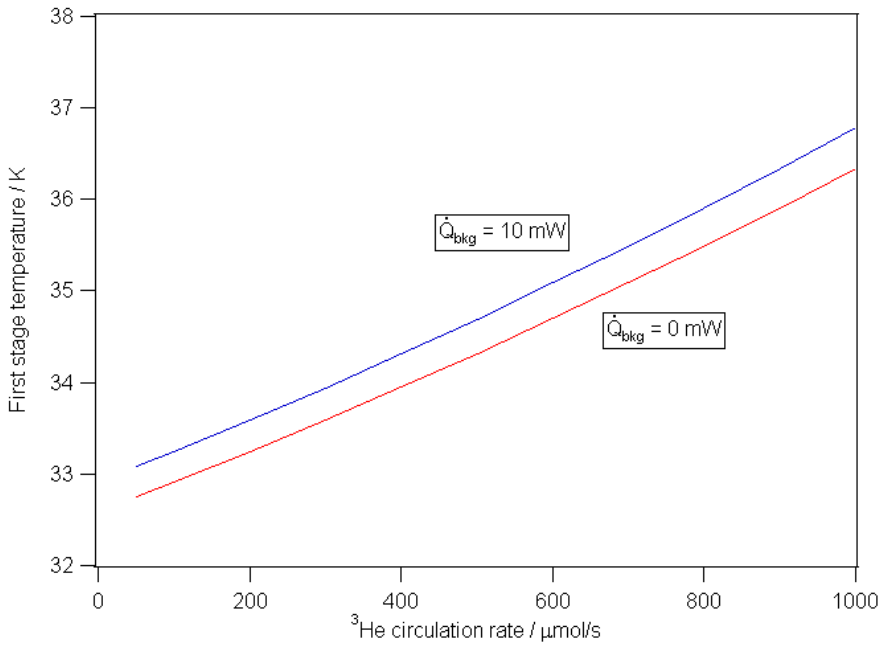


**Figure C.6:** Estimated temperature of the pulse tube first stage, $T_1$, due to load from the circulation of helium estimated from Eq. (C.3) and depicted in Fig. C.5, and assuming an additional load due to conduction from 300 K of 10 W. Models are given for $\dot{Q}_{bkg} = 0$ 10 mW as before.

the $^4$He. Assuming that the temperature of the PTC second stage is 4 K, then the $\dot{q}_2$ is given by

$$\dot{q}_2 = \dot{n}_4(H_4(T_1) - H_4(4\text{ K})) + \dot{n}_4 L_4(4\text{ K}) + \dot{n}_3(H_3(T_1) - H_3(4\text{ K})) \qquad \text{(C.6)}$$

where $L_4(4\text{ K})$, the latent heat of evaporation of $^4$He at 4 K, is 89 J/mol. The load on the second stage calculated from Eq. (C.6) is shown in Fig C.7, as previously for condenser background loads of 0 and 10 mW.

The horizontal line plotted in Fig. C.7 indicates a second stage loading of 1 W, equivalent to a temperature of 4 K for a PT410 pulse tube. This defines the limiting circulation rate for the system, since if the PTC runs warmer than 4 K, condensing the $^4$He returning to the condenser will become more problematic. Note that the data in Fig. C.7 does not include any contributed load from conduction to the 4 K stage, and hence represents an upper limit. Allowing for some conduction loading, the maximum

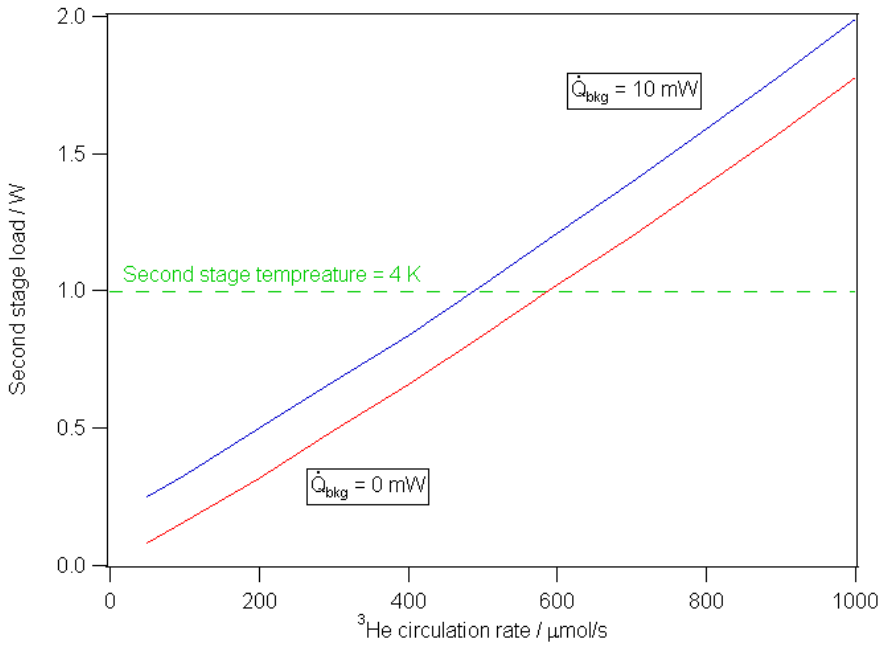


**Figure C.7:** Estimated load on the PTC second stage due to the circulation of $^3$He and the return $^4$He flow to the condenser stage. Condenser background loads, $\dot{Q}_{bkg}$, of 0 and 10 mW are depicted. These data do not include any contribution from structural conduction loads. The horizontal line indicates a second stage load of 1 W, equivalent to a temperature of 4 K for a Cryomech PT410 pulse tube.

circulation rate that could be supported using this arrangement is 400–600 $\mu$mol/s.

This limit may be overcome via the incorporation of a heat exchanger that utilises the temperature gradient along the regenerator of the PTC. Possible designs of such a heat exchanger have been described by Uhlig [171] and Prouvé *et al.* [173], and were discussed in Chapter 9. This would reduce the load on the second stage of the PTC, since the temperature at the output of the heat exchanger, $T_R$, will be lower than the first stage temperature. Including this in the model for the second stage of the pulse tube, then the loading on the PTC is considerably reduced, even allowing for modest performance compared to that reported in the literature. Fig. C.8 compares the second stage load for a system without the additional heat exchanger intermediate to the first and second stage, and for the inclusion of this heat exchanger with output temperatures of 10 and 5 K. These load lines indicate that by using the intermediate heat exchanger, high flow rates can be maintained without overloading the pulse tube second stage.

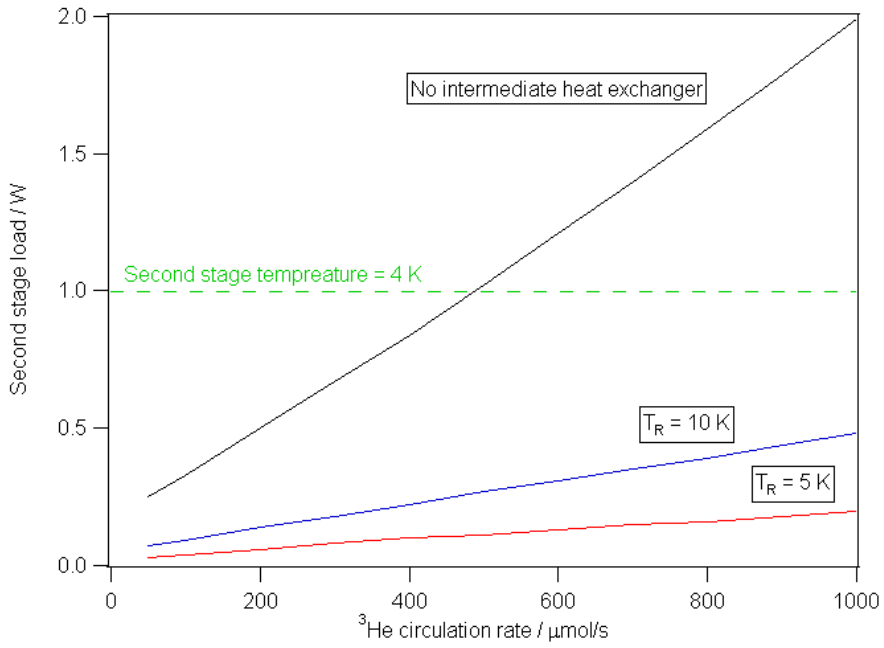


**Figure C.8:** Estimated heat load on the PTC second stage with an intermediate heat exchanger included in the model. The predicted loads are plotted for heat exchanger output temperatures of 5 and 10 K. The original model without additional cooling is also shown for comparison. This data assumes a condenser background load of $\dot{Q}_{bkg} = 10$ mW. These data do not include any contribution from structural conduction loads. The horizontal line indicates a second stage load of 1 W.

## C.5 Further Discussion

There are advantages and disadvantages to the two condenser schemes described. The sorption cooled condenser is a fully self-contained system within the cryostat, with no need for external gas handling equipment, unlike the continuous flow design. However, the system of heat switches required for the sorp coolers to handle the connection and isolation during operation is complicated. Two further issues to consider are the cooling capacity and hold time of the sorption coolers, particularly if the system were intended to support the higher flow rates for the dilution circuit. It may not be practical to build a cooler with sufficient cooling capacity and a reasonably long hold time for this scheme (around 8 to 12 hours would likely be necessary). Furthermore, the effects on the PTC and the condenser as the coolers are cycled may require extensive temperature control of the stages. Although the continuous flow condenser would require an additional

pump, the scheme potentially offers considerably higher cooling capacity and a more straightforward condenser design.

An alternative continuous flow condenser scheme, although one which has not been considered in any detail, employs a closed cycle Joule-Thomson circuit to cool the $^3$He condenser. Using $^4$He, such a circuit is capable of reaching temperatures <1.5 K. Although still requiring a room temperature pumping system as for the pumped condenser described above, this scheme is simplified in that there is no pot of liquid $^4$He. Such coolers are available commercially,[2] and are capable of providing the necessary cooling power for this application. The system referenced operates the JT circuit with an open cycle, but it would be a trivial matter to construct a system for closed cycle operation.

The work described here would require more detailed development, but demonstrates that a hybrid dilution refrigerator with a cryocooler and a 1 K condenser is feasible. Such an approach is unlikely to supersede the current designs of DRs incorporating JT expansion stages, since such system work well for many applications. However, for specific applications such as the large cryostats that are in use and will be designed for instruments and experiments in the field of astroparticle physics that may require considerable cooling power at 1 K, the schemes outlined here offer a number of advantages. Such a system could potentially allow a conventional DR cryostat to be converted to a dry system by retrofitting a cryocooler and modification of the condenser stage.

[2]Advanced Research Systems, Inc., http://www.arscryo.com.

# References


[1] P. A. R. Ade, J. E. Beckman, and C. D. Clark, "Solar chromosphere-Submillimetre maps of active regions," Nature, vol. 231, p. 55, May 1971.

[2] J. D. G. Rather, B. L. Ulich, and P. A. R. Ade, "Planetary brightness temperature measurements at 1.4-mm wavelength," *Icarus*, vol. 22, pp. 448–453, Aug. 1974.

[3] M. Rowan-Robinson, P. E. Clegg, and P. A. R. Ade, "Millimetre emission from extragalactic objects. I - Observational techniques and data analysis," MNRAS, vol. 172, pp. 603–615, Sept. 1975.

[4] P. A. R. Ade, M. Rowan-Robinson, and P. E. Clegg, "Millimetre emission from extragalactic objects. II - Luminosities, spectra and contribution to the microwave background," A&A, vol. 53, pp. 403–409, Dec. 1976.

[5] D. P. Rice and P. A. R. Ade, "Absolute measurements of the atmospheric transparency at short millimetre wavelengths.," *Infrared Physics*, vol. 19, pp. 575–584, 1979.

[6] W. D. Duncan, E. I. Robson, P. A. R. Ade, G. Sandell, and M. J. Griffin, "A millimetre/submillimetre common user photometer for the James Clerk Maxwell Telescope," MNRAS, vol. 243, pp. 126–132, Mar. 1990.

[7] G. Rieke, *Detection of Light*. Cambridge University Press, second ed., 2003.

[8] D. Johnstone and J. Bally, "JCMT/SCUBA Submillimeter Wavelength Imaging of the Integral-shaped Filament in Orion," ApJ, vol. 510, pp. L49–L53, Jan. 1999.

[9] D. Ward-Thompson, F. Motte, and P. Andre, "The initial conditions of isolated star formation - III. Millimetre continuum mapping of pre-stellar cores," MNRAS, vol. 305, pp. 143–150, May 1999.

[10] F. P. Israel, P. P. van der Werf, and R. P. J. Tilanus, "Submillimetre maps of the edge-on galaxy NGC 891," A&A, vol. 344, pp. L83–L86, Apr. 1999.

[11] W. S. Holland, J. S. Greaves, B. Zuckerman, R. A. Webb, C. McCarthy, I. M. Coulson, D. M. Walther, W. R. F. Dent, W. K. Gear, and I. Robson, "Submillimetre images of dusty debris around nearby stars," *Nature*, vol. 392, pp. 788–791, Apr. 1998.

[12] J. S. Greaves, W. S. Holland, G. Moriarty-Schieven, T. Jenness, W. R. F. Dent, B. Zuckerman, C. McCarthy, R. A. Webb, H. M. Butner, W. K. Gear, and H. J. Walker, "A Dust Ring around epsilon Eridani: Analog to the Young Solar System," ApJ, vol. 506, pp. L133–L137, Oct. 1998.

[13] D. H. Hughes, S. Serjeant, J. Dunlop, M. Rowan-Robinson, A. Blain, R. G. Mann, R. Ivison, J. Peacock, A. Efstathiou, W. Gear, S. Oliver, A. Lawrence, M. Longair, P. Goldschmidt, and T. Jenness, "High-redshift star formation in the Hubble Deep Field revealed by a submillimetre-wavelength survey," *Nature*, vol. 394, pp. 241–247, July 1998.

[14] G. J. White, R. P. Nelson, W. S. Holland, E. I. Robson, J. S. Greaves, M. J. McCaughrean, G. L. Pilbratt, D. S. Balser, T. Oka, S. Sakamoto, T. Hasegawa, W. H. McCutcheon, H. E. Matthews, C. V. M. Fridlund, N. F. H. Tothill, M. Huldtgren, and J. R. Deane, "The Eagle Nebula's fingers - pointers to the earliest stages of star formation?," A&A, vol. 342, pp. 233–256, Feb. 1999.

[15] P. Madau, H. C. Ferguson, M. E. Dickinson, M. Giavalisco, C. C. Steidel, and A. Fruchter, "High-redshift galaxies in the Hubble Deep Field: colour selection and star formation history to z∼4," MNRAS, vol. 283, pp. 1388–1404, Dec. 1996.

[16] A. W. Blain, I. Smail, R. J. Ivison, and J.-P. Kneib, "The history of star formation in dusty galaxies," MNRAS, vol. 302, pp. 632–648, Feb. 1999.

[17] P. de Bernardis, P. A. R. Ade, J. J. Bock, J. R. Bond, J. Borrill, A. Boscaleri, K. Coble, B. P. Crill, G. De Gasperis, P. C. Farese, P. G. Ferreira, K. Ganga, M. Giacometti, E. Hivon, V. V. Hristov, A. Iacoangeli, A. H. Jaffe, A. E. Lange, L. Martinis, S. Masi, P. V. Mason, P. D. Mauskopf, A. Melchiorri, L. Miglio, T. Montroy, C. B. Netterfield, E. Pascale, F. Piacentini, D. Pogosyan, S. Prunet, S. Rao, G. Romeo, J. E. Ruhl, F. Scaramuzzi, D. Sforna, and N. Vittorio, "A flat Universe from high-resolution maps of the cosmic microwave background radiation," *Nature*, vol. 404, pp. 955–959, Apr. 2000.

[18] G. S. Busswell and T. Shanks, "The contribution of faint blue galaxies to the submillimetre counts and background," MNRAS, vol. 323, pp. 67–74, May 2001.

[19] W. S. Holland, R. J. Ivison, J. S. Greaves, W. R. Dent, A. P. Russell, A. J. Longmore, T. G. Hawarden, J. A. Stevens, J. S. Dunlop, and T. Greve, "A large single-aperture telescope for submillimeter astronomy," in *Ground-based Telescopes* (J. M. Oschmann, Jr., ed.), vol. 5489 of *Proceedings of the SPIE*, pp. 47–61, 2004.

[20] P. L. Richards, T. M. Shen, R. E. Harris, and F. L. Lloyd, "Quasiparticle heterodyne mixing in SIS tunnel junctions," *Applied Physics Letters*, vol. 34, pp. 345–347, Mar. 1979.

[21] P. L. Richards and Q. Hu, "Superconducting components for infrared and millimeter-wave receivers," *IEEE Proceedings*, vol. 77, pp. 1233–1246, Aug. 1989.

[22] S. Cherednichenko and V. Drakinskiy, "Low Noise Hot-Electron Bolometer Mixers for Terahertz Frequencies," *Journal of Low Temperature Physics*, vol. 151, pp. 575–579, Apr. 2008.

[23] C. R. Kitchin, *Astrophysical Techniques*. Institute of Physics, third ed., 1998.

[24] J. D. Kraus, *Radio Astronomy*. Cygnus-Quasar, second ed., 1986.

[25] W. S. Holland, *Design and Development of Bolometric Detectior Systems*. PhD thesis, University of London, 1990.

[26] M. J. Griffin and W. S. Holland, "The influence of background power on the performance of an ideal bolometer," *International Journal of Infrared and Millimeter Waves*, vol. 9, pp. 861–875, Oct. 1988.

[27] P. L. Richards and L. T. Greenberg, "Infrared detectors for low-background astronomy: incoherent and coherent devices from one micrometer to one millimeter," in *Infrared and Millimeter Waves* (K. J. Button, ed.), vol. 6, pp. 149–207, Academic Press, 1982.

[28] P. L. Richards, "Bolometers for infrared and millimeter waves," *Journal of Applied Physics*, vol. 76, pp. 1–24, July 1994.

[29] S. H. Moseley, J. C. Mather, and D. McCammon, "Thermal detectors as x-ray spectrometers," *Journal of Applied Physics*, vol. 56, pp. 1257–1262, Sept. 1984.

[30] D. McCammon, S. H. Moseley, J. C. Mather, and R. F. Mushotzky, "Experimental tests of a single-photon calorimeter for x-ray spectroscopy," *Journal of Applied Physics*, vol. 56, pp. 1263–1266, Sept. 1984.

[31] P. D. Barnes, Jr., A. da Silva, D. S. Akerib, D. Bauer, P. Brink, B. Cabrera, D. O. Caldwell, B. Chugg, R. M. Clarke, A. Cummings, A. Davies, R. C. Diaz, B. L. Dougherty, J. Emes, S. R. Golwala, D. Hale, E. E. Haller, K. D. Irwin, W. B. Knowlton, V. Kuziminov, A. Lu, S. W. Nam, M. J. Penn, V. Novikov, B. V. Pritychenko, F. Queinnec, R. R. Ross, B. Sadoulet, D. Seitz, T. Shutt, A. Smith, G. Smith, A. Sonnenschein, W. Stockwell, J. D. Taylor, R. Therrien, T. L. Trumbull, S. White, R. C. Wolgast, S. Yellin, and B. A. Young, "Installation of the Cryogenic Dark Matter Search (CDMS).," *Nuclear Instruments and Methods in Physics Research A*, vol. 370, pp. 233–236, Feb. 1996.

[32] J. C. Mather, "Bolometer noise: nonequilibrium theory," *Applied Optics*, vol. 21, pp. 1125–1129, June 1982.

[33] W. Holland, W. Duncan, and M. Griffin, "Bolometers for Submillimeter and Millimeter Astronomy," in *Single-Dish Radio Astronomy: Techniques and Applications* (S. Stanimirovic, D. Altschuler, P. Goldsmith, and C. Salter, eds.), vol. 278 of *Astronomical Society of the Pacific Conference Series*, pp. 463–491, 2002.

[34] F. J. Low, "Low-Temperature Germanium Bolometer," *Journal of the Optical Society of America*, vol. 51, pp. 1300–1304, Nov. 1961.

[35] G. J. Melnick, J. R. Stauffer, M. L. N. Ashby, E. A. Bergin, G. Chin, N. R. Erickson, P. F. Goldsmith, M. Harwit, J. E. Howe, S. C. Kleiner, D. G. Koch, D. A. Neufeld, B. M. Patten, R. Plume, R. Schieder, R. L. Snell, V. Tolls, Z. Wang, G. Winnewisser, and Y. F. Zhang, "The Submillimeter Wave Astronomy Satellite: Science Objectives and Instrument Description," ApJ, vol. 539, pp. L77–L85, Aug. 2000.

[36] G. L. Pilbratt, "Herschel Space Observatory mission overview," in *IR Space Telescopes and Instruments* (J. C. Mather, ed.), vol. 4850 of *Proceedings of the SPIE*, pp. 586–597, 2003.

[37] D. J. Fixsen, E. S. Cheng, D. A. Cottingham, W. C. Folz, C. A. Inman, M. S. Kowitt, S. S. Meyer, L. A. Page, J. L. Puchalla, J. L. Ruhl, and R. F. Silverberg, "A Ballon-borne Millimeter-Wave Telescope for Cosmic Microwave Background Anisotropy Measurements," ApJ, vol. 470, pp. 63–100, Oct. 1996.

[38] P. de Bernardis, P. A. R. Ade, R. Artusa, J. J. Bock, A. Boscaleri, B. P. Crill, G. De Troia, P. C. Farese, M. Giacometti, V. V. Hristov, A. Iacoangeli, A. E. Lange, A. T. Lee, S. Masi, L. Martinis, P. V. Mason, P. D. Mauskopf, F. Melchiorri, L. Miglio, T. Montroy, C. B. Netterfield, E. Pascale, F. Piacentini, P. L. Richards, J. E. Ruhl, and F. Scaramuzzi, "Mapping the CMB sky: The BOOMERanG experiment," *New Astronomy Review*, vol. 43, pp. 289–296, July 1999.

[39] E. Pascale, P. A. R. Ade, J. J. Bock, E. L. Chapin, J. Chung, M. J. Devlin, S. Dicker, M. Griffin, J. O. Gundersen, M. Halpern, P. C. Hargrave, D. H. Hughes, J. Klein, C. J. MacTavish, G. Marsden, P. G. Martin, T. G. Martin, P. Mauskopf, C. B. Netterfield, L. Olmi, G. Patanchon, M. Rex, D. Scott, C. Semisch, N. Thomas, M. D. P. Truch, C. Tucker, G. S. Tucker, M. P. Viero, and D. V. Wiebe, "The Balloon-borne Large Aperture Submillimeter Telescope: BLAST," ApJ, vol. 681, pp. 400–414, July 2008.

[40] P. A. R. Ade, M. J. Griffin, C. T. Cunningham, J. V. Radostitz, S. Predko, and I. G. Nolt, "The Queen Mary College/University of Oregon photometer for submillimetre continuum observations," *Infrared Physics*, vol. 24, pp. 403–415, Apr. 1984.

[41] S. El-Ataway, J. V. Radostitz, I. G. Nolt, and P. A. R. Ade, "Evaluation of composite bolometers at 0.4 Kelvin," *International Journal of Infrared and Millimeter Waves*, vol. 1, pp. 459–468, Sept. 1980.

[42] V. Natale, "A He-3 cooled bolometer array for MM and submm continuum observations," *Memorie della Societa Astronomica Italiana*, vol. 61, pp. 247–250, Mar. 1990.

[43] W. S. Holland, E. I. Robson, W. K. Gear, C. R. Cunningham, J. F. Lightfoot, T. Jenness, R. J. Ivison, J. A. Stevens, P. A. R. Ade, M. J. Griffin, W. D. Duncan, J. A. Murphy, and D. A. Naylor, "SCUBA: a common-user submillimetre camera operating on the James Clerk Maxwell Telescope," MNRAS, vol. 303, pp. 659–672, Mar. 1999.

[44] N. Wang, T. R. Hunter, D. J. Benford, E. Serabyn, D. C. Lis, G. Phillips, S. H. Moseley, K. Boyce, A. Szymkowiak, and C. Allen, "Characterization of a submillimeter high-angular resolution camera with a monolithic silicon bolometer array for the Caltech Submillimeter Observatory," *Applied Optics*, vol. 35, pp. 6629–6640, Dec. 1996.

[45] C. D. Dowell, C. A. Allen, R. S. Babu, M. M. Freund, M. Gardner, J. Groseth, M. D. Jhabvala, A. Kovacs, D. C. Lis, S. H. Moseley, Jr., T. G. Phillips, R. F. Silverberg, G. M. Voellmer, and H. Yoshida, "SHARC II: a Caltech submillimeter observatory facility camera with 384 pixels," in *Millimeter and Submillimeter Detectors for Astronomy* (T. G. Phillips and J. Zmuidzinas, eds.), vol. 4855 of *Proceedings of the SPIE*, pp. 73–87, 2003.

[46] D. H. Andrews, R. M. Milton, and W. DeSorbo, "A Fast Superconducting Bolometer," *Journal of the Optical Society of America*, vol. 36, pp. 518–524, Sept. 1946.

[47] A. Goetz, "The Possible Use of Superconductivity for Radiometric Purposes," *Physical Review*, vol. 55, pp. 1270–1271, June 1939.

[48] N. Fuson, "The Infra-Red Sensitivity of Superconducting Bolometers," *Journal of the Optical Society of America*, vol. 38, pp. 845–853, Oct. 1948.

[49] W. S. Boyle and K. F. Rodgers, "Performance Characteristics of a New Low-Temperature Bolometer," *Journal of the Optical Society of America*, vol. 49, pp. 66–69, Jan. 1959.

[50] W. S. Holland, P. A. R. Ade, M. J. Griffin, I. D. Hepburn, D. G. Vickers, C. R. Cunningham, P. R. Hastings, W. K. Gear, W. D. Duncan, T. E. C. Baillie, E. E. Haller, and J. W. Beeman, "100 mK bolometers for the Submillimetre Common-User Bolometer Array (SCUBA) i. Design and construction," *International Journal of Infrared and Millimeter Waves*, vol. 17, pp. 669–692, Apr. 1996.

[51] E. E. Haller, "Advanced far-infrared detectors," *Infrared Physics and Technology*, vol. 35, pp. 127–146, Apr. 1994.

[52] R. V. Sudiwala, M. J. Griffin, and A. L. Woodcraft, "Thermal modelling and characterisation of semiconductor bolometers," *International Journal of Infrared and Millimeter Waves*, vol. 23, pp. 545–573, Apr. 2002.

[53] P. D. Mauskopf, J. J. Bock, H. Del Castillo, W. L. Holzapfel, and A. E. Lange, "Composite infrared bolometers with $Si_3N_4$ micromesh absorbers," *Applied Optics*, vol. 36, pp. 765–771, Feb. 1997.

[54] J. M. Lamarre, P. R. Ade, A. Benoît, P. de Bernardis, J. Bock, F. Bouchet, T. Bradshaw, J. Charra, S. Church, F. Couchot, J. Delabrouille, G. Efstathiou, M. Giard, Y. Giraud-Héraud, R. Gispert, M. Griffin, A. Lange, A. Murphy, F. Pajot, J. L. Puget, and I. Ristorcelli, "The High Frequency Instrument of Planck: Design and Performances," *Astrophysical Letters Communications*, vol. 37, p. 161, Feb. 2000.

[55] A. D. Turner, J. J. Bock, J. W. Beeman, J. Glenn, P. C. Hargrave, V. V. Hristov, H. T. Nguyen, F. Rahman, S. Sethuraman, and A. L. Woodcraft, "Silicon nitride micromesh bolometer array for submillimeter astrophysics," *Applied Optics*, vol. 40, pp. 4921–4932, Oct. 2001.

[56] M. J. Griffin, L. G. Vigroux, and B. M. Swinyard, "SPIRE: a bolometer instrument for FIRST," in *Advanced Technology MMW, Radio and Terahertz Telescopes* (T. G. Phillips, ed.), vol. 3357 of *Proceedings of the SPIE*, pp. 404–413, 1998.

[57] S. H. Moseley, C. A. Allen, D. Benford, C. D. Dowell, D. A. Harper, T. G. Phillips, R. F. Silverberg, and J. Staguhn, "The design and performance of the 384-element imaging submillimeter detector arrays for HAWC and SHARC II," *Nuclear Instruments and Methods in Physics Research A*, vol. 520, pp. 417–420, Mar. 2004.

[58] "Spiderweb bolometers." Available from http://www.planck.fr/article227.html.

[59] K. D. Irwin, "An application of electrothermal feedback for high resolution cryogenic particle detection," *Applied Physics Letters*, vol. 66, pp. 1998–2000, Apr. 1995.

[60] A. T. Lee, P. L. Richards, S. W. Nam, B. Cabrera, and K. D. Irwin, "A superconducting bolometer with strong electrothermal feedback," *Applied Physics Letters*, vol. 69, pp. 1801–1803, Sept. 1996.

[61] K. D. Irwin, G. C. Hilton, D. A. Wollman, and J. M. Martinis, "X-ray detection using a superconducting transition-edge sensor microcalorimeter with electrothermal feedback," *Applied Physics Letters*, vol. 69, pp. 1945–1947, Sept. 1996.

[62] B. A. Young, B. Cabrera, A. T. Lee, C. J. Martoff, B. Neuhauser, and J. P. McVittie, "Phonon-mediated detection of X-rays in silicon crystals using superconducting transition edge phonon sensors," *IEEE Transactions on Magnetics*, vol. 25, pp. 1347–1350, Feb. 1989.

[63] J. Hohne, M. Altmann, G. Angloher, P. Hettl, J. Jochum, T. Nussle, S. Pfnur, J. Schnagl, M. L. Sarsa, S. Wanninger, and F. van Feilitzsch, "High-resolution X-ray spectrometry using iridium-gold phase transition thermometers," *X-Ray Spectrometry*, vol. 28, pp. 396–398, May 1999.

[64] F. B. Kiewiet, M. P. Bruijn, H. F. C. Hoevers, A. C. Bento, W. A. Mels, and P. A. J. de Korte, "Fabrication and characterization of infrared and sub-mm spiderweb bolometers with low-$T_c$ superconducting transtion edge thermometers," *IEEE Transactions on Applied Superconductivity*, vol. 9, pp. 3862–3865, Apr. 1999.

[65] K. D. Irwin, G. C. Hilton, J. M. Martinis, S. Deiker, N. Bergren, S. W. Nam, D. A. Rudman, and D. A. Wollman, "A Mo-Cu superconducting transition-edge microcalorimeter with 4.5eV energy resolution at 6keV," *Nuclear Instruments and Methods in Physics Research A*, vol. 444, pp. 184–187, Apr. 2000.

[66] C. D. Reintsema, J. Beyer, S. W. Nam, S. Deiker, G. C. Hilton, K. Irwin, J. Martinis, J. Ullom, L. R. Vale, and M. MacIntosh, "Prototype system for superconducting quantum interference device multiplexing of large-format transition-edge sensor arrays," *Review of Scientific Instruments*, vol. 74, pp. 4500–4508, Oct. 2003.

[67] S.-F. Lee, J. M. Gildemeister, W. Holmes, A. T. Lee, and P. L. Richards, "Voltage-Biased Superconducting Transition-Edge Bolometer with Strong Electrothermal Feedback Operated at 370 mK," Appl. Opt., vol. 37, pp. 3391–3397, June 1998.

[68] C. L. Hunt, J. J. Bock, P. K. Day, A. Goldin, A. E. Lange, H. G. LeDuc, A. Vayonakis, and J. Zmuidzinas, "Transition-edge superconducting antenna-coupled bolometer," in *Millimeter and Submillimeter Detectors for Astronomy* (T. G. Phillips and J. Zmuidzinas, eds.), vol. 4855 of *Proceedings of the SPIE*, pp. 318–321, 2003.

[69] J. G. Staguhn, D. J. Benford, S. H. Moseley, C. A. Allen, C. R. Kennedy, S. Lefranc, S. F. Maher, F. Pajot, C. Rioux, R. A. Shafer, and G. M. Voellmer, "First astronomical images obtained with an array of multiplexed superconducting bolometers," *Nuclear Instruments and Methods in Physics Research A*, vol. 559, pp. 602–604, Apr. 2006.

[70] J. Staguhn, C. Allen, D. Benford, E. Sharp, T. Ames, R. Arendt, D. Chuss, E. Dwek, A. Kovacs, S. Maher, C. Marx, T. Miller, S. H. Moseley, S. Navarro, A. Sievers, G. Voellmer, and E. Wollack, "GISMO, a 2 mm Bolometer Camera Optimized for the Study of High Redshift Galaxies," *Journal of Low Temperature Physics*, vol. 151, pp. 709–714, May 2008.

[71] S. R. Dicker, J. A. Abrahams, P. A. R. Ade, T. J. Ames, D. J. Benford, T. C. Chen, J. A. Chervenak, M. J. Devlin, K. D. Irwin, P. M. Korngut, S. Maher, B. S. Mason, M. Mello, S. H. Moseley, R. D. Norrod, R. A. Shafer, J. G. Staguhn, D. J. Talley, C. Tucker, B. A. Werner, and S. D. White, "A 90-GHz bolometer array for the Green Bank Telescope," in *Millimeter and Submillimeter Detectors and Instrumentation for Astronomy III* (J. Zmuidzinas, W. S. Holland, S. Withington, and W. D. Duncan, eds.), vol. 6275 of *Proceedings of the SPIE*, 2006.

[72] J. van der Kuur, P. A. J. de Korte, P. de Groene, N. H. R. Baars, M. P. Lubbers, and M. Kiviranta, "Implementation of frequency domain multiplexing in imaging arrays of microcalorimeters," *Nuclear Instruments and Methods in Physics Research A*, vol. 520, pp. 551–554, Mar. 2004.

[73] J. van der Kuur, P. A. J. de Korte, H. F. C. Hoevers, M. P. Bruijn, M. L. Ridder, M. Kiviranta, and H. Seppä, "Frequency-domain multiplexing development for high-count-rate microcalorimeters," *Nuclear Instruments and Methods in Physics Research A*, vol. 559, pp. 820–822, Apr. 2006.

[74] M. A. Kinch and B. V. Rollin, "Detection of millimetre and sub-millimetre wave radiation by free carrier absorption in a semiconductor ," *British Journal of Applied Physics*, vol. 14, pp. 672–676, Oct. 1963.

[75] M. G. Hauser and H. A. Notarys, "Composite Bolometers for Millimeter-Wave Astronomy.," in *Bulletin of the American Astronomical Society*, vol. 7, p. 409, June 1975.

[76] N. S. Nishioka, P. L. Richards, and D. P. Woody, "Composite bolometers for submillimeter wavelengths.," *Applied Optics*, vol. 17, pp. 1562–1567, May 1978.

[77] L. Lesyna, T. P. L. Roellig, and P. Kittel, "Bolometers operated at 0.1 K and 0.2 K cooled by adiabatic demagnetization," *International Journal of Infrared and Millimeter Waves*, vol. 5, pp. 755–760, June 1984.

[78] D. C. Alsop, C. Inman, A. E. Lange, and T. Wilbanks, "Design and construction of high-sensitivity, infrared bolometers for operation at 300mK.," *Applied Optics*, vol. 31, pp. 6610–6615, Nov. 1992.

[79] J. M. Gildemeister, A. T. Lee, and P. L. Richards, "A fully lithographed voltage-biased superconducting spiderweb bolometer," *Applied Physics Letters*, vol. 74, pp. 868–891, Feb. 1999.

[80] J. Hubmayr, F. Aubin, E. Bissonnette, M. Dobbs, S. Hanany, A. T. Lee, K. MacDermid, X. Meng, I. Sagiv, and G. Smecher, "Design and characterization of TES bolometers and SQUID readout electronics for a balloon-borne application," in *Millimeter and Submillimeter Detectors and Instrumentation for Astronomy IV*, vol. 7020 of *Proceedings of the SPIE*, p. 70200J, Aug. 2008.

[81] P. Mauskopf, D. Morozov, D. Glowacka, D. Goldie, S. Withington, M. Bruijn, P. DeKorte, H. Hoevers, M. Ridder, J. Van Der Kuur, and J.-R. Gao, "Development of transition edge superconducting bolometers for the SAFARI far-infrared spectrometer on the SPICA space-borne telescope," in *Millimeter and Submillimeter Detectors and Instrumentation for Astronomy IV*, vol. 7020 of *Proceedings of the SPIE*, p. 70200N, Aug. 2008.

[82] P. D. Mauskopf, E. Gerecht, and B. K. Rownd, "BOLOCAM: A 144 Element Bolometer Array camera for Millimeter-Wave Imaging," in *Imaging at Radio through Submillimeter Wavelengths* (J. G. Mangum and S. J. E. Radford, eds.), vol. 217 of *Astronomical Society of the Pacific Conference Series*, pp. 115–123, 2000.

[83] E. Kreysa, H.-P. Gemuend, J. Gromke, C. G. Haslam, L. Reichertz, E. E. Haller, J. W. Beeman, V. Hansen, A. Sievers, and R. Zylka, "Bolometer array development at the Max-Planck-Institut fuer Radioastronomie," in *Advanced Technology MMW, Radio, and Terahertz Telescopes* (T. G. Phillips, ed.), vol. 3357 of *Proceedings of the SPIE*, pp. 319–325, 1998.

[84] E. Kreysa, F. Bertoldi, H.-P. Gemuend, K. M. Menten, D. Muders, L. A. Reichertz, P. Schilke, R. Chini, R. Lemke, T. May, H.-G. Meyer, and V. Zakosarenko, "LABOCA: a first generation bolometer camera for APEX," in *Millimeter and Submillimeter Detectors for Astronomy* (T. G. Phillips and J. Zmuidzinas, eds.), vol. 4855 of *Proceedings of the SPIE*, pp. 41–48, 2003.

[85] W. Holland, M. MacIntosh, A. Fairley, D. Kelly, D. Montgomery, D. Gostick, E. Atad-Ettedgui, M. Ellis, I. Robson, M. Hollister, A. Woodcraft, P. Ade, I. Walker, K. Irwin, G. Hilton, W. Duncan, C. Reintsema, A. Walton, W. Parkes, C. Dunare, M. Fich, J. Kycia, M. Halpern, D. Scott, A. Gibb, J. Molnar, E. Chapin, D. Bintley, S. Craig, T. Chylek, T. Jenness, F. Economou, and G. Davis, "SCUBA-2: a 10,000-pixel submillimeter camera for the James Clerk Maxwell Telescope," in *Millimeter and Submillimeter Detectors and Instrumentation for Astronomy III* (J. Zmuidzinas, W. S. Holland, S. Withington, and W. D. Duncan, eds.), vol. 6275 of *Proceedings of the SPIE*, p. 62751E, 2006.

[86] D. Twerenbold and A. Zehnder, "Superconducting Sn/Sn-oxide/Sn tunneling junctions as high-resolution x-ray detectors," *Journal of Applied Physics*, vol. 61, pp. 1–7, Jan. 1987.

[87] S. Ariyoshi, C. Otani, A. Dobroiu, H. Sato, K. Kawase, H. M. Shimizu, T. Taino, and H. Matsuo, "Terahertz imaging with a direct detector based on superconducting tunnel junctions," *Applied Physics Letters*, vol. 88, pp. 203503–203508, May 2006.

[88] P. K. Day, H. G. LeDuc, B. A. Mazin, A. Vayonakis, and J. Zmuidzinas, "A broadband superconducting detector suitable for use in large arrays," *Nature*, vol. 425, pp. 817–821, Oct. 2003.

[89] W. S. Holland, W. Duncan, B. D. Kelly, K. D. Irwin, A. J. Walton, P. A. R. Ade, and E. I. Robson, "SCUBA-2: a new generation submillimeter imager for the James Clerk Maxwell Telescope," in *Millimeter and Submillimeter Detectors for Astronomy* (T. G. Phillips and J. Zmuidzinas, eds.), vol. 4855 of *Proceedings of the SPIE*, pp. 1–18, 2003.

[90] B. C. Matthews, J. S. Greaves, W. S. Holland, M. C. Wyatt, M. J. Barlow, P. Bastien, C. A. Beichman, A. Biggs, H. M. Butner, W. R. F. Dent, J. Di Francesco, C. Dominik, L. Fissel, P. Friberg, A. G. Gibb, M. Halpern, R. J. Ivison, R. Jayawardhana, T. Jenness, D. Johnstone, J. J. Kavelaars, J. L. Marshall, N. Phillips, G. Schieven, I. A. G. Snellen, H. J. Walker, D. Ward-Thompson, B. Weferling, G. J. White, J. Yates, M. Zhu, and A. Craigon, "An Unbiased Survey of 500 Nearby Stars for Debris Disks: A JCMT Legacy Program," *Publications of the Astronomical Society of the Pacific*, vol. 119, pp. 842–854, Aug. 2007.

[91] D. Ward-Thompson, J. Di Francesco, J. Hatchell, M. R. Hogerheijde, D. Nutter, P. Bastien, S. Basu, I. Bonnell, J. Bowey, C. Brunt, J. Buckle, H. Butner, B. Cavanagh, A. Chrysostomou, E. Curtis, C. J. Davis, W. R. F. Dent, E. van Dishoeck, M. G. Edmunds, M. Fich, J. Fiege, L. Fissel, P. Friberg, R. Friesen, W. Frieswijk, G. A. Fuller, A. Gosling, S. Graves, J. S. Greaves, F. Helmich, R. E. Hills, W. S. Holland, M. Houde, R. Jayawardhana, D. Johnstone, G. Joncas, H. Kirk, J. M. Kirk, L. B. G. Knee, B. Matthews, H. Matthews, C. Matzner, G. H. Moriarty-Schieven, D. Naylor, R. Padman, R. Plume, J. M. C. Rawlings, R. O. Redman, M. Reid, J. S. Richer, R. Shipman, R. J. Simpson, M. Spaans, D. Stamatellos, Y. G. Tsamis, S. Viti, B. Weferling, G. J. White, A. P. Whitworth, J. Wouterloot, J. Yates, and M. Zhu, "The James Clerk Maxwell Telescope Legacy Survey of

Nearby Star-forming Regions in the Gould Belt," *Publications of the Astronomical Society of the Pacific*, vol. 119, pp. 855–870, Aug. 2007.

[92] P. Bastien, É. Bissonnette, P. Ade, G. Pisano, G. Savini, T. Jenness, D. Johnstone, and B. Matthews, "POL-2: A Polarimeter for SCUBA-2," *Journal of the Royal Astronomical Society of Canada*, vol. 99, pp. 133–135, Aug. 2005.

[93] D. A. Naylor and B. G. Gom, "SCUBA-2 imaging Fourier transform spectrometer," in *Imaging Spectrometry IX* (S. S. Shen and P. E. Lewis, eds.), vol. 5159 of *Proceedings of the SPIE*, pp. 91–101, 2003.

[94] D. Gostick, D. Montgomery, B. Wall, H. McGregor, M. Cliffe, A. Woodcraft, and F. Gannaway, "The cryo-mechanical design of SCUBA-2: a wide-field imager for the James Clerk Maxwell Telescope," in *Ground-based Instrumentation for Astronomy* (A. F. M. Moorwood and I. Masanori, eds.), vol. 5492 of *Proceedings of the SPIE*, pp. 1743–1754, 2004.

[95] A. L. Woodcraft, F. C. Gannaway, D. C. Gostick, and D. Bintley, "Thermal design of the SCUBA-2 instrument detector stage and enclosure," in *Millimeter and Submillimeter Detectors for Astronomy II* (J. Zmuidzinas, W. S. Holland, and S. Withington, eds.), vol. 5498 of *Proceedings of the SPIE*, pp. 446–454, 2004.

[96] P. A. R. Ade, G. Pisano, C. Tucker, and S. Weaver, "A review of metal mesh filters," in *Millimeter and Submillimeter Detectors and Instrumentation for Astronomy III* (J. Zmuidzinas, W. S. Holland, S. Withington, and W. D. Duncan, eds.), vol. 6275 of *Proceedings of the SPIE*, p. 62750U, 2006.

[97] T. Chylek, S. C. Craig, T. C. Chuter, H. J. Lewsley, and E. A. Hileman, "JCMT Telescope structure modifications and facility upgrades for SCUBA-2 instrument," in *Ground-based and Airborne Telescopes* (L. M. Stepp, ed.), vol. 6267 of *Proceedings of the SPIE*, p. 62673L, 2006.

[98] I. J. Saunders, L. Ploeg, M. Dorrepaal, and B. van Venrooij, "Fabrication and metrology of freeform aluminum mirrors for the SCUBA-2 instrument," in *Optical Manufacturing and Testing VI* (H. P. Stahl, ed.), vol. 5869 of *Proceedings of the SPIE*, pp. 14–25, 2005.

[99] E. Atad-Ettedgui, T. Peacocke, D. Montgomery, D. Gostick, H. McGregor, M. Cliff, I. J. Saunders, L. Ploeg, M. Dorrepaal, and B. van Venrooij, "Optomechanical design of SCUBA-2," in *Optomechanical Technologies for Astronomy* (E. Atad-Ettedgui, J. Antebi, and D. Lemke, eds.), vol. 6273 of *Proceedings of the SPIE*, p. 62732H, 2006.

[100] W. Duncan, W. S. Holland, M. D. Audley, M. Cliffe, T. Hodson, B. D. Kelly, X. Gao, D. C. Gostick, M. MacIntosh, H. McGregor, T. Peacocke, K. D. Irwin, G. C. Hilton, S. W. Deiker, J. Beier, C. D. Reintsema, A. J. Walton, W. Parkes, T. Stevenson, A. M. Gundlach, C. Dunare, and P. A. R. Ade, "SCUBA-2: Developing the Detectors," in *Millimeter and Submillimeter Detectors for Astronomy* (T. G. Phillips and J. Zmuidzinas, eds.), vol. 4855 of *Proceedings of the SPIE*, pp. 19–29, 2003.

[101] M. D. Audley, G. Pisano, W. S. Holland, W. D. Duncan, W. Parkes, and P. A. R. Ade, "Modeling the electromagnetic properties of the SCUBA-2 detecotrs," in *Millimeter and Submillimeter Detectors for Astronomy II* (J. Zmuidzinas, W. S. Holland, and S. Withington, eds.), vol. 5498 of *Proceedings of the SPIE*, pp. 416–427, 2004.

[102] J. A. Chervenak, K. D. Irwin, E. N. Grossman, J. M. Martinis, C. D. Reintsema, and M. E. Huber, "Superconducting multiplexer for arrays of transition edge sensors," *Applied Physics Letters*, vol. 74, pp. 4043–4045, June 1999.

[103] P. A. J. de Korte, J. Beyer, S. Deiker, G. C. Hilton, K. D. Irwin, M. Macintosh, S. W. Nam, C. D. Reintsema, L. R. Vale, and M. E. Huber, "Time-division superconducting quantum interference device multiplexer for transition-edge sensors," *Review of Scientific Instruments*, vol. 74, pp. 3807–3815, Aug. 2003.

[104] M. J. MacIntosh. Personal communication.

[105] R. P. Welty and J. M. Martinis, "A series array of dc SQUIDs," *IEEE Transactions on Magnetics*, vol. 27, pp. 2924–2926, Mar. 1991.

[106] M. D. Audley, W. S. Holland, T. Hodson, M. MacIntosh, I. Robson, K. D. Irwin, G. Hilton, W. D. Duncan, C. Reintsema, A. J. Walton, W. Parkes, P. A. R. Ade, I. Walker, M. Fich, J. Kycia, M. Halpern, D. A. Naylor, G. Mitchell, and P. Bastien, "An update on the SCUBA-2 project," in *Millimeter and Submillimeter Detectors for Astronomy II* (J. Zmuidzinas, W. S. Holland, and S. Withington, eds.), vol. 5498 of *Proceedings of the SPIE*, pp. 63–77, 2004.

[107] D. A. Naylor, G. R. Davis, B. G. Gom, T. A. Clark, and M. J. Griffin, "Atmospheric Transmission at Submillimetre Wavelengths from Mauna Kea," MNRAS, vol. 315, pp. 622–628, Mar. 2000.

[108] "SCUBA tau ratios." http://www.jach.hawaii.edu/JCMT/continuum/.

[109] K. D. Irwin and G. C. Hilton, "Transition-edge sensors," in *Cryogenic Particle Detectors* (C. Enss, ed.), vol. 99 of *Topics in Applied Physics*, pp. 63–149, Springer-Verlag, 2005.

[110] M. D. Niemack, *Towards Dark Energy: Design, Development and Preliminary Data from ACT*. PhD thesis, Princeton University, 2008.

[111] M. D. Audley. Personal communication.

[112] P. Léna, *Observational Astrophysics*. Springer-Verlag, 1988.

[113] "SCUBA-2 Array Technology Proof-of-Concept Review," Nov. 2002.

[114] C. Kittel, *Introduction to Solid State Physics*. John Wiley, seventh ed., 1996.

[115] M. A. Lindeman, S. Bandler, R. P. Brekosky, J. A. Chervenak, E. Figueroa-Feliciano, F. M. Finkbeiner, M. J. Li, and C. A. Kilbourne, "Impedance measurements and modeling of a transition-edge-sensor calorimeter," *Review of Scientific Instruments*, vol. 75, pp. 1283–1289, Apr. 2004.

[116] D. Bintley. Personal communication.

[117] W. Parkes. Personal communication.

[118] W. S. Holland. Personal communication.

[119] D. Bintley, "Detector Speed of Response," SCUBA-2 Verification Report SC2/TRE/A300/013, UK Astronomy Technology Centre, 2008.

[120] G. K. White and P. J. Meeson, *Experimental Techniques in Low-Temperature Physics*. Oxford University Press, fourth ed., 2002.

[121] F. Pobell, *Matter and Methods at Low Temperatures*. Springer-Verlag, third ed., 2007.

[122] O. V. Lounasmaa, *Experimental Principles and Methods Below 1K*. Academic Press, 1974.

[123] R. Radebaugh and J. D. Siegwarth, "Dilution refrigerator technology," *Cryogenics*, vol. 11, pp. 368–384, Oct. 1971.

[124] H. London, G. R. Clarke, and E. Mendoza, "Osmotic Pressure of $He^3$ in Liquid $He^4$, with Proposals for a Refrigerator to Work below 1°K," *Phys. Rev.*, vol. 128, p. 1992, May 1962.

[125] D. O. Edwards, D. F. Brewer, P. Seligman, M. Skertic, and M. Yaqub, "Solubility of $He^3$ in Liquid $He^4$ at 0°K," *Physical Review Letters*, vol. 15, pp. 773–775, Nov. 1965.

[126] D. S. Greywall, "Specific heat of normal liquid $^3$He," Phys. Rev. B, vol. 27, pp. 2747–2766, Mar. 1983.

[127] D. S. Greywall, "$^3$He specific heat and thermometry at millikelvin temperatures," Phys. Rev. B, vol. 33, pp. 7520–7538, June 1986.

[128] G. E. Watson, J. D. Reppy, and R. C. Richardson, "Low-Temperature Density and Solubility of $He^3$ in Liquid $He^4$ under Pressure," *Physical Review*, vol. 188, pp. 384–396, Dec. 1969.

[129] G. Frossati, "Experimetal techniques: Methods for cooling below 300 mK," *Journal of Low Temperature Physics*, vol. 87, pp. 595–633, May 1992.

[130] D. S. Betts, *An Introduction to Millikelvin Technology*. Cambridge University Press, 1989.

[131] J. Kraus, "New condensation stage for a $He^3$–$He^4$ dilution refrigerator," *Cryogenics*, vol. 17, pp. 173–175, Mar. 1977.

[132] K. Uhlig, "$^3$He/$^4$He dilution refrigerator without a pumped $^4$He stage," *Cryogenics*, vol. 27, pp. 454–457, Aug. 1987.

[133] K. Uhlig and W. Hehn, "$^3$He/$^4$He dilution refrigerator with Gifford-McMahon precooling," *Cryogenics*, vol. 33, pp. 1028–1031, Nov. 1993.

[134] K. Uhlig and W. Hehn, "$^3$He/$^4$He dilution refrigerator combined with Gifford-McMahon cooler," *Cryogenics*, vol. 34, pp. 587–589, July 1994.

[135] K. Uhlig and W. Hehn, "$^3$He/$^4$He dilution refrigerator precooled by Gifford-McMahon refrigerator," *Cryogenics*, vol. 37, pp. 279–282, July 1997.

[136] K. Uhlig, "$^3$He/$^4$He dilution refrigerator precooled by Gifford-McMahon cooler II. Measurements of the vibrational heat leak," *Cryogenics*, vol. 42, pp. 569–575, July 2002.

[137] Y. Koike, Y. Morii, T. Igarashi, M. Kubota, Y. Hiresaki, and K. Tanida, "A dilution refrigerator using the pulse tube and GM hybrid cryocooler for neutron scattering," *Cryogenics*, vol. 39, pp. 579–583, Nov. 1999.

[138] K. Uhlig, "$^3$He/$^4$He dilution refrigerator with pulse-tube refrigerator precooling," *Cryogenics*, vol. 42, pp. 73–77, Feb. 2002.

[139] K. Uhlig, ""Dry" dilution refrigerator with pulse-tube precooling," *Cryogenics*, vol. 44, pp. 53–57, Jan. 2004.

[140] T. Prouvé, H. Godfrin, C. Gianése, S. Triqueneaux, and A. Ravex, "Pulse-Tube Dilution Refrigeration Below 10 mK," *Journal of Low Temperature Physics*, vol. 148, pp. 909–914, Sept. 2007.

[141] V. S. Edel'man, "A dilution refrigerator with condensation pump," *Cryogenics*, vol. 12, pp. 387–389, Oct. 1972.

[142] G. Teleberg, S. T. Chase, and L. Piccirillo, "A miniature dilution refrigerator for sub-kelvin detector arrays," in *Millimeter and Submillimeter Detectors and Instrumentation for Astronomy III* (J. Zmuidzinas, W. S. Holland, S. Withington, and W. D. Duncan, eds.), vol. 6275 of *Proceedings of the SPIE*, p. 62750D, 2006.

[143] C. Wang and P. E. Gifford, "Development of 4 K pulse tube cryorefrigerators at Cryomech," in *Advances in Cryogenic Engineering* (S. Breon, M. Dipirro, D. Glaister, J. Hull, P. Kittel, V. R. R. Pecharsky, J. Theilacker, S. van Sciver, J. I. Weisend, and A. Zeller, eds.), vol. 613 of *American Institute of Physics Conference Series*, pp. 641–648, 2002.

[144] C. Wang, G. Thummes, and C. Heiden, "A two-stage pulse tube cooler operating below 4 K," *Cryogenics*, vol. 37, pp. 159–164, Mar. 1997.

[145] C. Wang, G. Thummes, and C. Heiden, "Experimental study of staging method for two-stage pulse tube refrigerators for liquid $^4$He temperatures," *Cryogenics*, vol. 37, pp. 857–863, Dec. 1997.

[146] M. I. Hollister, A. L. Woodcraft, W. S. Holland, and D. Bintley, "Performance of the SCUBA-2 Dilution Refrigerator," in *Millimeter and Submillimeter Detectors and Instrumentation for Astronomy IV* (J. Zmuidzinas, W. S. Holland, S. Withington, and W. D. Duncan, eds.), vol. 7020 of *Proceedings of the SPIE*, p. 70200Y, 2008.

[147] J. Kraus, K. Uhlig, and W. Wiedemann, "EnthalpyŮpressure ($H$—$p$) diagram of $He^3$ in the range 1.0 K$\leq T \leq$4.17 K and 0$\leq p \leq$6.5 atm and inversion curve for $T \leq$ 4.17 K," *Cryogenics*, vol. 14, pp. 29–35, Jan. 1974.

[148] D. I. Bradley. Personal communication.

[149] A. L. Woodcraft, "COMMENT: Comment on 'thermal boundary resistance of mechanical contacts between solids at sub-ambient temperatures'," *Journal of Physics D Applied Physics*, vol. 34, pp. 2932–2934, Sept. 2001.

[150] I. Didschuns, A. L. Woodcraft, D. Bintley, and P. C. Hargrave, "Thermal conductance measurements of bolted copper to copper joints at sub-kelvin temperatures," *Cryogenics*, vol. 44, pp. 293–299, May 2004.

[151] P. R. Roach, "Kevlar support for thermal isolation at low temperatures," *Review of Scientific Instruments*, vol. 63, pp. 3216–3217, May 1992.

[152] L. Duband, L. Hui, and A. Lange, "Thermal isolation of large loads at low temperature using Kevlar rope," *Cryogenics*, vol. 33, pp. 643–647, June 1993.

[153] D. Bintley, A. L. Woodcraft, and F. C. Gannaway, "Millikelvin thermal conductance measurements of compact rigid thermal isolation joints using sapphire sapphire contacts, and of copper and beryllium copper demountable thermal contacts," *Cryogenics*, vol. 47, pp. 333–342, May 2007.

[154] M. I. Hollister, M. D. Audley, W. D. Duncan, and W. S. Holland, "Finite-element Modelling of Magnetic Shielding for SCUBA-2," in *Millimeter and Submillimeter Detectors and Instrumentation for Astronomy III* (J. Zmuidzinas, W. S. Holland, S. Withington, and W. D. Duncan, eds.), vol. 6275 of *Proceedings of the SPIE*, p. 627522, 2006.

[155] G. Hilton and K. Irwin. Personal communication.

[156] D. R. Ladner, D. S. Martinez-Galarce, and D. McCammon, "Adiabatic Demagnetization Refrigerator Field Mapping and Shielding Models for a 70 mK Superconducting Transition Edge Sensor Array and Associated Electronics," in *AIP Conf. Proc. 823: Advances in Cryogenic Engineering* (J. G. Weisend, II, J. Barclay, S. Breon, J. Demko, M. Dipirro, J. P. Kelley, P. Kittel, A. Klebaner, J. Lock, J. Maddocks, T. Peterson, J. Pfotenhauer, A. Rowe, S. van Sciver, and A. Zeller, eds.), pp. 960–968, 2006.

[157] A. M. Forrest, "Meissner and Ochsenfeld revisited," *European Journal of Physics*, vol. 4, pp. 117–120, Apr. 1983.

[158] "Introduction to Magnetic Shielding." Available from http://www.amuneal.com.

[159] A. Woodcraft, R. V. Sudiwala, and R. S. Bhatia, "The thermal conductivity of C17510 beryllium-copper alloy below 1 K," *Cryogenics*, vol. 41, pp. 603–606, Aug. 2001.

[160] M. I. Hollister, H. M. McGregor, A. L. Woodcraft, D. Bintley, M. MacIntosh, and W. S. Holland, "Cryogenic Magnetic Shielding for SCUBA-2," in *Millimeter and Submillimeter Detectors and Instrumentation for Astronomy IV* (J. Zmuidzinas, W. S. Holland, S. Withington, and W. D. Duncan, eds.), vol. 7020 of *Proceedings of the SPIE*, p. 702023, 2008.

[161] A. L. Woodcraft, P. A. R. Ade, D. Bintley, J. S. House, C. L. Hunt, R. V. Sudiwala, W. B. Doriese, W. D. Duncan, G. C. Hilton, K. D. Irwin, C. D. Reintsema, J. N. Ullom, M. D. Audley, M. A. Ellis, W. S. Holland, M. Macintosh, C. C. Dunare, W. Parkes, A. J. Walton, J. B. Kycia, M. Halpern, and E. Schulte, "Electrical and optical measurements on the first SCUBA-2 prototype 1280 pixel submillimeter superconducting bolometer array," *Review of Scientific Instruments*, vol. 78, pp. 4502–4508, Feb. 2007.

[162] "National Geophysics Data Centre Earth's Magnetic Field Calculators." http://www.ngdc.noaa.gov/geomag/magfield.shtml.

[163] M. D. Niemack, "Measuring two-millimeter radiation with a prototype multiplexed TES receiver for ACT," in *Millimeter and Submillimeter Detectors for Astronomy III* (J. Zmuidzinas, W. S. Holland, and S. Withington, eds.), vol. 6275 of *Proceedings of the SPIE*, pp. 80–90, 2006.

[164] G. Hilton and M. J. MacIntosh. Personal communication.

[165] D. Bintley and P. Friberg. Personal communication.

[166] J. N. Ullom, M. F. Cunningham, T. Miyazaki, S. E. Labov, J. Clarke, T. M. Lanting, A. T. Lee, P. L. Richards, J. Yoon, and H. Spieler, "A frequency-domain read-out technique for large microcalorimeter arrays demonstrated using high-resolution gamma-ray sensors," *IEEE Transactions on Applied Superconductivity*, vol. 13, pp. 643–648, Feb. 2003.

[167] K. D. Irwin, J. A. Beall, W. B. Doriese, W. D. Duncan, G. C. Hilton, J. A. B. Mates, C. D. Reintsema, D. R. Schmidt, J. N. Ullom, L. R. Vale, B. L. Zink, and K. W. Lehnert, "Microwave SQUID multiplexers for low-temperature detectors," *Nuclear Instruments and Methods in Physics Research A*, vol. 559, pp. 802–804, Apr. 2006.

[168] J. Schlaerth, A. Vayonakis, P. Day, J. Glenn, J. Gao, S. Golwala, S. Kumar, H. Leduc, B. Mazin, J. Vaillancourt, and J. Zmuidzinas, "A Millimeter and Submillimeter Kinetic Inductance Detector Camera," *Journal of Low Temperature Physics*, vol. 151, pp. 684–689, May 2008.

[169] S. Doyle, P. Mauskopf, J. Naylon, A. Porch, and C. Duncombe, "Lumped Element Kinetic Inductance Detectors," *Journal of Low Temperature Physics*, vol. 151, pp. 530–536, Apr. 2008.

[170] R. S. Bhatia, J. J. Bock, P. A. R. Ade, A. Benoit, T. W. Bradshaw, B. P. Crill, M. J. Griffin, I. D. Hepburn, V. V. Hristov, A. E. Lange, P. V. Mason, A. G. Murray, A. H. Orlowska, and A. D. Turner, "The susceptibility of incoherent

detector systems to cryocooler microphonics.," *Cryogenics*, vol. 39, pp. 701–715, Aug. 1999.

[171] K. Uhlig, "Condensation stage of a pulse tube pre-cooled dilution refrigerator," *Cryogenics*, vol. 48, pp. 138–141, Mar. 2008.

[172] K. Uhlig, "$^3$He/$^4$He dilution refrigerator with high cooling capacity and direct pulse tube pre-cooling," *Cryogenics*, vol. 48, pp. 511–514, Nov. 2008.

[173] T. Prouvé, H. Godfrin, C. Gianése, S. Triqueneaux, and A. Ravex, "Pulse-Tube Dilution Refrigeration below 10 mK for Astrophysics," *Journal of Low Temperature Physics*, vol. 151, pp. 640–644, May 2008.

[174] M. Nahum, T. M. Eiles, and J. M. Martinis, "Electronic microrefrigerator based on a normal-insulator-superconductor tunnel junction," *Applied Physics Letters*, vol. 65, pp. 3123–3125, Dec. 1994.

[175] T. Nakagawa and H. Murakami, "Mid- and far-infrared astronomy mission SPICA," *Advances in Space Research*, vol. 40, pp. 679–683, Jan. 2007.

[176] F. P. Helmich and R. J. Ivison, "FIRI — A far-infrared interferometer," *Experimental Astronomy*, p. 15, July 2008.

[177] R. Giovanelli and S. Radford, "The CCAT Project," in *Bulletin of the American Astronomical Society*, vol. 38, p. 951, 2007.

[178] R. Radebaugh, "Pulse tube cryocoolers for cooling infrared sensors," in *Infrared Technology and Applications XXVI* (B. F. Andersen, G. F. Fulop, and M. Strojnik, eds.), vol. 4130 of *Proceedings of the SPIE*, pp. 363–379, 2000.

[179] W. L. Swift, M. V. Zagarola, G. F. Nelis, J. A. McCormick, H. Sixsmith, and J. A. Gibbon, "Developments in Turbo Brayton technology for low temperature applications," *Cryogenics*, vol. 39, pp. 989–995, Dec. 1999.

[180] J. W. L. Köhler and C. O. Jonkers, "Fundamentals of the Gas Refrigeration Machine," *Philips Tech. Rev.*, vol. 16, pp. 69–78, Mar. 1654.

[181] H. O. McMahon and W. E. Gifford, "A New Low-temperature Gas Expansion Cycle - Part I," in *Advances in Cryogenic Engineering* (K. D. Timmerhaus, ed.), vol. 5, pp. 354–366, 1960.

[182] T. Hashimoto, T. Eda, M. Yabuki, T. Kuriyama, and H. Nakagome, "Recent Progress on Application of High Entropy Magnetic Material to the Regenerator in Helium Temperature Range," in *Proc. 7th Int. Cryocooler Conf.*, 1993.

[183] H. Smith, R. E. Hills, S. Withington, J. Richer, J. Leech, R. Williamson, H. Gibson, R. Dace, P. G. Ananthasubramanian, R. W. Barker, R. Baldwin, H. Stevenson, P. Doherty, D. Molloy, V. Quy, C. Lush, S. Hales, W. R. F. Dent, I. Pain, R. Wall, P. R. Hastings, B. Graham, T. E. C. Baillie, K. Laidlaw, R. J. Bennett, I. Laidlaw, W. Duncan, M. A. Ellis, R. O. Redman, R. Wooff, K. K. Yeung, J. T. Fitzsimmons, L. Avery, D. Derdall, D. Josephson, A. Anthony, R. Atwal,

T. Chylek, D. J. Shutt, P. Friberg, N. P. Rees, R. Philips, M. Kroug, T. M. Klapwijk, and T. Zijlstra, "HARP-B: a 350-GHz 16-element focal plane array for the James Clerk Maxwell telescope," in *Millimeter and Submillimeter Detectors for Astronomy* (T. G. Phillips and J. Zmuidzinas, eds.), vol. 4855 of *Proceedings of the SPIE*, pp. 338–348, 2003.

[184] W. E. Gifford and R. C. Longsworth, "Pulse tube refrigeration," *Trans. of the ASME, Journal of Engineering for Industry*, Aug. 1964.

[185] E. I. Mikulin, A. A. Tarasov, and M. P. Shkrebyonock, "Low temperature expansion pulse tubes," in *Advances in Cryogenic Engineering* (R. W. Fast, ed.), vol. 29, pp. 629–637, 1984.

[186] N. Jiang, U. Lindemann, F. Giebeler, and G. Thummes, "A $^3$He pulse tube cooler operating down to 1.3 K," *Cryogenics*, vol. 44, pp. 809–816, Nov. 2004.

[187] M. J. Devlin, S. R. Dicker, J. Klein, and M. P. Supanich, "A high capacity completely closed-cycle 250 mK $^3$He refrigeration system based on a pulse tube cooler," *Cryogenics*, vol. 44, pp. 611–616, Sept. 2004.

[188] P. Debye, "Einige Bemerkungen zur Magnetisierung bei tiefer Temperatur," *Annalen der Physik*, vol. 386, pp. 1154–1160, 1926.

[189] W. F. Giauque, "A Thermodynamic Treatment of Certain Magnetic Effects. A Proposed Method for Producing Temperatures Considerably Below 1° Absolute," *Journal of the American Chemistry Society*, vol. 49, pp. 1864–1870, Oct. 1927.

[190] W. J. De Haas, E. C. Wiersma, and H. A. Kramers, "Temperatures below 0.27K reached in Holland," *Nature*, vol. 131, p. 719, May 1933.

[191] W. F. Giauque and D. P. MacDougall, "Attainment of Temperatures Below 1° Absolute by Demagnetization of $Gd_2(SO_4)_3 \cdot 8\,H_2O$," *Physical Review*, vol. 43, p. 768, May 1933.

[192] N. Kürti and F. Simon, "A simple arrangement for the magnetic cooling method," *Physica*, vol. 1, pp. 1107–1108, May 1934.

[193] K. W. Mess, J. Lubbers, L. Niesen, and W. J. Huiskamp, "Thermal and magnetic properties of cerium magnesium nitrate below 1K," *Physica*, vol. 41, pp. 260–288, Feb. 1969.

[194] J. Darby, J. Hatton, B. V. Rollin, E. F. W. Seymour, and H. B. Silsbee, "Experiments on the Production of Very Low Temperatures by Two-Stage Demagnetization," *Proceedings of the Physical Society A*, vol. 64, pp. 861–867, Oct. 1951.

[195] C. V. Heer, C. B. Barnes, and J. G. Daunt, "The Design and Operation of a Magnetic Refrigerator for Maintaining Temperatures below 1°K," *Review of Scientific Instruments*, vol. 25, pp. 1088–1098, Nov. 1954.

[196] D. McCammon, R. Almy, S. Deiker, J. Morgenthaler, R. L. Kelley, F. J. Marshall, S. H. Moseley, C. K. Stahle, and A. E. Szymkowiak, "A sounding rocket

payload for X-ray astronomy employing high-resolution microcalorimeters.," *Nuclear Instruments and Methods in Physics Research A*, vol. 370, pp. 266–268, Feb. 1996.

[197] D. K. Griffin, H. Sugita, L. Duband, N. Luchier, B. Winter, and P. Hargrave, "Thermal design of the SPICA/ESI instrument," in *Millimeter and Submillimeter Detectors for Astronomy III* (J. Zmuidzinas, W. S. Holland, S. Withington, and W. D. Duncan, eds.), vol. 6275 of *Proceedings of the SPIE*, p. 62750E, 2006.

[198] C. M. Bradford, P. A. R. Ade, J. E. Aguirre, J. J. Bock, M. Dragovan, L. Duband, L. Earle, J. Glenn, H. Matsuhara, B. J. Naylor, H. T. Nguyen, M. Yun, and J. Zmuidzinas, "Z-Spec: a broadband millimeter-wave grating spectrometer: design, construction, and first cryogenic measurements," in *Millimeter and Submillimeter Detectors for Astronomy II* (J. Zmuidzinas, W. S. Holland, and S. Withington, eds.), vol. 5498 of *Proceedings of the SPIE*, pp. 257–266, 2004.

[199] M. Dobbs, N. W. Halverson, P. A. R. Ade, K. Basu, A. Beelen, F. Bertoldi, C. Cohalan, H. M. Cho, R. Güsten, W. L. Holzapfel, Z. Kermish, R. Kneissl, A. Kovács, E. Kreysa, T. M. Lanting, A. T. Lee, M. Lueker, J. Mehl, K. M. Menten, D. Muders, M. Nord, T. Plagge, P. L. Richards, P. Schilke, D. Schwan, H. Spieler, A. Weiss, and M. White, "APEX-SZ first light and instrument status," *New Astronomy Review*, vol. 50, pp. 960–968, Dec. 2006.

[200] B. Neganov, N. Borisov, and M. Liburg, "A Method of Producing Very Low Temperatures by Dissolving $He^3$ in $He^4$," *Soviet Journal of Experimental and Theoretical Physics*, vol. 23, p. 959, Dec. 1966.

[201] D. J. Cousins, S. N. Fisher, A. M. Guènault, R. P. Haley, I. E. Miller, G. R. Pickett, G. N. Plenderleith, P. Skyba, P. Y. A. Thibault, and M. G. Ward, "An advanced dilution refrigerator designed for the new Lancaster microkelvin facility," *Journal of Low Temperature Physics*, vol. 114, pp. 547–570, Mar. 1999.

[202] P. A. Fisher, J. N. Ullom, and M. Nahum, "High-power on-chip microrefrigerator based on a normal- metal/insulator/superconductor tunnel junction," *Applied Physics Letters*, vol. 74, pp. 2705–2709, May 1999.

[203] N. A. Miller, J. A. Beall, D. J. Benford, T. C. Chen, J. A. Chervenak, W. D. Duncan, F. Finkbeiner, G. C. Hilton, K. D. Irwin, S. H. Moseley, G. C. O'Neil, D. R. Schmidt, L. R. Vale, R. F. Silverberg, and J. N. Ullom, "First demonstration of a superconducting detector cooled by solid-state refrigerators.," *APS Meeting Abstracts*, p. 9012, Mar. 2007.

[204] R. F. Silverberg, D. J. Benford, T. Chen, J. Chervenak, F. M. Finkbeiner, N. A. Miller, D. Schmidt, and J. N. Ullom, "Superconducting Transition-Edge Sensor Bolometers with Integrated Electron-tunneling Refrigerators," *Journal of Low Temperature Physics*, vol. 151, pp. 489–494, Apr. 2008.

[205] T. van Duzer and C. W. Turner, *Principles of Superconductive Devices and Circuits*. Prentice Hall, second ed., 1998.

[206] J. C. Gallop, *SQUIDs, the Josephson Effects and Superconducting Electronics*. Taylor & Francis, 1991.

[207] M. I. Hollister and A. L. Woodcraft, "Proposed designs for a "dry" dilution refrigerator with a 1K condenser," *Cryogenics*, 2009. In press.

[208] D. J. Frank and T. C. Nast, "Getter-activated cryogenic thermal switch," in *Advances in Cryogenic Engineering* (R. W. Fast, ed.), vol. 31, pp. 933–940, 1986.

[209] A. C. Rose-Innes, *Low Temperature Laboratory Techniques*. English Universities Press, 1973.